

Hamed Tasalloti Kashani

ON DISSIMILAR WELDING: A NEW APPROACH FOR ENHANCED DECISION-MAKING

Thesis for the degree of Doctor of Science (Technology) to be presented with due permission for public examination and criticism in the Auditorium 2310 at Lappeenranta University of Technology, Lappeenranta, Finland on the 7th of July, 2017, at noon.

Acta Universitatis
Lappeenrantaensis 749

- Supervisors Associate Professor, Docent Paul Kah
LUT School of Energy Systems
Lappeenranta University of Technology
Finland
- Professor Jukka Martikainen
LUT School of Energy Systems
Lappeenranta University of Technology
Finland
- Reviewers Professor Thomas Böllinghaus
Department of Component Safety
Federal Institute of Material Research and Testing
Germany
- Professor Suck-Joo Na
Department of Mechanical Engineering
Korea Advanced Institute of Science and Technology
South Korea
- Opponent Professor Volodymyr Ponomarev
Faculty of Mechanical Engineering
Federal University of Uberlândia
Brazil

ISBN 978-952-335-093-9
ISBN 978-952-335-094-6 (PDF)
ISSN-L 1456-4491
ISSN 1456-4491

Lappeenrannan teknillinen yliopisto
Yliopistopaino 2017

Abstract

Hamed Tasalloti Kashani

On dissimilar welding: a new approach for enhanced decision-making

Lappeenranta 2017

100 pages

Acta Universitatis Lappeenrantaensis 749

Diss. Lappeenranta University of Technology

ISBN 978-952-335-093-9, ISBN 978-952-335-094-6 (PDF), ISSN-L 1456-4491, ISSN 1456-4491

Demand for dissimilar welding has shown continuous growth in a wide variety of industrial fields, including power generation, petrochemical plants, oil and gas exploration, transportation and aerospace manufacturing. Dissimilar welding enables the desirable properties of different materials to be combined in a single welded joint. Although dissimilar welding is advantageous in many applications, it is usually a more difficult and problematic operation than similar metals welding. The challenges stem from disparity in the physics, mechanics and metallurgy of the constituent materials in the welded joint.

The objective of the current thesis is to provide a critical literature review and experimental study of a number of dissimilar welds with different combinations of base metals and welding processes. Additionally, the study aims to utilize the findings from the experiments and review in design of a novel decision-making method to improve the design and reliability of welded structures.

This dissertation is an article-based study that includes the outcome of seven articles presented in the second part of the work. The results of the experimental studies and review show the consequential alterations in the microstructure and mechanical properties of the welds focusing on their relation to the process parameters and techniques used. The results testify to the critical role of selection of the materials, welding process and parameters in achieving a quality weld with appropriate metallurgical and mechanical characteristics.

A new database-driven and application-based selection method is presented that aims to reduce the risk of failure in manufacture or during service. To this end, a modified design for manufacturing and assembly (DFMA) approach for welding is utilised to introduce an application-based selection method with a built-in expertise feature in agreement with the concurrent engineering (CE) concept into dissimilar welding decision-making. To realise the benefits of CE and enable effective adoption of the approach in manufacturing companies, integration of the new DFMA-based model into product data management (PDM) systems is proposed. An application is devised as a proof of principle and is tested with offshore conditions as the nominated service conditions. The proposed approach can facilitate the design of weldments and accelerate decision-making in weld design as its use demands only minimal knowledge of welding and metallurgy.

Keywords: Dissimilar welding, microstructural analysis, mechanical testing, fatigue behaviour, compositional analysis, DFMA, CE, PDM, decision making.

Acknowledgements

This doctoral study was carried out in the Laboratory of Welding Technology of the Department of Mechanical Engineering at Lappeenranta University of Technology, Finland, between 2013 and 2017.

My special thanks go to my supervisor, Associate Professor Paul Kah, who was always a source of help and encouragement and was ready to offer his insight and experience throughout the development of the work. I am very grateful for his guidance and instructions in honing my academic skills. Dear Paul, I am very thankful for your help in finding solutions to the different challenges faced during this study and I would say that without your support completion of this work would not have been possible.

I would like to thank the head of the Laboratory of Welding, Professor Jukka Martikainen, for his assistance and support during this study. My sincere thanks go to all the staff of the Laboratory of Welding, whose cooperation made this work possible. I express my gratitude to Esa Hiltunen for his assistance with the experimental work. I would like to thank my fellow researchers Dr. Xiaochen Yang, Dr. Pavel Layus, Dr. Eric Mvola, and Emanuel Gyasi for their feedback and, of course, friendship.

I would also like to thank Peter Jones for his valuable contribution to the scientific publications. I would like to express my appreciation to Dr. Huapeng Wu and Dr. Harri Eskelinen for their positive response to the work, encouragements and help with the final parts of the study.

I would like to express my appreciation to the reviewers of this work, Professor Thomas Böllinghaus and Professor Suck-Joo Na, for the time and effort taken to appraise my work.

I would like to thank my mother, Zohreh Sabertahan, from the bottom of my heart for seeding love, patience, and faith in God in my heart and encouraging me to step forth on this long trek. I wish I could see your content and heavenly smile from heaven.

My greatest appreciation and profound gratefulness go to my father, Reza Tasalloti Kashani, and my sister, Shadi Tasalloti Kashani, who walked side by side with me throughout this long journey and during the darkest days of my life and gave me their unflinching support and unending encouragement. The accomplishment of this work would not have been possible without them.



Hamed Tasalloti Kashani
June 2017
Lappeenranta, Finland

*To my parents, Zohreh Sabertahan and Reza Tasalloti
Kashani*

Contents

Abstract

Acknowledgements

Contents

List of publications	11
Nomenclature	13
1 Introduction	15
1.1 Research background and motivation	16
1.2 Objective and focus	18
1.3 Overview of the work.....	19
1.4 Impact on society and the environment.....	19
1.5 Limitation and scope	19
2 State of the art of the DFMA-PDM integrated model	21
3 Experimental results and literature review	23
3.1 Dissimilar GMAW of S 355 MC and AISI 304 L	23
3.1.1 Experimental Procedure	23
3.1.2 Overview of the results	24
3.1.3 Factors affecting corrosion resistance.....	29
3.1.4 Factors affecting fatigue strength.....	30
3.2 Dissimilar laser welding of Zn-coated steel and aluminium.....	31
3.2.1 Applied techniques to reduce defects related to Zn vaporization.....	31
3.2.2 Applied techniques to reduce intermetallic compounds	33
3.2.3 Applied techniques for improved corrosion resistance.....	35
3.2.4 Factors affecting fatigue strength.....	36
3.3 Dissimilar GMAW of Optim S 960 QC and UNS S32205	36
3.3.1 Materials and welding procedure	38
3.3.2 Metallurgical and mechanical characterization of weldments	39
3.3.3 Microstructure	39
3.3.4 Chemical composition.....	49
3.3.5 Hardness	51
3.3.6 Bend properties	54
3.3.7 Tensile behaviour	54
3.3.8 Impact toughness.....	55
3.3.9 Fatigue behaviour.....	57
3.3.10 Factors affecting corrosion resistance.....	60
4 A novel method for enhanced decision making	61
4.1 Novel DFMA-based design procedure.....	62

4.2	Integration of the application-based approach with PDM systems	65
4.3	Simplified example for application-based selection	70
5	Overview of the publications	78
6	Suggestions for further study	85
7	Conclusion	86
	References	89
	Publications	

List of publications

This thesis is based on the following papers. The rights have been granted by publishers to include the papers in the dissertation.

- I. Tasalloti, H., Kah, P., Martikainen, J. (2014). Effects of welding wire and torch weaving on GMAW of S355MC and AISI 304L dissimilar welds. *Int. J. Adv. Manuf. Technol.* 71 (1), pp. 197-205.
- II. Tasalloti, H., Kah, P., Martikainen, J. (2015) Laser overlap welding of Zn-coated steel on aluminium alloy for patchwork blank applications in the automotive industry. *Rev. Adv. Mater. Sci.* 40, pp. 295-302.
- III. Tasalloti, H., Kah, P., Martikainen, J. (2015) Laser overlap welding of zinc-coated steel on aluminum alloy. *Physics Procedia*, 78. pp. 265-271.
- IV. Tasalloti, H., Eskelinen, H., Kah, P., Martikainen, J. (2016) An integrated DFMA–PDM model for the design and analysis of challenging similar and dissimilar welds. *Mater. Des.* 89, pp. 421-431
- V. Tasalloti, H., Kah, P. (2016) A DFMA-based approach for the design of challenging welds. *International Society of Offshore and Polar Engineers (ISOPE)*, pp 189-197.
- VI. Tasalloti, H., Kah, P., Martikainen, J. (2017) Effect of heat input on dissimilar welds of ultra high strength steel and duplex stainless steel: Microstructural and compositional analysis. *Mater. Charact.* 123, pp. 29-41
- VII. Tasalloti, H., Dabiri, M., Kah, P., Martikainen J. Effect of GMAW heat-input on the microstructure, mechanical and fatigue behaviour of dissimilar welds of ultrahigh strength steel and duplex stainless steel. (Accepted Manuscript)

Author's contribution

Hamed Tasalloti Kashani is the principal author and investigator in papers I –VII. The experiments were designed by the author. The co-authors contributed to performing the experiments and analysis of the results as well as reviewing and improving the articles.

Nomenclature

In the present work, different dissimilar welds are denoted using *italic type*.

Latin alphabet

E	Arc Energy	kJ/mm
I	Arc Current	A
Q	Heat Input	kJ/mm
U	Arc Voltage	V
v	Welding Speed	mm/s
WFS	Wire Feed Speed	m/min

Greek alphabet

γ	Austenite (Gama)
δ	Ferrite (Delta)
γ_2	Secondary Austenite
σ	Sigma
χ	Chi

Superscripts

<i>W</i>	Weaving applied
----------	-----------------

Subscripts

eq	Equivalent
LB	Liquidous base metal
LW	Liquidous weld metal
L	Lower
U	Upper

Abbreviations

AF	Primary Austenite
ASS	Austenitic Stainless Steel
B	Bainite
B _L	Lower Bainite
BSE	Back Scattered Electron
B _U	Upper Bainite
C.C.T	Continuous Cooling Transformation
CAD	Computer Aided Design
CAE	Computer Aided Engineering

CAM	Computer Aided Manufacturing
CE	Concurrent Engineering
DFMA	Design for Manufacturing and Assembly
DP	Dual Phase
DQ	Direct Quenched
DSS	Duplex Stainless Steel
EDS	Energy-Dispersive Spectroscopy
FA	Primary Ferrite
FAT	Fatigue Class Number
FN	Ferrite Number
GBA	Grain Boundary Austenite
GMAW	Gass Metal Arc Welding
HAZ	Heat Affected Zone
HSLA	High Strength Low Alloy
HV	Vickers Hardness
IGA	Inter Granular Austenite
M	Martensite
PDM	Product Data Management
PMZ	Partially Mixed Zone
QT	Quenched and Tempered
R	Ratio
SASS	Super Austenitic Stainless Steel
SEM	Scanning Electron Microscopy
S-N	Stress-Cycle Number
T.T.P.	Time Temperature Percipitation
TFB	Transverse Face Bending
T _{LB}	Liquidus Temperature of the Base Metal
T _{LW}	Liquidus Temperature of the Weld Metal
TRB	Transverse Root Bending
TWB	Tailor Welded Blanks
UHSS	Ultra High Strength Steel
UMZ	Unmixed Zone
WA	Widmanstätten Austenite
WPQT	Welding Procedure Qualification Tests
WPS	Welding Procedure Specification
WQT	Welder Qualification Tests
WRC	Welding Research Council

1 Introduction

The use of dissimilar welding of metals has seen continuous growth in industrial applications in many fields, including, power generation, and the automotive, petrochemical and aerospace industries. Dissimilar welding enables the favourable chemical-mechanical properties of different materials to be combined in a single welded joint. In many cases, the main motivation for using dissimilar welds of metals is economic, and a higher cost material is generally used in combination with a lower cost material. Consequently, when different parts of a welded structure are subject to different environmental and service conditions, for example on oil platforms and in petrochemical plants, usage of the more expensive material is limited to sections that need to withstand demanding service conditions. Dissimilar welding can also be beneficial in lightweight structures, where a high strength material is used for local reinforcement in combination with a lightweight material (e.g. aluminium).

The pitfalls of dissimilar welding lie in the heterogeneity of the physical, mechanical and metallurgical features of the constituent materials of the welded joint. Dissimilarity in the characteristics and behaviour of the metals necessitates extremely careful attention to selection of a compatible combination of the substrate materials, welding process, process parameters and consumables. Incompatibility of the aforementioned parameters can potentially result in catastrophic failure of the welded joint or severe degradation of the weld quality and weld properties. Hence, successful design of dissimilar welded structures needs consideration of all the parameters involved and analysis and understanding of their interactions. Clearly, finding an optimal solution becomes a complex task for the designer, particularly in view of the interconnected and diverse nature of the physical, process and cost parameters related to the material, welding process and joint design. This complexity underlines the importance of a systematic and reliable decision-making method to assist designers and reduce the complexity of the task and the risk of improper parameter and materials selection.

This dissertation comprises two parts. The first part presents a study of three different dissimilar metal welds: structural steel (S 355 MC) and austenitic stainless steel (AISI 304 L), aluminium and Zn-coated steel, and a novel combination of direct-quenched ultra-high strength steel (S 960 QC) and duplex stainless steel (SUS S32205) using a fully austenitic filler wire.

The following aspects were investigated for the dissimilar welds studied:

The effect of filler metal and welding technique (weave or stringer bead) on the microstructure and hardness of a weld between S 355 MC and AISI 304 L.

The effect of process parameters and joint design on the formation of brittle intermetallic compounds and the quality of dissimilar welds of Zn-coated steel and aluminium in overlap configuration.

The effect of heat input on the microstructure, chemical composition, mechanical properties and fatigue behaviour of a dissimilar weld of S 960 QC and SUS S32205.

The dissimilar welds studies demonstrate the consequential effects of the welding process parameters and filler metals on the resultant microstructure of the fusion zone and HAZ, and, thereby, the final mechanical-chemical characteristics of the welded joint.

The second part of the dissertation introduces a DFMA-based approach that can enable appropriate and effective decision-making when selecting material attributes, filler metals and welding process variables. The approach can potentially provide a solution guaranteeing high reliability in design of similar and dissimilar welded joints in real world welding operations. In addition, the work proposes a method for integration of the DFMA-based approach with PDM systems or CAD tools, thus making the approach more applicable for the companies that are already using CAD / PDM tools in their design activities.

1.1 Research background and motivation

Successful design of a welded structure relies on selecting suitable base metals, proper joint geometries and thicknesses commensurate with the demanded load carrying capacity, life expectancy and service environment. However, these criteria cannot guarantee the performance of the weldment if the characteristics of the weld, including metallurgical aspects, are not carefully considered. The mechanical and metallurgical properties of a weld are the result of complex interactions of the base and filler metals, and the welding process and its parameters. In addition to performance and functionality, the cost of the final product, which is of prime importance, has to be adjusted to meet customer demands and market competition. However, reaching a favourable balance between service and function requirements and cost is not usually straightforward since these factors are directly or indirectly connected. For instance, functionality and life span are primarily determined by materials and defined geometries, as well as the manufacturing process, all of which are also determining factors in the cost of final product.

Selection of materials is a major step in structure design and determines functionality, serviceability, life span and cost. The wide range and diverse nature of material options available complicate material selection. For weldment design, however, material selection becomes an extremely demanding task for the designer because in addition to compatibility issues related to the function, structure or process, the weldability should also be taken into consideration. Weldability is a complex quality that is dependent on multiple criteria, including material, welding process type, process parameters and consumables, as well as joint geometry. The interaction of the material and the welding process is the main determinant of weldability. The welding process and procedure can cause fundamental changes in the inherent properties of the base materials. Thus, welding in the manufacturing stage can undermine all efforts in preceding design steps, if the material is not compatible with the welding process and/or the welding process

specification (WPS) is improperly defined. When a designer selects a material for a weldment, the effect of the joining process used should thus be taken into account. It should be noted that the type of joining process can introduce limitations on the joint geometries and locations, and thicknesses, or alternatively, the joint design can impose restrictions on the welding process used.

Concurrent engineering (CE) is an approach that enables simultaneous consideration of functionality, manufacturability and cost-related issues. However, effective implementation of CE needs an appropriate strategy and adaptation for the specific design and production operation under consideration. Design for manufacturing and assembly (DFMA) is considered one of the main approaches to achieving CE. Traditional DFMA combines two concepts: namely, design for assembly (DFA) and design for manufacturing (DFM). Analysis of a design concept is usually initiated with DFA, which aims to improve the ease of assembly by reducing the parts count and parts variation, as well as minimizing the variety of assembly instructions and their complexity. This DFA analysis is followed by design for manufacturing (DFM) using the framework provided by DFA. DFM aims to improve the product design at minimum manufacturing cost for maximum manufacturing quality using the best techniques and practices available. DFMA emphasizes the responsibility of the designer to ensure the functionality, reliability and manufacturing feasibility of the design (Tasalloti et al., 2016) (Eskelinen, 2013b).

In many welding practices, dissimilar combinations of metals are desirable for applications where a combination of good functional and service properties and competitive cost are major considerations. Obviously, the complex relation between functionality, materials, process, and cost concerns introduces huge complication to the design process. This complexity makes it unfeasible to define an essentially linear design procedure starting from the structure blueprints and ending at the finalized sketches with determined materials for manufacturing. Such a linear procedure, which is used in traditional design methods, would cause many difficulties during dissimilar weld manufacturing and/or service.

A number of obvious reasons can be named for possible problems and failures, including inappropriate compatibility between materials, thicknesses, joint positions and dimensions relative to the capabilities or limitations of the welding phase. Such defects can lead to a need for major revisions and reworks, which will adversely affect the cost and production cycle time. However, the adverse effect of a failure to accurately account for these considerations can be more critical if a defective weld reaches the end-user. Poor weldability of the materials used or incompatibility of the materials for an intended application are the main causes of service failure. The cost of such failure can be immense, with a possibility of catastrophic effects on human lives or the environment. Consequently, it is important to consider all aspects of manufacturing and service together with the function and geometrical design in a systematic way and from the initial stages of design.

Finding a solution to address the challenges described above was the main motivation of this study and the motive behind the adoption of the CE concept and DFMA methodology for the purpose of welded structures design. Hence, a DFMA-based approach with built-in expertise is proposed that takes into consideration a range of decisive chemical-mechanical and metallurgical features together with cost attributes.

1.2 Objective and focus

The focus of interest of the current study is dissimilar welding, which is inherently more difficult than similar welding due to the physicochemical and mechanical mismatches between the base materials and the filler metal, when used. The initial objective of this work was to study some dissimilar welds between high strength and ultra high strength steel, austenitic and duplex stainless steel, as well as between aluminium and Zn-coated steel, and the influence of process parameters and/or consumables. Selection of material grade, welding process and parameters and consumables is an extremely demanding task that involves comprehensive study of previous research work, and even trial and error, to reach an acceptable weld quality.

The experimental results and literature review demonstrated the significance of the welding process variables and consumables for the microstructural and mechanical characteristics of the weld. It is clear that in real world welding operations and design of welded structures, such time-consuming prior studies and trial work is not sustainable and would cause considerable increase in the production cycle time and cost of products. On the other hand, it is not reasonable to expect that all designers have the requisite metallurgical, mechanical and cost know-how.

The main objective of this work is to introduce a systematic and improved design procedure and decision-making method with a built-in expertise feature that can provide highly reliable solutions for critical welding operations that need similar or dissimilar welding. To enhance and expedite decision making in selection of the material, welding process and filler metal, the CE concept and an adapted DFMA methodology for weldment design were employed that can provide significant assistance to designers, since the weldability aspects, and mechanical and cost properties are imbedded in the decision-making method.

The proposed method could be especially effective in dissimilar welding practices, where the selection of materials is more intricate and involves the use of multiple materials often having a high mismatch in mechanical and metallurgical properties. A further objective was to make the method readily implementable and applicable in companies dealing with weldment design. To this end, an approach was proposed for integration of the introduced application-based method with design and manufacturing tools commonly found in companies using product data management (PDM) systems. The applicability of the DFMA-based approach to companies' production through integration with PDM systems is the main advantage of the proposed method from a practicality aspect.

1.3 Overview of the work

In this dissertation, a number of dissimilar welds of industrial significance are studied as regards the effect of welding process type, variables, and consumables. The studied dissimilar welds are: GMAW of austenitic stainless steel and structural steel, laser overlap welding of Zn-coated steel and aluminium, and GMAW of a novel combination of direct-quenched ultra high strength steel and duplex stainless steel using a fully austenitic filler metal. In addition, the study outlines an application-based method that is based on the CE concept and utilization of the DFMA strategy. Furthermore, an approach is proposed for integration of the introduced application-based method with design and manufacturing tools commonly found in companies using product data management (PDM) systems. The proposed approach can also be used in conjunction with a material database of CAD applications as well as manufacturers' PDM software to enhance the reliability of weldments design and expedite decision-making, as its use by designers requires only minimal welding and metallurgy knowledge. The usability of the application-based method is illustrated with a demo application developed for the purposes of this study and as a proof of concept. The built-in expertise of the approach can increase the reliability of the solutions proposed for selection of materials and filler metals.

1.4 Impact on society and the environment

This study describes a novel decision-making method for selection of welding materials, welding processes and filler metals. The method aims to provide reliable solutions for welding operations. The method is of particular significance to welding applications in sensitive areas where failure in design and manufacture can lead to expensive rework or have catastrophic effects on the environment or human lives. Successful implementation of the model would result in optimal solutions for critical welding applications with improved reliability and manufacturability. The study can also increase manufacturing efficiency by reducing the cycle time of welded products and decreasing the risk of failure at the manufacturing stage or while in service. More reliable and safer welded structures will boost industry and infrastructure development and extend the range of industrial applications in which welding can be used.

Offshore construction, including offshore wind power generation, and oil and gas exploration are among the sensitive applications that can take advantage of improvements in the reliability of weld design and manufacture. By minimizing the risk of catastrophic effects on the environment and human lives, the novel decision-making method will enhance sustainable development of modern society.

1.5 Limitation and scope

The findings, conjectures and conclusions of the current dissertation are limited to the base materials, welding process, variables and filler materials that are studied. Nevertheless, they provide a basis for study of other materials and processes, and indicate possible approaches and metallurgical considerations for other dissimilar welds.

The usability of the DFMA-based approach is illustrated for selection of the base metals and filler metals of an offshore application and an Arctic application. Because of limited resources, characterization of the complete database to cover all the guidelines related to process parameters, joint and design standards and specification and qualification tests was not feasible within the scope of the current study. Hence, selection of the process and process variables were excluded from the exemplification. For the specific examples considered in this work, the proposed model offers easier and faster selection of material and filler metals and empowers designers to expeditiously assess different material and filler metal options. However, further studies are required to evaluate the efficacy and validity of the model for other applications in terms of selection of materials, welding processes and filler metals, as well as design reliability and manufacturability.

2 State of the art of the DFMA-PDM integrated model

The success of a DFMA strategy relies on the effective distribution of data within the multidisciplinary product development teams involved. Streamlined data distribution can be obtained by integrating DFMA with product data management (PDM) systems that are used to organize, access, and control product data as well as to manage the life cycle of products (Gascoigne, 1995). Many researchers have studied the possibility of incorporating DFMA into welding operations (LeBacq et al., 2005) (Lovatt and Shercliff, 1998) (Maropoulos et al., 2000) (Kwon, Wu and Saldivar, 2004) (Niebles et al., 2006). However, the potential of an integrated PDM and DFMA for welded structures has yet to be presented.

Maropoulos et al. (Maropoulos et al., 2000) investigated a computerized aggregate process planning system for DFMA analysis of weldment assembly design. The model discussed utilized design attributes such as geometry, orientation, joint class and weld features to assess fabrication constraints. A drawback to this approach can be the complexity of assigning multiple attributes to diverse super- and sub-classes of assembly components.

LeBacq et al. (LeBacq et al., 2005) developed a computer based DFMA model for selection of an applicable joining process for a specified design. In their model, they implemented a task-based approach (Lovatt and Shercliff, 1998) that uses a series of questionnaires about joint specifications, geometry and material to narrow down the available options of joining methods to the most suitable one. The predefined questions are simple and manageable by non-expert users. Nonetheless, oversimplification, especially in terms of material characteristics, may sometimes lead to non-optimal solutions.

Kwon et al. (Kwon, Wu and Saldivar, 2004) developed a numerical model integrated with a commercial CAD program to determine welding process parameters for maximum productivity congruent with joint geometry. Their approach computes the weld bead cross-section according to structural constraints designated by standards for fillet welds to determine the welding process parameters required to deposit the weld bead with maximum travel speed. The model is practicable for sheet metal thicknesses up to 6.4 mm to be joined with a single pass fillet weld. This approach can be useful for assessment and alterations of the design to attain effective solutions at the initial stage of the design. However, the applicability of the derived production welding parameters remains questionable due to the geometric deviations that real parts usually have from the CAD source model, and also due to the simplifications that generally exist in the model algorithm when compared with actual welding practice. Additionally, the derived parameters for maximum heat input might not always result in a workable solution because of the adverse effects on the mechanical properties of the heat affected zone (HAZ).

Niebles et al. (Niebles et al., 2006) developed a DFMA procedure for welded products using a wide range of factors involved in the design and product development stages. Their approach can be used for different welding operations when combined with related standards and codes and a heuristic knowledge base. However, their model remains mainly theoretical since the connection to the required actions in design and welding practice is not explicitly defined.

This study uses the concept of CE to facilitate and improve the design process of welded structures, especially complex structures and dissimilar welds, where different design teams are involved and great caution in design and manufacturing is required. To achieve these targets, the traditional DFMA model was modified to enable improved usability for structural welding applications. In this revised model, welding is considered as a discrete design module that can be integrated with the PDM database. The model expedites the decision-making process by employing an application-based selection approach that provides the designers with a permitted list of materials and welding procedures specifications (WPS) together with brief data and analysis to guide the designer to find an optimal solution. The model can be usable for many similar and dissimilar welded structures on condition that pertinent database and DFMA rules and guidelines are provided for the application. The built-in expertise feature of the application-based selection method makes the model practicable for designers with limited knowledge of welding and metallurgy. The model can potentially be customized with a unified interface for companies' PDM for storage and smooth distribution of data between the design teams involved. The model also has the potential to be used conjointly with the material database of CAD tools to assist designers in reliable material selection for welded structures.

3 Experimental results and literature review

3.1 Dissimilar GMAW of S 355 MC and AISI 304 L

The combination of austenitic stainless steel (ASS) and low alloy structural steel offers desirable mechanical properties, good formability and weldability, resistance to stress corrosion cracking and other forms of corrosion (Hasçalik, Ünal and Özdemir, 2006), along with fairly cost-effective (Lippold and Kotecki, 2005; Arivazhagan et al., 2012) manufacturing methods (Nascimento et al., 2001; Arivazhagan et al., 2011). Due to these advantageous characteristics, such combinations of metals are extensively used in the power generation industry (Shushan, Charles and Congleton, 1996), as well as in petrochemical plants and buildings (Celik and Alsaran, 1999; Missori and Koerbe, 1997; Fuentes et al., 2011).

A range of metallurgical concerns are associated with dissimilar welding of ASS to low-alloy structural steel. Martensite formation on the ferritic side of the weld interface and the risk of hot cracking in fully austenite microstructure on the austenitic side are the main concerns in this kind of weld (DuPont, Kiser and Lippold, 2009).

The ferrite number (FN) is another consequential aspect in the dissimilar metals welding of ASS to low-alloy structural steel. Ferrite can favourably reduce the tendency of cracking in the weld. However, excessive amounts of ferrite have a detrimental effect on corrosion resistance and mechanical properties (ASME Boiler and Pressure Vessel Committee, 2007). The amount of ferrite can to some extent be regulated by careful selection of the filler metal composition and control of substrate dilution (SUN and ION, 1995) (Du Toit, 2002). The aim is to obtain a fusion zone with austenitic structure and a small amount of ferrite, which is a microstructure that reduces the chance of weld solidification cracking (Lippold and Kotecki, 2005). Solidification behaviour and ferrite content can be affected by the welding process and welding parameters due to variations in heat input and solidification speed (Brooks and Lippold, 1993).

With GMAW welding of ASS and ferritic steel, the effect of torch weaving in relation to the filler material of the dissimilar weld has not yet been explicitly studied. This section concentrates on evaluating the effect of different welding wire compositions and implementation of the weaving technique on dissimilar welds of AISI 304 L to S 355 MC low alloy structural steel.

3.1.1 Experimental Procedure

S 355 MC structural steel and AISI 304 L austenitic stainless steel were used to produce fillet weld joints using three different filler wires, namely, Esab OK Autrod 16.54 (*EOA16.54*), Esab OK Autrod 16.55 (*EOA16.55*), and Elga Cromarod 316LSi (*EC316LSi*). These three filler wires were used to weld the base materials (5 mm thick) with a robotised GMAW process using either stringer or weave (3Hz) bead technique. A

shielding gas mixture of 98 % Ar + 2 % CO₂ with a constant flow rate of 16 l/min was used for welding all the samples. The cross-sections of the weld specimens were polished (1 μ m) and etched for the metallographic inspections. The material specifications and the process parameters are presented in Tables 1 and 2. The weld metals are denominated with the last number of the building filler wire code plus “W” when weaving was used; for instance, 16.54 and 16.54^W designate weld metal made from EOA16.54 filler wire without and with weaving, respectively.

Table 1. Chemical composition (wt. %) of base materials and welding wires.

Material	C	Cr	Mn	Ni	P	S	Si	N	Al	Mo	Cu
AISI 304 L	0.025	18	1.57	8.1	0.033	0.002	0.4	0.044	-	-	-
S 355 MC	0.12	-	1.5	-	0.02	0.015	0.03	-	0.015	-	-
EOA16.54	<0.03	21.5	1.4	15	-	-	0.4	-	-	2.7	-
EOA16.55	<0.02	20.5	1.7	25	-	-	0.4	-	-	4.5	1.4
EC316LSi	0.02	18.5	0.7	12	0.02	0.02	0.8	-	-	2.7	0.1

Table 2. Welding parameters for dissimilar metal welding: wire diameter (Φ), wire feed speed (V_w), welding current (I), welding voltage (U), travel speed (v) and heat input per unit length of weld (Q).

Wire	Φ (mm)	V_w (m/min)	Stick-out (mm)	I (A)	U (V)	v (mm/s)	Q (KJ/mm)
EOA16.54	1.2	11.2	20	260	24.5	8.4	0.61
EOA16.55	1	11.4	17	227	24	7.5	0.58
EC316LSi	1	11.4	17	227	24	7.5	0.58

3.1.2 Overview of the results

In Figure. 1, the overall dilution rates of the weld metals by the substrates are shown and compared. From this figure, it is clear that dilution is less when using the weaving technique than the stringer deposit approach.

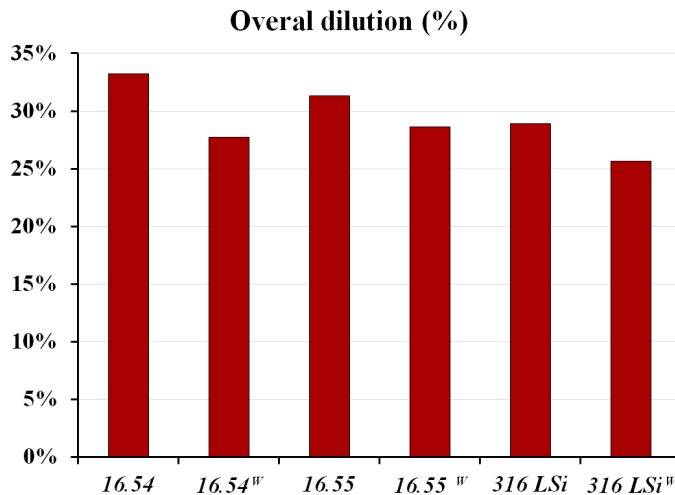


Figure 1. Overall dilution of the deposited weld by substrates.

The ferrite number was measured using a ferritescope. Figure 2 shows a comparison of the measured ferrite numbers and the predicted ferrite content from the Schaeffler diagram (Schaeffler, 1948). A noticeable point of interest in Figure 2 is the higher FN found in weldments made using the same filler wires but with the weaving method. One possible explanation may be that faster solidification occurs, because weaving spreads the heat away from the arc and deposits metal over a less concentrated area (Yongjae and Sehn, 2005; Klimpel et al., 2007).

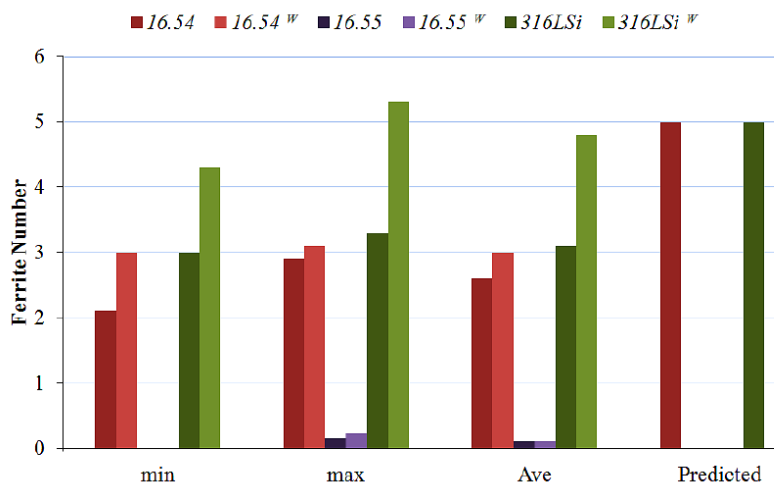


Figure 2. Ferrite number measured for different weldments and predicted from the Schaeffler diagram (Schaeffler, 1948).

The connection between solidification behaviour and Cr_{eq}/Ni_{eq} was established by Suutala and Moisis (Suutala and Moisis, 1983; Brooks and Lippold, 1993). Figure 3 shows the composition of the welding wires superimposed on the Suutala and Moisis diagram (Suutala and Moisis, 1983) using the presented coefficients of Ni_{eq} and Cr_{eq} . The Ni_{eq} and Cr_{eq} delineate the solidification mode reliably for most conventional 300-series alloys welded under normal arc-welding conditions (Brooks and Lippold, 1993). The diagram outlines the four solidification modes as follows: single-phase austenite (Type-A), primarily austenitic with a minor fraction of eutectic ferrite (Type-AF), primary ferrite with peritectic/eutectic solidification of austenite (Type-FA) and single-phase ferrite (Type-F) (Brooks and Lippold, 1993). From the diagram, the predicted solidification mode for *EOA16.55* is Type-A, and for both *EOA16.54* and *EC316LSi*, it is Type-FA.

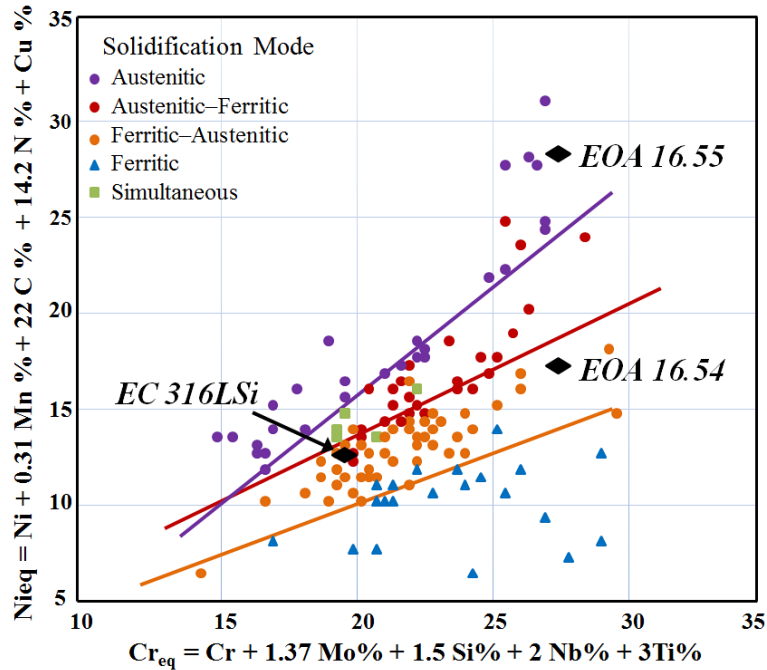


Figure 3. Composition of welding wires plotted on the Suutala and Moisiso diagram (Suutala and Moisiso, 1983).

As can be seen from the micrographs shown in figures 4-9, on the austenitic side of the weld interface the solidification mode was FA for 16.54^W , $316LSi$, and $316LSi^W$. While Type-AF was noticed for 16.54 and Type-A was apparent for both 16.55 and 16.55^W . On the ferritic side of the weld, Type-FA solidification was found for all the weld samples, except for 16.55^W , which presented Type-A solidification.

As can be inferred from the results, no clear relation between the welding technique and solidification mode can be discerned. Moreover, it is clear from the optical micrographs that the observed solidification modes for all the samples, except for 16.54 , are quite consistent with the predictions derived from the Suutala and Moisiso diagram.

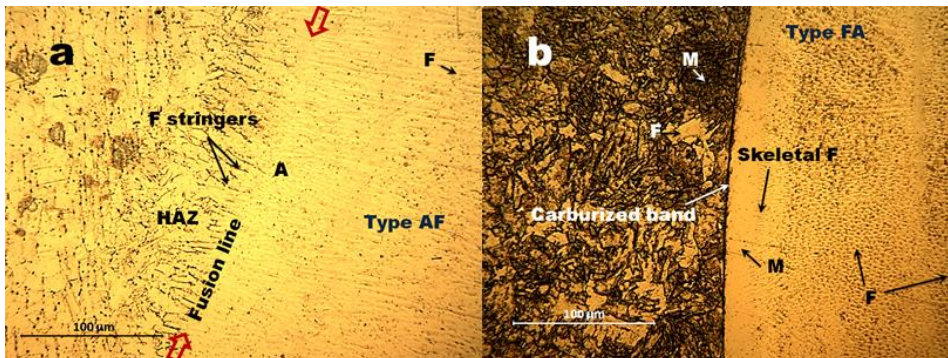


Figure 4. Optical micrograph of the weld zone: interfaces between the weld and base metals **a** 16.54 and AISI 304 L, **b** 16.54 and S 355 MC (Tasalloti, Kah and Martikainen, 2014).

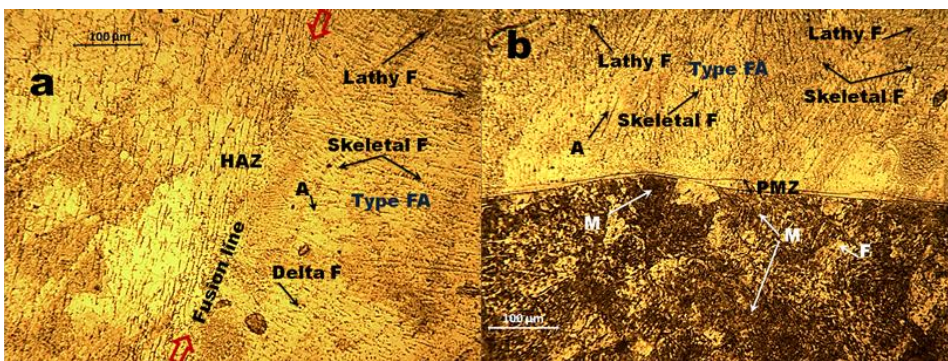


Figure 5. Optical micrograph of the weld zone: interfaces between the weld and base metals **a** 16.54^W and AISI 304 L, **b** 16.54^W and S 355 MC (Tasalloti, Kah and Martikainen, 2014).

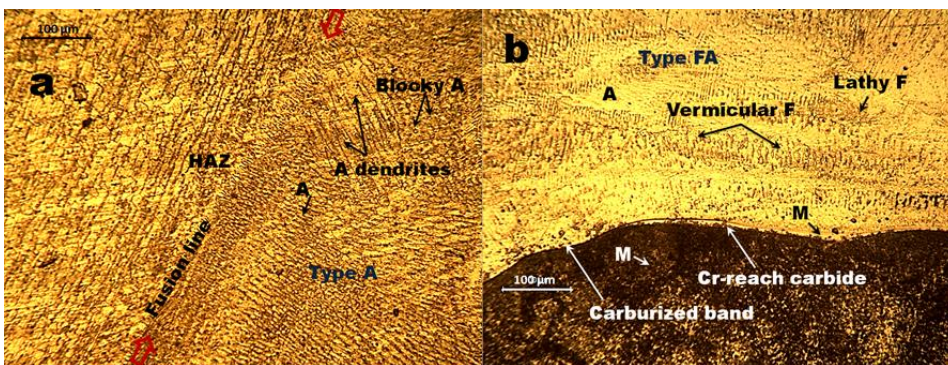


Figure 6. Optical micrograph of the weld zone: interfaces between the weld and base metals, **a** 16.55 and AISI 304 L, **b** 16.55 and S 355 MC (Tasalloti, Kah and Martikainen, 2014).

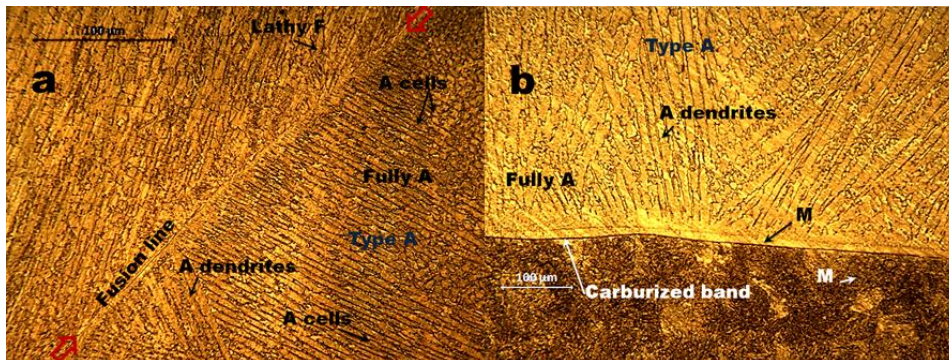


Figure 7. Optical micrograph of the weld zone: interfaces between the weld and base metals **a** 16.55^W and AISI 304 L, **b** 16.55^W and S 355 MC (Tasalloti, Kah and Martikainen, 2014).

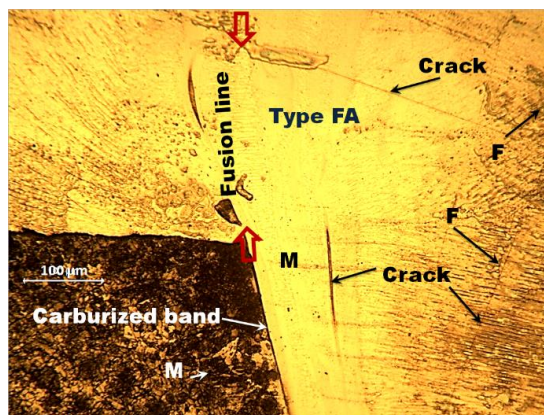


Figure 8. Optical micrograph of the weld zone: interfaces between the weld and base metals, $316LSi$ and both AISI 304 L and S 355 MC (Tasalloti, Kah and Martikainen, 2014).

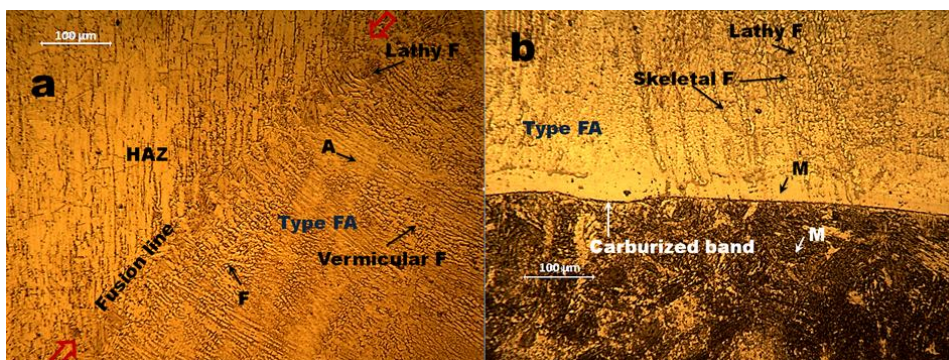


Figure 9. Optical micrograph of the weld zone: interfaces between the weld and base metals, **a** $316LSi^W$ and AISI 304 L, **b** $316LSi^W$ and S 355 MC (Tasalloti, Kah and Martikainen, 2014).

The microhardness across the welds was measured using a digital Vickers microhardness tester. All hardness indents were made with 500-g force (4.905 N). Figure 10 presents a

comparison of the evaluated hardness values for welds made with and without the use of weaving. For all the specimens, the hardness of the fusion zone is inferior to that of the AISI 304 L base steel, with some exceptional points. The lower hardness can be ascribed to the presence of a higher amount of a strong austenite stabilising elements such as Ni and Mn (Das et al., 2009).

For *16.54*, *16.54^W*, *16.55* and *316LSi*, there is a prodigious increase in hardness on the ferritic side adjacent to the weld interface, which can be indicative of martensite formation, as seen from Figure 10a and 10b. These results are in agreement with the observed martensitic layer on the ferritic side of the fusion zone interfaces, seen from the optical micrographs shown in Figure 4 and Figure 6-9. It can be expected that the higher hardness values of the fusion zone correspond to higher ferrite contents of this zone. As can be seen from the hardness profiles, hardness values are highest for *316LSi*, *16.54* and *16.55*, respectively, both with and without the use of weaving, which is as would be expected from the measured ferrite numbers in Figure 2.

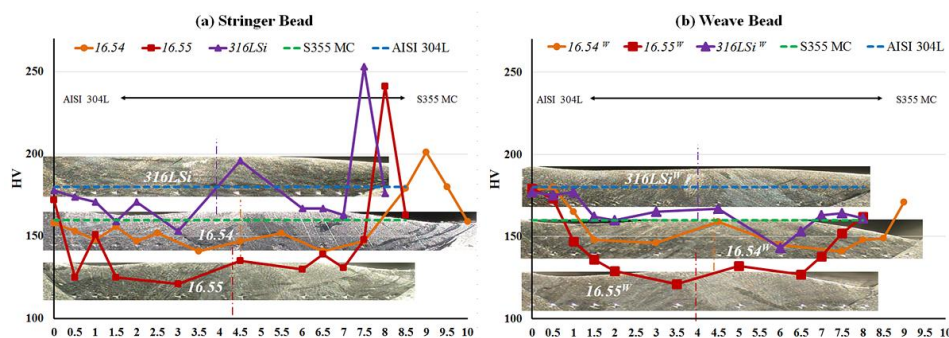


Figure 10. Comparison of hardness distribution along the weld metals with (a) stringer and (b) weave bead, the vertical dotted lines represent the weld centrelines (Tasalloti, Kah and Martikainen, 2014).

3.1.3 Factors affecting corrosion resistance

Austenitic stainless steels (ASS) have excellent resistance to different forms of corrosion. However, material properties of weldments of these steel grades can be considerably inferior to those of the base metal. In general, the heat affected zone is the most critical region, because of variations in microstructure caused by the welding heat cycle. With regard to dissimilar welds of ASS and structural steel, the fusion zone characteristics should be taken carefully into consideration when assessing the corrosion resistance of the weldment. In such welds, the resultant chemical composition of the fusion zone is related to the dilution level of the filler metal and base metals. Generally, a microstructure made of austenite plus δ -ferrite is expected for the fusion zone. However, the proportion of δ -ferrite and the microstructure morphology may vary significantly depending on the degree of mixing between the filler and base metals, and the percentage of ferritizing and austenitizing elements, as well as the cooling rate. Degradation of ASS weldments can make them susceptible to different forms of localized corrosion, such as pitting corrosion,

crevice corrosion, and intergranular corrosion (IGC). Most of these defects have been found to be related to sensitization of austenitic stainless steels from heat treatment or use in a high-temperature environment. Sensitization of austenitic stainless steel leads to precipitation of Cr-rich carbides at or near the grain boundaries. Cr-rich carbides also contain molybdenum, and thus a depletion of Cr+Mo occurs in the grain boundary region during sensitization. When sensitized ASS is exposed to a corrosive environment, IGC occurs on the Cr-depleted regions (Ziętała et al., 2016) (Ghorbani et al., 2017) (Silva et al., 2013) (Unnikrishnan et al., 2014) (Ramkumar et al., 2016).

3.1.4 Factors affecting fatigue strength

Austenitic stainless steels exhibit high strength, high ductility and excellent fracture toughness even at cryogenic temperatures. However, the integrity and fatigue performance of welded ASS can be reduced considerably by the presence of weld metal defects such as porosity, undercut, incomplete fusion and slag inclusion (J et al., 2001). Martensite formation on the ferritic side of the dissimilar weld interface between ferritic steel and ASS can considerably reduce the fatigue strength of the weld metal and the initiation time of cracks and can increase the crack growth rate under cyclic loading. Formation of the martensitic layer is dependent on the chemical composition of the filler and base metal and the degree of mixing between them, as well as carbon diffusion from the ferritic steel to the weld metal (Al-Haidary, Wahab and Salam, 2006).

Some studies show that sensitization of ASS and formation of brittle intermetallics can also adversely affect fatigue strength. To avoid premature failure, some researchers suggest thermal treatment to dissolve the martensitic structure (Fuentes et al., 2011) (Vach et al., 2008). In general, low heat input and less dilution of weld metal from the ferritic side can be beneficial for prevention of the appearance of a martensitic layer on the weld interface (Cortie, Fletcher and Louw, 1995).

It has been shown in the literature that a small percentage of δ -ferrite in the weld metal can be beneficial for minimizing the susceptibility of ASS weldments to microfissuring during cooling and upon solidification. Generally, formation of δ -ferrite is dependent mainly on Ni and Cr equivalents present in the weld metal and the cooling rate (Dadfar et al., 2007).

Another factor affecting the crack propagation characteristics are residual stresses introduced by the welding process. The residual stresses within a weldment are a consequence of restrained contraction of the weld metal as it solidifies and cools down to ambient temperature. If fatigue cracks encounter a region of residual tensile stresses, the rate of crack propagation increases (Al-Haidary, Wahab and Salam, 2006) (Cortie, Fletcher and Louw, 1995).

3.2 Dissimilar laser welding of Zn-coated steel and aluminium

Galvanised steels have been extensively used in exposed car body panels to increase corrosion resistance (Thomy, Seefeld and Vollertsen, 2005) (Milberg and Trautmann, 2009). Currently, laser butt and lap welding of Zn-coated steels are widely used in the automotive industry for tailored blanks and patchwork blanks (Chen, Ackerson and Molian, 2009) (Ding et al., 2006). Tailor welded blanks (TWBs) are made of two or more sheet metals of different thicknesses, shapes, mechanical properties and/or coatings that are butt-welded together prior to forming (Mäkikangas et al., 2007) (Merklein et al., 2014). Another type of tailored blank is the patchwork blank, which is commonly used for local reinforcement purposes in auto-body structures. A welded patchwork blank is made of one or more pieces of reinforcing sheet metal (patches) lap-welded onto the mainsheet. Currently, laser welding is the most commonly used welding process for TWBs and welded patchwork blanks (Mäkikangas et al., 2007) (Merklein et al., 2014). CO₂ and Nd:YAG lasers are traditionally the welding processes used for TWB applications (Reisgen et al., 2010). However, over the past few years, fibre lasers have become the leading choice for welding applications because of their high power, excellent beam quality and high energy efficiency (Eva and Joaquín, 2012) (Duley, 1999) (Vollertsen, 2005). Local reinforcement of aluminium with laser-welded patches of Zn-coated steel can effectively contribute to improved crashworthiness and durability, and weight reduction of car body parts. The vaporisation of Zn due to its low boiling temperature (906 °C) is the main issue reported for the laser welding of galvanised steel. The vaporisation is particularly problematic in lap joint setups because of the restriction of Zn vapour venting (Reisgen et al., 2010) (Milberg and Trautmann, 2009) (Li, Lawson and Zhou, 2007). The intense pressure of Zn vapour within the keyhole can cause an unstable and violent flow of the melting pool, resulting in the formation of cavities, spatter and craters (Chen et al., 2011) (Amo et al., 1996) (Dasgupta and Li, 2007). The laser welding of Zn-coated steel to Al has been studied by a number of researchers (Milberg and Trautmann, 2009) (Tzeng, 2000) (Fabbro et al., 2006). However, it is still very difficult to achieve a defect-free and high-strength weld. In addition to Zn vaporization, difficulties arise from differences in the thermophysical properties of the two base metals and the formation of brittle intermetallic compounds (IMCs) because of the poor miscibility and solubility of steel and aluminium (Tasalloti, Kah and Martikainen, 2015).

In the next section, the aforementioned processing problems are explained further and their effects on weld quality and strength are discussed. Additionally, an overview of the approaches proposed by different researchers to minimize the adverse effects of the pre-mentioned challenges and improve the strength and quality of welds between galvanised steel and Al alloy is presented (Tasalloti, Kah and Martikainen, 2015).

3.2.1 Applied techniques to reduce defects related to Zn vaporization

Different approaches have been put forward in the literature to decrease the porosity occurring in laser lap welding of Zn-coated steels. Amo et al. (Amo et al., 1996) suggested keeping a gap between the surfaces to be welded to let the evaporated Zn vent out from

the gap. They reported a defect-free weld, without any cracks or porosities, when using a gap opening up to 0.1 mm. Chen et al. (Chen et al., 2011) tried use of double pass laser welding with a defocused beam. Welding was performed in the first pass with a focused laser beam. Subsequently, a defocused beam was utilized for the second pass. Double pass welding was performed using either Ar or N₂ as the shielding gas. The study reported an unstable weld pool and spatter was observed with both the Ar and N₂ gases. According to the findings reported, utilization of a second pass weld with a defocused laser beam refined and improved the weld appearance, shown in Figure 11.

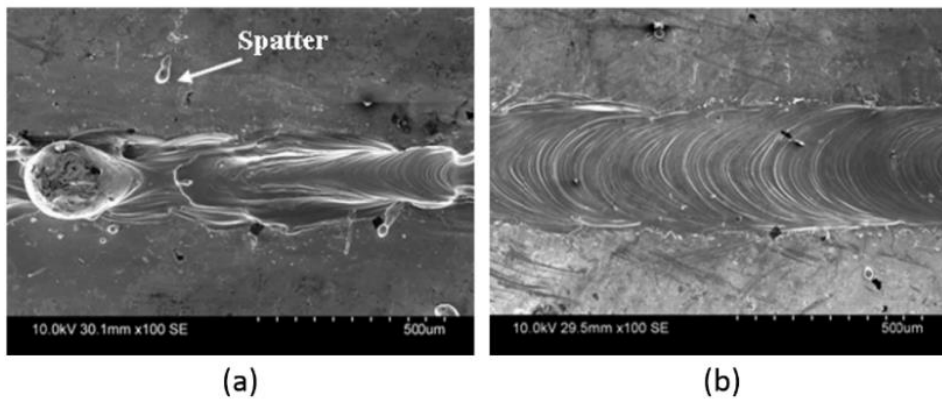


Figure 11. Comparison between weld appearances produced from (a) a single pass and (b) double pass fibre laser welding with N₂ shielding gas, (first pass welding parameters: 650 W, 100 mm/s, f.p.p. of 0 mm, second pass welding parameters: 200 W, 75 mm/s, f.p.p. of +2 mm) (Chen et al., 2011).

A greater risk of porosity has been found to exist when a higher density gas is applied, because the gas is more likely to become trapped in the keyhole and within the fusion zone after solidification (Katayama et al., 2009). However, Chen et al. (Chen et al., 2011) reported porosity and cracking in welds made with double pass laser welding using either N₂ or Ar gas without any perceivable relation between the type of gas applied and the porosity found in the weld samples, as can be seen in Figure 12.

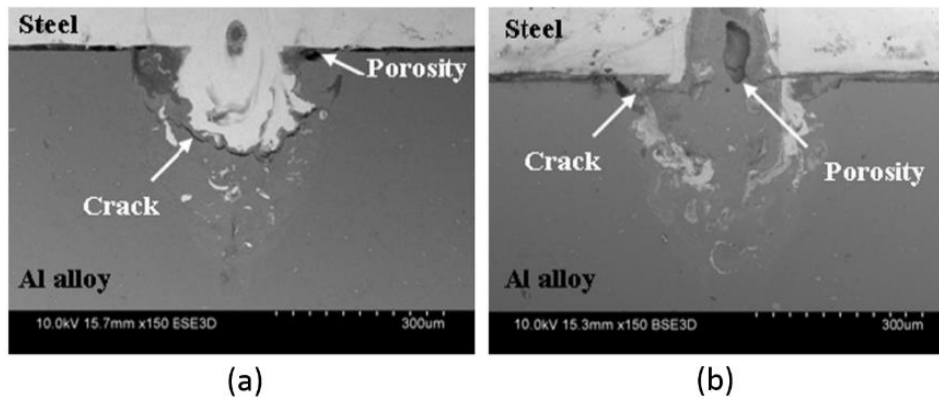


Figure 12. Backscattered electron image of the cross-section of the weld made using laser double pass welding with (a) Ar gas and (b) N₂ gas, (first pass welding parameters: 650 W, 100 mm/s, f.p.p. of 0 mm, second pass welding parameters: 200 W, 75 mm/s, f.p.p. of +2 mm) (Chen et al., 2011).

Ma et al. (Ma et al., 2014) examined two-pass laser welding for welding a lap joint between Zn-coated high-strength steel and Al alloy. In their approach, a defocused laser beam is applied in the first pass to preheat the components and to partially melt and vaporize the Zn coating of the galvanized steel sheet. Then, in the second pass, the welding is performed using a focused beam. They reported a defect-free laser welded lap joint with partial penetration produced by the use of two-pass laser welding. In addition, they stated that the process was very stable and almost no spatter, crack or blowholes were present in the welds.

3.2.2 Applied techniques to reduce intermetallic compounds

As noted earlier, a significant concern in welding of Al and steel is the formation of brittle Fe–Al intermetallic compounds (IMCs) within the fusion zone as a result of poor solid solubility of the Fe element in Al (Torkamany, Tahamtan and Sabbaghzadeh, 2010) (Sierra et al., 2007) (Meco et al., 2013). IMCs are composed of ductile Fe-rich and brittle Al-rich phases. FeAl and Fe₃Al are Fe-rich phases, whereas Al-rich phases include FeAl₂, Fe₂Al₅, FeAl₃, and Fe₄Al₁₃ (Lee and Kumai, 2006) (Rathod and Kutsuna, 2004) (Katayama et al., 2005). Brittle Al-rich IMCs are a cause of concern, because they have a detrimental effect on the mechanical performance of the weld and can instigate cracks within the fusion zone (Meco et al., 2013).

Ozaki et al. (Ozaki et al., 2010) suggested laser roll welding to diminish the deleterious effects of IMCs. This process combines a CO₂ laser and a roller compressing the frying surfaces of the Al alloy and Zn-coated steel to be welded. The motivation behind this technique is to minimize the formation of brittle IMCs by shortening the heating cycle and enhancing the heat transfer rate between the contacting surfaces under pressure. The study reported production of a weld with a maximum shear strength of 162 N/mm when

the welding speed was 8.3 mm/s and the roller pressure was set to 150 MPa. It was noticed that the shear strength declined when the thickness of the IMC layer exceeded 10 μm .

Meco et al. (Meco et al., 2013) evaluated the use of fibre lasers for the conduction welding of Al to Zn-coated steel in overlap configuration. They reported that using conduction mode laser welding enabled them to control the heat input and thereby control IMC formation. They also stated that improved shear strength in welds of the Zn-coated steel and Al was achieved when a higher energy density was utilized, as shown in Figure 13. This finding appears to be inconsistent with the assumption that higher heat input can increase the formation of IMCs and cause degradation in the mechanical strength of the weld (Chen et al., 2011). It was concluded that mechanical strength is not solely dependent on the thickness of the IMC layer. Instead, a combination of the intermetallic layer thickness and its composition, the orientation of the IMCs, as well as bonding and diffusion between the elements can affect the mechanical strength of such welds (Meco et al., 2013).

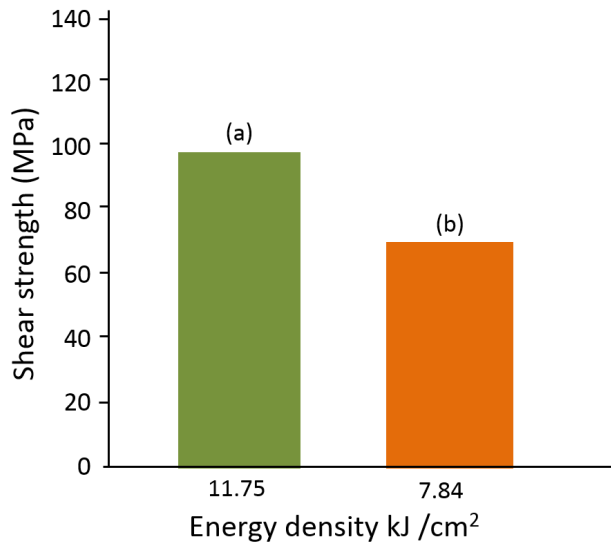


Figure 13. Shear strength of a laser welded lap joint between low-carbon galvanized steel and AA2024 aluminium alloy using fibre laser (spot diameter: 13 mm, power density: 4.52 kW/cm², (a) travel speed: 0.3 m/min, (b) travel speed: 0.45 m/min) (Meco et al., 2013).

Chen et al. (Chen et al., 2011) reported a substantial decline in IMCs formation as a result of using N₂ shielding gas in the fibre laser welding of Zn-coated steel on Al alloy. They stated that a higher shear strength was obtained with N₂ gas than with Ar, observable in Figure 14. They also noticed lower variations in hardness in the fusion zone when N₂ gas was used, which can also imply less IMCs formation. The more even hardness profile may be associated with the higher thermal conductivity of N₂ compared to Ar, which may result in an increased cooling rate of the melt pool during laser welding. The increased cooling rate can restrict the extent of heat flow and diffusion activity in the melt pool. Hence, the base materials will be mixed to some degree and the growth of IMCs will be

obstructed, resulting in a more even hardness distribution and also improved shear strength (Borrisutthekul et al., 2007). The reactivity of N_2 plasma with Al is reported in the literature (Borrisutthekul et al., 2007) (Katayama et al., 2009) (Visuttiptikul, Aizawa and Kuwahara, 2003) to be beneficial in reducing the extent of Al-rich intermetallic phases, particularly in laser keyhole welding. The reaction between the vaporized Al and ionized N_2 can lead to the formation of aluminium nitride (AlN), which can substitute the Fe–Al intermetallics. Ma et al. (Ma et al., 2014) found that too much heat input during preheating can entirely remove the Zn-coating, which makes the weld prone to the formation a Fe–Al layer. They also claimed that the existence of Zn in the IMCs could improve the strength of the welded lap joint of Zn coated steel and Al. It was further stated that lower heat input during the welding process can result in higher shear strength.

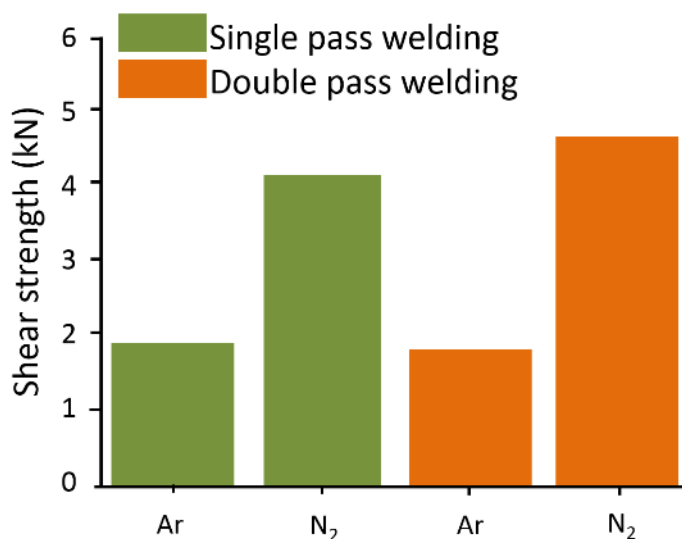


Figure 14. Comparison between the effect of Ar and N_2 shielding gases on the shear strength of a laser welded lap joint of Zn-coated steel (DX54) and Al alloy (5754), using either single pass or double pass fibre laser welding (first pass welding parameters: 650 W, 100 mm/s, f.p.p. of 0 mm, second pass welding parameters: 200 W, 75 mm/s, f.p.p. of +2 mm) (Chen et al., 2011).

3.2.3 Applied techniques for improved corrosion resistance

Corrosion resistance is an essential requirement of welded joints between Zn-coated steel and Al. The corrosion resistance of the weld can be adversely affected by microsegregation, the growth of intermetallic phases, loss of Zn due to vaporization, and weld defects (Kodama et al., 2010) (Kwok et al., 2006). The degradation of corrosion resistance can occur within both the fusion and heat affected zones, due to intergranular corrosion and segregation or growth of a secondary phase (Chen et al., 2011) (Kwok et al., 2006) (E. Ghali, V. S. Sastri and M. Elboudjaini, 2007). It is known that inert gases with a higher density can provide more effective protection against oxidation and loss of alloying elements over the melt pool (Chen, Ackerson and Molian, 2009), and it has been reported that weld samples made with Ar shielding gas exhibit better corrosion resistance

than those made with N₂ gas (Chen et al., 2011). This finding may be due to the higher density of Ar, which means that the Ar more effectively protects the base metals against oxidation (Chen et al., 2011). In general, prevention of weld defects and better smoothness of the weld surface can contribute to improvement in the corrosion resistance of the weld (Chen et al., 2011) (Yan, Yang and Liu, 2007) (Kwok et al., 2006).

3.2.4 Factors affecting fatigue strength

The fatigue performance and fracture behavior of laser welding of Zn-coated steel to aluminum suffers from several defects caused by differences between the thermal, physical, and chemical properties of aluminum and steel. Hot cracks, porosity, and incomplete fusion are some of the defects found with such welding processes. The very low miscibility between aluminum alloys and steels leads to the formation of a variety of hard and brittle Fe-Al intermetallic compounds, which can severely decrease the plasticity and toughness properties of the weld joint. The poor metallurgical compatibility in the weld is further aggravated by large differences in thermophysical properties. The thermal conductivity and thermal expansion rates of aluminum and steel are very different, which leads to the development of significant thermal stresses during welding. These stresses give rise to complex residual stresses in the final weldment at room temperature, which have a great influence on fracture strength and fatigue failure. Moreover, due to the considerable difference in the density of aluminum and steel (aluminum is 2.69 g/cm³ and steel is 7.8 g/cm³) aluminum liquid can float on the melted steel during welding, which produces a macro-scale segregation at the surface of the steel and substantially degrades the mechanical properties of the weld joint. It should further be noted that aluminum is very active chemically and reacts quickly with oxygen to form an adherent Al₂O₃ film on the surface of the aluminum. During welding, the Al₂O₃ film can cover the surface of the molten pool and impede the flow and coalescence of the melted metals, which can create slag in the weld and can significantly impair the mechanical properties of the weld joint. In addition, aluminum oxide, which has a very high melting point of 2050 °C, on the surface of the base metal readily absorbs moisture. During welding, the vaporized moisture in the weld zone is decomposed into hydrogen and oxygen and the hydrogen can create porosity in the weld. Zn vapor is another well-known source of instability and the formation of porosity in the weld. The aforementioned IMCs formation and defects tend to embrittle the weld joint and increase the crack propagation rate (Wang et al., 2016) (Yang, Li and Zhang, 2016) (Sierra et al., 2008).

3.3 Dissimilar GMAW of Optim S 960 QC and UNS S32205

Direct-quenched (DQ) ultra high strength steel (UHSS) is a rather new development that combines lower production cost and excellent engineering properties compared to traditional quenched and tempered (QT) grades (Xiao et al., 2010) (Hwang et al., 1998). Knowledge of the weldability of UHSS DQ in similar and dissimilar configurations is a prerequisite to enable full exploitation of the promising features of this new steel grade in a wide range of weldment designs where resistance to intense load and suitability for

demanding service conditions are required. The mechanical features and fracture behaviour of welded UHSS DQ have recently become the focus of much research (Farrokhi, Siltanen and Salminen, 2015) (Guo et al., 2015) (Wallin et al., 2015) (Siltanen, Tihinen and Kömi, 2015) (Nykänen, Björk and Laitinen, 2012) (Dabiri et al., 2016) (Kah et al., 2013). In contrast to similar welding of UHSS DQ, which has been the subject of several studies in the literature, dissimilar welding of this grade has received little attention (Tasalloti, Kah and Martikainen, 2017).

In many welding applications, dissimilar combinations of metals is desirable for economic reasons. The dissimilar welding of ferritic steels and stainless steels has been of great significance in numerous fields of industry. Of the stainless steels currently available, duplex grades offer good mechanical properties together with excellent resistance to different forms of corrosion at a moderate price compared to high Ni grades (Tucker, Miller and Young, 2015).

The excellent mechanical characteristics and competitive cost of UHSS DQ and DSS grades, together with the superb corrosion resistance of DSS, suggest that dissimilar welds of these grades have considerable potential for many contemporary industrial applications, such as transportation, offshore and lightweight structures, as well as for novel applications requiring a combination of excellent mechanical properties and good corrosion resistance where cost and weight are major concerns. However, dissimilar welding of direct-quenched UHSS and DSS has not been widely studied and the weldability of such a dissimilar weld in terms of microstructure and mechanical performance is not sufficiently well understood. Further work is thus necessary to develop comprehensive understanding of the weld metallurgy and characteristics of such combinations as regards appropriate welding process parameters and welding specifications. In such dissimilar welding, selection of the welding parameters is complex because of a need for consideration of effects resulting from the special characteristics of each parent metal. The practical complexity can increase further when filler metal of a dissimilar composition to the base metals is used.

With UHSS, regardless of the specific welding process and alloy used, major documented problems include: heat affected zone (HAZ) cracking, HAZ softening, and deficient toughness and ductility (Hernandez, Nayak and Zhou, 2011) (Wang et al., 2016) (Farrokhi, Siltanen and Salminen, 2015). The aforementioned defects are generally caused by inappropriate heat input and cooling rate, which lead to the formation of coarse grains and changes in the proportion of ductile to brittle morphologies in the microstructure of the HAZ and fusion zone (Wang et al., 2016) (Roshanghias et al., 2010) (Guo et al., 2015).

With DSS, degradation of mechanical performance and corrosion resistance are the principal issues presented in the literature. These problems generally stem from inappropriate heat input and excessive thermal cycles, which can cause disparity between the proportion of ferrite and austenite and detrimental precipitations such as sigma (σ), chi (χ), and chromium nitride (Cr_2N) in the fusion zone and HAZ of DSSs (Ramirez,

Lippold and Brand, 2003) (Pardal, Tavares and al., 2010) (Garzón and Ramirez, 2006) (Martin et al., 2012).

The objective of this study reported in Publication VI and Publication VII, is to provide new insights and comprehensive understanding of the microstructural, mechanical and fatigue behaviour of dissimilar welds of UHSS DQ and DSS steels with respect to heat input. To this end, dissimilar welds were made between Optim 960 QC, a commercial UHSS DQ grade, and UNS S32205 duplex stainless steel using GMAW with an austenitic filler wire and applying three different heat inputs. The study presents detailed analysis of the microstructure, chemical composition in the fusion zone, fusion boundaries and HAZs as well as mechanical properties and fatigue behaviour of the weld samples for three different heat inputs.

3.3.1 Materials and welding procedure

As-received plates of Optim 960 QC ultrahigh strength steel (UHSS) and UNS S32205 duplex stainless steel (DSS) were machined to dimensions of 350×150×5 mm (ISO 15614-1) and V-grooves prepared with an angle of 60° in butt joint configuration. The root-face and air gap were both zero and removable fiberglass tapes were used for backing. Single pass welds were made on the joints using a fully automated GMAW machine with three different welding speeds, namely, 7.1 m/s, 8 m/s and 9 m/s. An austenitic filler wire, Esab OK Autrod 16.55 (1 mm diameter), was utilized for the welds under a constant shielding gas (98 % Ar + 2 % CO₂) at a flowrate of 15 l/min. The tip-to-work (stick out) distance was maintained at 13 mm throughout the entire welding process. The chemical composition of the base and filler metals are presented in Table 3. The three sets of parameters used for the welding samples are presented in Table 4.

Table 3. Welding parameters used for the weld samples: Arc current (I), arc voltage (U), welding speed (v), wire feed speed (WFS), arc energy (E), and heat input (Q).

Metal.	C	Si	Mn	P + S	Al	Nb	Cu	Cr	Ni	Mo	Other
S 960	.09	.21	1.05	.014	.030	.003	.025	.82	.04	.158	.002 (B) .008 (V) .032 (Ti)
S 32205	.015	.39	1.34	.026	–	.009	.25	22.59	5.79	3.24	.130 (Co)
16.55	.02	.4	1.7	–	–	–	1.4	20.5	25	4.5	.179 (N)

Table 4. Welding parameters used for preparing the samples: Arc current (I), arc voltage (U), welding speed (v), wire feed speed (WFS), arc energy (E) and heat input (Q).

I (A)	U (V)	v (mm/s)	WFS (m/min)	E (kJ/mm)	Q (kJ/mm)
257	29.8	7.1	10.6	1.08	0.86
224	28.7	8	10	0.80	0.64
204	26.4	9	9	0.60	0.48

3.3.2 Metallurgical and mechanical characterization of weldments

The weld specimens were cut from the as-welded plates in accordance with EN ISO 15614-1 for destructive tests. The ferrite number (FN) of the welds was measured using a ferritescope device according to EN ISO 8249 standard. Metallography samples were polished (final polish with 1 μm diamond paste) and etched in compliance with EN ISO 17639 standard for microscopic examination of welds and ISO/TR 16060 for etchants. The DSS side was etched using a standard Cuprochloric solution 2 (5g CuCl_2 + 100 ml HCl + 100 ml $\text{C}_2\text{H}_5\text{OH}$ + 100 ml H_2O) and Nital (95 ml $\text{C}_2\text{H}_5\text{OH}$ + 5 ml HNO_3) was used for etching the UHSS side. The etching time was 15 s and 30 s for Nital and Cuprochloric solution 2, respectively. Both light microscopy scanning and electron microscopy (SEM) were used to delineate the microstructural features in the HAZs and welds.

Vickers hardness tests (HV_5) were carried out on the etched samples at room temperature using 49.03 N force, in compliance with EN ISO 9015-1 and ISO 6507-1.

Weld specimens were machined to the geometries recommended by EN ISO 4136, EN ISO 5173 and EN ISO 9016 standards for tensile, bending and Charpy impact tests, respectively. Tensile tests were performed at room temperature on two sets of samples made from each type of weld. Transverse face bending (TFB) and transverse root bending (TRB) tests were performed separately on two specimens for each type of weld. The Charpy V-notch impact test was performed at $-40\text{ }^\circ\text{C}$ using a pendulum impact testing machine with an impact energy of 150 J. The test was replicated on 6 specimens with a notch either on the weld centre or 1 mm offset from the weld centre toward the UHSS DQ base metal. In addition, three specimens of each type of weld were machined for fatigue testing and the results were analysed according to IIW recommendations (Hobbacher, 2016)

For convenience, the base and filler metals are henceforth referred to as S 960, S 32205 and 16.55, and the weld samples are named *WS 7.1*, *WS 8*, and *WS 9*, based on the welding speed used.

3.3.3 Microstructure

SEM images of the as-received parent metals are shown in Figure 15. The microstructure of S 960 comprises fine martensitic-bainitic grains that are formed in the rolling direction, shown in Figure 15 (a). The martensitic phase is apparent in the form of pancaked or elongated prior austenite (γ) grains in the rolling direction (Muckelroy, Findley and Bodnar, 2013). Figure 15 (b) displays a typical DSS microstructure with nearly equal elongated lamella of ferritic-austenitic regions.

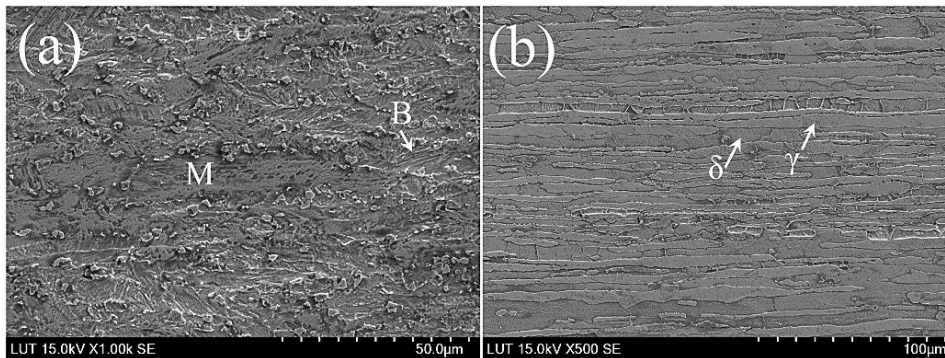


Figure 15. SEM images of as-received parent metals: (a) S 960 containing bainite (B) and martensite (M); (b) S 32205 containing nearly parallel lamella of austenite (γ) and ferrite (δ) (Tasalloti, Kah and Martikainen, 2017).

The optical micrographs of the HAZ of the weld samples on the UHSS side at a distance of about 1 mm from the fusion boundary are shown in Figure 16 (a) - (c). The microstructure has been subjected to significant grain coarsening. Moreover, it appears that the amount and proportion of formed morphologies have been to some extent influenced by the heat input. For instance, bainitic phase prevails in *WS 7.1*, while martensite dominates in the HAZ of *WS 9*, as can be seen in Figure 16 (a) and (c) respectively. In contrast, bainite and martensite are almost evenly formed in the HAZ of *WS 8*, as seen from Figure 16 (c).

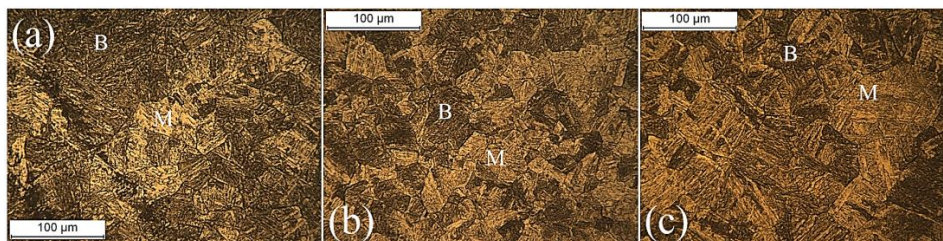


Figure 16. Formation of coarse grains in the HAZ at the S 960 side. Bainite (B) with darker appearance can be differentiated from martensite (M). (a) *WS 7.1*, predominantly bainitic morphologies; (b) *WS 8*, roughly even balance of bainitic and martensitic morphologies; and (c) *WS 9*, predominantly martensitic morphologies (Tasalloti, Kah and Martikainen, 2017).

Figure 17 shows a time-temperature graph of the HAZ (at 2 and 3 mm distance from the fusion line) on the UHSS side, plotted on a continuous cooling transformation (C.C.T) diagram of a quenched and tempered steel with nearly matching chemical composition to S 960 (Voort, 1991). From the figure, it is evident that with initiation of welding, the HAZ heated to temperatures beyond the upper intercritical temperature (AC_2), where the microstructure, theoretically, mostly transferred to γ . This is followed by rapid cooling below the lower intercritical temperature (AC_1), at which decomposition of γ started. Subsequently, further cooling, down to a temperature of about 550 °C, initiated bainitic transformation, which preceded martensitic formation at lower temperatures. As can be

seen from the diagram, the bainite start temperature decreases as the cooling rate increases. Thus, more bainitic phase can be expected with lower cooling rates, in agreement with the observation in Figure 16. Note that the diagram reached a plateau above AC_2 due to the temperature exceeding the upper-limit of the thermocouples used.

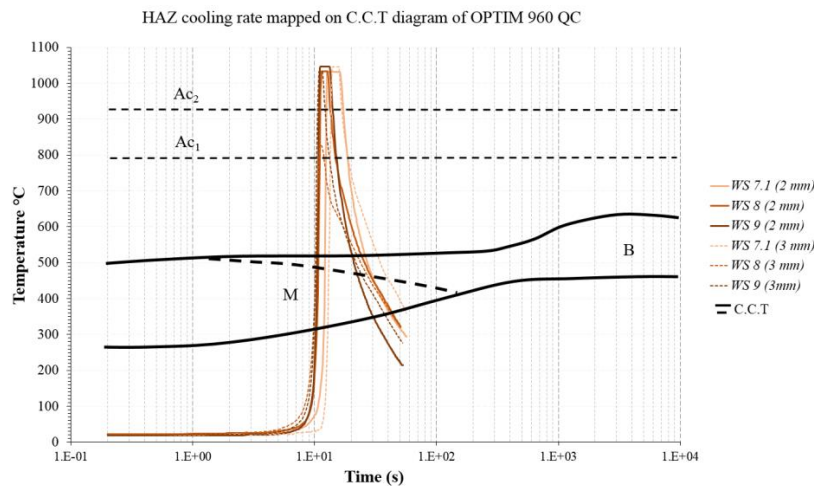


Figure 17. HAZ time-temperature diagram plotted on a C.C.T diagram of a quenched and tempered steel of a comparable composition to S 960. Variation of temperature with time as a result of welding was measured at distances of 2 and 3 mm from the fusion boundary in the HAZ of the S 960 metal (Tasalloti, Kah and Martikainen, 2017).

The SEM image shown in Figure 18 illustrates details of the HAZ microstructure. In the figure, only the HAZ of WS 9 is presented, as the microstructural features were similar for all the samples.

A distinct network of prior-austenite boundaries is visible in Figure 18. Martensitic structure is detectable with a characteristic of almost uniform and barely etched plates within prior-austenite boundaries. The bainitic phase is composed of dominantly lower bainite (B_L) and upper bainite (B_U) morphology in a lower proportion. The bainitic regions featuring laths of lower and upper bainite are indicated on Figure 18. The coarse laths of lower bainite generally intersect each other and partition the prior-austenite grains, which differentiates them from upper bainite morphology with almost parallel laths filling the prior-austenite grains (Guo et al., 2010), as seen in Figure 18.

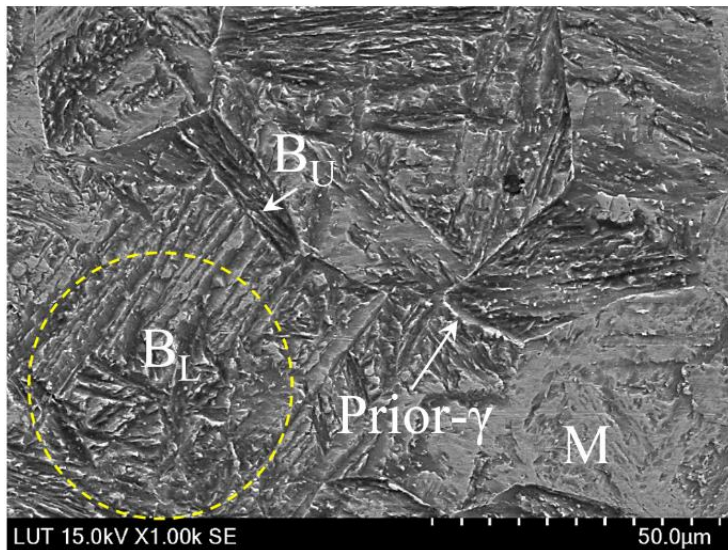


Figure 18. Microstructure of the HAZ on the S 960 side of WS 9. The SEM image shows the coexistence of martensite (M), lower bainite (B_L) laths (within the region circled with a dotted line), and upper bainite (B_U) laths within a prior-austenite (γ) grain. Prior- γ boundaries are clearly visible (Tasalloti, Kah and Martikainen, 2017).

The microstructure of the HAZ on the DSS side is shown in Figure 19 (a) - (c). The eventual microstructure of the HAZ is determined by solid state phase transformations from γ to δ and vice versa that occur during welding (Zhang et al., 2005). As can be seen in the micrographs, the HAZ has undergone a substantial phase transition in the microstructure. The main morphology of γ is grain boundary austenite (GBA), which is differentiable by allotriomorphic formations at the prior- δ grain boundaries (Ramirez, Lippold and Brand, 2003) (Eghlimi et al., 2015), and which is apparent at the boundaries of coarse ferrite grains in Figure 19. The morphology of GBA is better visible in the BSE image shown in Figure 20. For S 32205, transformation from γ to δ initiates at a temperature around 855 °C and observations in (Palmer, Elmer and Babu, 2004) suggest nearly complete decomposition of γ to δ as the temperature exceeds 1350 °C.

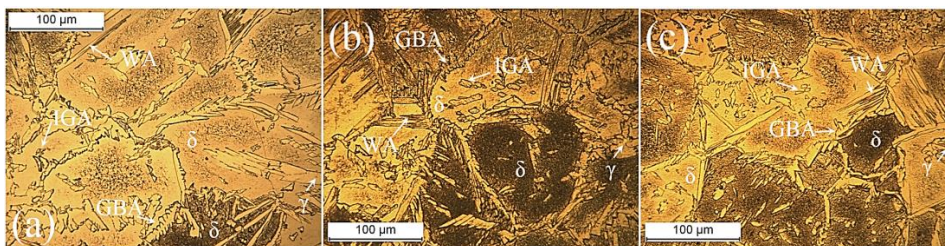


Figure 19. Microstructure of the HAZ of S 32205: (a) WS 7.1, (b) WS 8, (c) WS 9. Different morphologies of austenite (γ), namely, grain boundary austenite (GBA), Widmanstätten austenite (WA) and intragranular austenite (IGA) are discernible in the figure (Tasalloti, Kah and Martikainen, 2017).

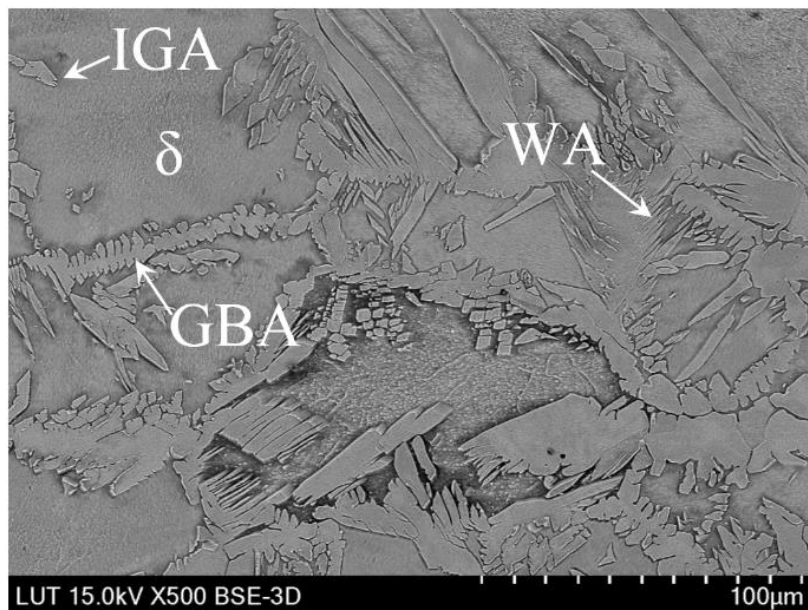


Figure 20. BSE image of the HAZ on the S 32205 side. Different morphologies of austenite are seen, namely: grain boundary austenite (GBA), Widmanstätten austenite (WA), and intragranular austenite (IGA). Fine etched and coarse etched domains of ferrite (δ) are also detectable (Tasalloti, Kah and Martikainen, 2017).

As can be seen from the cooling rate diagram in Figure 21, the temperature in the HAZ (at 2 mm distance from the fusion line) exceeded 1100 °C for a period of less than 10 s, which can be considered too short for full ferritization. Subsequently, upon cooling, GBA started to nucleate from larger untransformed γ , which shaped the jagged appearance that is evident in Figure 20.

Widmanstätten austenite (WA), another prevalent morphology, nucleates at lower temperatures than GBA (Rahmani, Eghlimi and Shamanya, 2014). WA forms as needle-like elongated plates, usually initiating from GBA and extending toward the δ grains (Eghlimi et al., 2015), as can be seen in Figure 19 and Figure 20. In addition, some growth of intragranular austenite (IGA), dispersed within the δ grains, can be discerned in Figure 19 and 20. The lattice diffusion of IGA is known to be slower than the allotropic growth of GBA and WA. Therefore, IGA will principally grow when enough undercooling is available (Eghlimi et al., 2015). As a result, IGA morphology only emerged in small amounts in comparison with GBA and WA, as can be seen in Figure 19 and 20.

Figure 21 depicts temperature over time for the HAZ (measured at 2 and 3 mm distance from the fusion boundary) plotted on a time temperature precipitation (T.T.P.) diagram of S 32205 (Voort, 1991). It should be noted that Cr_2N can form under both isothermal (i.e., the T.T.P. diagram) and cooling conditions (Pettersson, Pettersson and Wessman, 2015). It is well established in the literature that rapid cooling rates can favour precipitation

of Cr_2N (Ramirez, Lippold and Brand, 2003) (Palmer, Elmer and Babu, 2004) (Pettersson, Pettersson and Wessman, 2015) (Hsieh, Liou and Pan, 2001) (Kang and Lee, 2012) (Hertzman, Ferreira and Brolund, 1997). As shown in Figure 21, initiation of welding almost instantaneously heated the HAZ of S 32205 to temperatures beyond 1100 °C, i.e. temperatures at which degeneration of the austenite into ferrite begins. The DSSs are alloyed with nitrogen, which is almost entirely retained in solid solution within the austenite, which has much higher nitrogen solubility than the ferrite. Consequently, on rapid cooling to temperatures below 1100 °C, the partially or totally ferritized microstructure of the HAZ becomes supersaturated with nitrogen (Ramirez, Lippold and Brand, 2003). Accordingly, the transformation behaviour will not conform to that of a duplex structure but will behave as a metastable nitrogen supersaturated ferrite structure with very low solubility of nitrogen, which can lead to competition between Cr_2N and austenite precipitation (Ramirez, Lippold and Brand, 2003). However, the high magnification SEM image of the coarse etched ferritic region in Figure 22 suggests that no detrimental precipitations have taken place in this region.

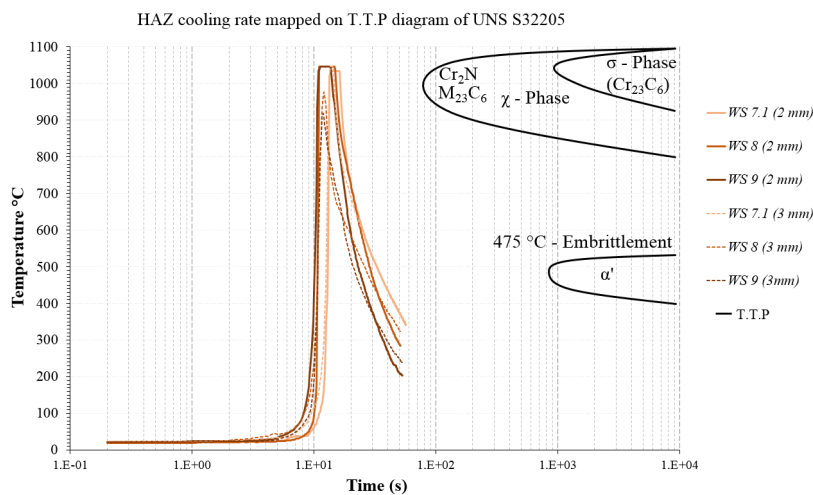


Figure 21. Time temperature precipitation (T.T.P.) diagram for S 32205 (Voort, 1991) and temperature variation against time in the HAZ of S 32205 (Tasalloti, Kah and Martikainen, 2017).

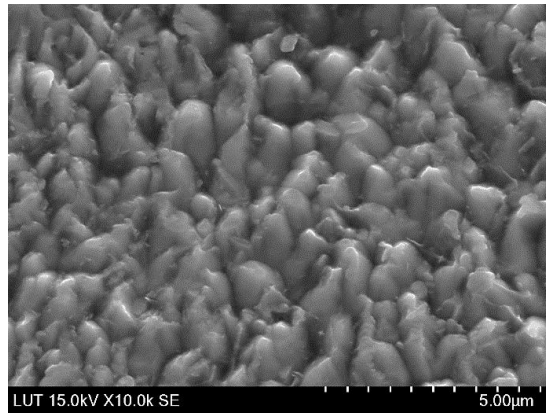


Figure 22. SEM image of the microstructure of coarse etched ferritic sites. No detrimental secondary precipitation is detectable in the micrograph (Tasalloti, Kah and Martikainen, 2017).

The microstructure of the fusion boundary on the ferritic side of the dissimilar weld can be seen in Figure 23 (a)-(c). The fusion zone in the figure appears as a fully austenitic structure without noticeable formation of ferrite in the interdendritic regions. This can indicate a fully austenite (Type-A) solidification mode (Lippold and Savage, 1979). However, the EDS analysis, discussed in the next section, revealed ferrite stabilizing elements (i.e. Cr and Mo) partitioned into the interdendritic regions in some parts of the fusion zone (Figure 29 and 30). Hence, formation of a small percentage of δ in the interdendritic regions during the last stage of solidification can be inferred, which further suggests a primary austenite (Type-AF) solidification mode (Kujanpää, David and White, 1986). The correlation of C_{req}/Ni_{eq} and the solidification mode can be noted from a schematic of the pseudo-binary diagram (Lippold and Savage, 1979) shown in Figure 24. Equiaxed grain growth of austenite in *WS 7.1*, in contrast with columnar and dendritic growth in *WS 8* and *WS 9*, is also conspicuous in Figure 23.

A prominent feature of the weld metal in Figure 23 (a) and (c) is a narrow unetched intermediate zone with a planar solidification. Such a feature is commonly observed at the weld interface of austenitic and ferritic steels and is generally identified as martensite in the literature (Dupont and Kusko, 2007).

Figure 23 (b) displays a distinct intermediate zone with a composite structure of base and weld metals that characterizes a partially mixed zone (PMZ) (Kou, 2003) (Omar, 1998). Both the aforementioned martensitic and PMZ zones are classified as macrosegregation in the literature (Kou, 2003) (Kou and Yang, 2007) because the compositions have a gradient over a bulky span (100-200 μm), whereas in microsegregation, the compositions vary over the span of a dendrite arm or cell spacing (Kou and Yang, 2007).

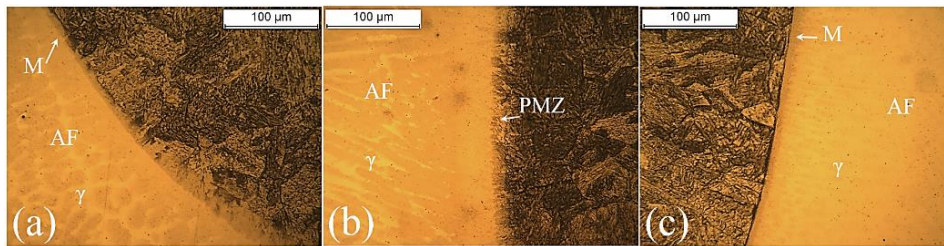


Figure 23. Microstructure of weld metal proximate to the fusion boundary on the S 960 side of the weld. (a) WS 7.1, (b) WS 8, and (c) WS 9. The weld metal is characterized as primary austenite (AF) solidification mode. Equiaxed grain growth of γ is distinguishable in WS 7.1, which contrasts with columnar and dendritic growth in WS 8 and WS 9. Martensitic layers (M) and a partially mixed zone are marked on the micrographs (Tasalloti, Kah and Martikainen, 2017).

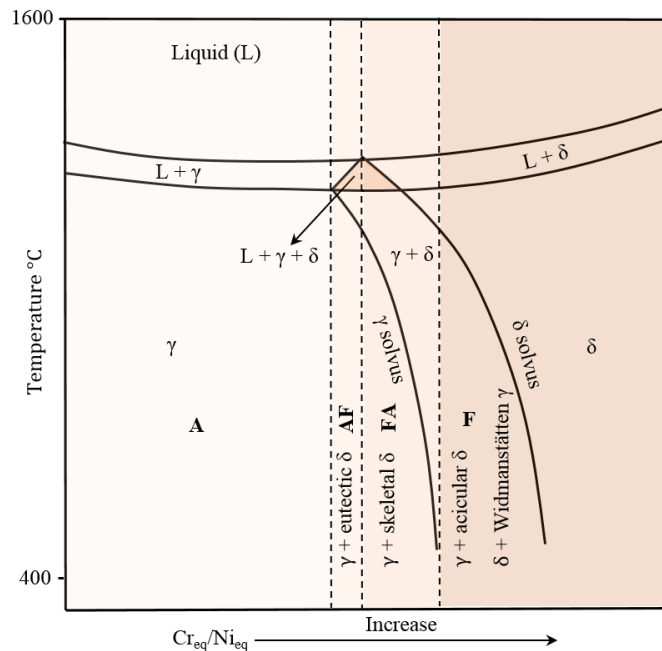


Figure 24. Schematic of a pseudo-binary diagram (Lippold and Savage, 1979) for an alloy containing about 70 wt. % Fe. In the diagram, values are not assigned to Cr_{eq}/Ni_{eq} ratios and temperatures since the composition of the alloy used may not correspond with that in the original diagram (Tasalloti, Kah and Martikainen, 2017).

Figure 25 (a) and (b) present a SE/BSE scan of the PMZ and the associated martensitic band. The martensitic band formed in all the weld samples, although this feature was more prominent in WS 7.1, clearly visible with a width of $\sim 20 \mu m$ in Figure 25 (a). By comparison, the PMZ adjoining to the weld metal in WS 8 features a composite structure made of a predominant martensitic region and some parts with bainitic appearance, typically surrounded with ghost prior- γ boundaries, as can be seen in Figure 25 (b).

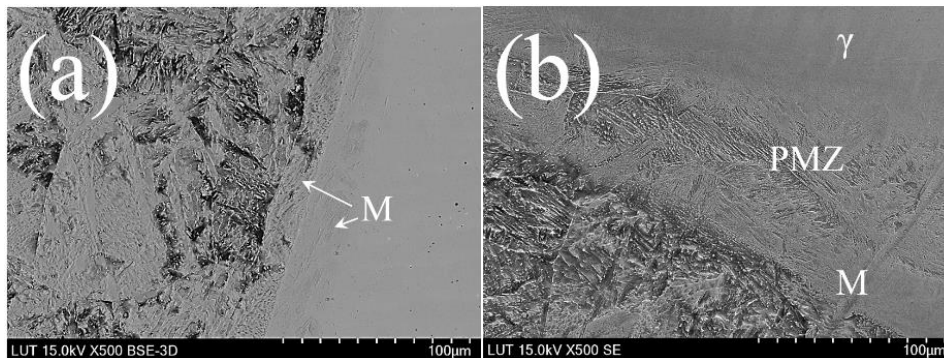


Figure 25. SE and BSE SEM images of the WS 7.1 and WS 8 fusion boundary on the S 960 side. (a) BSE image of the WS 7.1 fusion boundary showing planar solidification of the martensitic band and formation of martensitic grains parallel to the fusion line. (b) SEM image of the partially mixed zone (PMZ) along the fusion boundary of the WS 8. The PMZ is characterized by a composite structure, dominantly martensite (M), and some regions resembling a bainitic structure, generally boarded by the remains of a prior-austenite (γ) boundary (Tasalloti, Kah and Martikainen, 2017).

It is reported in the literature that the martensitic layer has a composition between the ferritic steel and the austenitic weld metal (Dupont and Kusko, 2007) (Doody, 1992) (Mukherjee and Pal, 2012) due to the existence of a layer of stagnant or laminar flow of liquid base metal alongside the weld pool boundaries (Kou and Yang, 2007) and fast cooling from the weld thermal cycle on the fusion boundary (Ornath et al., 1991). The amount of dilution, which is influenced by the amount of heat input, can be a determinant factor in creation of a martensitic layer (Eghlimi et al., 2015). Diffusion of carbon from the ferritic base metal to the Ni-based weld metal is another critical factor in formation of a martensitic layer (Lippold, Kiser and DuPont, 2009). However, no significant carbon migration is typically found in as-welded condition, and it is only important during postweld heat treatment (PWHT) (Lundin, 1982).

Another form of macrosegregation, in the form of islands that resemble the base metal structure (Omar, 1998), was found close to the fusion boundary of WS 9, as clearly seen in Figure 26. According to Kou et al. (Kou and Yang, 2007), formation of segregated islands is a result of the difference in liquidus temperature of the base metal ($\sim 1530\text{ }^{\circ}\text{C}$) and weld metal ($\sim 1400\text{ }^{\circ}\text{C}$). As stated in (Kou and Yang, 2007), given that the liquidus temperature of the base metal (T_{LB}) is higher than that of the weld metal (T_{LW}), which is the case in this experiment, the temperature of the liquid weld metal in the regions immediately ahead of the mushy zone can be below T_{LB} . Consequently, the liquid base metal swept from the mushy zone into this cooler region by convection can rapidly solidify without significant mixing with the liquid weld metal (Kou and Yang, 2007).

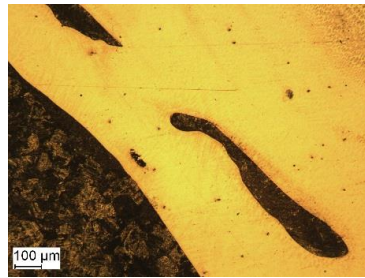


Figure 26. Macrosegregation formed inside the weld metal parallel to the fusion boundary. The islands appear to have a similar structure as the base metal (Tasalloti, Kah and Martikainen, 2017).

Figure 27 (a)-(c), displays a fully austenitic microstructure of the weld metal on the duplex side of the weld. Nearly equiaxed cellular growth was prominent in *WS 7.1*, while columnar growth of dendrites or a combination of cellular and columnar growth were noticeable for *WS 8* and *WS 9*. Similar to the ferritic side, accumulation of Cr and Mo was detected in some interdendritic areas (Figure 31) in the fusion zone, which can be a confirmative indication of ferrite formation and AF solidification mode.

Figure 27 (b) and (c) clearly reveal the presence of an intermediate zone with a different structure from the base and bulk weld metal. In like manner as on the S 960 side, macrosegregation is considered the reason for the disparity in chemical composition that led to a different solidification mode in the intermediate zone. In Figure 27 (b), macrosegregation appears in the form of a PMZ, while in Figure 27 (c) it presents as a composite structure consisting of a PMZ and unmixed zone (UMZ). The PMZ characterises a primary ferritic solidification (FA) mode during which the transformation of primary- δ to γ took place through a peritectic-eutectic reaction in the liquid state (Rahmani, Eghlimi and Shamanya, 2014). The structure contains a vermicular or skeletal morphology of the delta ferrite in a matrix of γ , delineated in Figure 27 (b) and (c). The UMZ, which appears in the form of a peninsula in Figure 27 (c), indicates a ferritic structure comparable to the coarse grains formed in the HAZ. It is put forward in the literature that the UMZ can appear due to a stagnant or laminar flow layer at the solid-liquid interface between the weld pool and base metal (Kou and Yang, 2007) (S. Kou, 1996).

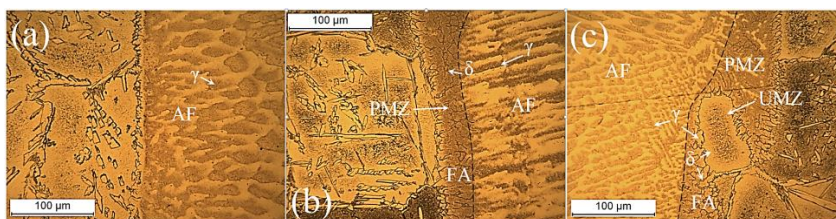


Figure 27. Microstructure of the fusion boundary and weld metal at the S 32205 side of (a) *WS 7.1*, (b) *WS 8*, and (c) *WS 9*. Micrographs (b) and (c) delineate an intermediate zone in the form of a partially mixed zone (PMZ) and unmixed zone (UMZ). Primary ferrite (FA) solidification in the PMZ is noticeable in contrast to primary austenite (AF) in the weld zone. Austenite (γ) grains and retained skeletal ferrite (δ) are also seen in this figure (Tasalloti, Kah and Martikainen, 2017).

Figure 28 presents micrographs of the fusion zone around the weld axis for the weld samples. In line with expectations, as the cooling rate decreases with increase of distance from the fusion boundary toward the weld axis, equiaxed growth became more dominant in all weld samples, as can be seen in Figure 28.

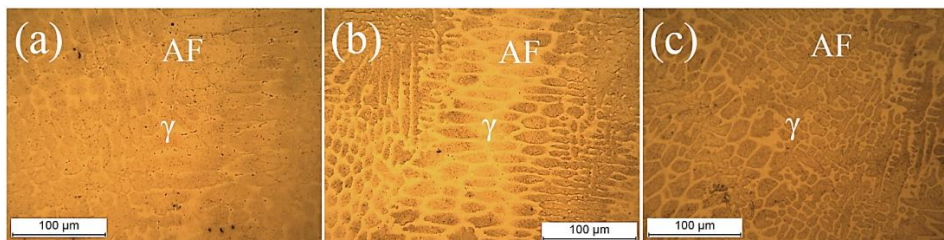


Figure 28. Microstructure of the weld metal around the weld axis: (a) WS 7.1, (b) WS 8, and (c) WS 9. In all samples, more granular and equiaxed austenitic growth was noticed at the lower cooling rates farther from the fusion line (Tasalloti, Kah and Martikainen, 2017).

3.3.4 Chemical composition

Figure 29 shows EDS mapping of the major alloying elements (i.e. Fe, Cr, Ni, Mo) across the fusion zone and HAZ. It should be noted that C is excluded due to inaccuracy in the analysis as a result of its light element character. A chemical composition gradient in the weld samples is noticeable in Figure 29 (a)-(c). It should be noted that for WS 9, the figure is mirrored relative to (a) and (b), i.e. for WS 9 the UHSS is on the right and DSS on the left side of the figure.

Generally, three forms of macrosegregation are propagated in the literature (Kou, 2003) (Kou and Yang, 2007) (Robert and Messler, 2004) (Yang and Kou, 2007). These macrosegregation types are filler-depleted zones along the fusion boundary (i.e. PMZ and UMZ) or across the width of the fusion zone as its centreline approaches (i.e. islands with composition between the base metal and bulk weld metal) and a filler-enriched zone at the weld bottom. All of the above-mentioned forms are observable in Figure 29 (a)-(c).

As was noted earlier, a PMZ and a narrow martensitic band were detected on the ferritic side of the welds (Figure 23 and 25). Ornath et al. (Ornath et al., 1991) specified that this narrow band is richer in Fe and Cr than Ni. Such a composition is discernible at the intermediate boundary of all the samples, shown in Figure 29 (a)-(c).

Filler-depleted islands are another distinct feature highlighted in Figure 29 (a) and (c). The composition suggests that the islands in both Figure 29 (a) and (c) originated from the S 960 side and solidified prior to being completely mixed and dispersed in the weld pool. In Figure 29 (c), the composition suggests that the islands solidified virtually without mixing with the weld metal.

Another type of macrosegregation in the form of accumulation of alloying elements (filler-rich zone) within the weld-bottom is apparent in Figure 29 (b). A solidification

mechanism is suggested by Yang and Kou (Yang and Kou, 2007) to explain macrosegregation at the weld-bottom. However, in the specific weld specimen examined in this work, the segregation probably took place due to asymmetrical geometry of the melted joint, which is evident in Figure 29 (b). It is known that during arc welding, the electromagnetic force enhances mixing in the weld pool by conveying the filler droplets to the bottom of the pool and then driving the melt upward alongside the fusion boundary and finally pushing the melt toward the centre of the pool (Kou and Wang, 1986). Nevertheless, in the examined weld pad, projected base metal in the weld pool obstructed the mixing pass. Accordingly, the transferred filler droplets for the weld bottom primarily found their way upward along the ferritic side of the fusion boundary, while the rest solidified as a filler-rich area at the bottom of the weld before being able to melt down the projected obstacle.

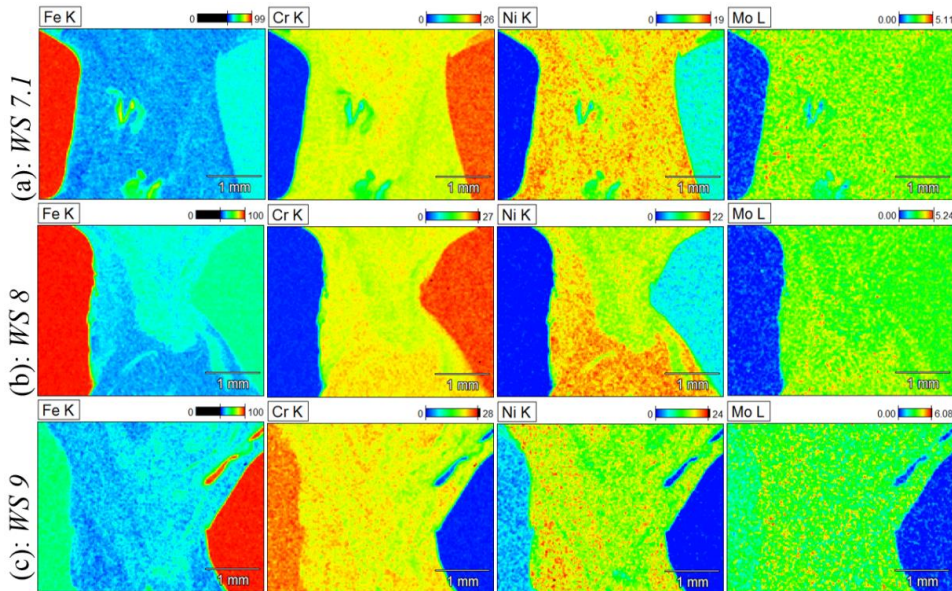


Figure 29. Concentration gradient of some major alloying elements (Fe, Cr, Ni, and Mo) through the weld as shown by EDS analysis of (a) *WS 7.1*, (b) *WS 8*, and (c) *WS 9*. Note that the ferritic and duplex side is mirrored in (c), i.e. UHSS is on the right side and DSS on the left side of the figure (Tasalloti, Kah and Martikainen, 2017).

The segregation of Cr and Mo (ferrite stabilizers) into interdendritic regions is demonstrated in Figure 29 and more clearly in Figure 30. Segregation of Cr and Mo can be strong corroborative evidence for nucleation of eutectic ferrite in the interdendritic regions. According to Lippold and Savage (Lippold and Savage, 1979), during the final transition stage of primary-austenite solidification, Cr strongly partitions to the dendritic interstices, while segregation of Ni remains inconsiderable, which is in agreement with the EDS analysis shown in Figure 30.

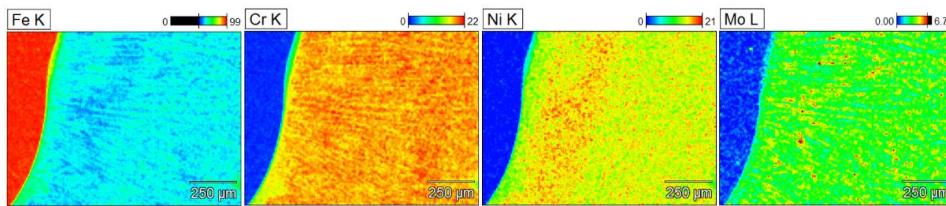


Figure 30. EDS compositional analysis of WS 7.1 on the ferritic side of the weld (Tasalloti, Kah and Martikainen, 2017).

Figure 31 presents the EDS analysis of the PMZ and UMZ in the intermediate zone at the duplex side of WS 9 (Figure 27). In the figure, the PMZ exhibits Ni content between the base and the bulk weld metals, which provides a further indication for diffusion of Ni from filler metal into this region.

As was seen in Figure 27, the PMZ exhibits primary- δ solidification mode. This conclusion can also be derived from Figure 31. The formation of a PMZ occurred at the Cr-rich side of the eutectic liquidus (Figure 24), which supports FA solidification.

Figure 31 reveals the composition of the detected peninsula, which resembles a thumb in this figure. In line with expectations, this expanse has in essence the same composition as the base DSS, which validates its recognition as UMZ.

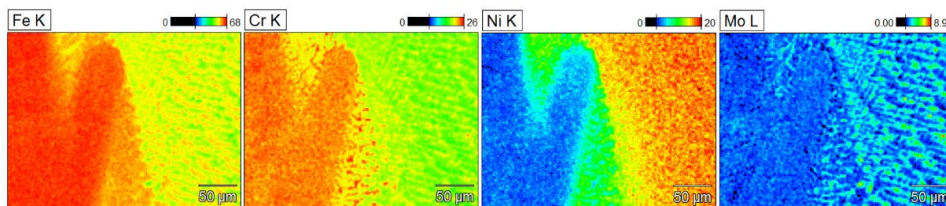


Figure 31. EDS compositional analysis of WS 9 on the duplex side of the weld (Tasalloti, Kah and Martikainen, 2017).

3.3.5 Hardness

Hardness values were obtained across a parallel distance of about 1 mm from the free faces of the weld samples along the indentation line shown in Figure 32. The hardness profile of the face and root side of the specimens is shown in Figure 33 and Figure 34, respectively. In the diagrams, the labelled hardness values are associated with the indents that were placed approximately on the unaffected base metals, beginning at the coarse grain heat affected zones, proximate to the fusion boundaries, and on the fusion zone centrelines.

As can be seen in Figure 33 and 34, the hardness of the unaffected S 960 was between 310-340 HV. A decline in hardness can be clearly seen in the direction toward the fusion boundary. It can be noticed from the hardness profile that HAZ softening is more severe in WS 7.1, with about 25 % decline in hardness at the lowest hardness level, close to the

fusion boundary. However, the reduction in hardness ameliorated when lower heat inputs were applied, so that for *WS 9* the maximum decrease in hardness was only about 16 %, shown in Figure 33 and 34.

Intermittent increases in hardness to a level close to that of the base metal (300-320 HV₅) can be seen in association with the martensitic phase in the microstructure. Hardness values of about 290 HV₅ may be correlated with the bainitic phase. Moving forward from the coarse grain HAZ toward the fusion boundary, substantial reduction of hardness at some points can be noticed in both the root and face hardness profiles. The hardness of the softened zone varies between 231-258 HV₅ in *WS 7.1*, 250-262 HV₅ in *WS 8*, and 268-269 HV₅ in *WS 9*, observable in Figure 33 and 34. Attenuation of the dislocation density of the new coarse grains formed from the intercritical austenite at this region can be a significant contributor to this softening (Guo et al., 2015) (Qiu et al., 2010).

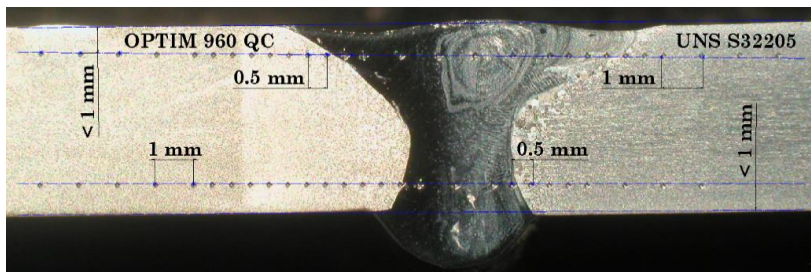


Figure 32. Indentation along face and root side of the weld specimen.

The variation of hardness in the HAZ of the duplex side is less considerable. However, a moderate increasing trend in the hardness profile can be discerned as measurements approach the fusion boundary, except for *WS 7.1* on the face side. This increase may be related to the increased ratio of ferrite to austenite in the HAZ as a result of the thermal cycle experienced (Sadeghian, Shamanian and Shafyei, 2014).

The austenitic fusion zone has the lowest hardness levels, in the range of 150-190 HV₅. The hardness values were generally higher for *WS 8* and *WS 9* than *WS 7.1*. The harder weld metal may be a result of the change in the austenitic weld texture from more equiaxed grains in *WS 7.1* to more dendritic and columnar forms in *WS 8* and *WS 9*. In addition, possible disparities in the chemical composition of the fusion zone as a result of macrosegregation in the weld may affect the hardness measurements.

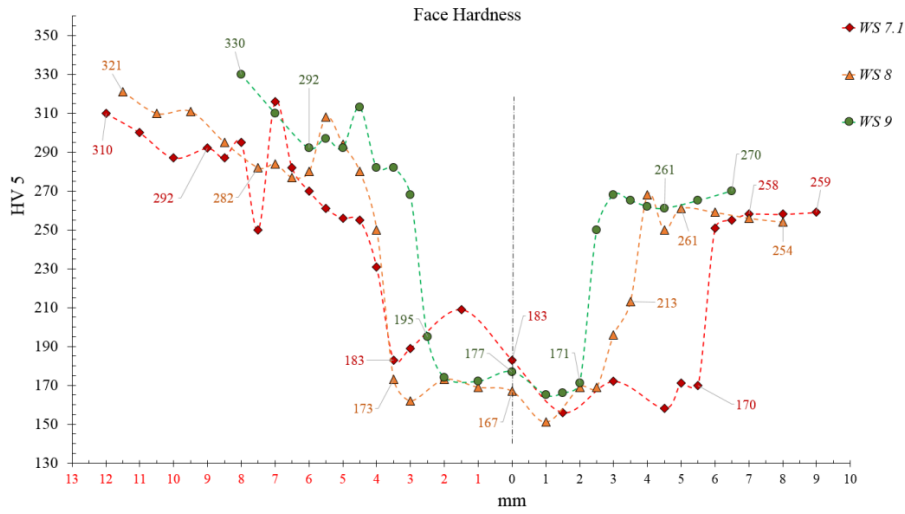


Figure 33. Hardness profile at a distance less than 1 mm from the face side of the weldments in the transverse direction from unaffected S 960 base metal (left) and toward unaffected base metal S 32205 (right). The vertical dotted line approximately indicates the centre line of the weld samples. The points that are labelled with values are approximately on the unaffected base metals, the beginning of coarse grain heat affected zones, weld metal adjacent to the fusion boundaries, and the centreline of the welds.

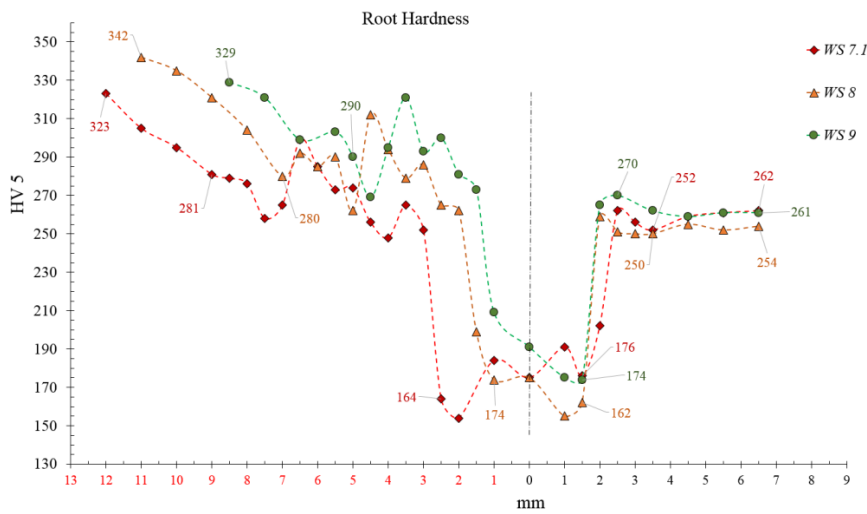


Figure 34. Hardness profile at a distance less than 1 mm from the root side of the weldments in the transverse direction from unaffected S 960 base metal (left) and toward unaffected base metal S 32205 (right). The vertical dotted line approximately indicates the centre line of the weld samples. The points that are labelled with values are approximately on the unaffected base metals, the beginning of coarse grain heat affected zones, weld metal adjacent to the fusion boundaries, and the centreline of the welds.

3.3.6 Bend properties

Transverse root and face bending tests were carried out on the specimens using a mandrel with a diameter of 65 mm. The results are presented in Table 5. As can be seen from the results, all weld samples showed excellent ductile properties and passed the face bending test. However, all the specimens failed at the root side. It can be postulated that the accumulation of strain mainly took place at the narrow soft weld and proceeded by plastic deformation beyond the endurance of the weld, leading to fracture. A lower strain capacity can be anticipated on the root side as it has a narrower weld cross-section. The narrower weld resulting from the lower heat input can also shed light on the decrease in ductility and failure angle of *WS 9*.

Table 5. Transverse face bending (TFB) and transverse root bending (TRB). The results are in degree angle.

Specimen	TFB	TRB
<i>WS 7.1</i>	180°	67°
<i>WS 8</i>	180°	64°
<i>WS 9</i>	180°	37°

3.3.7 Tensile behaviour

The yield and ultimate tensile strength of the samples are tabulated and compared with those of the parent metals in Table 6. The diagram shown in Figure 35 presents a comparison of the average tensile strength values. All specimens failed at the weld. This may be a result of stress concentration at this soft region leading to strain beyond the range of the weld endurance and subsequent fracture. As can be seen in Figure 35, increase in strength shows a direct connection with decrease in heat input. It was seen from the hardness profiles (Figure 33 and 34) that lower heat input generally increased the hardness throughout the fusion zone and HAZ, by altering either the microstructural phases (i.e., increased proportion of martensite to bainite) or the texture of the HAZ and fusion zone. A slight increase in the hardness could more effectively constrain plastic deformation, thus increasing the strength.

The results signify that the yield strength of the specimens declined compared with that of the S 960 base metal, with a drop of 36 % in *WS 7.1* and 33 % in *WS 9*. Nonetheless, the yield values still remained 1.5 % - 6.5 % higher than that of the S 32205 parent metal. In comparison, the ultimate strength of the specimens was 35% - 36% lower than that of S 960 and 13 % - 17% inferior to that of S 32205.

It can be seen from Figure 35 that the variation in elongation of the specimens was insignificant and did not show a clear correlation to the heat input. Due to the significant mismatch between the mechanical properties of the base and weld metals, evaluation of elongation of the weldment through standard tensile tests can be open to question. As mentioned above, the concentration of strain and the plastic deformation was mainly at

the fusion zone, which constitutes the softest region. Therefore, the elongation results may principally represent the fracture strain of the fusion zone.

Table 6. Yield strength and ultimate tensile strength. Test results obtained from two replicates (Test 1 and Test 2) for each weld sample. The average (Ave.) quantities are calculated from Test 1 and Test 2. (*) indicates values for the base metals taken from the supplier’s certificate.

Specimen	Yield strength (N/mm ²)			Ultimate tensile strength (N/mm ²)			Elongation Ave. (%)
	Test 1	Test 2	Ave.	Test 1	Test 2	Ave.	
WS 7.1	636.83	643.27	640.05	681.91	684.90	683.40	5.76
WS 8	651.43	666.34	658.88	687.02	701.99	694.51	5.10
WS 9	680	663.88	671.94	720.98	713.06	717.02	6.20
S 960	–	–	1004.5 *	–	–	1114.50 *	11.5
S 32205	–	–	631 *	–	–	825 *	28.5

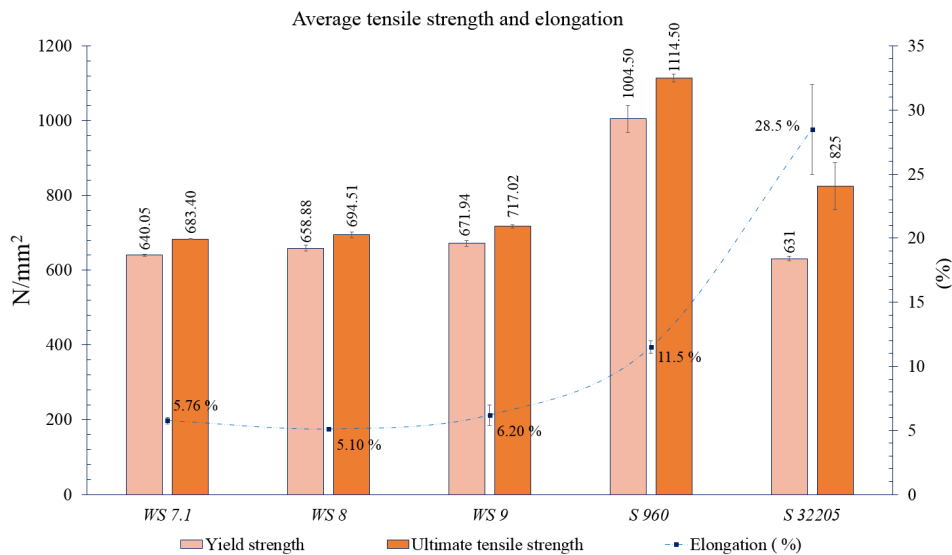


Figure 35. Comparison between the weld specimens and the parent metals in terms of average yield and ultimate strength as well as elongation (%).

3.3.8 Impact toughness

Table 7 displays a summary of absorbed energy values from the Charpy V-notch impact test. The impact energies of the weld metal and HAZ were procured from three sets of tests carried out separately on the specimens with a notch either on the weld centre or at 1 mm distance from the centre toward the S 960 side, respectively. Average impact toughness values are also listed in the table.

Table 7. Impact test results obtained when applying 150 J impact energy at -40 °C. Three sets of experiments were performed separately on the weld specimens with a V-notch either on the weld

centre or with 1 mm offset toward HAZ of the S 960 side. (*) indicates values taken from the supplier's certificate.

Specimen	Weld metal (J.cm ⁻²)				HAZ of S 960 (J.cm ⁻²)			
	Test 1	Test 2	Test 3	Ave.	Test 1	Test 2	Test 3	Ave.
WS 7.1	71	31	50	50.67	43	23	48	38
WS 8	56	45	54	51.67	35	70	61	55.33
WS 9	44	41	46	43.67	43	59	44	48.67
S 960	60*	60*	57*	59*	–	–	–	–
S 32205	40*	60*	–	50*	–	–	–	–

Figure 36 provides a comparison between the median absorbed impact energy of the weld samples and the impact toughness of the base metals. As can be realized from the figure, all the weld samples passed the minimum requirement of 27 J for the weld. However, the magnitudes were 14 % to 26 % inferior to the absorbed energy of the S 960 parent metal.

The results demonstrate outstanding impact toughness for WS 8, whereas WS 9 showed the highest brittleness. The impact toughness of the specimens roughly matches the duplex parent metal, except for WS 9, where the toughness was approximately 12 % lower than that of S 32205.

The HAZ of WS 7.1 exhibited the most severe embrittlement, with an absorbed energy about 35.5 % less than that of the S 960 parent metal. However, the toughness was still well higher than the minimum requirement. In comparison, the impact toughness of WS 8 was 55.33 J, only about 6 % lower than that of S 960 but about 10 % greater than that of S 32205. For the HAZ of WS 9, the absorbed energy was approximately between that of WS 7.1 and WS 8 and about 17 % lower than that of S 960. The higher amount of hard martensite in the HAZ of WS 9 compared with WS 7.1 and WS 8 (Figure 16) could be the principal cause of the brittleness in WS 9.

The superior impact toughness of WS 8 implies that moderate heat input had a favourable effect on the microstructure. The improved toughness of the HAZ may be a consequence of more balanced martensitic-bainitic phases in the HAZ as well as less intense grain coarsening compared with WS 7.1.

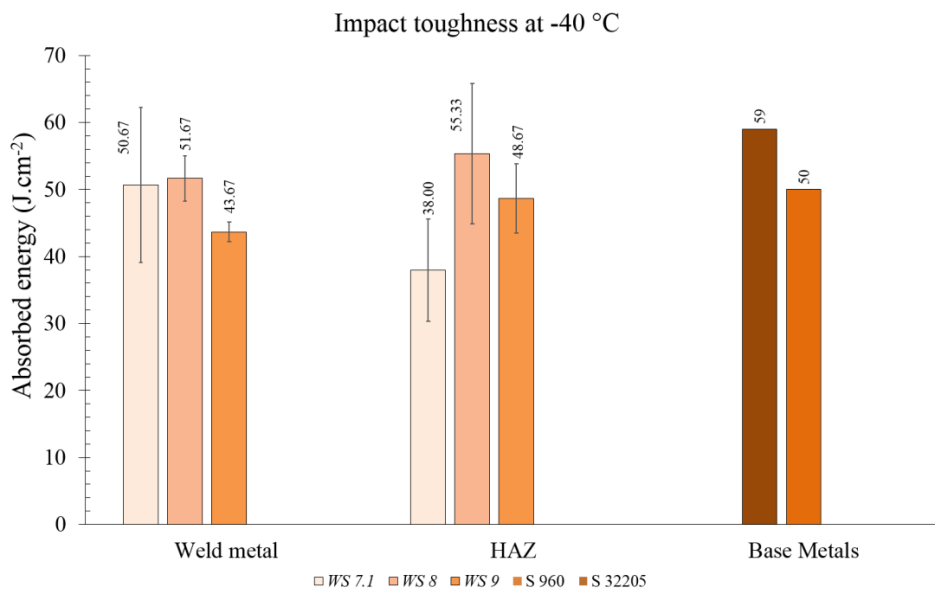


Figure 36. Average impact strength at the weld and in the HAZ of S 960. The results were obtained by applying 150 J impact energy at -40 °C and compared with the impact strength of the base metals at the same temperature. The V-notch was on the weld centre and at a distance of 1 mm from the weld metal toward the S 960 side for weld metal and HAZ, respectively. Note that impact toughness values of the base metals are taken from the supplier's certificate.

3.3.9 Fatigue behaviour

A servo hydraulic testing machine capable of 100 kN was used to perform the fatigue tests. The geometry of welded specimens used for fatigue testing is shown in Figure 37. For a satisfactory result, a transverse section of butt weld with a width of 70-75 mm is recommended (Gurney, 1979). Having a wide weld section is preferred because it represents a larger volume of the weld sample and increases the probability of sampling regions containing a flaw (unintentional weld defect) (Gurney, 1979).

All attempts were made to remove possible misalignments in the samples during both the welding and testing. According to the standard in (Hobbacher, 2013), for the class of weld used, full penetration is mandatory (unless otherwise stated) and misalignment should be kept to less than 10 percent of the plate thickness. These standard requirements were met for this study. Neither pre-treatments, such as preheating and edge-preparation, nor post-treatments, such as stress relieving and reinforcement machining, were performed, and all the tests were carried out on specimens in as-weld condition.

Tests were conducted in three different stress ranges for each power class. In order to compare the results with a standard design curve, the stress ratio for two repetitions (Test 1 and Test 2) was kept at $R=0.1$. All tests were carried out at room temperature and

frequency of 8 Hz. The results are presented in Figure 38, which presents a log-log plot of the data.

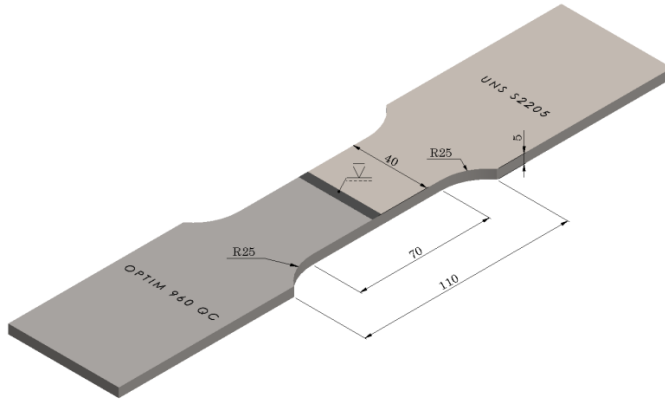


Figure 37. Schematic of the specimens prepared for the fatigue tests.

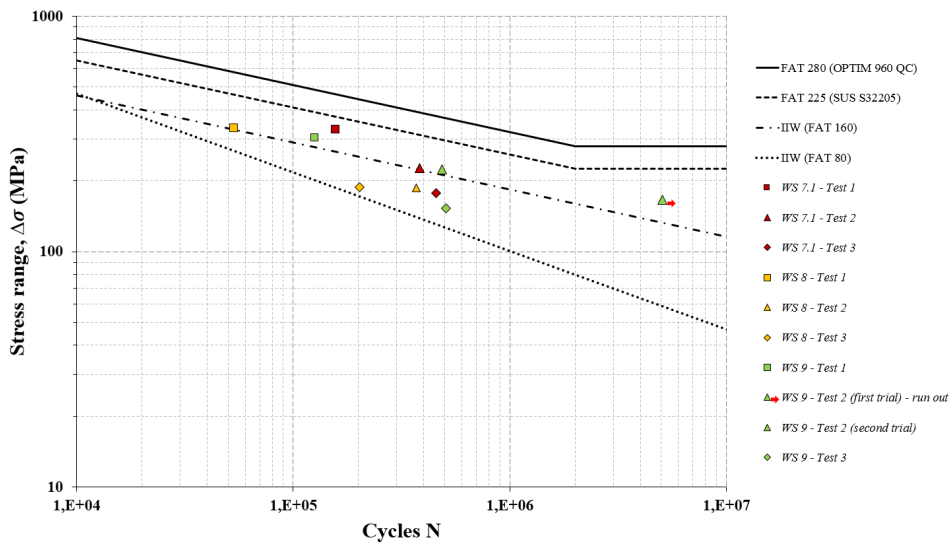


Figure 38. Comparison of fatigue test results for different power classes. Fatigue resistance S–N curves ($P_f = 2.3\%$) based on IIW recommendations (Hobbacher, 2013) and values from study of the base materials (Laitinen, Valkonen and Kömi, 2013) are included.

The standard design curve is based on the equation (1) for the FAT class 80 corresponding to the type of welded joint tested (Radaj, Sonsino and Fricke, 2006):

$$N = \frac{C}{\Delta\sigma^m} \quad (1)$$

In this equation, N and $\Delta\sigma$ denote the number of cycles and stress range, respectively. The values of the slope, m , and the design value of the fatigue capacity, C , are considered to

be 3 and 1.024×10^{12} , respectively (Hobbacher, 2013). At each power class, the test on specimen 3 was performed at $R = 0.5$ in order to simulate the high residual stresses existing in real structures. It is worth mentioning that the endurable or permissible nominal stress amplitudes could be significantly reduced by high tensile residual stresses caused by welding large structural members in contrast with small test specimens (Radaj, Sonsino and Fricke, 2006). These permissible stresses are independent of mean stress (R ratio) in standard recommended curves. Thus, when using laboratory specimens, fatigue testing to determine permissible stress amplitudes in welded joints should generally be performed with high R -values ($R = 0.5$) to appropriately reproduce the detrimental effect of high residual stresses in large structures. Another recommendation is to perform the test at low stress ratio ($R = 0$) and lower the fatigue limit at 2 million cycles by 20 % (Hobbacher, 2013). This alteration makes the slope of the curve steeper.

As can be seen from the results in Figure 38, the specimens tested at higher stress ratios to simulate conditions in real structures are closest to the recommended curve for this weld class (FAT 80). It seems that FAT class 80 works reliably for all power classes of dissimilar joints in this study, although it is rather conservative for specimens tested at low stress ratios. It is recommended (Hobbacher, 2013) that the upper band should be limited by the S-N curve of the parent material, if properly verified test data is available. If not, FAT class 160 for steels is recommended (Hobbacher, 2013), which has been added to Figure 38 to check the scatter of the results. All specimens tested at high stress ratios are positioned between the limits, with the upper limit being slightly conservative for tests conducted at low stress ratios.

To add the upper limits as the S-N curve of the parent materials, the results of study on the same materials by Laitinen et al. (Laitinen, Valkonen and Kömi, 2013) are used. Laitinen et al. recommended FAT 280 for 960 QC and FAT 225 for material with yield strength between 600-700 MPa. It can be clearly seen from Figure 38 that all the test results are covered by the curve for the weaker parent material (S 32205). Hence, using the upper bands based on the S-N curves of the parent materials cannot be considered a safe criterion, whereas the IIW recommendation of using FAT class 160 for the upper boundary would be more conservative and safe in real structures.

No clear relation between the fatigue strength and heat input variations can be derived from the results. The reason is that the specimens were tested in as-welded condition without reinforcement removal, and as a result, geometrical effects could have a controlling influence on the fatigue results. It can be conjectured that the effect of heat input in dissimilar welds of such combinations may not be a prime determinant factor in the fatigue life when the joints are expected to be used in as-welded condition and with no subsequent heat treatment. Whereas, geometrical effects should be taken as the major cause of failure in the specimens.

It is noteworthy that all specimens made of WS 7.1 and WS 8 failed at the weld toe of the S 960 side. In comparison, only one WS 9 specimen failed on the S 960 side of the weld interface; the rest failed at the duplex side of the weld toe. It can be deduced that the weld

reinforcements acted as stress raisers that concentrated the stress at the weld toe. The geometrical effects and possible weld flaws make the crack initiation life negligible. As a crack initiates, the fatigue life of the welded samples is governed by the crack propagation rate, which is reliant on the fracture resistance and ductile properties of the structure around the crack tips. The results imply that variation in the microstructure at the weld interfaces as a result of different heat input could have influenced the fracture location. It appears that the fracture resistance of the coarse austenitic-ferritic structure of the DSS side of the interface was superior to that of the predominantly coarse martensitic-bainitic structure at the UHSS side in the majority of the samples. Shang et al. (Shang et al., 2015) have demonstrated that the fatigue crack path and propagation rate in a weld between austenitic stainless steel and ferritic steel is crucially influenced by the microstructural characteristics, including columnar grain growth of austenite in the fusion zone, a martensitic layer at the interface, and coarse martensite in the HAZ (Shang et al., 2015). Their work emphasized the significance of columnar grain growth in the crack propagation transgranularly parallel to the dendrite structure.

The microstructural observations showed that with the lowest heat input the integrity of the *WS 9* weld on the duplex side was noticeably affected by macrosegregation in the form of a PMZ and UMZ on the DSS side. The impaired integrity could have a detrimental effect on the fracture strength and intrinsic ductile properties of the weld interface with the DSS base metal. Nevertheless, the appearance of macrosegregation might not be consistent throughout the weld, which could account for the inconsistent failure pattern in *WS 9*.

3.3.10 Factors affecting corrosion resistance

Duplex stainless steels (DSS) exhibit outstanding corrosion resistance in chloride-ion containing environments. Their good corrosion-resistance properties arise from the duplex microstructure, which consists of approximately equivalent amounts of austenite and δ -ferrite without other undesirable precipitates. However, weldments of DSS can show a severely impaired corrosion resistance, especially local pitting corrosion resistance. The inferior corrosion properties can be the result of an unbalanced duplex phase proportion with excess ferrite phase and the precipitation of detrimental secondary phases such as Cr_2N , secondary austenite (γ_2), sigma (σ), and chi (χ). With dissimilar welds of DSS and UHSS, most degradation related problems of welded DSS can be expected to occur on the duplex HAZ, and not within the weld metal zone (WMZ), since the properties of the weld metal zone are modified by high-alloyed filler metal. Controlled heat input should be employed in welding of DSSs. Very high heat inputs intensify the precipitation of deleterious brittle intermetallic phases. On the other hand, very fast cooling rates can result in less austenite reformation, and also can lead to Cr_2N precipitation (Al-Haidary, Wahab and Salam, 2006) (Cortie, Fletcher and Louw, 1995) (Ramkumar et al., 2015).

4 A novel method for enhanced decision making

Traditional design processes and commercial CAD/CAE software usually employ the thermo-mechanical characteristics of the base materials and joint geometries and thicknesses to assess the suitability of base metals for demanded load carrying capacity, life expectancy and the service environment. However, these criteria cannot guarantee the performance of the weldment if the characteristics of the weld, including metallurgical aspects, are not carefully considered. Complex interactions of base metals, base and filler metals, and the welding process and its parameters determine the final mechanical and metallurgical features of the welded joint. With traditional design methodology, the weld characteristics (e.g., corrosion resistance, ductility, strength, toughness and hardness) are generally taken into consideration at the manufacturing stage, when detailed design is done. Such late consideration of these fundamental factors brings a high risk of failure, a need for costly rework and delays at the manufacturing phase. The failure risk stems from possible weldability incompatibilities between the base metals, welding process, and thicknesses and joint geometries. The prerequisites for assessment of weld properties at the design stage are in-depth knowledge of mechanical, metallurgical and weldability characteristics of the materials. Obviously, it is not always possible to find designers with such knowledge. The knowledge gap existing between the design and manufacturing stages is a serious challenge that can lead to problematic design and, consequently, possible catastrophic failure, especially in critical applications and demanding service environments.

The concepts of concurrent engineering (CE) and design for manufacturing and assembly (DFMA) methodology can provide an effective solution to bridge the gap between the design and manufacturing phases. The DFMA rules can be used to enable construction of a database driven selection method with a built-in expertise feature to provide designers with optimal solutions to address the challenges associated with the design of welded structures.

Effective data distribution within the multidisciplinary teams involved in product development is a precondition for successful implementation of DFMA. In this study, a solution is proposed for streamlined data distribution by integrating the capabilities of PDM with the DFMA rules. The PDM can enable efficient linkage and technical communication of the different design and manufacturing units involved. PDM systems also provide organized access and control of product data as well as life cycle management throughout the development and manufacture of the welded structure (Gascoigne, 1995). Many researchers have proposed different methods for incorporating DFMA into welding operations (LeBacq et al., 2005) (Lovatt and Shercliff, 1998) (Maropoulos et al., 2000) (Kwon, Wu and Saldivar, 2004) (Niebles et al., 2006) (Boothroyd, Dewhurst and Knight, 2000) (Knight, 2005) (Zha, Lim and Fok, 1998). Nevertheless, an examination of integrated PDM and DFMA for weldment design has yet to be presented.

In this study, the concept of CE is utilized to facilitate and improve the design process of welded structures, especially complex structures that require great caution in design and manufacturing, where different design teams are involved and heterogeneous combinations of dissimilar materials are used.

For the purposes of this study, the traditional DFMA model was adapted to the requirements of structural welding applications. In this revised model, welding is considered as a separate design module. The model aims to expedite the decision-making process by using an application-based selection approach that delivers solutions to the designers by providing a permitted list of materials and welding procedures specifications (WPS) together with brief data and analysis that aids the designer find an optimal solution. The model can be put into practice by integration with a PDM database. A demo application was developed as a proof of concept and tested using the task of selecting appropriate dissimilar base metals and filler metal for an application operating in a demanding service condition, i.e., in an offshore environment.

4.1 Novel DFMA-based design procedure

To develop a DFMA-based model for welded structures, the DFMA aspects of weldment design and welding stages must first be carefully defined. Figure 39 shows important factors in the DFMA of welded structures. The factors shown in Figure 39 are grouped under four main DFMA categories, namely, complexity, compatibility, quality and cost, all of which are interconnected and can affect one another. For example, a decrease in the complexity of a design by improving the geometry and tolerances as well as paring down the weight and number of components can reduce the manufacturing cost of the product. In the same way, quality can be conditioned by the metallurgical compatibility of the base and filler metals, the compatibility of the welding process with the material thicknesses and needed weld deposition, as well as the compatibility of the welding procedure with the material and joint position and configuration. It is understandable that improved compatibility and quality can also reduce costs by minimizing defects and waste.

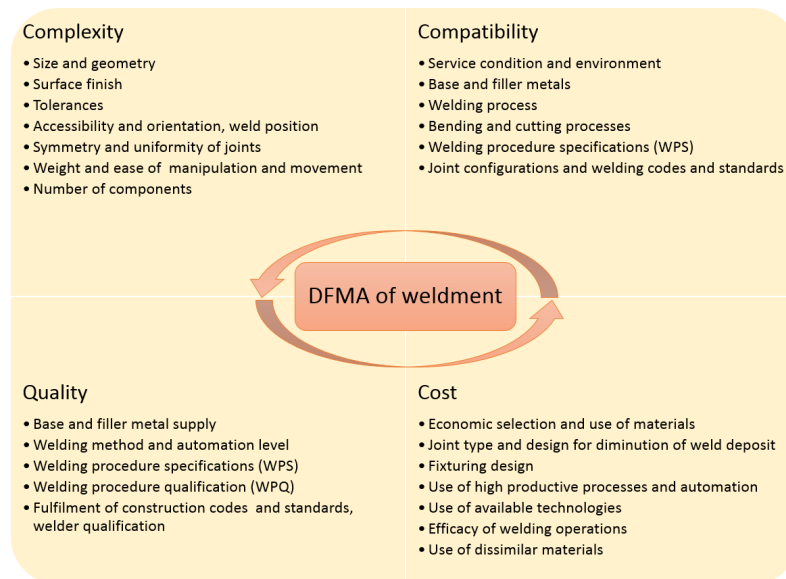


Figure 39. Influential factors in DFMA of weldments (Tasalloti et al., 2016).

The study in (Tasalloti and Kah, 2016) introduces an application-based selection method that is a variation of the questionnaire-based approach in (Ashby et al., 2004) combined with an inductive reasoning strategy (Ashby et al., 2004) (Kolodner, 1993) (Kolodner, 1992) (Ashby and Johnson, 2001). Different selection strategies for materials and manufacturing processes are suggested in the literature (Dieter, 2012) (Charles, Crane and Furness, 1997) (Farg, 1989) (Ashby, 1999). However, the approach proposed in this work can significantly shorten the decision-making procedure and can also eliminate the risk of improper selection due to its built-in expertise. For material selection, for example, the designer first selects the application (e.g. offshore construction) in the DFMA-based system. Subsequently, based on the service requirements of the application, suitable materials are retrieved from the database prior to being made available for selection. As shown in Figure 40, the selection can be performed either manually with the help of the DFMA guidelines or through automatic ranking by weighting of the intended application and the fabrication properties demanded of the materials, such as strength, toughness, corrosion resistance, weldability, formability, machinability and cost.

In a similar manner, the welding process is selected from the database based on the application (i.e. the materials to be welded, thicknesses, homogenous or non-homogenous welding) and then ranked according to requirements such as availability, applicability, cost and productivity.

Filler metals are categorized and indexed according to the application, i.e., materials to be welded, dissimilar or similar metals welding, and the welding process. The filler metal can then be selected according to the suitability of the predicted microstructure and the conformity of the filler with the welding process, shown in Figure 41.

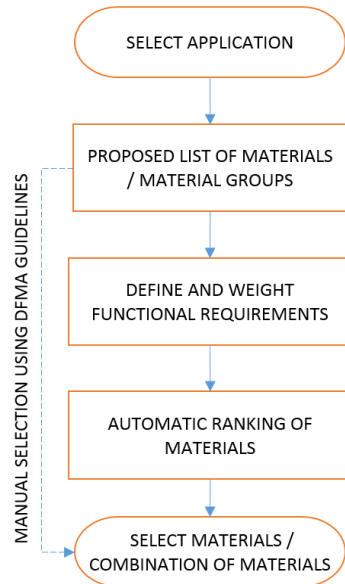


Figure 40. Procedure for selecting materials using an application-based selection interface (Tasalloti and Kah, 2016).

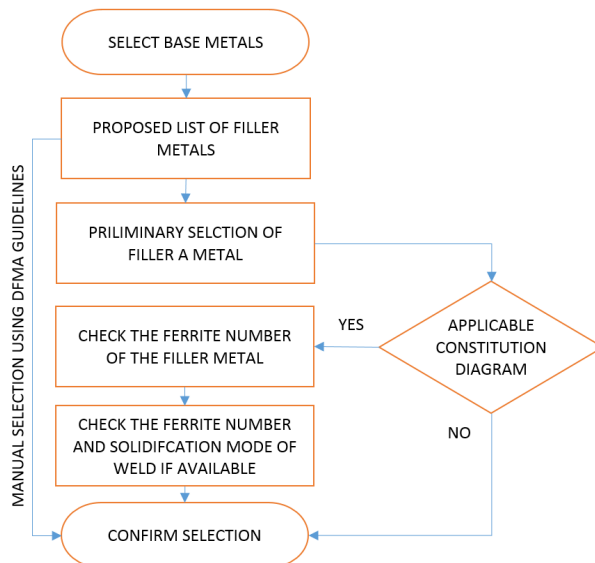


Figure 41. Procedure for selecting the filler metal using an application-based selection interface (Tasalloti and Kah, 2016).

In the model, additional DFMA rules and guidelines are included for weldment design and structural welding standards, welding procedures specifications (WPS), welding procedure qualification tests (WPQT) and welder qualification tests (WQT). The WPS should be compatible with the selected parent materials and processes. The WPS should

also include comprehensive instructions of actions required to produce the weld, such as joint type and preparation, weld type, welding parameters and technique, consumables, interpass temperature and heat treatments. WPS is qualified using WPQT provided by the DFMA guidelines. Depending on the requirements of the relevant standards and the functional requirements of the structure, the WPQT may include various destructive tests such as tensile, toughness, hardness, bending and corrosion tests, as well as different non-destructive tests. The acceptability of the WPS or the need for modification of the WPS is determined based on the WPQT results.

4.2 Integration of the application-based approach with PDM systems

As mentioned earlier, the success of DFMA-based approaches relies on appropriate and effective distribution of data among the designers and product development teams. Generally, despite recognition of its importance, the DFMA-based approaches in (LeBacq et al., 2005) (Lovatt and Shercliff, 1998) (Maropoulos et al., 2000) (Kwon, Wu and Saldivar, 2004) (Boothroyd, Dewhurst and Knight, 2000) lack a practical solution for comprehensive data distribution between the design and manufacturing teams, from the conceptual phase to the detailed design and manufacturing stage, for simultaneous development and optimization of a product according CE methodology. In addition, the applicability of the DFMA-based strategies for real world welding operations and the possibility of incorporating the approaches in companies' production lines usually remains unaddressed.

The study in (Tasalloti et al., 2016) suggests the use of the presented application-based approach in conjunction with a PDM system for data storage and data distribution. PDM tools are used to capture and keep track of changes during the lifecycle of a product and to support the product development process according to the specific way a company operates (Gascoigne, 1995) (Eskelinen, 2013a). PDM systems have a repository for data storage of CAD/CAM files and revisions, documentation and standards, specifications, manufacturing information and requirements, calculations, illustrations and supplier information. PDM programs are increasingly being used to promote systematic, modular and cost-effective design and manufacture of products (Eskelinen, 2013a). While PDM software can effectively help designers to reuse design modules and specifications, it generally cannot provide solutions for improving the functionality and fabrication friendliness of designs, nor for determining the optimum manufacturing technology. Integration of DFMA and PDM can overcome the shortcomings of the PDM system as regards providing solutions and at the same time mitigate the deficiencies of DFMA-based models as regards data distribution.

In the integrated model, the DFMA aspects are taken into consideration in relation to the technical data in the PDM system. The PDM can assist successful implementation of the application-based selection approach according to the CE design purpose. The PDM brings the data associated with cross-functional design teams together so that all teams have proper access to the latest data and changes made during the design process.

Figure 42 illustrates the new DFMA procedure developed for structural welding applications interfaced with a PDM system. The integrated DFMA-PDM model was developed to improve and enhance the application-based approach discussed in the previous section. Unlike approaches such as those in (Boothroyd, Dewhurst and Knight, 2000) (LeBacq et al., 2005) (Lovatt and Shercliff, 1998) (Maropoulos et al., 2000) (Kwon, Wu and Saldivar, 2004), the proposed integrated model takes the weldment into consideration as a separate design module to address the requirements of welded products more specifically. This makes the model readily applicable to various welded products, as long as a pertinent database and DFMA guidelines are provided.

As can be seen from Figure 42, DFMA rules and guidelines are conjointly used with the PDM database to enable designers decide on optimal configurations, materials, filler metals and welding processes. The database is a supportive knowledge base with benchmarks for decision making in both the conceptual and detailed design phases. All the design documents, changes and modification proposals are captured, stored and distributed via the PDM system.

The PDM side of the integrated model can furnish additional advantages, including:

- Up-to-date data of all modifications and revisions for all teams involved in the design.
- Records of all revisions and a history of why and by whom a revision has been made.
- Controlled access to the database by defining roles and privileges so that certified roles according to their need can acquire access to the categorized database of CAD designs and drawings, materials, filler metals, cutting and bending processes, welding processes, documentations and standards, costs and prices, suppliers, manufacturers and subcontractors.
- Unified interface for DFMA and PDM tasks.

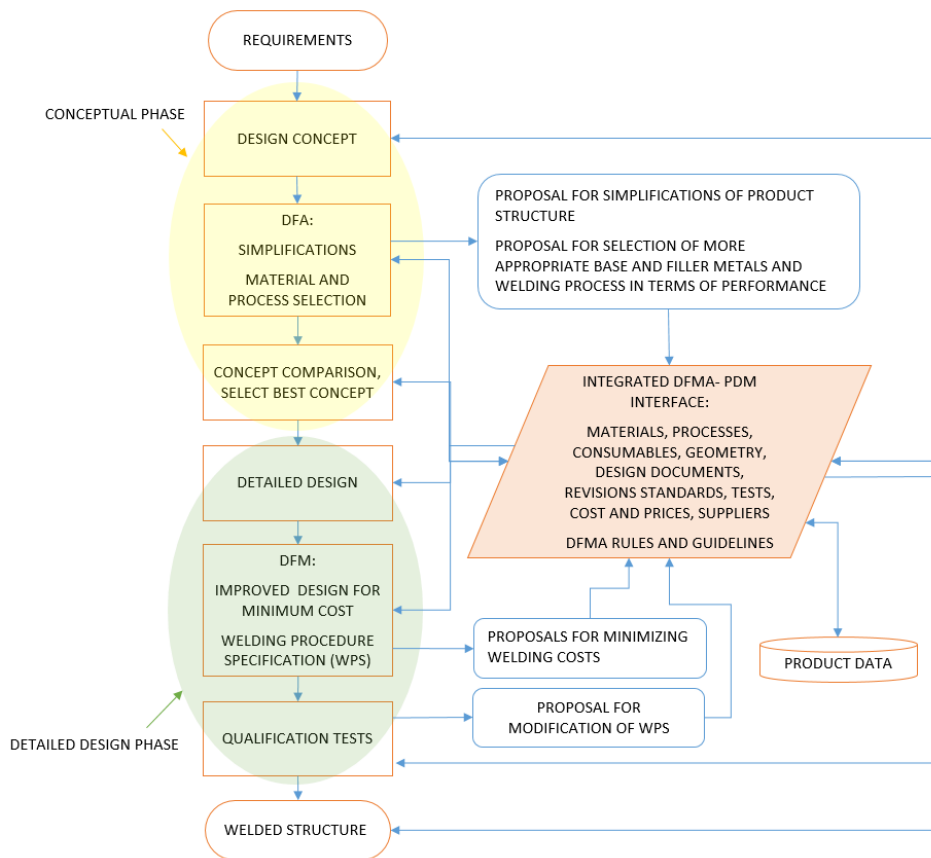


Figure 42. Integrated DFMA-PDM procedure for welded structures (Tasalloti et al., 2016).

Figure 43 and 44 illustrate the application-based selection flow chart in the integrated DFMA and PDM procedure. As can be seen from these two figures, the procedure is essentially the same as the flowsheets shown in Figure 40 and 41. The major difference is that in Figure 43 and 44 the application-based selection model is interfaced with the PDM database. In the integrated model, following selection of an application by the designer, suitable materials are loaded from the PDM database, prior to being made available for selection. As shown in Figure 43, similar to Figure 40, the selection can be done either manually with the help of the DFMA guidelines or through automatic ranking by weighting of the required material properties.

In a similar way, filler metals are categorized and indexed according to the application (i.e. materials to be welded, dissimilar or similar metals welding, and the welding process) and selected based on the suitability of the predicted microstructure and the ease of the process, shown in Figure 44.

In the integrated model, the PDM side controls the data storage, data selection and data modification, while the DFMA side oversees the database and filtering of the available

options toward an optimal solution. Figure 45 gives a more detailed view of the proposed DFMA procedure, illustrating actions commonly needed at each stage.

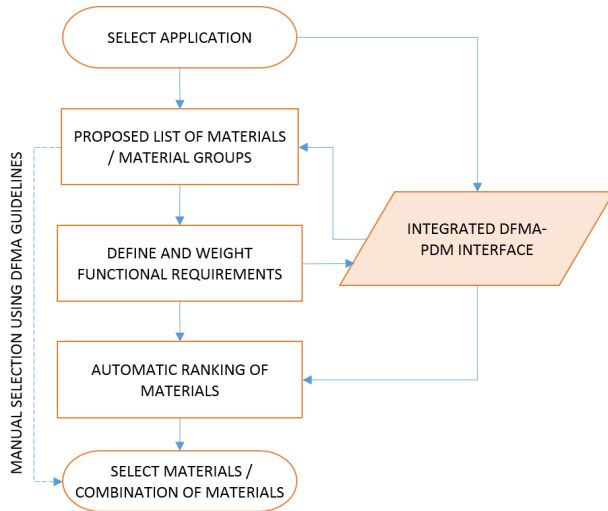


Figure 43. Application-based selection of materials using the integrated DFMA-PDM interface (Tasalloti et al., 2016).

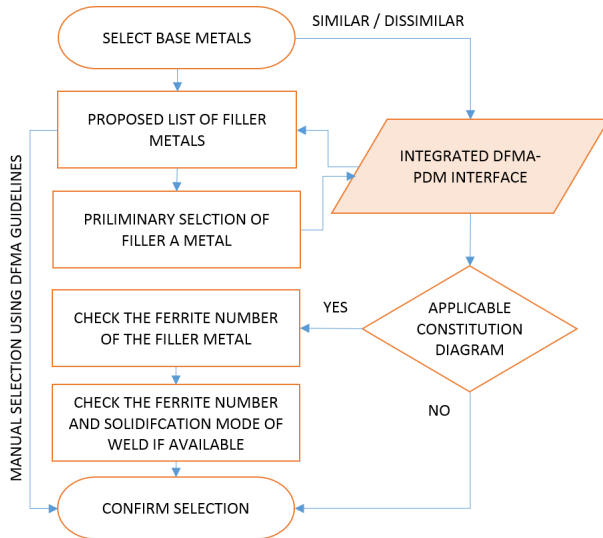


Figure 44. Procedure for selecting the filler metal in the integrated DFMA-PDM interface (Tasalloti et al., 2016).

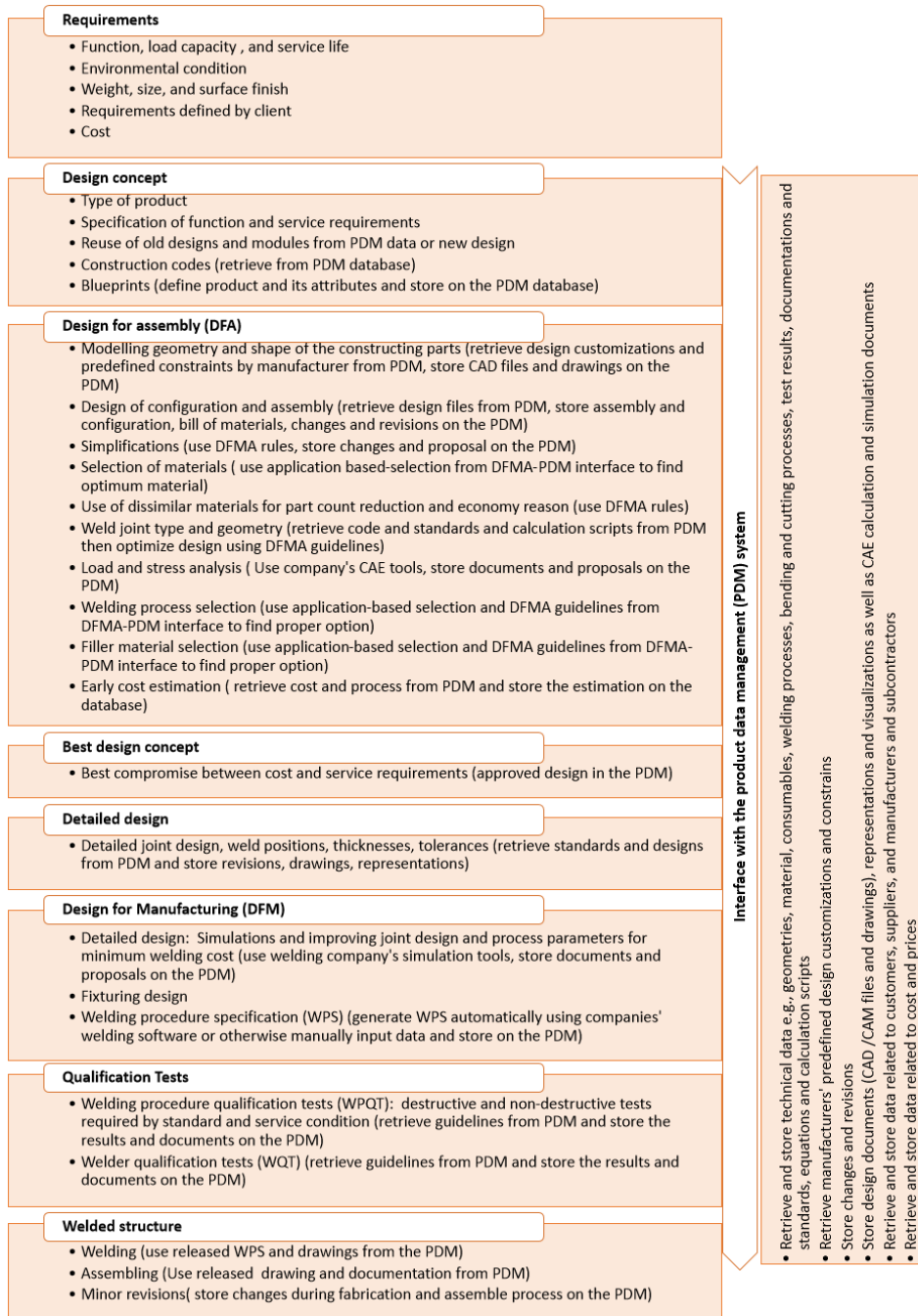


Figure 45. DFMA procedure of welded structures integrated with the PDM system showing typical actions required in each stage (Tasalloti et al., 2016).

The approach restricts selection to an approved list of materials, welding processes, welding parameters and filler metals for a specified service environment and function. Nevertheless, the inductive reasoning feature of this approach helps to incorporate the intellect of designers in decision making. This feature adds more flexibility to the model and enables the designer to test and analyse different options and make selections based on personal knowledge and previous experience or the technical data provided. Although the approach cannot easily be used for innovation, the model provides optimal solutions within the confines of current knowledge and reduces the risk of erroneous design decisions, which is a significant advantage in critical applications. The built-in expertise most benefits designers without specialized knowledge of welding and metallurgy. The benefits include a reduced risk of improper selection and consequent design failure as well as an easier decision-making and shortened design time.

4.3 Simplified example for application-based selection

Figures 46-53 present the interface of a simplified software application developed for this study as a proof of concept based on the flowsheets presented in Figures 40 and 41. It should be noted that this demo tool only embodies one way (limited by the programming skill of the author) of utilizing the approach illustrated in the flowsheet in Figure 42 and the application-based selection flowcharts in Figure 40 and 41. Obviously, professional programmers can develop much more elaborate tools with better practicality and user experience for real world applications. It should also be noted that in the presented demo tool no changes in relation to the PDM and CAD databases are made. In the illustrative tool developed, an isolated database with a limited number of materials, specifications, and DFMA guidelines is used to demonstrate the feasibility of the approach. As mentioned earlier, selection of the welding process and welding parameters is excluded from this presentation due to the many processes and multifactorial elements involved, which raise the complexity of the software application beyond the scope and resources of the current dissertation.

Figure 46 displays initiation of the material selection by specification of the application. Figure 47 shows a selection of materials recommended for offshore applications. In the presented example, five materials are considered; namely, A633 high strength low alloy (HSLA) steel, S 960 QC direct-quenched ultra-high strength steel (UHSS), 316 L austenitic stainless steel (ASS), 1.4529 super-austenitic stainless steel (SASS) and AISI 2205 duplex stainless steel (DSS). Clearly, the listed steels are only a selection of possible steels available on the market.

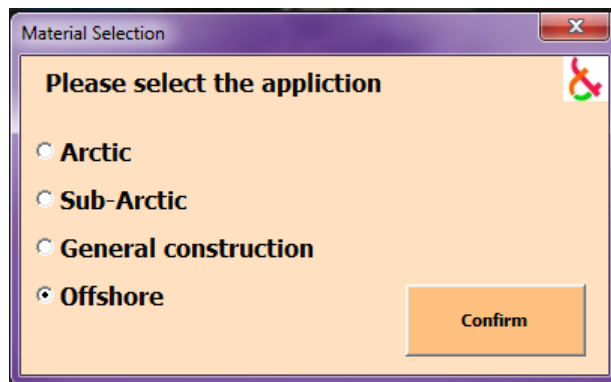


Figure 46. Selection of the application in the application-based interface (Tasalloti and Kah, 2016).

A 633 is a normalized HSLA steel with improved notch toughness, which makes it suitable for welded structures operating in temperatures as low as -45°C (Davis, 2001). S 960 QC is a low-carbon, low-alloyed direct-quenched steel that is characterized by a favourable combination of very high strength, good toughness at ambient temperatures even below -40°C , as well as satisfactory formability and weldability (Farrokhi, Siltaanen and Salminen, 2015) (Hemmilä et al., 2010) (Pallaspuro et al., 2014). Alloy 316 L is a low-carbon ASS with excellent resistance to atmospheric corrosion. 316 L possesses excellent strength and toughness at cryogenic temperatures and is resistant to intergranular corrosion in marine environments (Davis, 1995). Alloy 1.4529 offers excellent toughness at cryogenic temperature together with good formability and weldability. This SASS is remarkably stronger than other 300 ASS series and shows superior resistance to numerous corrosive environments (Outokumpu, 2013). AISI 2205 is a duplex stainless steel that shows excellent resistance to general corrosion as well as stress corrosion cracking. Additionally, AISI 2205 presents good toughness down to 45°C , greater mechanical strength than austenitic grades, and a satisfactory weldability (Outokumpu, 2013). The chemical composition of the five aforementioned alloys is shown in Table 8.

Table 8. Chemical composition of five steels recommended for offshore applications.

Mat.	C	Mn	Cr	Ni	Mo	Nb	Cu	N	P+S	Si	Ti
A 633	0.2	1.5	-	-	-	0.05	-	-	0.09	0.5	-
S 960 QC	0.09	1.05	0.82	0.04	0.158	0.003	0.029	-	0.002	0.21	0.07
316 L	0.02	-	16.9	10.7	2.6	-	-	0.1	0.075	0.75	-
1.4529	0.01	-	20.5	24.8	6.5	-	1	0.2	0.04	0.5	-
AISI 2205	0.015	1.34	22.6	5.79	3.24	0.009	0.25	0.179	0.02	0.39	-

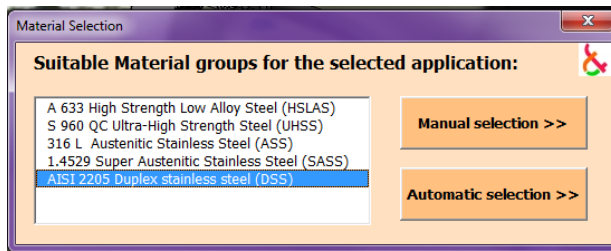


Figure 47. Material selection. Recommended materials can be loaded from the application database (Tasalloti and Kah, 2016).

As shown in Figure 47, material selection can be done either manually or automatically from the list comprising recommended metals. For manual selection, the designer needs to decide which material(s) would best serve the design requirements using the technical information presented in the form of a guideline next to each material, shown in Figure 48. The guideline contains mechanical properties, weldability, formability and machinability information, as well as carbon equivalent (C_{eq}) when applicable. The C_{eq} is calculated using Equation (2) (Dearden, 1940):

$$C_{eq} = C + \frac{Mn}{6} + \frac{(Cr+Mo+V)}{5} + \frac{(Ni+Cu)}{15} \quad (2)$$

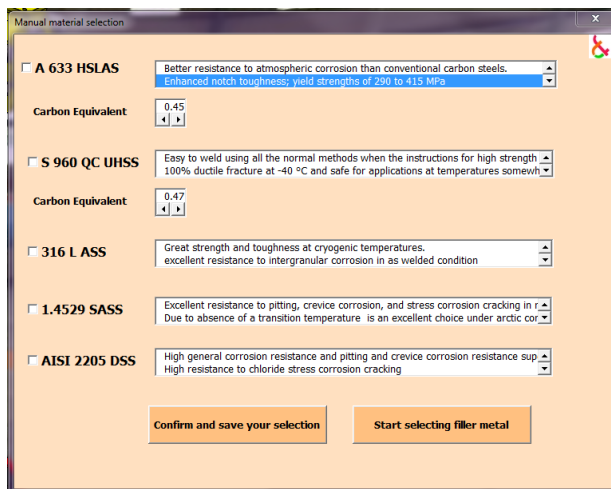


Figure 48. Manual material selection interface. The guideline next to each material aids the designer in selection of suitable material (Tasalloti and Kah, 2016).

For automatic selection, the designer needs to decide how important a specific property of the material is for the design purpose. As shown in Figure 49, a range of attributes are presented to be rated by the designer. These attributes include quantitative and qualitative properties and provide a baseline for comparison and ranking. Table 9 presents an example of properties that can be compared quantitatively.

Table 9. Comparison of the proposed materials based on properties having quantitative value.

Quantitative properties	A 633	S 960	316 L	1.4529	AISI 2205
Ultimate tensile strength (MPa)	≈ 630	1114	570	670	825
Charpy impact values at -40 °C (J)	34	60	180	200	50
Estimated price / ton (\$)	800	1200	3000	5000	2000

The greatest material property within a range (e.g. strength) is valued with a 5 on a scale of 0-5, where 0 equals “unsuitable” and 5 equals “best value”, and the other properties are proportionally calculated compared to the best value. An example of the comparison of quantitative attributes is presented in Table 10.

Table 10. Comparative values calculated with respect to the best corresponding material property valued with a 5 on a scale where 0 equals “unsuitable” and 5 equals “best value”.

Material	Comparative values		
	Ultimate tensile strength	Charpy impact	Price per ton
A 633	2.8	0.9	5
S 960 QC	5	1.5	3.3
316 L	2.5	4.5	1.3
1.4529	3	5	0.8
AISI 2205	3.7	1.2	2

Material properties that cannot be readily characterized with a definite quantity, due to a lack of valid experimental data or the nature of the property being evaluated, are qualitatively compared. As can be seen from Table 11, weldability, formability, and machinability are qualitatively evaluated from 0 to 5, where 0 indicates an attribute is unsuitable and 5 evaluates a property as excellent. The values are assigned based on data extracted from material handbooks and supplier catalogues (Outokumpu, 2013) (Davis, 1995) (Davis, 2001) (ASM International Handbook Committee, 1990).

Rating Design Requirements

Rate the design requirements (0-5)

4 Good Weldability

2 Machinability

1 Formability

1 High Toughness

5 High Strength

5 Good Corrosion resistance

4 Low-cost

Confirm

Figure 49. Rating menu for assigning the weighting of different material attributes in a design (Tasalloti and Kah, 2016).

Table 11. Qualitative properties are evaluated from 0-5, where each number in succession stands for “unsuitable”, “fair”, “good”, “suitable” and “excellent”, respectively. Due to a lack of experimental data, the properties indicated with “*” are compared qualitatively.

Qualitative properties	A 633	S 960 QC	316 L	1.4529	AISI 2205
Weldability	3	3	4	3	3
*Formability	4	3	4	3	3
*Machinability	4	2	3	1	1
*Corrosion resistance	1	2	4	5	5

Weldability, for example, is evaluated based on chemical composition, microstructure, hardness, thermal expansion, joint preparation, required pre-work and post-heat treatment, and heat input sensitivity.

In the rating menu, shown in Figure 49, a weight should be defined for each property on the basis of the service demands. The weights can be allocated from 0-5, where the numbers in the sequence stand for “not relevant”, “not important”, “important”, “very important” and “crucial” respectively. The ranking is performed simply by comparing the overall score of each material, which is reckoned from summation of the defined weights multiplied with the relevant comparative values.

Figure 50 displays the ranking done by the application followed by the weighting shown in Figure 49. For dissimilar welding, the first and second ranked materials can freely be chosen to fulfil the intended service requirements.

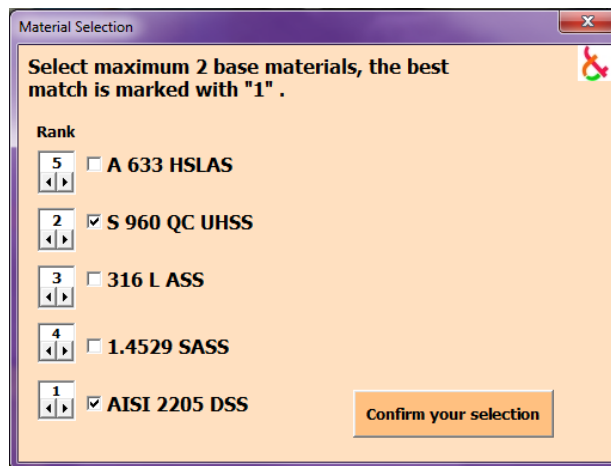


Figure 50. Proposed materials ranked by their suitability for the design purpose (Tasalloti and Kah, 2016).

The filler material is another critical aspect of the weld that determines many of the key properties of the welded joint, including strength, toughness, corrosion resistance and surface properties. Figures 51-53 show the interface of the developed application for selecting filler metal with a presumption of GMAW as the welding process. As shown in Figure 51, applicable filler metals for the selected base metals and similar or dissimilar welding are loaded from the database. For GMAW and the selected dissimilar parent metals in Figure 50, applicable filler metals include 904 L, 316 L-Si, 307 L, P 12, and 16.55, which in this particular case are extracted from the Avesta and Esab welding manual (Larén, 2004) (ESAB, 2005), although other manuals can also be used.

A guideline next to each filler metal encompassing technical information can assist the designer in the selection process, as seen in Figure 51. A crucial factor in dissimilar welding of stainless steels is the ferrite number. A fully austenitic structure would be desirable for improved mechanical properties and corrosion resistance. However, this increases the risk of solidification cracking and necessitates low heat input and accurate interpass temperature control. A small percentage of ferrite up to 4% would minimize this risk without having highly adverse effects on the toughness and corrosion resistance of the weld (Tasalloti, Kah and Martikainen, 2014). The ferrite number of the filler metal and the predicted ferrite number of the weld metal are also presented as an additional benchmark for decision-making, as shown in Figure 51.

Figure 51. Filler metals and their specifications recommended for a dissimilar weld between AISI 2205 and S 960 QC. The interface has an option to check the WRC-1992 diagram for the weld and filler metal (Tasalloti and Kah, 2016).

The ferrite numbers are acquired from the Welding Research Council (WRC) -1992 (Kotecki and Siewert, 1992) constitution diagram using Cr and Ni equivalents presented in equation (3) and (4) and with an assumption of equal dilution of 15% from either of the parent metals in the weld.

$$Cr_{eq} = Cr + Mo + 0.7 Nb \quad (3)$$

$$Ni_{eq} = Ni + 35 C + 20 N + 0.25 Cu \quad (4)$$

As shown in Figure 52 and Figure 53, the ferrite numbers and solidification mode can also be verified on the WRC-1992 diagram using the option available on the interface, illustrated in Figure 51. For example, in Figure 53, a fully-austenitic solidification mode is probable using 16.55 austenitic filler metal and the selected base metals shown in Figure 50.

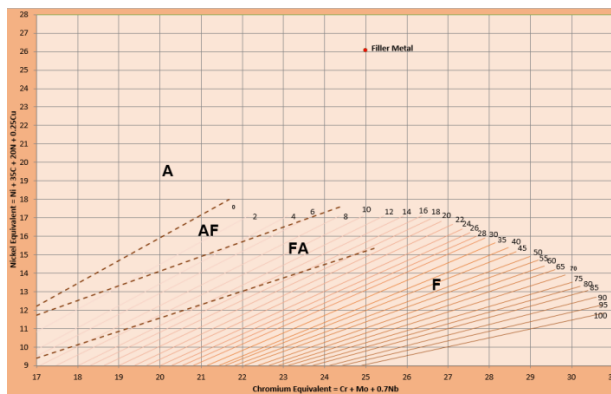


Figure 52. 16.55 filler metal positioned on the WRC-1992 diagram (Tasalloti and Kah, 2016).

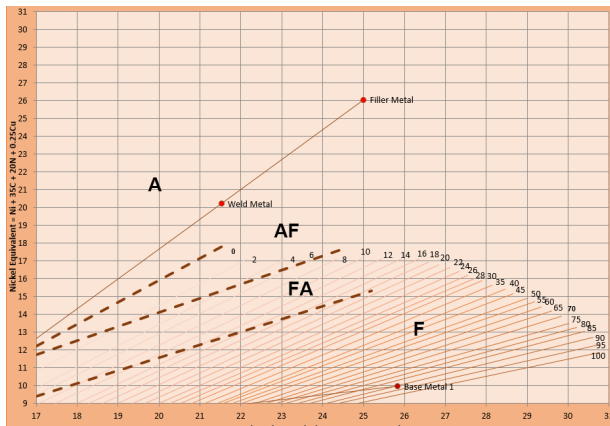


Figure 53. Prediction of ferrite number and solidification mode for a weld between S 960 QC and AISI 2205 made using 16.55 filler metal with 70% dilution (Tasalloti and Kah, 2016).

5 Overview of the publications

The following section provides a summary of the research publications presented as a part of this doctoral dissertation and related to the experiments performed, literature review, and the proposed DFMA-based approach and its integration with a PDM database.

Publication I. Effects of welding wire and torch weaving on GMAW of S355MC and AISI 304L dissimilar welds.

In this publication, dissimilar welds of austenitic stainless steel (AISI 304 L) and low-alloy structural steel (S 355 MC), a widely used weld in the power generation industry, were studied. The base metal plates (5 mm thick) were welded in T-joint configuration. The dissimilar fillet welds were made with three different filler metals in either stringer or weaving mode (weaving frequency was 3 Hz). The objective was to study the macro- and microstructure and the hardness of the weld metal with reference to the type of filler metal used and the weaving or stringer bead applied. Formation of brittle martensite and hot cracking susceptibility in the single-phase austenite microstructure are the main concerns related to the metallurgy of this kind of weld.

The microstructural and hardness properties of the dissimilar welds were characterized in relation to the filler metal used and the welding technique applied. The results show a decrease and increase in penetration on the ferritic and austenitic sides, respectively, when a weaving technique applied. In some samples, undercut was also observed, without a clear correlation to the welding technique. Some porosity was detected in the weld root of some samples made with the weaving technique. The porosity may be a result of decreased shielding efficiency when weaving is applied. The cross-sectional measurements of the weld samples showed lower dilution by the base metals when weaving was used.

The measured ferrite numbers were very close to the predictions derived from the Schaeffler diagram (Schaeffler, 1948). The solidification mode for all specimens, with one exception, also followed the predictions made from the Suutala and Moisio approach (Suutala and Moisio, 1983; Brooks and Lippold, 1993). The presence of a martensitic layer on the ferritic side of the weld was detected in all samples. The existence of the hard martensite was further confirmed from the hardness measurements, which showed a sharp increase in hardness values close to the fusion boundary on the ferritic side. The hardness profiles did not provide any clear correlation between the hardness values and the dilution rate.

Publication II. Laser overlap welding of Zn-coated steel on aluminium alloy for patchwork blank applications in the automotive industry

In this publication, the importance of this dissimilar weld in the automotive industry was explained. The study discussed the application of laser welding of Zn-coated steel on

aluminium for tailor welded blank (TWB) and welded patchwork blank techniques in the automotive industry. The objective was to provide a critical review of issues related to dissimilar laser welding of Zn-coated steel on aluminium and obtain information regarding incompatibility concerns between aluminium and Zn-coated steel at the microstructural level. In addition, the study provides an overview of methods available in the literature for ameliorating mechanical and metallurgical concerns. Vaporization of Zn in overlap laser welding of Zn-coated steel on aluminium is the main technical difficulty causing process instability and defects in the weld. Another difficulty is formation of brittle intermetallic compounds (IMCs) that degrade the strength and mechanical properties of the weld. Degradation of the corrosion resistance performance, which is a result of losing the protective Zn layer, can also be considered a challenge in this type of dissimilar weld.

One approach for preventing the problematic effects of Zn vaporization is pre-drilling of vent holes on the Zn-coated steel along the welding line, prior to welding. The vent holes facilitate the escape of Zn vapour and thus reduce spatter and porosity. A more practical solution would be partial vaporization of Zn using a defocused laser beam prior to welding.

The study demonstrates that higher heat inputs favour the growth of IMCs. It is also shown that the dissimilar welds possess better mechanical properties when the thickness of the formed IMCs is less than 10 μm . This study shows that in addition to the thickness of the IMCs, other factors such as the composition and orientation of the IMCs are influential in defining the strength of the weld. A practical solution for reducing the growth of IMCs may be use of double pass welding with regulated and optimized parameters for preheating and welding.

The study shows that the formation of IMCs can be restricted by using N_2 as a shielding gas in place of Ar. This result may be due to the higher thermal conductivity of N_2 compared to Ar, as well as a probable reaction between N_2 plasma and Al vapour to form aluminium nitride instead of Al-rich IMCs.

For improvement of corrosion resistance of the weld, the study recommends the use of high density inert shielding gases for more efficient protection of the weld pool against oxidation.

Publication III. Laser overlap welding of zinc-coated steel on aluminium alloy

In this publication, dissimilar laser welding of Zn-coated steel on aluminium was reviewed. The main objective of the study was to provide a summary of the processing challenges in this type of weld, for example, spatter, cavities and cracking, as well as to give an overview of solutions available in the literature. This kind of weld can be used for local reinforcement of aluminium with patches of Zn-coated steel. However, the quality of the welds suffers from the aforementioned defects and formation of IMCs.

The study showed that a higher heat input can increase IMC formation. Generally, degradation of the mechanical properties can be expected when the thickness of the IMC layer exceeds 10 μm . The study notes that in addition to the thickness of the IMC layer, other factors such as the composition and orientation of IMCs as well as bonding and diffusion between the elements may be decisive in determining the weld strength.

The results show that the higher heat conductivity of N_2 compared to Ar can limit the growth of IMCs. The reaction between N_2 plasma and Al vapour, which can lead to the formation of aluminium nitride in place of Al-rich IMCs, is another favourable effect of utilizing N_2 as the shielding gas.

Publication IV. An integrated DFMA–PDM model for the design and analysis of challenging similar and dissimilar welds

In this publication, the deficiencies of traditional design approaches for design and manufacture of welded structures as regards prevention of failure during manufacturing or in service are explained. The existing information gap between the design and manufacturing stages is defined. The work describes how using traditional design approaches, where the metallurgical and chemical-mechanical aspects of the weld metal are only considered in the manufacturing stage, can result in a need for redesign and costly delays or failures. The objective of this study was to bridge the gap between the design and manufacturing phases and develop a practical model for improving the manufacturability and reliability of weldment design. The study also aimed to introduce a decision-making model that facilitates the task of designers and shortens the cycle time of welded products.

The study implemented the concurrent engineering (CE) concept and employed a design for manufacturing and assembly (DFMA) methodology to address the above-mentioned deficiencies. In the study, the weld is considered as a separate design module and traditional DFMA is modified to enable effective utilization for design of welded structures. The success of a DFMA strategy relies on effective and streamlined transfer of data among the product development teams. Therefore, information distribution is required in the design phase in order to monitor and analyse not only the probable performance of the weldment but also the proposed welded structure.

The study introduces an integrated view of DFMA-PDM that can resolve issues regarding data management among the product development teams and also enhance implementation of DFMA rules in the production line by companies using PDM systems. With this integrated DFMA-PDM model, the development and manufacturability of the product will be controlled and assessed in the design stage. In the integrated view of DFMA-PDM, the PDM side acts as a design support system through the design phase. The PDM system serves the model with a database of welding processes, materials, consumables, standards and guidelines. In addition, the PDM system is used to store and track changes in the weldment design. The creation and management of the product design data is effectively applied for the design data. The design data is shared at the right

time by considering the right concept in order to make sure that the design and manufacturing is performed in the efficient way. The DFMA side of the integrated model governs the database and filters the available options toward an optimal solution.

It is shown that the proposed approach can also be used in conjunction with CAD applications and manufacturers' PDM software to enhance the design of weldments and expedite decision making. The generic nature of the model makes it applicable to many welding operations if relevant databases and guidelines are prepared.

The study also introduces an application-based selection approach that is a variation of a questionnaire-based approach combined with an inductive reasoning strategy. The method uses built-in expertise that guides the designer toward an optimum solution, which considerably reduces the complexity of the task and the welding-specific knowledge needed by the designer.

A demo application was developed as a proof of principle and tested with Arctic conditions as the nominated service environment. For the specific example considered in the work, the application-based selection model offers easier and faster selection of material and filler metals and enables designers without specialized knowledge of welding and metallurgy to expeditiously evaluate different material and filler metal options.

Publication V. A DFMA-based approach for the design of challenging welds

In this publication, modification and adaptation of the traditional DFMA strategy for welding requirements is described. Traditional design processes burden welding engineers with a need to take into consideration metallurgical characteristics and incompatibilities when trying to meet requested functionality, e.g. corrosion resistance, ductility, strength and hardness. These material and weld considerations are usually only addressed when the detailed design is done, which can cause costly reworks and delays.

The objective of the study was to take advantage of DFMA strategy and CE in development of a model to address such considerations at an earlier stage in the design and manufacturing process and facilitate decision-making procedures in weldment design.

The modified DFMA methodology for welded structures can offer a solution to such late revisions if suitably extended to structural welding applications. In the study, in addition to modification of DFMA to enhance its performance in design of welded structures, an extended example of application-based selection in practice, for offshore construction, is presented using a demo application that was developed for the purposes of the study as a proof of principle.

For the application considered in the work, the proposed model offers the following advantages:

- Easier and faster selection of material and filler metals.
- Enabling of designers to evaluate different material and filler metal options quickly without a demand for expertise in welding metallurgy.
- Minimized risk of failure during manufacturing and service because the built-in expertise constrains selection to an approved list of base and filler metals for a specified application.

Publication VI. Effect of heat input on dissimilar welds of ultra high strength steel and duplex stainless steel: Microstructural and compositional analysis

In this publication, dissimilar welds of direct-quenched (DQ) ultra high strength steel (Optim 960 QC) and duplex stainless steel (UNS S32205) are studied. The objective was to study the microstructural transitions of this novel dissimilar combination as regards the effect of heat input on the weld metals, fusion boundaries and HAZs. The work provides an in-depth explanation of the mechanisms involved in the variation in chemical composition and formation of macrosegregation in the fusion zone.

With ultra high strength steel (UHSS), regardless of the specific welding process and alloy used, the main flaws include: heat affected zone (HAZ) cracking, HAZ softening, and degradation of toughness and ductility. These problems generally stem from inappropriate heat input and cooling rate, the chemical composition of the material, the growth of coarse grains, and variation in the proportion of ductile to brittle morphologies in the microstructure of the HAZ and weld.

With duplex stainless steel (DSS), degradation of mechanical properties and corrosion resistance are the major issues. These problems are usually a consequence of inappropriate heat input and excessive thermal cycles, which can cause disproportion between the volume percentage of ferrite and austenite, and deleterious precipitations such as sigma (σ), chi (χ), and chromium nitride (Cr_2N) in the fusion zone and HAZ.

In the study, single pass dissimilar welds were made on 5 mm thick plates of a commercial direct-quenched UHSS, Optim 960 QC, and a DSS, UNS S32205, using fully automated GMAW. The plates were machined to produce single V-groove butt joint configurations with an angle of 60° . Removable fiberglass tape was applied as backing, and the root-face and air gap were both zero. Butt joints were made at three different welding speeds: 7.1 mm/s, 8 mm/s and 9 mm/s. Esab OK Autrod 16.55 (AWS A5.9: ER 385), a fully austenitic filler wire (1 mm diameter), was used as the filler metal, and a mixture of 98% Ar + 2% CO_2 was supplied as a shielding gas at a constant flowrate of 15 l/min. The tip-to-work (stick out) distance was maintained at 13 mm throughout the entire welding process.

The microstructural observations of the HAZs on the ferritic side showed that higher heat input increased the bainitic growth. In contrast, higher cooling rate increased martensitic formation. On the HAZ of the duplex side, higher heat input was beneficial in austenitic

transformation. No trace of detrimental precipitations was detected in the microstructural observations.

Different forms of macrosegregation were detected when studying the microstructure of fusion boundaries on the ferritic and duplex sides of the welds. Macrosegregation on the ferritic side resulted in formation of a martensitic band in all samples and filler-depleted islands in the weld specimen made with the lowest heat input. On the duplex side of the fusion boundary, macrosegregation appeared in the form of partially mixed and/or unmixed zones (PMZ/UMZ) with a distinctly different solidification mode than the bulk weld metal.

The effect of different heat inputs was also noticeable in the fusion zone. In the case of the bulk weld metal, more granular and equiaxed austenite appeared with the higher heat input, while dendritic and columnar austenitic formation was observed with the higher cooling rates.

The study shows that formation of macrosegregation is influenced by mismatches in the chemical composition and thermal properties of the base and filler metals, as well as the amount of heat input. The composition of the weld metal was more homogeneous when higher heat input was applied. With lower heat inputs, the disparity in the composition (i.e. Cr, Ni and Mo) was sizeable.

Publication VII. Effect of GMAW heat input on the microstructure, mechanical and fatigue behaviour of dissimilar welds of ultrahigh strength steel and duplex stainless steel

In this publication, dissimilar welds of direct-quenched ultrahigh strength steel (Optim 960 QC) and duplex stainless steel (UNS S32205) were studied. The objective of the study was to investigate the effect of heat input on the microstructure, mechanical properties (i.e., hardness, tensile, bending, and impact toughness properties) and fatigue behaviour of this novel heterogeneous combination of base and weld metals. The study delineates the relation between the microstructural transmutation and variations in the mechanical properties of the weld specimens.

In this work, as-received plates of Optim 960 QC ultrahigh strength steel and UNS S32205 duplex stainless steel were machined to prepare V-grooves with an angle of 60° in butt joint configuration. The root-face and air gap were both zero and removable fiberglass tapes were used for backing. Single pass welds were made on the joints using a fully automated GMAW machine with three different welding speeds, namely, 7.1 m/s, 8 m/s and 9 m/s. An austenitic filler wire, Esab OK Autrod 16.55 (1 mm diameter), was used for the welds under a constant shielding gas (98 % Ar + 2 % CO₂) at a flowrate of 15 l/min and with a fixed tip-to-work distance of 13 mm.

The microstructural analyses showed intense grain coarsening on the HAZ of both the UHSS and DSS. On the ferritic side, it was noticed that higher heat input enhanced bainitic transformation and more martensite was formed with higher cooling rates.

On the duplex side of the fusion zone, macrosegregation was noticed in the form of partially mixed and/or unmixed zones (PMZ/UMZ) with a different solidification mode than the bulk weld metal. The appearance of macrosegregation showed a direct relation with higher cooling rates on the fusion boundary. In the bulk weld metal, higher heat input favoured more granular and equiaxed austenite growth, while dendritic and columnar austenitic growth was detected in connection with the higher cooling rates.

Intense grain coarsening in the HAZ of S 960 caused reduction in dislocation density and, consequently, a considerable reduction in the hardness close to the fusion boundary. With lower heat input, more martensitic transformation on the ferric side and limited austenitic transition on the duplex side increased the hardness in the HAZ of S 960 and S 32205, respectively.

A direct correlation between harder structures of the weldments and improvement in tensile and yield strength was noticed. Accordingly, the highest tensile and yield strength were recorded for the specimen made with the lowest heat input.

The three point bending test results were affected by the soft austenitic fusion zone. Although all samples passed the face bending test, accumulation of the strain in the narrow soft austenitic weld in root bending caused fracture in all specimens.

The impact toughness of the specimens was well above the minimum 27 J requirement, both in the weld and in the S 960 HAZ. In the ferritic HAZ, excellent impact toughness comparable to that of the S 960 parent metal was achieved with moderate heat input. The excellent impact toughness may indicate the beneficial effect of a more balanced bainitic-martensitic structure on the toughness properties.

The fatigue test demonstrated that the fatigue strength of the samples is covered by the S-N curve of the weaker base metal, which in this case was S 32205. Since the specimens were tested in as-welded condition without removal of the weld reinforcement, the fatigue life of the specimens was principally influenced by geometrical effects rather than variations in the microstructure as a result of the heat input.

6 Suggestions for further study

The experimental part of this dissertation work presents dissimilar welding between ferritic steels and stainless steel and duplex stainless steel. Only two grades of ferritic steels, namely, S 355 MC low alloy structural steel and Optim 960 QC direct-quenched ultra high strength steel, are studied, and only two grades of stainless steel, AISI 304 L austenitic stainless steel and UNS S32205 duplex stainless steel, were subject to experimental work. There are many other very popular steel grades, such as dual phase steels (DQ), and quenched and tempered (QT) steels, and their dissimilar joining with different stainless steel grades (i.e., ferritic, austenitic, duplex and martensitic) has not been much studied in the literature, even though such welds may be very attractive from an industrial perspective. Consequently, a great deal of further study into dissimilar welding of ferritic steels and stainless steels remains to be done. Moreover, the effect of shielding gas on dissimilar welds has not been taken into consideration in the presented studies in this work. The effect of different compositions of shielding gas on the dissimilar welds can be an interesting and meaningful area of study.

The developed DFMA-based approach is only tested with a few applications and a small number of related base and filler metals. In addition, practical integration with PDM systems and characterization of a complete database to cover all guidelines related to welding process parameters, joint and design standards, and welding process specification and qualification tests are not done. Thus, the presented DFMA-PDM model can be considered no more than a proof of concept and further studies are required to evaluate the efficacy and validity of the model for other applications in terms of selection of materials, welding processes and filler metals, as well as data management, concept sharing, design reliability and manufacturability.

7 Conclusion

This dissertation presents a study on microstructural and mechanical behaviour of three types of dissimilar welds focusing on the welding process, process parameters and technique, and filler wires. The dissimilar welds studied are: GMAW of structural steel (S 355 MC) and austenitic stainless steel (AISI 304 L), laser overlap welding of Zn-coated steel on aluminium, and GMAW of direct quenched ultra high strength steel (Optim 960 QC) and duplex stainless steel (UNS S32205). In addition, the study presents a new design manufacturing and assembly (DFMA) model. The DFMA-based approach developed aims to exploit the advantages of concurrent engineering (CE) in the design of welded structures. Integration of the presented DFMA-based approach and product data management (PDM) systems is discussed for implementation of the model in real world manufacturing and production lines. A software application-based selection approach is devised for enhanced decision-making in design of welded structures and selection of materials, welding processes, welding parameters and filler metals. The usability of the approach is illustrated for selection of the base and filler metals for an offshore structure.

From study of GMAW dissimilar welds of S 355 MC and AISI 304 L, the following points and conclusions are noteworthy:

- The measured dilution by the base metals was less when the weaving technique was applied than when using a stringer deposit.
- In general, the measured ferrite numbers were very close to those predicted by the Schaeffler diagram and higher ferrite numbers were found in weldments made using the weaving method.
- The presence of a martensitic region adjacent to the fusion boundary on the ferritic side was noticed for all weld specimens with the exception of *16.54*.
- Results seen in optical micrographs were quite consistent with predictions derived from the Suutala and Moisio approach and the Schaeffler diagram as regards the solidification mode and microstructure for all samples except *16.54* on the austenitic side.
- No obvious relation between the weaving technique and the resultant microstructure and solidification mode were recognizable in the weld samples.
- For *16.55*, *16.55^w* and *316LSi*, a sharp increase of hardness was detected on the ferritic side of the fusion boundary and close to the weld interface, which can indicate the presence of a martensite band within this region.

From study of the laser dissimilar weld of Zn-steel on aluminium in overlap configuration, the following conclusions can be drawn:

- Higher heat input can intensify the growth of brittle intermetallic compounds (IMCs).

- In most cases, greater mechanical strength of welds is achieved when the thickness of the brittle IMC layer is less than 10 μm . Besides the thickness of the IMC layer, other aspects such as the composition and orientation of the IMCs as well as bonding and diffusion between the elements may be decisive in determination of weld strength.
- The use of N_2 as a shielding gas can have favourable effects limiting the formation of brittle IMCs, thereby improving weld strength. The favourable effects may be due to the higher thermal conductivity of N_2 compared to Ar, as well as the likelihood of a reaction between N_2 plasma and Al vapour to form aluminium nitride in place of Al-rich IMCs.
- The type of shielding gas can be influential in determining the corrosion resistance of the weld. Inert gases with higher density protect the molten pool against oxidation more effectively, which can be advantageous for the corrosion resistance performance of the weld.

From study of dissimilar GMAW welds of Optim 960 QC (S 960) direct-quenched ultra high strength steel and UNS S32205 (S 32205) duplex stainless steel, the following observations are particularly noteworthy:

- Severe grain coarsening was noticed in the HAZs on both the ferritic and duplex sides. Higher heat input favoured bainitic transformation on the ferritic side, while more martensite was observed with higher cooling rates (*WS 8* and *WS 9*). A beneficial effect of higher heat input was noticed in that it enhanced the austenitic formation on the duplex side (*WS 7.1*). No detrimental precipitation was detected with the range of heat inputs applied.
- Macrosegregation was the most important feature found in study of the fusion boundaries. Mismatches in the chemical composition and thermal properties of the base and filler metals as well as the amount of heat input are the main determinative factors in the development of macrosegregation.
- On the ferritic side of the fusion zone, macrosegregation resulted in the formation of a martensitic band on the weld interface in all samples and filler-depleted islands in *WS 9*. On the duplex side, macrosegregation only appeared with higher cooling rates (*WS 8* and *WS 9*). The macrosegregation appeared in the form of partially mixed and/or unmixed zones (PMZ/UMZ) with a different solidification mode than the bulk weld metal.
- In the bulk weld metal, the higher heat input (*WS 7*) enhanced granular and equiaxed austenite formation. In contrast, dendritic and columnar austenitic growth was noticed with the higher cooling rates (*WS 8* and *WS 9*).

- The composition of the fusion zone was more homogeneous when higher heat input was applied (*WS 7.1*). With the higher cooling rates (*WS 8* and *WS 9*), the disparity in the composition (i.e. Cr, Ni and Mo) was considerable.
- Substantial reduction in the hardness close to the fusion boundary was noticed as a result of coarse grain formation and reduced dislocation density in the HAZ of S 960.
- With lower heat inputs, more martensitic transformation on the ferritic side and limited austenitic transition on the duplex side increased the hardness in the HAZ of S 960 and S 32205.
- The increase of tensile and yield strength showed a direct correlation with the harder structure of the weldments. Consequently, the highest tensile and yield strength were recorded for *WS 9*.
- The impact toughness of the weld samples was well above the minimum 27 J requirement, both in the weld and in the HAZ of S 960.
- In the S 960 HAZ, good impact toughness comparable to that of the S 960 base metal was achieved with a moderate heat input (*WS 8*). This finding may indicate the advantageous effect of a more balanced bainitic-martensitic structure on the toughness properties.
- The fatigue test results demonstrated that the fatigue life of the specimens is primarily influenced by geometrical effects rather than variation in the microstructure as a result of differences in heat input.

Regarding the application-based approach and integrated view of DFMA and PDM, the following conclusions are important:

- For the specific example considered in this work, the proposed model enables easier and faster selection of material and filler metals and empowers designers to expeditiously assess different material and filler metal options. However, further studies are essential to evaluate the efficacy and validity of the model for other applications in terms of selection of materials, welding processes and filler metals, as well as design reliability and manufacturability.

References

- Al-Haidary, J.T., Wahab, A.A. and Salam, E.H.A. (2006) 'Fatigue crack propagation in austenitic stainless steel weldments', *Metall. Mater. Trans. A*, vol. 37, pp. 3205–3214.
- Amo, J.M., Duran, J., Chao, J., and Sáez, J.F. (1996) 'Laser welding of Al55–Zn coated steel sheet', *J Mater Sci*, vol. 31, pp. 6595–6607.
- Arivazhagan, N., Narayanan, S., Singh, S., Prakash, S. and Reddy, G.M. (2012) 'High temperature corrosion studies on friction welded low alloy steel and stainless steel in air and molten salt environment at 650°C', *Mater. Des.*, vol. 34, pp. 459–468.
- Arivazhagan, N., Singh, S., Prak, S. and Reddy, G.M. (2011) 'Investigation on AISI 304 austenitic stainless steel to AISI 4140 low alloy steel dissimilar joints by gas tungsten arc, electron beam and friction welding', *Mater. Des.*, vol. 32, no. 5, pp. 3036–3050.
- Ashby, M.F. (1999) *Materials Selection in Mechanical Design*, 2nd edition, Oxford: Butterworth Heinemann.
- Ashby, M.F., Bréchet, Y.J.M., Cebon, D. and Salvo, L. (2004) 'Selection strategies for materials and processes', *Materials and Design*, vol. 25, pp. 51–67.
- Ashby, M.F. and Johnson, K.W. (2001) *Classification and choice in product design*, Cambridge: Cambridge Engineering Design Centre.
- ASM International Handbook Committee (ed.) (1990) *ASM Handbook, Volume 01 - Properties and Selection: Irons, Steels, and High-Performance Alloys.*, ASM International.
- ASME Boiler and Pressure Vessel Committee, S.o.M. (2007) 'Code II Part C Specifications for Welding Rods, Electrodes, and Filler Metals', in *ASME Boiler and Pressure Vessel Code*, ASME.
- Boothroyd, G., Dewhurst, P. and Knight, W.A. (2000) *Product Design for Manufacture and Assembly*, Marcel Dekker, NY: Springer.
- Borrisutthekul, R., Yachi, T., Miyashita, Y. and Mutoh, Y. (2007) 'Suppression of intermetallic reaction layer formation by controlling heat flow in dissimilar joining of steel and aluminum alloy', *Mater. Sci. Eng., A*, vol. 467, no. 1-2, pp. 108–113.
- Brooks, J.A. and Lippold, J.C. (1993) 'Selection of Wrought Austenitic Stainless Steels', in *ASM Handbook Volume 6, Welding, Brazing, and Soldering*, ASM International.
- Celik, A. and Alsaran, A. (1999) 'Mechanical and structural properties of similar and dissimilar steel joints', *Mater. Charact.*, vol. 43, no. 5, pp. 311–318.

- Charles, J.A., Crane, F.A.A. and Furness, J.A.G. (1997) *Selection and Use of Engineering Materials*, 3rd edition, Oxford: Butterworth Heinemann.
- Chen, W., Ackerson, P. and Molian, P. (2009) 'CO₂ laser welding of galvanized steel sheets using vent holes', *Mater. Des.*, vol. 30, no. 2, pp. 245–251.
- Chen, H.-C., Pinkerton, A.J., Lia, L., Liu, Z. and Mistry, A.T. (2011) 'Gap-free fibre laser welding of Zn-coated steel on Al alloy for light-weight automotive applications', *Mater Des*, vol. 32, pp. 495–504.
- Cortie, M.B., Fletcher, C.J. and Louw, K. (1995) 'Fatigue cracking of type 304 sheet in pasteurizer water', *Int. J. Fatigue*, vol. 17, no. 7, pp. 463-470.
- Dabiri, M., Isakov, M., Skriko, T. and Björk, T. (2016) 'Experimental fatigue characterization and elasto-plastic finite element analysis of notched specimens made of direct-quenched ultra-high-strength steel', *Proc IMechE Part C: J Mechanical Engineering Science*, pp. 1–18.
- Dadfar, M., Fathi, M.H., Karimzadeh, F., Dadfar, M.R. and Saatchi, A. (2007) 'Effect of TIG welding on corrosion behavior of 316L stainless steel', *Mater. Lett.*, vol. 61, pp. 2343–2346.
- Das, C.R., Bhaduri, A.K., Srinivasan, G., Shankar, V. and Mathew, S. (2009) 'Selection of filler wire for and effect of auto tempering on the mechanical properties of dissimilar metal joint between 403 and 304L(N) stainless steels', *J. Mater. Process. Technol.*, vol. 209, no. 3, pp. 1428–1435.
- Dasgupta, A.K. and Li, M.P. (2007) 'Physics of zinc vaporization and plasma absorption during CO₂', *J. Appl. Phys.*, vol. 102, p. 053108.
- Davis, J.R. (ed.) (1995) *ASM Specialty Handbook: Stainless Steels*, ASM International.
- Davis, J.R. (ed.) (2001) 'High-Strength Low-Alloy Steels', in *Alloying: Understanding the Basics*, Ohio: ASM International.
- Dieter, G.E. (2012) *Engineering Design, a Materials and Processing Approach*, 5th edition, New York: McGraw-Hill.
- Ding, J.J., Huang, H.J., Peyre, P. and Fabbro, R. (2006) 'Temperature criterion of laser welding for joining aluminum alloy with low-carbon steel', *Mater. Manuf. Processes*, vol. 21, pp. 59–61.
- Doody, T. (1992) 'Intermediate mixed zones in dissimilar metal welds for sour service', *Welding Journal*, vol. 71, no. 3, pp. 55–60.

- Du Toit, M. (2002) 'Filler metal selection for welding a high nitrogen stainless steel', *J. Mater. Eng. Perform.*, vol. 11, no. 3, pp. 306–312.
- Duley, W.W. (1999) *Laser Welding*, Toronto: Wiley Interscience.
- DuPont, J.N., Kiser, S.D. and Lippold, J.C. (2009) 'Dissimilar Welding', in *Welding metallurgy and weldability of nickel-base alloys*, New Jersey: Wiley & Sons, Inc.
- Dupont, J.N. and Kusko, C.S. (2007) 'Technical note: martensite formation in austenitic/ferritic dissimilar alloy welds', *Welding Journal*, vol. 86, no. 2, pp. 51-s–54-s.
- E. Ghali, V. S. Sastri and M. Elboudjaini (2007) *Corrosion Prevention and Protection: Practical Solutions*, Wiley.
- Eghlimi, A., Shamanian, M., Eskandarian, M., Zabolian, A., Nezakat, M. and Szpunar, J.A. (2015) 'Evaluation of microstructure and texture across the welded interface of super duplex stainless steel and high strength low alloy steel', *Surf. Coat. Technol.*, vol. 264, pp. 150–162.
- ESAB (2005) *Welding Consumables Handbook*, [Online], Available: www.esab.com.
- Eskelinen, H. (2013a) 'Aspects of integration between DFMA approaches and PDM data', Proceedings of the PDM2013 Conference, Lappeenranta, 13–21.
- Eskelinen, H. (2013b) 'Review of traditional DFMA principles', in Eskelinen, H. (ed.) *Advanced approaches to analytical and systematic DFMA analysis*, Lappeenranta: Lappeenranta University of Technology.
- Eva , V.C. and Joaquín, V.G. (2012) 'Structural connections for lightweight metallic structures', in *Advanced Structured Materials*, Berlin: Springer.
- Fabbro, R., Coste , F., Goebels , D. and Kielwasser, M. (2006) 'Study of CW Nd-YAG laser welding of Zn-coated steel sheets', *J Phys D Appl Phys*, vol. 39, pp. 401–409.
- Farag, M.M. (1989) *Selection of Materials and Manufacturing Processes for Engineering Design*, Englewood Cliffs: Prentice Hall.
- Farrokhi, F., Siltanen, J. and Salminen, A. (2015) 'Fiber laser welding of direct-quenched ultrahigh strength steels: evaluation of hardness, tensile strength, and toughness properties at subzero temperatures', *J. Manuf. Sci. Eng.*, vol. 137, pp. 061012-1–061012-10.
- Fuentes , A.L.G., Salas, R., Centeno , L. and Rosario, A.V.d. (2011) 'Crack growth study of dissimilar steels (Stainless - Structural) butt welded unions under cyclic loads', *Procedia Eng*, vol. 10, pp. 1917–1923.

- Fuentes, A.L.G., Salas, R., Centeno, L. and Rosario, A.V.d. (2011) 'Crack growth study of dissimilar steels (Stainless - Structural) butt-welded unions under cyclic loads', *Procedia Eng.*, vol. 10, pp. 1917–1923.
- Garzón, C.M. and Ramirez, A.J. (2006) 'Growth kinetics of secondary austenite in the welding microstructure of a UNS S32304 duplex stainless steel', *Acta Mater.*, vol. 54, pp. 3321–3331.
- Gascoigne, B. (1995) 'PDM: the essential technology for concurrent engineering', *World Class Design to Manufacture*, vol. 2, no. 1, pp. 38–42.
- Ghorbani, S., Ghasemi, R., Ebrahimi-Kahrizsangi, R. and Hojjati-Najafabadid, A. (2017) 'Effect of post weld heat treatment (PWHT) on the microstructure, mechanical properties, and corrosion resistance of dissimilar stainless steels', *Mater. Sci. Eng., A*, vol. 688, pp. 470–479.
- Guo, W., Crowther, D., Francis, J.A., Thompson, A., Liu, Z. and Li, L. (2015) 'Microstructure and mechanical properties of laser welded S960 high strength steel', *Mater. Des.*, vol. 85, pp. 534–548.
- Guo, W., Crowther, D., Francis, J.A., Thompson, A., Liu, Z. and Li, L. (2015) 'Microstructure and mechanical properties of laser welded S960 high strength steel', *Mater. Des.*, vol. 85, pp. 534–548.
- Guo, A., Misra, R.D.K., Xu, J., Guo, B. and Jansto, S.G. (2010) 'Ultrahigh strength and low yield ratio of niobium-microalloyed 900 MPa pipeline steel with nano/ultrafine bainitic lath', *Mater. Sci. Eng., A*, vol. 527, pp. 3886–3892.
- Gurney, T.R. (1979) *Fatigue of welded structures*, Cambridge: Cambridge University Press.
- Hasçalik, A., Ünal, E. and Özdemir, N. (2006) 'Fatigue behaviour of AISI 304 steel to AISI 4340', *J Mater Sci*, vol. 41, pp. 3233-3239.
- Hemmilä, M., Hirvi, A., Kömi, J., Laitinen, M., Laitinen, M., Mikkonen, P., Porter, D., Savola, J. and Tihinen, S. (2010) *Technological properties of direct-quenched structural steels with yield strength 900-960 MPa as cut length and hollow sections*, Rautaruukki Corporation.
- Hernandez, V.H.B., Nayak, S.S. and Zhou, Y. (2011) 'Tempering of martensite in dual phase steels and its effects on softening behavior', *Metall. Mater. Trans. A*, vol. 42, no. 10, pp. 3115–3129.
- Hertzman, S., Ferreira, P.J. and Brolund, B. (1997) 'An experimental and theoretical study of heat-affected zone austenite reformation in three duplex stainless steels', *Metall. Mater. Trans. A*, vol. 28, no. 2, pp. 277–285.

- Hobbacher, A. (2013) 'Recommendations for Fatigue Design of Welded Joints and Components' Paris: International Institute of Welding, doc. XIII-2460-13/XV-1440-13.
- Hobbacher, A.F. (2016) *Recommendations for fatigue design of welded joints and components*, Springer, Available: <http://www.iiwelding.org> [23 Jan 2016].
- Hsieh, R.I., Liou, H.Y. and Pan, Y.T. (2001) 'Effects of cooling time and alloying elements on the microstructure of the Gleeble-simulated heat affected zone of 22% Cr duplex stainless steels', *J. Mater. Eng. Perform.*, vol. 10, no. 5, pp. 526–536.
- Hwang, G.C., Lee, S., Yoo, J.Y. and Choo, W.Y. (1998) 'Effect of direct quenching on microstructure and mechanical properties of copper-bearing high-strength alloy steels', *Mater. Sci. Eng., A*, vol. 252, pp. 256–268.
- J, B., Kim, Y.P., Kim, W.S. and Kho, Y.T. (2001) 'Fracture toughness and fatigue crack growth properties of the base metal and weld metal of a type 304 stainless steel pipeline for LNG transmission', *Int. J. Press. Vessels Pip.*, vol. 78, pp. 351–357.
- Kah, P., Pirinen, M., Suoranta, R. and Martikainen, J. (2013) 'Welding of ultra high strength steels', *Advanced Materials Research*, pp. 357–365.
- Kang, D.H. and Lee, H.W. (2012) 'Effect of different chromium additions on the microstructure and mechanical properties of multipass weld joint of duplex stainless steel', *Metall. Mater. Trans. A*, vol. 43, no. 12, pp. 4678-4687.
- Katayama, S., Joo, S.M., Mizutani, M. and Bang, H.S. (2005) 'Laser weldability of aluminum alloy and steel', *Mater Sci Forum*, vol. 502, pp. 481–486.
- Katayama, S., Nagayama, H., Mizutani, M. and Kawahito, Y. (2009) 'Fibre laser welding of aluminium alloy', *Weld Int*, vol. 23, pp. 744–752.
- Klimpel, A., Janicki, D., Klimpel, A.S. and Rzeźnik, A. (2007) 'Abrasive and erosive wear resistance of GMA metal cored wire cermet deposits', *JAMME*, vol. 28, no. 9, pp. 565-572.
- Knight, W.A. (2005) 'Integrated design For manufacture, service and environment', in *Advances in Integrated Design and Manufacturing in Mechanical Engineering*, Dordrecht, The Netherlands: Springer.
- Kodama, S., Ishida, Y., Asai, K., Mizumoto, M., Namekata, T. and Nagasaki, H. (2010) 'Development of stainless steel welding wire for galvanized steel sheets', vol. 54, no. 1, pp. R42–R48.
- Kolodner, J.L. (1992) 'An introduction to case-based reasoning', *Artificial Intelligence Review*, vol. 6, pp. 3–34.

- Kolodner, J. (1993) *Case Based Reasoning*, San Mateo: Morgan Kaufmann.
- Kotecki, D.J. and Siewert, T.A. (1992) 'WRC-1992 constitution diagram for stainless steel weld metals: a modification of the WRC-1988 diagram', *Weld J*, vol. 71, pp. 171s–178s.
- Kou, S. (2003) *Welding Metallurgy*, John Wiley & Sons, Inc., Available: <http://onlinelibrary.wiley.com>.
- Kou, S. and Wang, Y.H. (1986) 'Weld pool convection and its effect', *Welding Research Supplement*, March, pp. 63-s–70-s.
- Kou, S. and Yang, Y.K. (2007) 'Fusion-boundary macrosegregation in dissimilar-filler welds', *Welding Research*, Dec., pp. 303-s–312-s.
- Kujanpää, V.P., David, S.A. and White, C.L. (1986) 'Formation of hot cracks in austenitic stainless steel welds—solidification cracking', *Welding Research Supplement*, Aug., pp. 203-s–212-s.
- Kwok, C.T., Fong, S.L., Cheng, F.T. and Man, H.C. (2006) 'Pitting and galvanic corrosion behavior of laser-welded stainless steels', *J Mater Process Technol*, vol. 176, pp. 168–178.
- Kwon, Y., Wu, T. and Saldivar, J.O. (2004) 'SMWA: A CAD-based decision support system for the efficient design of welding', *Concurrent Engineering*, vol. 12, no. 4, pp. 295–304.
- Laitinen, R., Valkonen, I. and Kömi, J. (2013) 'Influence of the base material strength and edge preparation on the fatigue strength of the structures made by high and ultra-high strength steels', 5th Fatigue Design Conference, 282-291.
- Larén, M. (ed.) (2004) *The Avesta Welding Manual, Practice and products for stainless steel welding*, Sweden: Avesta Welding AB.
- LeBacq, Brechet, Y., Shercliff, Jeggy, T. and Salvo, L. (2005) 'Selection of joining methods in mechanical design', *Materials and Design*, vol. 23, pp. 405 – 416.
- Lee, K.J. and Kumai, S. (2006) 'Characterization of intermetallic compound layer formed at the weld interface of the defocused laser welded low carbon steel/6111 aluminum alloy lap joint', *Mater Trans*, vol. 47, pp. 1178–1185.
- Li, X., Lawson, S. and Zhou, Y. (2007) 'Novel technique for laser lap welding of zinc coated sheet steels', *J. Laser Appl.*, vol. 19, pp. 259–264.
- Lippold, J.C., Kiser, S.D. and DuPont, J.N. (2009) *Welding Metallurgy and Weldability of Nickel-Base Alloys*, New Jersey: John Wiley & Sons.

- Lippold, J.C. and Kotecki, D.J. (2005) 'Dissimilar welding of stainless steel', in *Welding metallurgy and weldability of stainless steels*, New Jersey: Wiley-Interscience.
- Lippold, J.C. and Savage, W.F. (1979) 'Solidification of austenitic stainless steel weldments: part I—a proposed mechanism', *Welding Research Supplement*, Dec., pp. 362-s–374-s.
- Lovatt, A.M. and Shercliff, (1998) 'Manufacturing process selection in engineering design. Part 2: a methodology for creating task-based process selection procedures', *Materials & Design*, vol. 19, no. 5–6, pp. 217–230.
- Lundin, C.D. (1982) 'Dissimilar metal welds—transition joints literature review', *Weld. J.*, pp. 58-s–63-s.
- Ma, J., Harooni, M., Carlson, B. and Kovacevic, R. (2014) 'Dissimilar joining of galvanized high-strength steel to aluminum alloy in a zero-gap lap joint configuration by two-pass laser welding', *Mater. Des.*, vol. 58, pp. 390–401.
- Maropoulos, , Yao, Z., Bradley, H.D. and Par, (2000) 'An integrated design and planning environment for welding, Part 1: Product modelling', *Journal of Materials Processing Technology*, vol. 107, pp. 3 – 8.
- Martin, G., Yerra, S.K., Bre´chet, Y., Véron, M., Mithieux, J.D., Chéhab, B., Delannay, L. and Pardoën, T. (2012) 'A macro- and micromechanics investigation of hot cracking in duplex steels', *Acta Mater.*, vol. 60, pp. 4646–4660.
- Meco, S., Pardal, G., Ganguly, S., Miranda, R., Quintino, L. and Williams, S. (2013) 'Overlap conduction laser welding of aluminium to steel', *Int. J. Adv. Manuf. Technol.*, vol. 67, no. 1, pp. 647–654.
- Merklein, M., Johannes, M., Lechner, M. and Kuppert, A. (2014) 'A review on tailored blanks—Production, applications and evaluation', *J. Mater. Process. Technol.*, vol. 214, pp. 151–164.
- Milberg, J. and Trautmann, A. (2009) 'Defect-free joining of zinc-coated steels by bifocal hybrid laser welding', *Prod. Eng. Res. Devel.*, vol. 3, pp. 9–15.
- Missori, S. and Koerbe, C. (1997) ' Laser beam welding of austenitic–ferritic transition joints', *Welding J*, vol. 76, no. 3, pp. 125–134.
- Muckelroy, N.C., Findley, K.O. and Bodnar, R.L. (2013) 'Microstructure and mechanical properties of direct quenched versus conventional reaustenitized and quenched plate', *J. Mater. Eng. Perform.*, vol. 22, no. 2, pp. 512–522.

- Mukherjee, M. and Pal, T.K. (2012) 'Influence of heat input on martensite formation and impact property of ferritic-austenitic dissimilar weld metals', *J. Mater. Sci. Technol.*, vol. 28, no. 4, pp. 343–352.
- Mäkikangas, J., Mäntyjärvi, K., Keskitalo, M. and et.al (2007) 'Laser welding of coated sheet metal constructions', 11th NOLAMP Conference in Laser Processing of Materials, Lappeenranta.
- Nascimento, M.P., Souza, R.C., Pigatin, W.L. and Voorw, H.J.C. (2001) 'Effects of surface treatments on the fatigue strength of AISI 4340 aeronautical steel', *Int J Fatigue*, vol. 23, pp. 607–618.
- Niebles, E., Maury, H., H. Gómez, H. and Riba, C. (2006) 'Definition and validation of a knowledge base and the architecture of a computer tool to assist the design and manufacturing of welded products', 10th International Research/Expert Conference "Trends in the Development of Machinery and Associated Technology", Barcelona-Lloret de Mar, Spain.
- Nykänen, T., Björk, T. and Laitinen, T. (2012) 'Fatigue strength prediction of ultra high strength steel butt-welded joints', *Fatigue Fract. Eng. Mater. Struct.*, vol. 36, pp. 469–482.
- Omar, A.A. (1998) 'Effects of welding parameters on hard zone formation at dissimilar metal welds', *Welding Journal*, vol. 77, no. 2, pp. 86-s–93-s.
- Ornath, F., Soudry, J., Weiss, B. and Minkoff, I. (1991) 'Weld pool segregation during the welding of low alloy steels with austenitic electrodes', *Welding Journal*, vol. 60, pp. 227-s to 230-s.
- Outokumpu (2013) *Handbook of Stainless Steel*, Espoo, Finland: Outokumpu Oyj, Available: www.outokumpu.com.
- Ozaki, H., Kutsuna, M., Nakagawa, S. and Miyamoto, K. (2010) 'Laser roll welding of dissimilar metal joint of zinc coated steel to aluminum alloy', *J. Laser Appl.*, vol. 22, no. 1.
- Pallaspuro, S., Linnell, T., Suikkan, P. and Porter, D. (2014) 'T₀ – T_{28J} correlation of low-carbon ultra-high-strength quenched steels', *Procedia Materials Science*, vol. 3, pp. 1032 – 1037.
- Palmer, T.A., Elmer, J.W. and Babu, S.S. (2004) 'Observations of ferrite/austenite transformations in the heat affected zone of 2205 duplex stainless steel spot welds using time resolved X-ray diffraction', *Mater. Sci. Eng., A*, vol. 374, pp. 307–321.

- Pardal, J.M., Tavares, S.S. and al., e. (2010) 'Deleterious phases precipitation on superduplex stainless steel UNS S32750: characterization by light optical and scanning electron microscopy', *Mat. Res.*, vol. 13, no. 3, pp. 401–407.
- Pettersson, N., Pettersson, R.F.A. and Wessman, S. (2015) 'Precipitation of chromium nitrides in the super duplex stainless steel 2507', *Metall. Mater. Trans. A*, vol. 46, no. 3, pp. 1062–1072.
- Qiu, J., Ju, X., Xin, Y., Liu, S., Wang, Y.L., Wu, H.B. and Tang, D. (2010) 'Effect of direct and reheated quenching on microstructure and mechanical properties of CLAM steels', *J. Nucl. Mater.*, vol. 407, pp. 189–194.
- Radaj, D., Sonsino, C.M. and Fricke, W. (2006) *Fatigue assessment of welded joints by local approaches*, Cambridge: Woodhead Publishing Limited.
- Rahmani, M., Eghlimi, A. and Shamina, M. (2014) 'Evaluation of microstructure and mechanical properties in dissimilar austenitic/super duplex stainless steel joint', *J. Mater. Eng. Perform.*, vol. 23, pp. 3745–3753.
- Ramirez, A.J., Lippold, J.C. and Brand, S.D. (2003) 'The relationship between chromium nitride and secondary austenite precipitation in duplex stainless steels', *Metall. Mater. Trans. A*, vol. 34, no. A, pp. 1575–1597.
- Ramkumar, K.D., Chandrasekhar, A., Srivastava, A., Preyas, H., Chandra, S., Dev, S. and Arivazhagan, N. (2016) 'Effects of filler metals on the segregation, mechanical properties and hot corrosion behaviour of pulsed current gas tungsten arc welded super-austenitic stainless steel', *J. Manuf. Processes*, vol. 24, pp. 46–61.
- Ramkumar, K.D., Singh, A., Raghuvanshi, S., Bajpai, A., Solanki, T., Arivarasu, M., Arivazhagan, N. and Narayanan, S. (2015) 'Metallurgical and mechanical characterization of dissimilar welds of austenitic stainless steel and super-duplex stainless steel – A comparative study', *J. Manuf. Processes*, vol. 19, pp. 212–232.
- Rathod, M.J. and Kutsuna, M. (2004) 'Joining of aluminum alloy 5052 and low-carbon steel by laser roll welding', *Weld J*, vol. 83, pp. 16–26.
- Reisgen, U., Schleser, M., Mokrov, O. and Ahmed, E. (2010) 'Shielding gas influences on laser weldability of tailored blanks of advanced automotive steels', *Appl. Surf. Sci.*, vol. 257, no. 5, pp. 1401–1406.
- Robert, W. and Messler, J. (2004) *Principles of Welding: Processes, Physics, Chemistry, and Metallurgy*, NY: WILEY-VCH.
- Roshanghias, A., Barzegari, M., Kokabi, A.H. and Hosseini, H.R.M. (2010) 'Welding characteristics of ultrahigh strength steel in annealed and quench-tempered conditions', *J. Mater. Eng. Perform.*, vol. 19, pp. 963–969.

- S. Kou (1996) *Transport Phenomena and Materials Processing*, NY: Wiley & Sons.
- Sadeghian, M., Shamanian, M. and Shafyei, A. (2014) 'Effect of heat input on microstructure and mechanical properties of dissimilar joints between super duplex stainless steel and high strength low alloy steel', *Mater. Des.*, vol. 60, pp. 678–684.
- Schaeffler, A.L. (1948) 'Welding dissimilar metals with stainless electrodes', *Iron Age*, vol. 162, p. 72.
- Shang, Y.-B., Shi, H.-J., Wang, Z.-X. and Zhang, G.-D. (2015) 'In-situ SEM study of short fatigue crack propagation behavior in adissimilar metal welded joint of nuclear power plant', *Mater. Des.*, vol. 88, pp. 598–609.
- Shushan, S.M., Charles, E.A. and Congleton, J. (1996) 'The environment assisted cracking of diffusion bonded stainless steel to carbon steel joints in an aqueous chloride solution', *Corros Sci*, vol. 38, no. 5, pp. 673-686.
- Sierra, G., Peyre, P., Deschaux-Beaume, F., Stuart, D. and Fras, G. (2007) 'Steel to aluminium key-hole laser welding', *Mater Sci Eng A Struct Mater Prop Microstruct Process*, vol. 447, pp. 197–208.
- Sierra, G., Peyre, P., Beaume, F.D., Stuart, D. and Fras, G. (2008) 'Galvanised steel to aluminium joining by laser and GTAW processes', *Mater. Charact.*, vol. 59, pp. 1705 – 1715.
- Siltanen, J., Tihinen, S. and Kömi, J. (2015) 'Laser and laser gas-metal-arc hybrid welding of 960 MPa direct-quenched structural steel in a butt joint configuration', *J. Laser Appl.*, vol. 27, no. 52, pp. S29007-1–8.
- Silva, C.C., Miranda, H.C., Sant'Ana, H.B.d. and Farias, J.P. (2013) 'Austenitic and ferritic stainless steel dissimilar weld metal evaluation for the applications as-coating in the petroleum processing equipment', *Mater. Des.*, vol. 47, pp. 1–8.
- SUN, Z. and ION, J.C. (1995) 'Laser welding of dissimilar metal combinations', *J. Mater. Sci.*, vol. 30, pp. 4205-4214.
- Suutala, N. and Moio, T. (1983) *The Use of Chromium and Nickel Equivalents in Considering Solidification Phenomena in Austenitic Stainless Steels*, The Metals Society.
- Tasalloti, H., Eskelinen, H., Kah, P. and Martikainen, J. (2016) 'An integrated DFMA–PDM model for the design and analysis of challenging similar and dissimilar welds', *Mater. Des.*, vol. 89, pp. 421–431.

- Tasalloti, H. and Kah, P. (2016) 'A DFMA-Based Approach for the Design of Challenging Welds', International Society of Offshore and Polar Engineers (ISOPE) , Rodes.
- Tasalloti, H., Kah, P. and Martikainen, J. (2014) 'Effects of welding wire and torch weaving on GMAW of S355MC and AISI 304L dissimilar welds', *Int J Adv Manuf Technol*, vol. 71, pp. 197–205.
- Tasalloti, H., Kah, P. and Martikainen, J. (2015) 'Laser overlap welding of zinc-coated steel on aluminum alloy', *Physics Procedia* , Lappeenranta, 265 – 271.
- Tasalloti, H., Kah, P. and Martikainen, J. (2015) 'Laser overlap welding of Zn-coated steel on aluminium alloy for patchwork blank applications in the automotive industry', *Rev. Adv. Mater. Sci.*, vol. 40, pp. 295–302.
- Tasalloti, H., Kah, P. and Martikainen, J. (2017) 'Effect of heat input on dissimilar welds of ultra high strength steel and duplex stainless steel: Microstructural and compositional analysis', *Mater. Charact.*, vol. 123, pp. 29–41.
- Thomy, C., Seefeld, T. and Vollertsen , F. (2005) 'High-power fibre lasers – application potentials for welding of steel and aluminium sheet material', *Advanced Materials Research*, vol. 6-8, pp. 171-178.
- Torkamany, M.J., Tahamtan, S. and Sabbaghzadeh, J. (2010) 'Dissimilar welding of carbon steel to 5754 aluminum alloy by Nd: YAG pulsed laser', *Mater Des 2010*, vol. 31, pp. 458–465.
- Tucker, J.D., Miller, M.K. and Young, G.A. (2015) 'Assessment of thermal embrittlement in duplex stainless steels 2003 and 2205 for nuclear power applications', *Acta Mater.*, vol. 87, pp. 15–24.
- Tzeng, Y.F. (2000) 'Process characterization of pulsed Nd:YAG laser seam welding', *Int J Adv Manuf Technol*, vol. 16, pp. 10–18.
- Unnikrishnan, R., Idury, Satish, K.S.N., Ismail, T.P., Bhadauria, A., Shekhawat, S.K. and al., e. (2014) 'Effect of heat input on the microstructure, residual stresses and corrosion resistance of 304L austenitic stainless steel weldments', *Mater. Charact.*, vol. 93, pp. 10–23.
- Vach, M., Kuníková, T., Dománková, M., Ševc, P., Čaplovič, L., Gogola, P. and Janovec, J. (2008) 'Evolution of secondary phases in austenitic stainless steels during long-term exposures at 600, 650 and 800 °C', *Mater. Charact.*, vol. 9, pp. 1792–1798.
- Wallin , K., Pallaspuuro, S., Valkonen, I., Roikonen, P.K. and Suikkanen, P. (2015) 'Fracture properties of high performance steels and their welds', *Eng. Fract. Mech.*, vol. 135, pp. 219–231.

- Wang, P., Chen, X., Pan, Q., Madigan, B. and Long, J. (2016) 'Laser welding dissimilar materials of aluminum to steel: an overview', *Int. J. Adv. Manuf. Technol.*, vol. 87, pp. 3081–3090.
- Wang, J., Yang, L., Sun, M., Liu, T. and Li, H. (2016) 'Effect of energy input on the microstructure and properties of butt joints in DP1000 steel laser welding', *Mater. Des.*, vol. 90, pp. 642–649.
- Visuttipitukul, P., Aizawa, T. and Kuwahara, H. (2003) 'Feasibility of plasma nitriding for effective surface treatment of pure aluminum', *Mater. Trans., JIM*, vol. 44, no. 7, pp. 1412–1418.
- Vollertsen, F. (2005) 'Developments and trends in laser welding of sheet metal', *Adv Mater Res*, vol. 6–8, pp. 59–70.
- Voort, G.F.V. (ed.) (1991) *Atlas of Time Temperature Diagrams for Irons and Steels*, PA, USA: ASM international.
- Xiao, G., Di, H., Zhu, F., Chen, B. and Qiu, B. (2010) 'Influence of direct quenching on microstructure and mechanical properties of steel plate for large oil storage tanks', *J. Mater. Eng. Perform.*, vol. 19, no. 6, pp. 868–872.
- Yang, Y.K. and Kou, S. (2007) 'Weld-bottom macrosegregation caused by dissimilar filler metals', *Welding Journal*, vol. 86, pp. 379-s–387-s.
- Yang, J., Li, Y.-L. and Zhang, H. (2016) 'Microstructure and mechanical properties of pulsed laser welded Al/steel dissimilar joint', *Trans. Nonferrous Met. Soc. China*, vol. 26, p. 994–1002.
- Yan, X.J., Yang, D.Z. and Liu, X.P. (2007) 'Corrosion behavior of a laser-welded NiTi shape memory alloy', *Mater Charact*, vol. 58, pp. 623–628.
- Yongjae, K. and Sehun, R. (2005) 'A study of heat input distribution on the surface during torch weaving in gas metal arc welding', *JSME Int J., Ser. A*, vol. 48, no. 3, pp. 144–150.
- Zha, X.F., Lim, S.Y.E. and Fok, S.C. (1998) 'Integrated intelligent design and assembly planning: A survey', *Int J Adv Manuf Technol*, vol. 14, pp. 664–685.
- Zhang, W., DebRoy, T., Palmer, T.A. and Elmer, J.W. (2005) 'Modeling of ferrite formation in a duplex stainless steel weld considering non-uniform starting microstructure', *Acta Mater.*, vol. 53, no. 16, pp. 4441–4453.
- Ziętala, M., Durejko, T., Polański, M., Kuncze, I. and al., e. (2016) 'The microstructure, mechanical properties and corrosion resistance of 316L stainless steel fabricated using laser engineered net shaping', *Mater. Sci. Eng., A*, vol. 677, pp. 1–10.

Publication I

Tasalloti, H., Kah, p., and Martikainen, J.

Effects of welding wire and torch weaving on GMAW of S355MC and AISI 304L dissimilar welds

Reprinted with permission from

The International Journal of Advanced Manufacturing Technology

Vol. 71, pp. 197-205, 2014

© 2013, Springer-Verlag London

Effects of welding wire and torch weaving on GMAW of S355MC and AISI 304L dissimilar welds

H. Tasalloti · P. Kah · J. Martikainen

Received: 3 June 2013 / Accepted: 10 November 2013 / Published online: 22 November 2013
© Springer-Verlag London 2013

Abstract Dissimilar welding of austenitic stainless steel (ASS) to low-alloy structural steel is widely used in the power generation industry. The formation of brittle martensite and hot cracking susceptibility in the single-phase austenite microstructure are the main concerns related to the metallurgy of this kind of weld. This study investigates the effect of different welding wires and the weaving technique on the quality, microstructure and microhardness of fillet weld joints between AISI 304L austenitic stainless steel and S355MC low-alloy structural steel. Using robotised synergic gas metal arc welding (GMAW), three different filler wires were used to weld specimens with and without weaving. The macro-sections of the fillet welds were inspected and the dilution rates and ferrite numbers (FN) measured. The microstructure was also inspected and microhardness values recorded. Porosity was discerned in two weld samples made with the use of weave beads. The measured FNs for all the weldments were very close to estimations from the Schaeffler diagram. The formation of a narrow martensitic band on the ferritic side of the weld metal was detected for most of the specimens. It is concluded that weaving decreased the dilution rate and increased the FN. However, no obvious effect on the microstructure and hardness as a result of using the weaving technique was noticed.

Keywords Dissimilar metal welding · GMAW · Torch weaving · Interface properties · Microstructure · AISI 304L stainless steel · S355MC structural steel

1 Introduction

The combination of austenitic stainless steel (ASS) and low-alloy structural steel presents favourable mechanical properties, formability, weldability, resistance to stress corrosion cracking and other forms of corrosion [1], along with fairly cost-effective [2, 3] manufacturing methods [4, 5]. Due to these advantageous characteristics, such combinations of metals are extensively utilised in the power generation industry [6], as well as in petrochemical plants and architecture [7–9].

A range of metallurgical concerns are present in the dissimilar welding (DMW) of ASS to low-alloy structural steel. Martensite formation on the ferritic side of the DMW interface and the risk of hot cracking in the fully austenite microstructure on the austenitic side are the main concerns in this kind of weld [10]. Depending on the chemical composition of the weld metal (WM), the growth of brittle martensite can take place both in the weld and in the heat-affected zone (HAZ) [9]. The ferrite number (FN) is another critical aspect in the DMW of ASS to low-alloy structural steel. Ferrite can be beneficial in reducing the tendency of cracking in the weld. However, excessive amounts of ferrite have a detrimental effect on corrosion resistance and the mechanical properties [11]. The amount of ferrite can be controlled by careful regulation of the filler metal composition and substrate dilution [12]. The aim is to obtain stable austenite with a small amount of ferrite, a microstructure that reduces the chance of weld solidification cracking [2]. Approximate microstructural prediction from the Schaeffler diagram can be made for DMW of ASS and low-alloy structural steels [2]. Solidification behaviour and ferrite content can be affected by the welding process and welding parameters due to variations in the amount of heat input and the solidification speed [13].

For GMAW welding of ASS and ferritic steel, the effect of torch weaving in correlation with filler material on the

H. Tasalloti · P. Kah (✉) · J. Martikainen
Lappeenranta University of Technology, P.O. Box 20,
53851 Lappeenranta, Finland
e-mail: paul.kah@lut.fi

Table 1 Chemical composition (wt.%) of base materials and welding wires

	C	Cr	Mn	Ni	P	S	Si	N	Al	Mo	Cu
AISI 304L	0.025	18	1.57	8.1	0.033	0.002	0.4	0.044	–	–	–
S355MC	0.12	–	1.5	–	0.02	0.015	0.03	–	0.015	–	–
<i>EOA16.54</i>	<0.03	21.5	1.4	15.0	–	–	0.4	–	–	2.7	–
<i>EOA16.55</i>	<0.02	20.5	1.7	25.0	–	–	0.4	–	–	4.5	1.4
<i>EC316LSi</i>	0.02	18.5	0.7	12.0	0.02	0.02	0.8	–	–	2.7	0.1

dissimilar weld has not been explicitly investigated yet. This work concentrates on evaluating the effect of different welding wire compositions and implementation of the weaving technique on the DMW of AISI 304L to S355MC low-alloy structural steel. Another objective of this study is to compare the experimental results with theoretical approaches such as the Schaeffler diagram. For these purposes, a fillet weld was made between the two base metals (BMs) using robotised GMAW with a synergic power control. Three different filler wires were used for fabricating the fillet welds by means of weave and stringer bead for each wire separately. The macro-sections of the weld samples were inspected for possible defects. The penetration measurement and dilution calculation was done for the weld samples prepared for metallographic examination. FN was measured using magnetic induction method. An optical microscope was used to inspect the microstructures of the weld samples around the fusion boundary on both AISI304 and S355MC sides. The hardness variations on the cross-section of the dissimilar welds were obtained for the weld and base metals to find evidence for the presence of different phases.

2 Experimental procedure

Two dissimilar materials, S355MC structural steel and AISI 304L ASS, were used in fabricating the fillet weld joint in this experiment. The BMs (5-mm thick) were welded with three different filler wires, namely *Esab OK Autrod 16.54* (*EOA16.54*), *Esab OK Autrod 16.55* (*EOA16.55*) and *Elga Cromarod 316LSi* (*EC316LSi*). These three wires were used to weld the base materials with a robotised GMAW process. The material specifications and the process parameters are presented in Tables 1 and 2. Using each filler wire with either a stringer or weave bead, two separate single pass fillet welds,

300 mm in length, were made on one side of the prepared T-joint assemblies. Weaving frequency was 3 Hz, with amplitude of 1.5 mm from the centre of the weld. A mixture of 98 % Ar+2 % CO₂ with a constant flow rate of 16 l/min was used for welding all the samples. Specimens of 25 mm in length were cut out from the middle of the weld. The cross-sections of the weld specimens were ground and polished using 1- μ m diamond paste. Glyceregia etchant (15 ml glycerol, 10 ml HCl and 5 ml HNO₃) was used to expose both the macro- and the microstructure for metallographic inspection. In this study, WMs are denominated with the last number of the building filler wire code plus “W” when weaving was used; for instance, *16.54* and *16.54^W* indicate a WM made from *EOA16.54* filler wire without and with weaving, respectively.

3 Results and discussion

3.1 Visual inspection

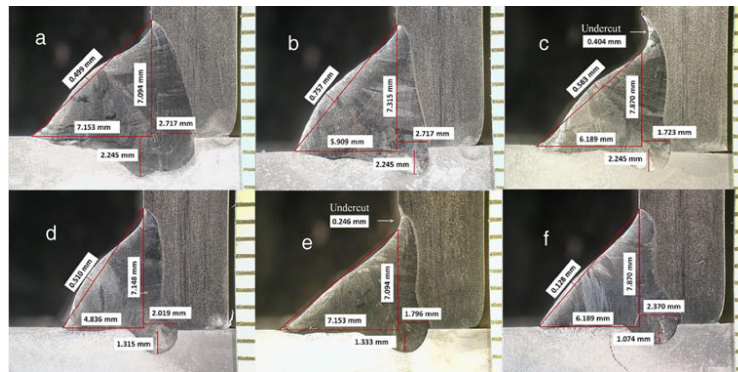
The metallographically prepared samples were inspected using a stereo-microscope. The macro-sections of the weld samples are shown in Fig. 1a–f. The leg size, convexity and maximum penetration on each side of the welds are marked in the figure. The cross-sections of the weld samples display thorough fusion between the WM and the substrates and a sufficient amount of penetration.

It can be seen from Fig. 1 that penetration is superior on the austenitic side. For S355MC, penetration ranges from 1.1 to 2.2 mm, and for AISI 304L from 2.4 to 2.7 mm. The difference may be due to the lower melting point of AISI 304L (~1,450 °C compared to ~154 °C) [14]. Figure 1 also shows that penetration on the S355MC side decreases when using weaving, whereas it increases on the AISI 304L side. The greater penetration is possibly due to heat accumulation on the

Table 2 Welding parameters for dissimilar welding: wire diameter (\varnothing), wire feed speed (V_w), welding current (I), welding voltage (U), travel speed (v) and heat input per unit length of weld (Q)

Wire	\varnothing (mm)	v_w (m/min)	Stick-out (mm)	I (A)	U (V)	v (mm/s)	Q (kJ/mm)
<i>EOA16.54</i>	1.2	11.2	20	260	24.5	8.4	0.61
<i>EOA16.55</i>	1	11.4	17	227	24	7.5	0.58
<i>EC316LSi</i>	1	11.4	17	227	24	7.5	0.58

Fig. 1 Macrostructure of weld cross-section after etching (a) 16.54, (b) 16.54^W, (c) 16.55, (d) 16.55^W, (e) 316LSi, (f) 316LSi^W



austenitic side because of its lower degree of heat conductivity. In contrast, the decreased penetration on the S355MC side is probably a result of faster heat dissipation due to weaving and the higher heat conductivity of S355MC. The maximum measured convexity, as can be seen in Fig. 1b, was 0.75 mm for 16.54^W. For 16.55 and 316LSi, undercut with a depth of 0.4 and 0.2 mm, respectively, was detected, which can be seen in Fig. 1c, e. Yongjae et al. [15] have shown through their numerical method that the heat input concentrates at the weaving end, which can cause undercut. However, such a result was not observed in this experiment. Minor undercuts were also detected in the stringer welds.

Porosity was detected in 16.54^W and 316LSi^W, observable in Fig. 2a, b. The diameter of the pores is about 50 μm for the smallest one and 200 μm for the biggest one, found in 16.54^W. The pores were situated at the root of the weld. Both samples were made with weaving and the porosity may result from the lower efficiency of the shielding gas when weaving is used [16].

3.2 Dilution rate

Dilution levels were calculated measuring the geometric cross-sectional areas of the deposited filler metal and melted BMs, presented in Table 3. In Fig. 3, the overall dilution rate

of WMs by BMs are shown and compared. From this figure, it is obvious that dilution is less when using the weaving technique compared to the stringer deposit. This is consistent with expectations since it is known that weaving reduces the dilution rate in BMs [17, 18]. Lower dilution, especially concerning S355MC, is very important. If the weld is heavily diluted by the structural steel, it may solidify as fully austenite or primary austenite because of insufficient ferrite potential in the filler metal, causing an increase in the potential for solidification cracking [2].

3.3 Schaeffler diagram

Schaeffler diagram is sensibly accurate for most 300-series alloys to predict weld behaviour when using conventional welding processes [2]. Figure 4 shows the composition of 16.54, 16.55 and 316LSi plotted on the Schaeffler diagram [19], using the dilution rates derived from Table 3. As can be seen in this figure, the phases present in 16.54 are anticipated to be austenite, ferrite and martensite. The ferrite content of 16.54 is predicted to be 2%. In similar fashion, the expected microstructures for 16.55 are austenite and martensite, whereas the ferrite content is predicted to be zero. The phases present in the 316LSi are expected to be ferrite, austenite and martensite, with a ferrite content of 6%.

Fig. 2 Porosity in dissimilar weldments (a) 16.54^W and (b) 316LSi^W

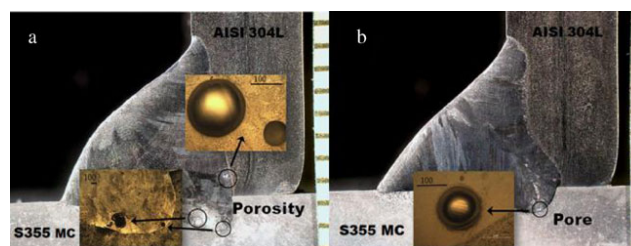


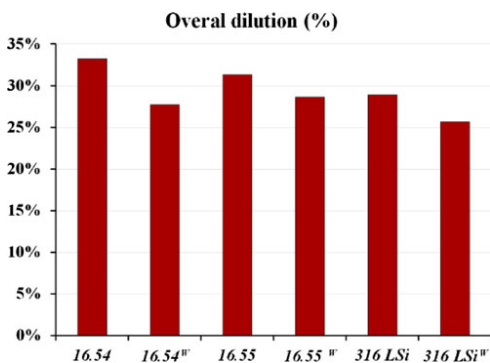
Table 3 Dilution percentage of FMs and BMs in the WM and the overall dilution rate of the WM by substrates

Classification	Wire	S355MC	AISI 304	Overall
16.54	66.77	16.14	17.09	33.23
16.54 ^W	72.28	12.43	15.28	27.72
16.55	68.66	9.83	21.51	31.34
16.55 ^W	71.37	8.32	20.31	28.63
316 LSi	71.12	10.94	17.94	28.88
316 LSi ^W	74.34	6.93	18.73	25.66

3.4 Ferrite number

The FN was volumetrically measured using a standard ferrite scope device. The measurement was done for five selected points located along the sectioned WM and around the weld axis. The maximum, minimum and average values recorded from the measurements are shown in Fig. 5. The figure also presents a comparison of the recorded FNs and the predicted ferrite content derived from the Schaeffler diagram.

The measurements for 16.55 and 16.55^W show the FN to be near to zero, consistent with predictions from the Schaeffler diagram. This is due to the high Ni contents of EO16.55, a strong austenite stabiliser element. Figure 5 shows that for 16.55, 16.55^W and 316LSi^W, the measured FNs are very close to those predicted by the Schaeffler diagram. For 16.54, 16.54^W, the measured FNs are higher than predicted. This may be due to the variations in the welding parameters. Another noticeable point of interest in Fig. 5 is the higher FN found in weldments made using the same filler wires but with the weaving method. One possible explanation may be that faster solidification occurs, since weaving spreads the heat out from the arc and deposits metal over a less concentrated area [15, 18]. The faster the solidification, the less ferrite

**Fig. 3** Overall dilution of the deposited weld by substrates

can be transformed to austenite in the primary ferritic solidification mode.

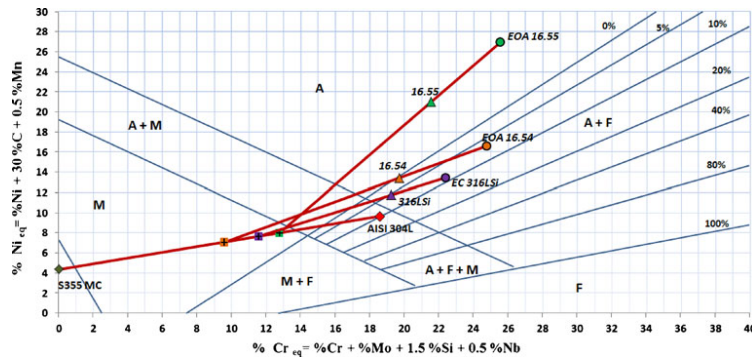
3.5 Microstructure

The connection between solidification behaviour and Cr_{eq}/Ni_{eq} was established by Suutala and Moio [13, 20]. Figure 6 shows the composition of the welding wires plotted on the Suutala and Moio diagram [13, 20] using the shown coefficients of Ni_{eq} and Cr_{eq} . The Ni_{eq} and Cr_{eq} delineate the solidification mode satisfactorily for most conventional 300-series alloys welded under normal arc-welding conditions [13]. This diagram outlines the four solidification types as follows: single-phase austenite (“A”), primarily austenitic with a small fraction of eutectic ferrite (“AF”), primary ferrite with the peritectic/eutectic solidification of austenite (“FA”) and single-phase ferrite (“F”) [13]. From this diagram, the expected solidification mode for EO16.55 is type “A” and for both EO16.54 and EC316LSi, it is “FA.”

Figures 7, 8, 9, 10, 11 and 12 show optical micrographs of the weld between S355MC and AISI 304L made with the different welding wires. In these figures, the bright zones are austenite and the dark zones ferrite, as revealed by the etching for the AISI 304L and welds. Figure 7a, b illustrates the microstructure between 16.54 and the austenitic and ferritic BMs, respectively. Figure 7a shows type “AF” solidification during which a small amount of second-phase ferrite, further away from the fusion line, has formed. The microstructure is quite similar to that of the single-phase austenite, except that ferrite particles are present at the cell boundaries. Some solid-state transformation has also occurred, leaving isolated spheres of ferrite at the cell or dendrite walls [21]. The presence of ferrite stringers in some of the austenite grains within the substrate close to the HAZ can be seen in Fig. 7a. The ferrite stringers have expanded and grown in places close to the fusion boundary. This expansion is most likely due to rapid cooling after the formation of delta ferrite during the heating cycle, which results in a higher amount of ferrite being retained [22].

Figure 7b shows a type “FA” solidified alloy. Adjacent to the fusion line, skeletal (or vermicular) structures of ferrite can be seen. Skeletal ferrite forms when weld cooling rates are moderate and/or when Cr_{eq}/Ni_{eq} is low but still within the “FA” range (see Fig. 6) [21]. Figure 7b also reveals ferrite located at the cell cores in intercellular austenite [21]. During solidification, the development of the austenite phase consumes the ferrite until the ferrite is sufficiently enriched in ferrite-promoting elements and depleted in austenite-promoting elements, stabilising the ferrite at lower temperatures [2]. The presence of a martensite layer adjacent to the weld interface, where the composition varies continuously from that of the ferritic steel to that of the austenitic WM [23], was also detected and is shown in Fig. 7b. At the fusion

Fig. 4 Composition of the base metals, welding wires and weld metals plotted on the Schaeffler diagram, dilution rates are experimentally measured



boundary of the S355MC, the microstructure exhibits a narrow dark line, seen in Fig. 7b. This most likely corresponds to a carburised Cr-rich structure in the austenitic WM [22] adhering to the fusion boundary.

Figure 8a, b shows “FA” solidification with 16.54^W. Lathy ferrite and skeletal ferrite are indicated. Lathy ferrite forms when cooling rates are high and/or when Cr_{eq}/Ni_{eq} increases within the “FA” range. The lathy morphology forms in place of the skeletal morphology as a result of limited diffusion during the ferrite–austenite transformation [2].

Figure 9a presents the microstructure of 16.55 and AISI 304L. Type “A” solidification is apparent. The single-phase austenite cells and dendrites are clearly apparent. This figure shows that the overall appearance of the microstructure is a regular array of austenite cells appearing as a hexagonal mesh, and some of the austenite cells emerge as long parallel dendrites [21].

The microstructure of 16.55 at the ferritic side of the joint with type “FA” solidification is shown in Fig. 9b. The vermicular structure of ferrite dendrites is apparent, and lathy

ferrite can be seen in this figure. Figure 9b also shows the formation of a narrow band of martensite along the weld interface. Additionally, a dark band inside the weld close to the fusion line was detected that could represent a Cr-rich carbide structure.

Figure 10a, b illustrates the microstructure of 16.55^W with type “A” solidification for both the austenitic and ferritic sides; the austenite cells are clearly visible. Figure 10b also depicts the formation of thin martensitic boundaries alongside the weld interface and the formation of a carburised band at the fusion line.

Figure 11 shows the micrograph of 316LSi between S355 MC and AISI 304L with the “FA” solidification mode at the root of the weld. The rather thick layer of martensite formed in the weld deposit along the fusion line makes this micrograph distinctive from the previous

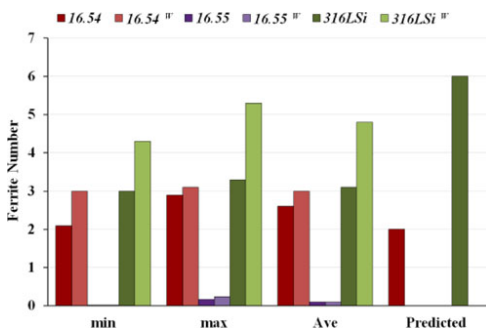


Fig. 5 Ferrite number measured for different weldments and predicted from the Schaeffler diagram

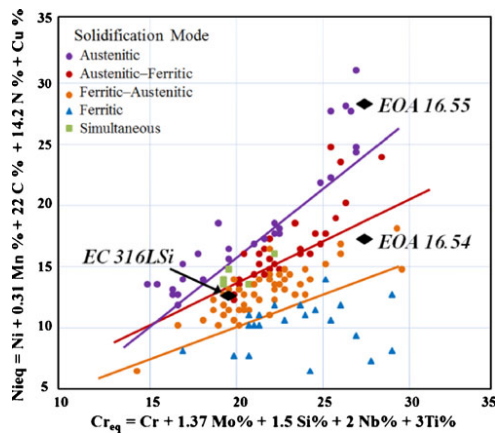


Fig. 6 Composition of welding wires plotted on the Suutala and Moiso diagram [13]

Fig. 7 Optical micrograph of the weld zone: interfaces between the weld and base metals **a** 16.54 and AISI 304L, **b** 16.54 and S355MC

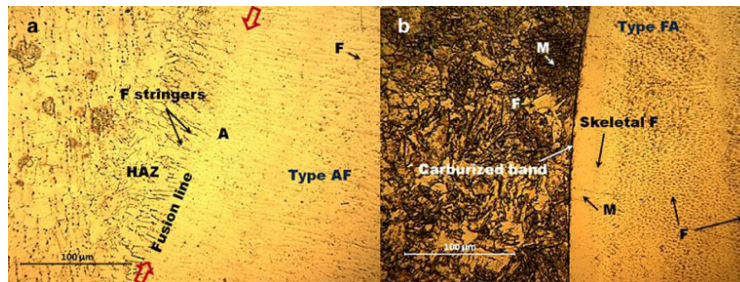
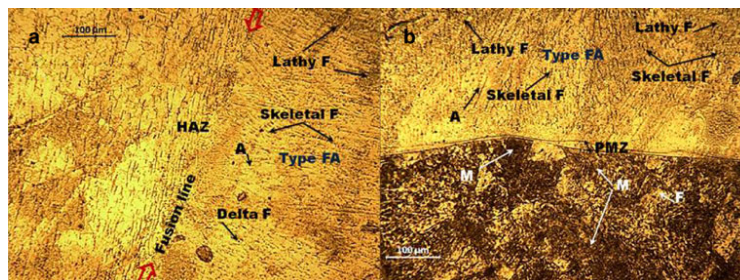


Fig. 8 Optical micrograph of the weld zone: interfaces between the weld and base metals **a** 16.54^W and AISI 304L, **b** 16.54^W and S355MC



micrographs. This thick martensitic structure makes the weld brittle, and, as seen from this figure, some micro-cracks are discernible within this martensitic area.

Figure 12a, b illustrates the microstructure of 316LSi^W with type “FA” solidification; lathy and vermicular ferrite, the two typical ferrite morphologies for this solidification mode, are clearly apparent. The retention of some delta ferrite in the weld is also observable. In Fig. 12b, the formation of a carburized band at the weld interface is visible. A thin band of martensitic structure is also observed along the fusion line and in the weld deposit region.

As can be seen from these results, the predicted microstructures for all the samples are quite consistent with the optical micrograph results. Furthermore, the solidification mode for 16.54^W, 16.55, 16.55^W, 316LSi and 316LSi^W precisely follow the predictions derived from the Suutala and Moisoio approach. However, the expected solidification mode contradicts the observed results for 16.54 on the austenitic side. In addition, the micrographs reveal no obvious relation between the dilution rate and martensite formation. Correspondingly, no effects of the weaving technique on the solidification mode and microstructure are recognisable.

Fig. 9 Optical micrograph of the weld zone: interfaces between the weld and base metals, **a** 16.55 and AISI 304L, **b** 16.55 and S355MC

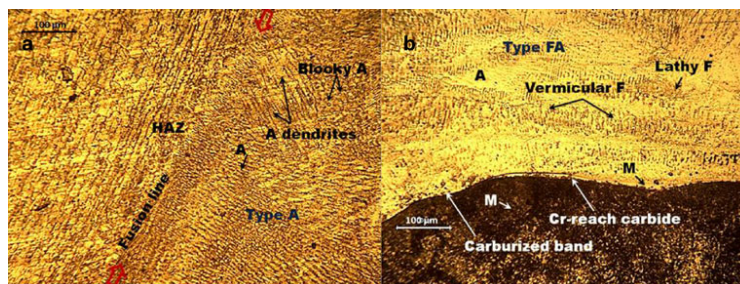


Fig. 10 Optical micrograph of the weld zone: interfaces between the weld and base metals a 16.55^W and AISI 304L, b 16.55^W and S355MC

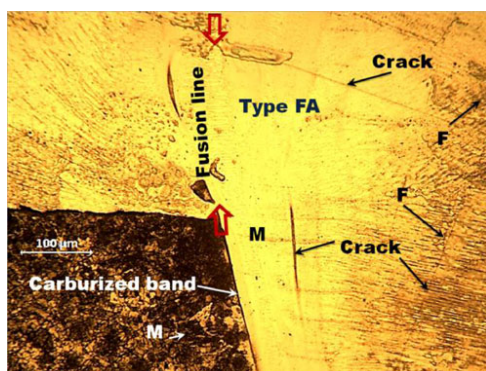
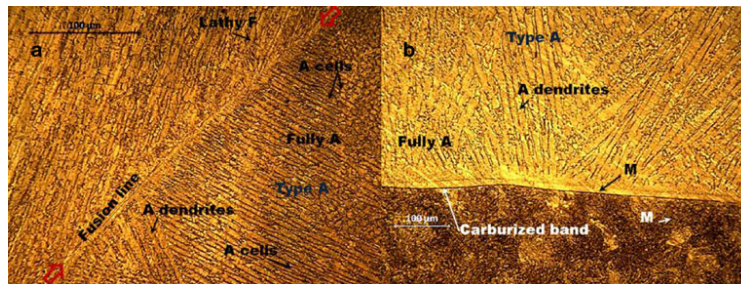


Fig. 11 Optical micrograph of the weld zone: interfaces between the weld and base metals, 316LSi and both AISI 304L and S355MC

microhardness nearly follows the same pattern for both methods with the same welding wire. For all the samples, the hardness of the weld is inferior to that of the AISI 304L base steel, with some exceptional points. This can be attributed to the presence of a higher amount of a strong austenite stabilising element, such as Ni [24].

For 16.54, 16.54^W, 16.55 and 316LSi, there is a large and sharp increase in hardness on the ferritic side adjacent to the weld interface that can be evidence of martensite formation, shown in Fig. 13a, b. These results are consistent with the optical micrograph findings.

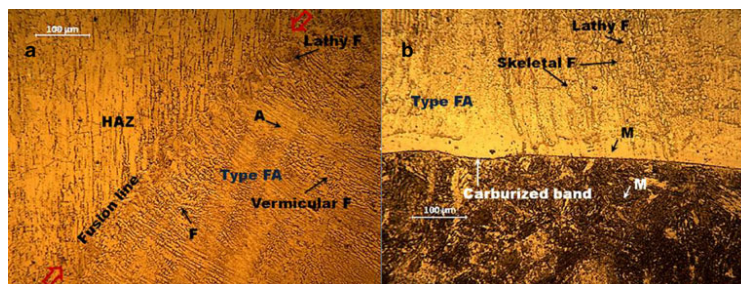
From the predicted ferrite content, microstructure and measured FNs, it can be expected that the hardness values will be the highest for 316LSi, 16.54 and 16.55, respectively, both with and without the use of weaving. As can be seen in Fig. 13, the results are quite consistent with the expectations.

It is claimed that the hardness of the weld metal depends on the amount of substrate dilution [17]. However, for the weld samples in this study, no explicit relation between the dilution ratio and hardness values was distinguished that could indicate low or non-critical dilution in the weld samples. Nevertheless, it seems that the variations in the hardness distribution profiles are smoother with the weaving method than with the string weld samples (Fig. 13a, b). This might be due to the lower dilution of the BMs and the more homogeneous composition of the weld in welds done with weaving.

3.6 Microhardness

The microhardness across the welds was evaluated using a digital Vickers microhardness tester. All hardness indents were made with 500-g force (4.905 N). Figure 13 compares the measured hardness values for welds made with and without the use of weaving. As can be seen from the figure,

Fig. 12 Optical micrograph of the weld zone: interfaces between the weld and base metals, a 316LSi^W and AISI 304L, b 316LSi^W and S355MC



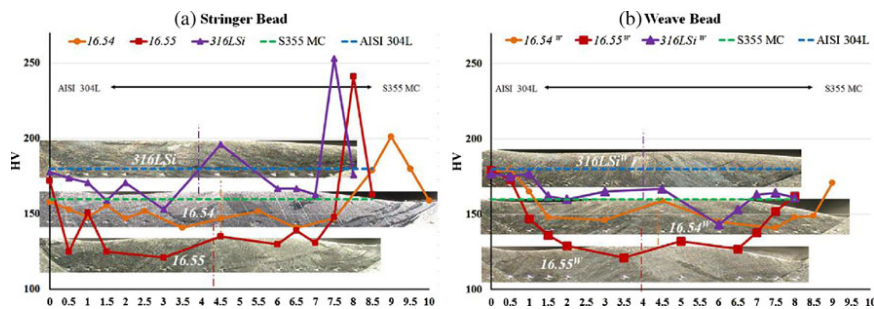


Fig. 13 Comparison of hardness distribution along the weld metals with a stringer and b weave bead, the vertical dotted lines represent the weld centrelines

4 Conclusions

The present study was conducted to investigate influence of different welding wires and torch weaving on the quality, microstructure, and microhardness of fillet weld joints between AISI 304L and S355 MC. The following conclusions are drawn from the present study:

1. Weaving decreased penetration on the S355MC side and increased penetration on the AISI 304L side. The increase in penetration might be due to heat accumulation on the austenitic side because of its lower heat conductivity. In contrast, the decrease in penetration on the S355MC side is probably a result of faster heat dissipation due to weaving and the higher heat conductivity of S355MC.
2. Undercut was detected with 16.55^W and $316LSi^W$. No connection between weaving and the undercut defect was found, and minor undercuts were also detected in the stringer weld.
3. Some pores were found at the weld root of 16.54^W and $316LSi^W$. This porosity may be a result of the lower efficiency of the shielding gas when weaving is used.
4. The measured dilution by the BMs was less when the weaving technique was used compared to the stringer deposit.
5. In general, the measured FNs are very close to those predicted by the Schaeffler diagram, especially for 16.55^W , 16.55^W and $316LSi^W$. Higher FNs were found in the weldments made using the weaving method. This might be a result of faster solidification.
6. All the weld samples, except for 16.54^W , exhibited the presence of a martensitic region adjacent to the fusion boundary on the ferritic side. The presence of microcracks was also discerned within the martensitic structure of the $316LSi$.
7. The predictions derived from the Suutala and Moisoio approach for the solidification mode and the predicted

microstructures from the Schaeffler diagram were quite consistent with the optical micrograph results for all the samples, except for 16.54 on the austenitic side. No obvious relation between the effects of the weaving technique on the solidification mode and the microstructure were recognisable from the microstructural analysis.

8. For 16.54 , 16.54^W , 16.55 and $316LSi$, a sharp increase in hardness was observed on the ferritic side and around the fusion interface, which may reflect the presence of martensite within this region. Based on the microhardness test, no explicit relation between the dilution rate and hardness values was distinguished for the weld samples.

References

1. Hasçalik A, Ünal E, Özdemir N (2006) Fatigue behaviour of AISI 304 steel to AISI 4340. *J Mater Sci* 41:3233–3239
2. Lippold JC, Kotecki DJ (2005) Dissimilar welding of stainless steel. In: *Welding Metallurgy and Weldability of Stainless Steels*. Wiley, New Jersey, pp 287–299
3. Arivazhagan N, Narayanan S, Singh S et al (2012) High temperature corrosion studies on friction welded low alloy steel and stainless steel in air and molten salt environment at 650 °C. *Mater Des* 34:459–468
4. Nascimento MP, Souza RC, Pigatin WL et al (2001) Effects of surface treatments on the fatigue strength of AISI 4340 aeronautical steel. *Int J Fatigue* 23:607–618
5. Arivazhagan N, Singh S, Prak S, Reddy G (2011) Investigation on AISI 304 austenitic stainless steel to AISI 4140 low alloy steel dissimilar joints by gas tungsten arc, electron beam and friction welding. *Mater Des* 32(5):3036–3050
6. Shushan SM, Charles EA, Congleton J (1996) The environment assisted cracking of diffusion bonded stainless steel to carbon steel joints in an aqueous chloride solution. *Corros Sci* 38(5):673–686
7. Celik A, Alsaran A (1999) Mechanical and structural properties of similar and dissimilar steel joints. *Mater Charact* 43(5):311–318
8. Missori S, Koerbe C (1997) Laser beam welding of austenitic–ferritic transition joints. *Welding J* 76(3):125–134
9. Fuentes ALG, Salas R, Centeno L et al (2011) Crack growth study of dissimilar steels (stainless-structural) butt welded unions under cyclic loads. *Procedia Eng* 10:1917–1923

10. DuPont JN, Kiser SD, Lippold JC (2009) Dissimilar welding. In: *Welding Metallurgy and Weldability of Nickel-Base Alloys*. Wiley, New Jersey, pp 327–346
11. ASME Boiler and Pressure Vessel Committee (2007) Code II Part C Specifications for Welding Rods, Electrodes, and Filler Metals. In: *ASME Boiler and Pressure Vessel Code*, ASME, p. 92
12. Sun Z, Ion JC (1995) Laser welding of dissimilar metal combinations. *J Mater Sci* 30:4205–4214
13. Brooks JA, Lippold JC (1993) Selection of wrought austenitic stainless steels. In: *ASM Handbook*, vol 6. ASM International, pp 456–470
14. Committee of Stainless Steel Producers (1979) *Welding of stainless steels and other joining methods*. AISI, pp 4–6
15. Yongjae K, Sehun R (2005) A study of heat input distribution on the surface during torch weaving in gas metal arc welding. *JSME Int J Ser A* 48(3):144–150
16. Davies AC (1993) *The science and practise of welding*. In: *The Practise of Welding*, vol 2. Cambridge University Press, Cambridge, pp 37–121
17. Kearns WH (ed) (1984) *Welding Handbook*, vol 5. AWS, Miami, pp 54–253
18. Klimpel A, Lisiecki A, Klimpe AS et al (2007) Abrasive and erosive wear resistance of GMA metal cored wire cermet deposits. *JAMME* 28(9):565–572
19. Schaeffler AL (1948) Welding dissimilar metals with stainless electrodes. *Iron Age* 162:72
20. Suutala N, Moisio T (1983) The use of chromium and nickel equivalents in considering solidification phenomena in austenitic stainless steels. *The Metals Society*
21. Elmer J, Allen S, Eagar T (1989) Microstructural development during solidification of stainless steel alloys. *Metall Trans A* 20A:1989–2121
22. Naffakh H, Shamanian M, Ashrafizadeh F (2008) Influence of artificial ageing on microstructure and mechanical properties of dissimilar welds between 310 stainless steel and INCONEL 657. *Metall Mater Trans A* 39(10):2403–2415
23. Dupont JN, Kusko CS (2007) Technical note: Martensite formation in austenitic/ferritic dissimilar alloy welds. *Welding J*: pp 51–53
24. Das C, Bhaduri A, Srinivasan G, Shankar V et al (2009) Selection of filler wire for and effect of auto tempering on the mechanical properties of dissimilar metal joint between 403 and 304L(N) stainless steels. *J Mater Process Technol* 209(3):1428–1438

Publication II

Tasalloti, H., Kah, P., and Martikainen, J.

Laser overlap welding of Zn-coated steel on aluminium alloy for patchwork blank applications in the automotive industry

Reprinted with permission from
Reviews On Advanced Materials Science
Vol. 40, pp. 295-302, 2015
© 2015, Advanced Study Center Co. Ltd.

LASER OVERLAP WELDING OF Zn-COATED STEEL ON ALUMINIUM ALLOY FOR PATCHWORK BLANK APPLICATIONS IN THE AUTOMOTIVE INDUSTRY

H. Tasalloti, P. Kah and J. Martikainen

Lappeenranta University of Technology, P. O. Box 20, 53851 Lappeenranta, Finland

Received: December 12, 2015

Abstract. The new generation of cars have to fulfil the strict regulations regarding fuel consumption and gas emission. Thus, lightweight structures are becoming an increasingly critical target in the car body design. At the same time, other indispensable design obligations, such as safety, ride quality and affordability, also have to be met. Tailor welded blank (TWB) and welded patchwork blank techniques have been extensively used in the automotive industry as an effective way of weight reduction and stiffness improvement. TWBs facilitate further weight and strength optimisation in design by integrating sheets of different materials with different thicknesses and/or coatings into one part. Local reinforcement with welded patchwork blanks also contributes to the weight reduction and crashworthiness of the car body. The laser welding of tailored and patchwork blanks made of galvanised steel and aluminium is widely used in the automotive industry. The weld between Zn-coated steel and aluminium commonly suffers from defects such as spatter, cavity and crack. The vaporisation of Zn is commonly known as the main source of instability in the weld pool and cavity formation, especially in a lap joint configuration. Cracks are mainly due to the brittle intermetallic compounds growing at the weld interface of aluminium and steel. This study provides a review on the main metallurgical and mechanical concerns regarding laser overlap welding of Zn-coated steel on Al-alloy and the methods used by researchers to avoid the weld defects related to the vaporisation of Zn and the poor metallurgical compatibility between steel and aluminium.

1. INTRODUCTION

Automakers around the world have focused their efforts on developing cars with lightweight structures to reduce the energy consumption and environmental impact of vehicles. In 1964 the concept of tailor welded blank (TWB) was introduced to the automotive industry, as a new way of manufacturing body panels, in order to reduce the weight of structures and improve the body stiffness [1,2]. TWBs enable designers to include different sheets of different thicknesses and material characteristics into one part, prior to forming, to optimise their design for weight and strength [3].

TWBs became more attractive to the automotive industry when the laser welding process was introduced in the 1980s [2–4]. The significant advancements in laser sources and systems, over the past few decades, have evolved laser welding to an indispensable manufacturing process in the automotive industry [2,5,6]. Laser welding has been increasingly used for tailored blank applications because of its benefits such as high welding speed, high precision, low heat input and ease of automation [6–10]. CO₂ and Nd:YAG laser were traditionally the welding processes mainly used for TWB applications [3]. However, over the past few years, fibre laser has evolved as the automakers' prime

Corresponding author: H. Tasalloti, e-mail: hamed.tasalloti.kashani@lut.fi

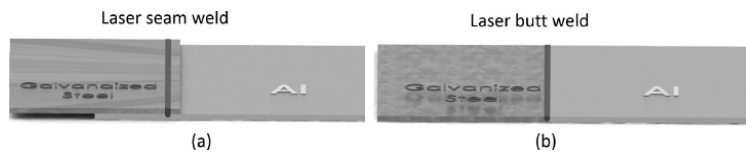


Fig. 1. Schematic of (a) laser welded patchwork blank and (b) laser welded tailored blank.

choice for welding applications because of its high power, excellent beam quality and high energy efficiency [2,11,12].

Galvanised steels have been extensively used in exposed car body panels to increase corrosion resistance [13,14]. The thickness of zinc-coating, in galvanised steels, is usually less than 10 μm on each side of the steel. Occasionally, steels with a coating thicker than 20 μm have been used for improved protection [15,16]. Currently, laser butt and lap welding of Zn-coated steels are broadly used in the automotive industry for tailored and patchwork blank applications [15–18].

The vaporisation of Zn due to its low boiling temperature (906 $^{\circ}\text{C}$) is the main issue reported during the laser welding of galvanised steel. The vaporisation is particularly problematic in lap joint setups because of the restriction of Zn vapour venting [3,13,14]. The intense pressure of Zn vapour within the keyhole can cause an unstable and violent flow of the melting pool, resulting in the formation of spatter, cavities and craters [19–21].

TWBs of aluminium alloy and Zn-coated steel have been considered as a cost-effective solution to the car body mass reduction and to the increase of the structure strength [8]. Galvanised steels are also used for reinforcement purposes in patchwork blanks [2]. The laser welding of Zn-coated steel to Al has been studied by many researchers [13,14,17,22]. However, it is still very difficult to achieve a defect-free and high-strength weld. The difficulties arise from the differences in the thermo-physical properties of the two base metals and the formation of brittle intermetallic compounds (IMCs) because of poor miscibility and solubility of steel and aluminium.

Brittle IMCs can reduce the weld strength by inducing cracking in the weld [23]. In the current study, the above-mentioned challenges are explained and their effects on the weld quality and strength are discussed. This study also provides an overview of the approaches proposed by different researchers to minimise the adverse effects of the pre-mentioned challenges and to improve the strength and quality of the weld between galvanised steel and Al alloy.

2. TAILOR WELDED BLANKS AND PATCHWORK BLANKS

Tailor welded blanks (TWBs) are made of two or more sheet metals, with different thicknesses, shapes, mechanical properties and/or coatings that are butt-welded together prior to forming [2,24,25]. TWBs are increasingly used with rather complex designs to minimise the weight and to optimise the engineering properties and cost of car body panels [3,6,26]. Another type of tailored blank is called patchwork blank which is commonly used for local reinforcement applications in the auto-body structures. A welded patchwork blank is made of one or more pieces of reinforcing sheet metal (patches) lap-welded onto the mainsheet. A comparison between laser welded patchwork and tailored blanks is schematically shown in Fig. 1.

Currently, laser welding is the most often used welding process for TWBs and welded patchwork blanks [24,25,27]. Some of the various applications of TWBs and patchwork blanks include the reinforcement of rails and pillars, inner door panels, cross-rail bumpers, floor panels and wheel housings [2,24,28]. The main applications of TWBs and patchwork blanks are illustrated in Fig. 2.

3. LASER LAP WELDING OF Zn-COATED STEEL ON AL ALLOY

To increase the corrosion resistance and durability of car body panels, Zn-coated steel sheets, galvanised or galvanealed, are increasingly used in the automotive industry [30]. The demand for environmentally friendly cars has made the manufacturers to reduce the overall weight of the vehicles. For this purpose, steel parts in the car body structures are progressively replaced with Al alloys [31]. However, making an all-aluminium car may not be a feasible solution due to the affordability concerns and because of the poor formability and insufficient fracture resistance of Al products [8,32,33]. The combination of Zn-coated steel and Al is a promising alternative to meet the design requirements in terms of safety, pollution and cost. Recently, the lap welding of Zn-coated steel on Al has been com-

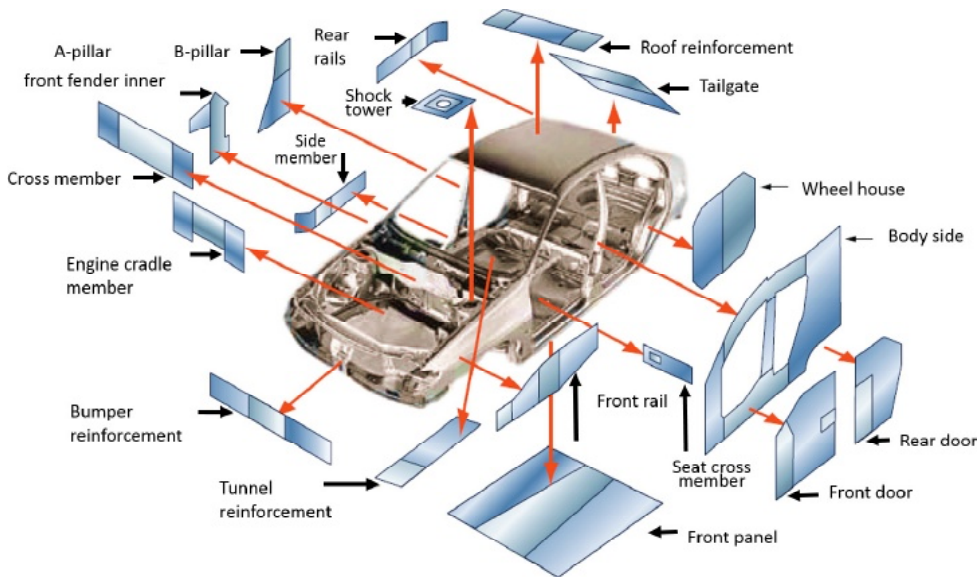


Fig. 2. The main applications of tailor welded blanks and patchwork blanks in a car-body, reprinted with permission from ArcelorMittal Tailored Blanks, Merelbeke, Belgium, www.arcelormittal.com.

monly used for the manufacture of car doors [10,15]. Laser welding is the most preferred process in the automotive industry because of its high speed, low heat input and ease of interface with robots [15,30].

Laser has been studied by many researchers for overlap welding of Zn-coated steels with Al alloys [13,14,17,22] or un-coated steel on Al alloys [7,32,34–39]. Despite successful achievements in the laser welding of Zn-coated steel on Al in lap joint setup, producing a defect-free weld can be still very challenging, especially under high welding speeds [8]. The formation of defects, such as porosity, spatter and the brittle intermetallic compound (IMC) layer at the weld interface are the main issues concerning the laser welding of Zn-coated steel on Al alloy [32,40,41].

During the laser welding of Zn-coated steel on Al, Zn vapour causes instability in the melting pool, resulting in spatter, porosity and crater defects [19–21]. The vaporisation of Zn is almost inevitable because the boiling point of Zn (906 °C) is considerably lower than that of Al (2520 °C) and Fe (1538 °C) [8].

Different approaches have been suggested in the literature to reduce the porosity occurring in the laser lap welding of Zn-coated steels. Milberg et al. [13] proposed the use of a bi-focal hybrid laser which combines an Nd:YAG laser with a high power diode laser to increase the robustness of laser welding.

Pre-drilling vent holes along the welding line was suggested by Chen et al. [15] and Gualini et al. [42]. Chen et al. [15] claimed that the vent hole method allowed a proper outflow of Zn vapour. Moreover, a considerably strong weld was produced by the riveting mechanism. The rivet-shaped weld produced in this experiment can be seen in Fig. 3.

Li et al. studied the use of a commercial purity Al foil between the frying surfaces of Zn-coated steel.

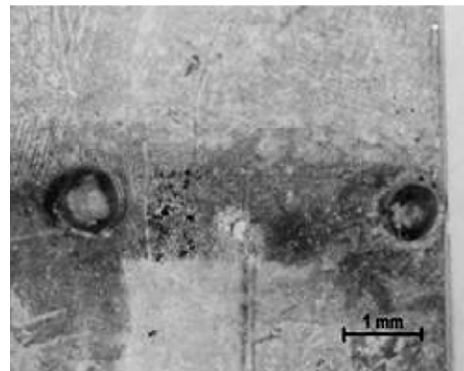


Fig. 3. Laser lap-welded sheets using vent hole produced rivet-shaped welds (welding parameter: 1.5 kW CO₂ laser, 7.62 m/min), reprinted with permission from W. Chen, P. Ackerson and P. Molian // *Mater. Des.* 30 (2009) 245, (c) 2009 Elsevier.

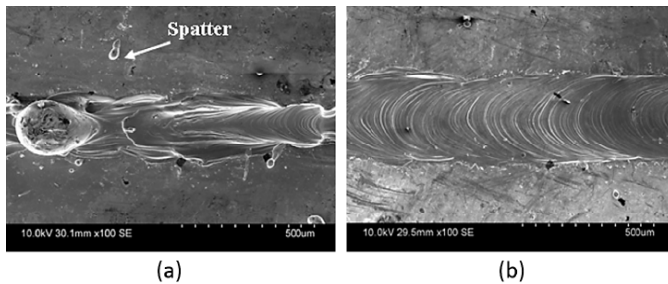


Fig. 4. Comparison between weld appearances produced from (a) a single pass and (b) double pass fibre laser welding with N_2 shielding gas, (first pass welding parameters: 650 W, 100 mm/s, f.p.p. of 0 mm, second pass welding parameters: 200 W, 75 mm/s, f.p.p. of +2 mm), reprinted with permission from H.C. Chen, A. J. Pinkerton, L. Li, Z. Liu and A.T. Mistry // *Mater. Des.* 32 (2011) 495, (c) 2011 Elsevier.

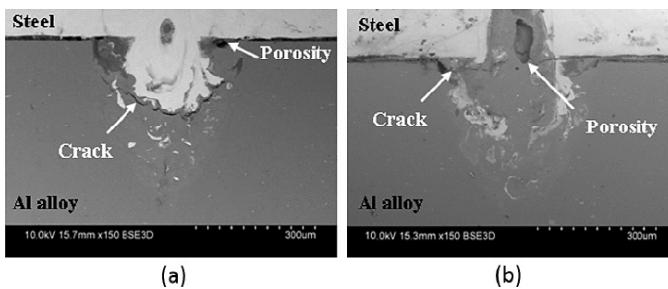


Fig. 5. Backscattered electron image of the cross-section of the weld made using laser double pass welding with (a) Ar gas and (b) N_2 gas, (first pass welding parameters: 650 W, 100 mm/s, f.p.p. of 0 mm, second pass welding parameters: 200 W, 75 mm/s, f.p.p. of +2 mm), reprinted with permission from H.C. Chen, A. J. Pinkerton, L. Li, Z. Liu and A.T. Mistry // *Mater. Des.* 32 (2011) 495, (c) 2011 Elsevier.

They used Al foil as a process stabiliser in high-speed keyhole welding. The test was based on the hypothesis that the reaction between Al and Zn prevents the evaporation of Zn by forming Al-Zn which has a higher boiling point than Zn and remains in the crevice. It was claimed that the addition of Al foil resulted in a considerable improvement in the stability of welding and a significant reduction in porosity [14].

Amo et al. [20] and Graham et al. [43] proposed keeping a gap between the surfaces to be welded to let the evaporated Zn escape from the gap. Amo et al. [20] reported a successful weld without any cracks or porosities, using a gap opening of no more than 0.1 mm. However, this method may not be proper for production environments [30].

Chen et al. [10] tried the use of double pass laser welding with a defocused beam. Welding was performed in the first pass with a focused laser beam, and then a defocused beam was applied for the second pass. Double pass welding was performed using either Ar or N_2 as a shielding gas. The weld pool was reported unstable and spatter was

observed with both the Ar and N_2 gases. According to this experiment, applying a second pass weld with a defocused laser beam improved the weld appearance, shown in Fig. 4.

A higher risk of porosity has been found to exist when a higher density gas is used, because the gas is more likely of being trapped in the keyhole and the weld after solidification [44]. However, Chen et al. [10] reported porosity and crack in the weld produced with double pass laser welding using either N_2 or Ar gas, without any obvious relation between the type of gas used and the porosity found in the weld samples, seen from Fig. 5.

Ma et al. [8] proposed two-pass laser welding for producing a lap joint between Zn-coated high-strength steel and Al alloy. For the first pass, they used a defocused laser beam to preheat the components and to partially melt and vaporise the zinc coating of the galvanised steel sheet. Then, welding was performed with a focused beam in the second pass. They reported that a defect-free lap joint with partial penetration was produced with the use of two-pass laser welding. They also stated that the

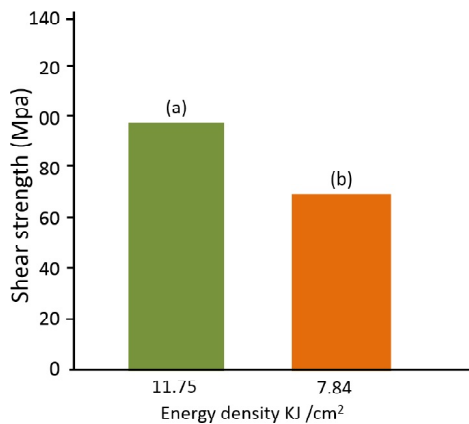


Fig. 6. Shear strength of the laser welded lap joint between low-carbon galvanised steel and AA2024 aluminium alloy using fibre laser (spot diameter: 13 mm, power density: 4.52 kW/cm², (a) travel speed: 0.3 m/min, (b) travel speed: 0.45 m/min), reprinted with permission from S. Meco // Int. J Adv. Manuf. Technol. 67 (2013) 647, (c) 2012 Springer.

process was very stable and almost no spatter, crack or blowholes were present in the welds.

As was mentioned before, another concern in welding Al and steel is the growth of brittle Fe–Al intermetallic compounds (IMCs) within the welds as a result of poor solid solubility of the Fe element in Al [7,31,34]. IMCs consist of ductile Fe-rich and brittle Al-rich phases. FeAl and Fe₃Al belong to Fe-rich phases, whereas Al-rich phases include FeAl₂, Fe₂Al₅, FeAl₃, and Fe₇Al₁₃ [35,45–47]. Brittle Al-rich IMCs have a deteriorative effect on the mechanical performance of the weld and can induce cracks within the fusion zone [31]. The type and morphology of IMCs are highly dependent on the type of steel and aluminium alloy; even small variations in the melting temperature, the fluidity of the molten pool, solute diffusivity and thermal conductivity can affect the kinetics of intermetallic phase formation [32].

Ozaki et al. [45] proposed laser roll welding to reduce the effect of IMCs. This method combines a CO₂ laser and a roller compressing the facing surfaces of the Al alloy and Zn-coated steel to be welded. The idea behind this technique was to minimise the formation of brittle IMCs by shortening the heat cycle and increase the heat transfer rate between the contacting surfaces under pressure. They produced a weld with a maximum shear strength of 162 N/mm when the welding speed was 8.3 mm/s and the roller pressure was set to 150 MPa. They also reported that the shear strength

declines when the thickness of the IMC layer exceeds 10 μm. It has also been reported that when the thickness of the IMC layer is less than 10 μm the specimen under a shear test fails in the base, not in the weld [45,48,49].

Meco et al. [31] studied the use of fibre laser for the conduction welding of Al to Zn-coated steel in overlap configuration. They stated that using conduction mode laser welding enabled them to control the heat input and thereby control IMC formation. They also reported that shear strength in the Zn-coated steel and Al joint was higher when a higher energy density was used, seen in Fig. 6. This could be contrary to the assumption that a higher heat input can increase the formation of IMCs and cause degradation in the mechanical strength of the weld [10]. They concluded that mechanical strength is not solely dependent on the thickness of the IMC layer. Instead, a combination of the intermetallic layer thickness and its composition, the orientation of IMCs, as well as bonding and diffusion between the elements can affect the mechanical strength [31].

Chen et al. [10] reported a considerable reduction in IMCs as a result of using N₂ shielding gas in the fibre laser welding of Zn-coated steel on Al alloy. They also noticed lower variations in hardness in the fusion zone when N₂ gas was used which can also indicate less IMC formation. They stated that a higher shear strength was obtained with N₂ gas than with Ar, observable in Fig. 7. This can be attributed to the higher thermal conductivity of N₂ compared to Ar that can increase the cooling rate of the melt pool during laser welding. The increased cooling rate can reduce the extent of heat flow and diffusion activity in the melt pool. Thus, the base materials will be mixed in a limited degree and the growth of IMCs will be obstructed, leading to even more hardness distribution and improved shear strength [50]. The reactivity of N₂ plasma with Al can also be beneficial in limiting the extent of Al-rich intermetallic phases, particularly in laser keyhole welding. The reaction between the vaporised Al and ionised N₂ leads to the formation of aluminium nitride AlN [10,44–51] in the weld in place of Fe–Al intermetallics [10].

Ma et al. [8] claimed that controlled preheating and welding parameters during double-pass laser welding of Zn-coated steel and Al, can limit the thickness of Al-rich IMCs to around 5 μm. They found that too much heat input during preheating can entirely remove the Zn-coating which makes the weld prone to the formation of a Fe–Al layer. They declared that a lower heat input during the welding process

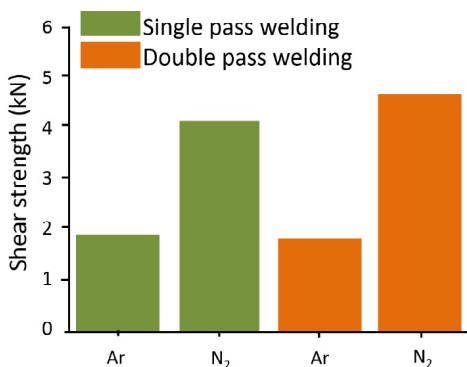


Fig. 7. Comparison between the effect of Ar and N₂ shielding gases on the shear strength of the laser welded lap joint of Zn-coated steel (DX54) and Al alloy (5754), using either single pass or double pass fibre laser (first pass welding parameters: 650 W, 100 mm/s, f.p.p. of 0 mm, second pass welding parameters: 200 W, 75 mm/s, f.p.p. of +2 mm), reprinted with permission from H.C. Chen, A. J. Pinkerton, L. Li, Z. Liu and A.T. Mistry // *Mater. Des.* 32 (2011) 495, (c) 2011 Elsevier.

resulted in a higher shear strength. They also claimed that the presence of Zn in the IMCs could improve the strength of the welded lap joint between Zn-coated steel and Al.

Corrosion resistance is a principal requirement of the welded joint between Zn-coated steel and Al. The corrosion resistance of the weld can be mainly affected by microsegregation, the growth of intermetallic phases, loss of Zn due to vaporisation and defects [52,53]. The degradation of corrosion performance can occur within the fusion and heat-affected zones due to intergranular corrosion and segregation or the growth of a secondary phase [10,53,54]. It is known that inert gases with a higher density can provide better protection over the melt pool against oxidation and loss of alloying elements [15]. It has been reported that weld samples made with Ar shielding gas showed better corrosion resistance than with N₂ gas [10]. This can be due to the higher density of Ar that protected the base metals more efficiently against oxidation [10]. Generally, the prevention of the weld defects and smoothness of the weld surface can be considered as an effective way to improve the corrosion resistance of the weld [10,53,55].

4. CONCLUSIONS

In this study the application of tailor welded blanks (TWBs) and patchwork blanks in the weight reduc-

tion and reinforcement of car-body panels was explained. The main issues associated with the laser lap welding of zinc-coated steel on aluminium, which is commonly used in patchwork blank applications for the manufacture of car bodies were discussed and different approaches presented in the literature to avoid these issues were reviewed. The main conclusions are:

Pre-drilling vent holes along the welding line can let the Zn vapour to escape and eliminate the risk of porosity in the weld. Keeping a gap between the surfaces to be welded can be another solution for venting Zn vapour. A more practical solution would be using a defocused laser beam to partially remove the Zn layer and to preheat the top surface, followed by second-pass welding with a focused laser beam.

Higher heat input can expedite the growth of brittle intermetallic compounds (IMCs). Generally, a higher mechanical strength of welds has been achieved when the thickness of the brittle IMC layer has been less than 10 µm. Besides the thickness of the IMC layer, other factors such as the composition and orientation of IMCs, as well as bonding and diffusion between the elements may be determining the weld strength. Double pass welding with optimised parameters for preheating and welding can be a workable solution to the formation of a brittle IMC layer.

The use of N₂ as a shielding gas can have beneficial effects as to the formation of brittle IMCs, thereby improving the weld strength. This may be due to the higher thermal conductivity of N₂ compared to Ar as well as the likeliness of reaction between N₂ plasma and Al vapour to form aluminium nitride instead of Al-rich IMCs.

The type of shielding gas can have influence on the corrosion resistance of the weld. Inert gases with higher density can protect the molten pool against oxidation which may benefit the corrosion resistance performance of the weld.

REFERENCES

- [1] M. Ono, A. Yoshitake and M. Omura // *Weld. Intern.* **18(10)** (2004) 777.
- [2] V.C. Eva and V.G. Joaquín, In: *Structural Connections for Lightweight Metallic Structures*, ed. by Pedro M.G.P. Moreira, Lucas F. M. da Silva, Paulo M.S.T. de Castro (Berlin, Springer, v. 8, 2012), p. 59.
- [3] U. Reisgen, S. Markus, O. Mokrov and A. Essam // *Appl. Surf. Sci.* **257** (2010) 1401.
- [4] W.W. Duley, *Laser Welding* (Wiley Interscience, Toronto, 1999).

- [5] J.C. Ion, *Laser Processing of Engineering Materials: Principles, Procedure and Industrial Application* (Oxford, Elsevier Butterworth-Heinemann, 2005).
- [6] M. Spöttl and H. Mohrbacher // *Adv. Manuf.* **2** (2014) 193.
- [7] M.J. Torkamany, S. Tahamtan and J. Sabbaghzadeh // *Mater. Des.* **31** (2010) 458.
- [8] J. Ma, M. Harooni, B. Carlson and R. Kovacevic // *Mater. Des.* **58** (2014) 390.
- [9] Y.W. Park, H. Park, S. Rhee and M. Kang // *Opt. Laser. Techno.* **34** (2002) 135.
- [10] H.C. Chen, A.J. Pinkerton, L. Li, Z. Liu and A.T. Mistry // *Mater. Des.* **32** (2011) 495.
- [11] F. Vollertsen and C. Thomy, In: *ICALEO 2005 – 24th International Congress on Applications of Laser and Electro-Optics* (Miami, Florida, USA, 2005), p. 254.
- [12] F. Vollertsen // *Adv. Mater. Res.* **6–8** (2005) 59.
- [13] J. Milberg and A. Trautmann // *Prod. Eng. Res. Devel.* **3 (1)** (2009) 9.
- [14] X. Li, S. Lawson, Y. Zhou and F. Goodwin // *J. Laser Appl.* **19** (2007) 259.
- [15] W. Chen, P. Ackerson and P. Molian // *Mater. Des.* **30** (2009) 245.
- [16] K.R. Ayres and P.A. Hilton // *Weld. Met. Fabr.* **62** (1994) 10.
- [17] R. Fabbro, F. Coste, D. Goebels and M. Kielwasser // *J. Phys. D. Appl. Phys.* **39** (2006) 401.
- [18] S.T. Riches // *Weld. Met. Fabr.* **61** (1993) 79.
- [19] H.C. Chen, A.J. Pinkerton, L. Li and A.T. Mistry, In: *ICALEO 2009 – Proceedings of the 28th International Congress on Applications of Lasers and Electro-optics* (Orlando, Florida USA, 2009), p. 104.
- [20] J.M. Amo, J. Duran, J. Chao and J. Fernandez-Saez // *J. Mater. Sci.* **31** (1996) 6595.
- [21] A.K. Dasgupta, J. Mazumder and P. Li // *J. Appl. Phys.* **102** (2007) 053108.
- [22] Y.F. Tzeng // *Int. J. Adv. Manuf. Technol.* **16** (2000) 10.
- [23] J.J. Ding, H.J. Huang, P. Peyre and R. Fabbro // *Mater. Manuf. Processes.* **21** (2006) 59.
- [24] K. Lamprecht, M. Merklein and M. Geiger, In: *Numerical Simulation of 3D Sheet Metal Forming Processes: 6th International Conference and Workshop on Numerical Simulation of 3D Sheet Metal Forming Processes* (Detroit, Michigan, USA, 2005), p. 526.
- [25] M. Merklein, J. Maren, M. Lechner and A. Kuppert // *J. Mater. Process. Tech.* **214** (2014) 151.
- [26] H. Mohrbacher, In: *Proceedings of the International Conference Sheet Metal* (Leuven, Belgium, 2001), p. 305.
- [27] B.A. Behrens and K. Dilger // *Journal for Technology of Plasticity.* **35(1–2)** (2010) 1.
- [28] H. Karbasian and A.E. Tekkaya // *J. Mater. Process. Tech.* **210** (2010) 2103.
- [29] *ArcelorMittal*, [Online]. Available: <http://automotive.arcelormittal.com>. [Accessed December 2014].
- [30] C. Dharmendra, K.P. Rao, J. Wilden and S. Reichb // *Mater. Sci. Eng. A.* **528** (2011) 1497.
- [31] S. Meco, G. Pardal, S. Ganguly, R.M. Miranda and L. Quintino // *Int. J. Adv. Manuf. Technol.* **67** (2013) 647.
- [32] K.J. Lee, S. Kumai, N. Ishikawa and K. Furuya, In: *ICAA-10 – 10th International Conference on Aluminium Alloys* (Vancouver, Canada, 2006), p. 1847.
- [33] A. Mathieua, R. Shabadib, A. Deschampsb, S. Michel, S. Mattei, D. Grevey and E. Cicala // *Opt. Laser. Techno.* **39** (2007) 652.
- [34] G. Sierra, P. Peyre, F. Deschaux-Beaume, D. Stuart and et.al // *Mater. Sci. Eng. A. Struct. Mater. Prop. Microstruct. Process.* **447** (2007) 197.
- [35] K.J. Lee and S. Kumai // *Mater. Trans.* **47** (2006) 1178.
- [36] T. Takemoto, S. Kimura, Y. Kawahito, H. Nishikawa and et.al // *Weld. Int.* **23** (2009) 316.
- [37] K.J. Lee, S. Kumai and T. Arai // *Mater. Trans.* **46** (2005) 1847.
- [38] M. Kreimeyer, F. Wagner and G. Sepold, In: *ICALEO 2004 – 23rd International Congress on Applications of Laser and Electro-Optics* (San Francisco, USA, 2004).
- [39] S. Yan, Z. Hong, T. Watanabe and T. Jingguo // *Opt. Lasers. Eng.* **48** (2010).
- [40] H. Laukant, C. Wallmann, M. Korte and U. Glatzel // *Adv. Mater. Res.* **6–8** (2005) 163.
- [41] Y.C. Chen, T. Komazaki, T. Tsumura and K. Nakata // *Mater. Sci. Technol.* **24** (2008) 33.
- [42] M.M.S. Gualini, S.A. Mehmood and I. Awan, In: *ICALEO 2002 – 21st International Congress on Applications of Laser and Electro-Optics* (Orlando, Florida, United States, 2002), p. 1829.

- [43] M.P. Graham, H.W. Kerr and D.C. Weckman // *Proc. SPIE. Int. Soc. Opt. Eng.* **2703** (1996) 170.
- [44] S. Katayama, H. Nagayama, M. Mizutani and Y. Kawahito // *Weld. Int.* **23** (2009) 744.
- [45] H. Ozaki, M. Kutsuna, S. Nakagawa and K. Miyamoto // *J. Laser. Appl.* **22 (1)** (2010) 1.
- [46] M.J. Rathod and M. Kutsuna // *Weld. J.* **83** (2004) 16.
- [47] S. Katayama, J. Sung-Min, M. Mizutani and B. Han-Sur // *Mater. Sci. Forum.* **502** (2005) 481.
- [48] J. Bruckner // *Weld. J.* **84 (6)** (2005) 38.
- [49] K. Furukawa // *Welding Technology.* **53 (8)** (2005) 94.
- [50] R. Borrisutthekul, T. Yachi, Y. Miyashita and Y. Mutoh // *Mater. Sci. Eng. A.* **467** (2007) 108.
- [51] P. Visuttipitukul, T. Aizawa and H. Kuwahara // *Mater. Trans. JIM.* **42 (7)** (2003) 1412.
- [52] S. Kodama, Y. Ishida, K. Asai, M. Mizumoto, T. Namekata and H. Nagasaki // *Weld. World.* **54(1-2)** (2010) 42.
- [53] C.T. Kwok, S.L. Fong, F.T. Cheng and H.C. Man // *J. Mater. Process. Technol.* **176** (2006) 168.
- [54] V.S. Sastri, E. Ghali and M. Elboudjaini, In: *Corrosion Prevention and Protection: Practical Solutions* (Chichester, UK, John Wiley & Sons, 2007), p. 290.
- [55] X.J. Yan, D.Z. Yang and X.P. Liu // *Mater. Charact.* **58** (2007) 623.

Publication III

Tasalloti Kashani, Hamed, Kah, Paul, and Martikainen, Jukka.
Laser overlap welding of zinc-coated steel on aluminum alloy

Reprinted with permission from
Physics Procedia
Vol. 78, pp. 265-271, 2015
© 2015, Elsevier B.V.



Available online at www.sciencedirect.com

ScienceDirect

Physics Procedia 78 (2015) 265 – 271

Physics

Procedia

15th Nordic Laser Materials Processing Conference, Nolamp 15, 25-27 August 2015,
Lappeenranta, Finland

Laser overlap welding of zinc-coated steel on aluminum alloy

Hamed Tasalloti Kashani* , Paul Kah, Jukka Martikainen

Lappeenranta University of Technology, P. O. Box 20, 53851 Lappeenranta, Finland

Abstract

Local reinforcement of aluminum with laser welded patches of zinc-coated steel can effectively contribute to crashworthiness, durability and weight reduction of car body. However, the weld between Zn-coated steel and aluminum is commonly susceptible to defects such as spatter, cavity and crack. The vaporization of Zn is commonly known as the main source of instability in the weld pool and cavity formation, especially in a lap joint configuration. Cracks are mainly due to the brittle intermetallic compounds growing at the weld interface of aluminum and steel. This study provides a review on the main metallurgical and mechanical concerns regarding laser overlap welding of Zn-coated steel on Al-alloy and the methods used by researchers to avoid the weld defects related to the vaporization of Zn and the poor metallurgical compatibility between steel and aluminum.

© 2015 The Authors. Published by Elsevier B.V. This is an open access article under the CC BY-NC-ND license (<http://creativecommons.org/licenses/by-nc-nd/4.0/>).

Peer-review under responsibility of the Lappeenranta University of Technology (LUT)

Keywords: automotive industry; tailor welded blank (TWB); laser welded patchwork blanks; lightweight structure; Zn-coated steel; galvanized steel; aluminium alloy; dissimilar weld

1. Introduction

Automakers around the world have focused their efforts on developing cars with lightweight structures to reduce the energy consumption and environmental impact of vehicles. In 1964 the concept of tailor welded blank (TWB) was introduced to the automotive industry, as a new way of manufacturing body panels, in order to reduce the weight of structures and improve the body stiffness (Ono et al. 2004), (Eva et al. 2012). TWBs enable designers to include different sheets of different thicknesses and material characteristics into one part, prior to forming, to optimize their

* Corresponding author. Tel.: +358 294 462 111; fax: +358 5 411 7201.

E-mail address: hamed.tasalloti.kashani@lut.fi

design for weight and strength (Reisgen et al. 2010). Patchwork blank is a variation of tailored blank which is commonly used for local reinforcement applications in the auto-body structures. A welded patchwork blank is made of one or more pieces of reinforcing sheet metal (patches) lap-welded onto the mainsheet. The potential applications of TWBs and patchwork blanks are illustrated in Fig. 1.

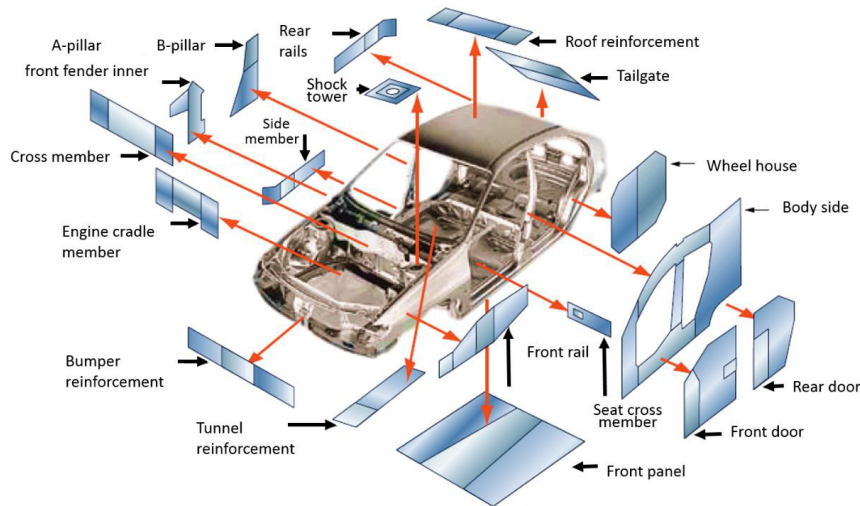


Fig. 1. The main applications of tailor welded blanks and patchwork blanks in a car body, reprinted with permission from ArcelorMittal Tailored Blanks, Merelbeke, Belgium, www.arcelormittal.com.

Laser welding is the most preferred process for tailored blank applications because of its high welding speed, high precision, low heat input and ease of interface with robots (Spöttl et al. 2014), (Torkamany et al. 2010), (Ma et al. 2014), (Park et al. 2002), (Chen et al. 2011), (Dharmendra et al. 2011), (Chen et al. 2009). CO₂ and Nd:YAG laser were traditionally the welding processes mainly used for TWB applications (Reisgen et al. 2010). However, over the past few years, fiber laser has evolved as the automakers' prime choice for welding applications because of its high power, excellent beam quality and high energy efficiency (Eva et al. 2012), (Vollertsen et al. 2005), (Vollertsen 2005). TWBs of aluminum alloy and Zn-coated steel have been considered as a cost-effective solution to the car body mass reduction and to the increase of the structure strength and durability (Ma et al. 2014), (Milberg et al. 2009), (Li et al. 2007). Galvanized steels have been extensively used in exposed car body panels to increase corrosion resistance (Milberg et al. 2009), (Li et al. 2007), (Fabbro et al. 2006). Galvanized steels are also used for reinforcement purposes in patchwork blanks (Eva et al. 2012). The thickness of zinc-coating, in galvanized steels, is usually less than 10 μm on each side of the steel. Occasionally, steels with a coating thicker than 20 μm have been used for improved protection (Chen et al. 2009), (Ayres et al. 1994). Recently, the lap welding of Zn-coated steel on Al has been commonly used for the manufacture of car doors (Chen et al. 2009). The vaporization of Zn due to its low boiling temperature (906 °C) is the main issue reported during the laser welding of galvanized steel. The vaporization is particularly problematic in lap joint setups because of the restriction of Zn vapor venting (Reisgen et al. 2010), (Milberg et al. 2009), (Li et al. 2007). The intense pressure of Zn vapor within the keyhole can cause an unstable and violent flow of the melting pool, resulting in the formation of spatter, cavities and craters (Chen et al. 2011), (Amo et al. 1996), (Dasgupta et al. 2007). Laser welding of Zn-coated steel to Al alloy is even more challenging because of the formation of brittle intermetallic compounds (IMCs) as a result of poor miscibility and solubility of steel and aluminum. Brittle IMCs can reduce the weld strength by inducing cracking in the weld (Ding et al. 2006). In the current study, the above-mentioned challenges are explained and their effects on the weld quality and strength are discussed. This study also provides an overview of

the approaches proposed by different researchers to minimize the adverse effects of the pre-mentioned challenges and to improve the strength and quality of the weld between galvanized steel and Al alloy.

2. Laser welding of Zn-coated steel on Al alloy

Different approaches have been proposed in the literature for laser overlap welding of Zn-coated steels with Al alloys (Milberg et al. 2009), (Li et al. 2007), (Fabbro et al. 2006), (Tzeng 2000). Despite successful achievements in the laser welding of Zn-coated steel on Al in lap joint setup, producing a defect-free weld can be still very challenging, especially under high welding speeds (Ma et al. 2014). The formation of defects, such as porosity, spatter and the brittle intermetallic compound (IMC) layer at the weld interface are the main issues concerning the laser welding of Zn-coated steel on Al alloy (Lee et al. 2006), (Laukant et al. 2005), (Chen et al. 2008). During the laser welding of Zn-coated steel on Al, Zn vapor causes instability in the melting pool, resulting in spatter, porosity and crater defects (Chen et al. 2011), (Amo et al. 1996), (Dasgupta et al. 2007). The vaporization of Zn is almost inevitable because the boiling point of Zn (906 °C) is considerably lower than that of Al (2520 °C) and Fe (1538 °C) (Ma et al. 2014). Different approaches have been suggested in the literature to reduce the porosity occurring in the laser lap welding of Zn-coated steels. Amo et al. (Amo et al. 1996) proposed keeping a gap between the surfaces to be welded to let the evaporated Zn escape from the gap. They reported a successful weld without any cracks or porosities, using a gap opening of no more than 0.1 mm. Chen et al. (Chen et al. 2011) tried the use of double pass laser welding with a defocused beam. Welding was performed in the first pass with a focused laser beam, and then a defocused beam was applied for the second pass. Double pass welding was performed using either Ar or N₂ as a shielding gas. The weld pool was reported unstable and spatter was observed with both the Ar and N₂ gases. According to this experiment, applying a second pass weld with a defocused laser beam improved the weld appearance, shown in Fig. 2.

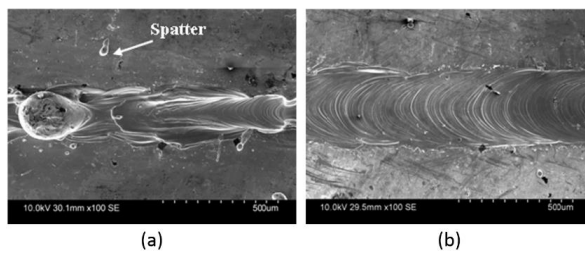


Fig. 2. Comparison between weld appearances produced from (a) a single pass and (b) double pass fiber laser welding with N₂ shielding gas, (first pass welding parameters: 650 W, 100 mm/s, f.p.p. of 0 mm, second pass welding parameters: 200 W, 75 mm/s, f.p.p. of +2 mm) (Chen et al. 2011).

A higher risk of porosity has been found to exist when a higher density gas is used, because the gas is more likely of being trapped in the keyhole and the weld after solidification (Katayama et al. 2009). However, Chen et al. (Chen et al. 2011) reported porosity and crack in the weld produced with double pass laser welding using either N₂ or Ar gas, without any obvious relation between the type of gas used and the porosity found in the weld samples, seen from Fig. 3.

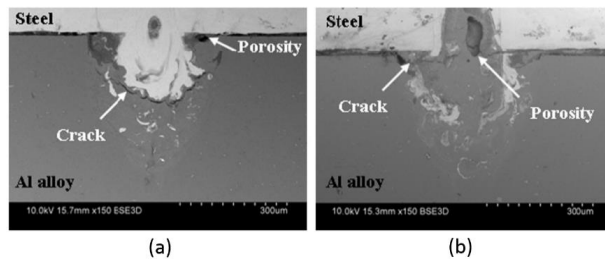


Fig. 3. Backscattered electron image of the cross-section of the weld made using laser double pass welding with (a) Ar gas and (b) N₂ gas, (first pass welding parameters: 650 W, 100 mm/s, f.p.p. of 0 mm, second pass welding parameters: 200 W, 75 mm/s, f.p.p. of +2 mm) (Chen et al. 2011).

Ma et al. (Ma et al. 2014) proposed two-pass laser welding for producing a lap joint between Zn-coated high-strength steel and Al alloy. For the first pass, they used a defocused laser beam to preheat the components and to partially melt and vaporize the zinc coating of the galvanized steel sheet. Then, welding was performed with a focused beam in the second pass. They reported that a defect-free lap joint with partial penetration was produced with the use of two-pass laser welding. They also stated that the process was very stable and almost no spatter, crack or blowholes were present in the welds. As was mentioned before, another concern in welding Al and steel is the growth of brittle Fe–Al intermetallic compounds (IMCs) within the welds as a result of poor solid solubility of the Fe element in Al (Torkamany et al. 2010), (Meco et al. 2013), (Sierra et al. 2007). IMCs consist of ductile Fe-rich and brittle Al-rich phases. FeAl and Fe₃Al belong to Fe-rich phases, whereas Al-rich phases include FeAl₂, Fe₂Al₅, FeAl₃, and Fe₄Al₁₃ (Lee et al. 2005), (Ozaki et al. 2010), (Rathod et al. 2004), (Katayama et al. 2005). Brittle Al-rich IMCs have a deteriorative effect on the mechanical performance of the weld and can induce cracks within the fusion zone (Meco et al. 2013). The type and morphology of IMCs are highly dependent on the type of steel and aluminum alloy; even small variations in the melting temperature, the fluidity of the molten pool, solute diffusivity and thermal conductivity can affect the kinetics of intermetallic phase formation (Lee et al. 2005). Ozaki et al. (Ozaki et al. 2010) proposed laser roll welding to reduce the effect of IMCs. This method combines a CO₂ laser and a roller compressing the facing surfaces of the Al alloy and Zn-coated steel to be welded. The idea behind this technique was to minimize the formation of brittle IMCs by shortening the heat cycle and increase the heat transfer rate between the contacting surfaces under pressure. They produced a weld with a maximum shear strength of 162 N/mm when the welding speed was 8.3 mm/s and the roller pressure was set to 150 MPa. They also reported that the shear strength declines when the thickness of the IMC layer exceeds 10 μm. It has also been reported that when the thickness of the IMC layer is less than 10 μm the specimen under a shear test fails in the base, not in the weld (Ozaki et al. 2010), (Bruckner 2005), (Furukawa 2005). Meco et al. (Meco et al. 2013) studied the use of fiber laser for the conduction welding of Al to Zn-coated steel in overlap configuration. They stated that using conduction mode laser welding enabled them to control the heat input and thereby control IMC formation. They also reported that shear strength in the Zn-coated steel and Al joint was higher when a higher energy density was used, seen in Fig. 4. This could be contrary to the assumption that a higher heat input can increase the formation of IMCs and cause degradation in the mechanical strength of the weld (Chen et al. 2009). They concluded that mechanical strength is not solely dependent on the thickness of the IMC layer. Instead, a combination of the intermetallic layer thickness and its composition, the orientation of IMCs, as well as bonding and diffusion between the elements can affect the mechanical strength (Meco et al. 2013).

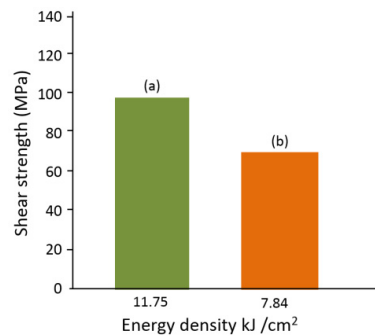


Fig. 4. Shear strength of the laser welded lap joint between low-carbon galvanized steel and AA2024 aluminum alloy using fiber laser (spot diameter: 13 mm, power density: 4.52 kW/cm², (a) travel speed: 0.3 m/min, (b) travel speed: 0.45 m/min) (Meco et al. 2013).

Chen et al. (Chen et al. 2011) reported a considerable reduction in IMCs as a result of using N₂ shielding gas in the fibre laser welding of Zn-coated steel on Al alloy. They also noticed lower variations in hardness in the fusion zone when N₂ gas was used which can also indicate less IMC formation. They stated that a higher shear strength was obtained with N₂ gas than with Ar, observable in Fig. 5. This can be attributed to the higher thermal conductivity of N₂ compared to Ar that can increase the cooling rate of the melt pool during laser welding. The increased cooling rate can reduce the extent of heat flow and diffusion activity in the melt pool. Thus, the base materials will be mixed in a limited degree and the growth of IMCs will be obstructed, leading to even more hardness distribution and improved shear strength (Borrisutthekul et al. 2007). The reactivity of N₂ plasma with Al can also be beneficial in limiting the extent of Al-rich intermetallic phases, particularly in laser keyhole welding. The reaction between the vaporized Al and ionized N₂ leads to the formation of aluminum nitride AlN in the weld in place of Fe–Al intermetallics (Chen et al. 2011), (Chen et al. 2009), (Katayama et al. 2009), (Visuttipitukul et al. 2003). Ma et al. (Ma et al. 2014) claimed that controlled preheating and welding parameters during double-pass laser welding of Zn-coated steel and Al, can limit the thickness of Al-rich IMCs to around 5 μm. They found that too much heat input during preheating can entirely remove the Zn-coating which makes the weld prone to the formation a Fe–Al layer. They declared that a lower heat input during the welding process resulted in a higher shear strength. They also claimed that the presence of Zn in the IMCs could improve the strength of the welded lap joint between Zn-coated steel and Al.

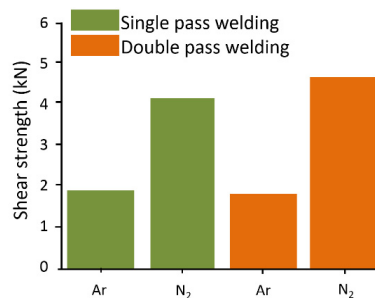


Fig. 5. Comparison between the effect of Ar and N₂ shielding gases on the shear strength of the laser welded lap joint of Zn-coated steel (DX54) and Al alloy (5754), using either single pass or double pass fiber laser (first pass welding parameters: 650 W, 100 mm/s, f.p.p. of 0 mm, second pass welding parameters: 200 W, 75 mm/s, f.p.p. of +2 mm) (Chen et al. 2011).

Corrosion resistance is a principal requirement of the welded joint between Zn-coated steel and Al. The corrosion resistance of the weld can be mainly affected by microsegregation, the growth of intermetallic phases, loss of Zn due

to vaporization and defects (Kodama et al. 2010), (Kwok et al. 2006). The degradation of corrosion performance can occur within the fusion and heat affected zones due to intergranular corrosion and segregation or the growth of a secondary phase (Chen et al. 2009), (Kwok et al. 2006), (Sastri et al. 2007). It is known that inert gases with a higher density can provide better protection over the melt pool against oxidation and loss of alloying elements (Chen et al. 2009). It has been reported that weld samples made with Ar shielding gas showed better corrosion resistance than with N₂ gas (Chen et al. 2011). This can be due to the higher density of Ar that protected the base metals more efficiently against oxidation (Chen et al. 2011). Generally, the prevention of the weld defects and smoothness of the weld surface can be considered as an effective way to improve the corrosion resistance of the weld (Chen et al. 2011), (Kwok et al. 2006), (Yan et al. 2007).

3. Conclusions

In this study the main issues associated with the laser lap welding of zinc-coated steel on aluminum, which is commonly used in patchwork blank applications for the manufacture of car bodies were discussed and different approaches presented in the literature to avoid these issues were reviewed. The main conclusions are:

Higher heat input can expedite the growth of brittle intermetallic compounds (IMCs). Generally, a higher mechanical strength of welds has been achieved when the thickness of the brittle IMC layer has been less than 10 μm . Besides the thickness of the IMC layer, other factors such as the composition and orientation of IMCs, as well as bonding and diffusion between the elements may be determining the weld strength.

The use of N₂ as a shielding gas can have beneficial effects as to the formation of brittle IMCs, thereby improving the weld strength. This may be due to the higher thermal conductivity of N₂ compared to Ar as well as the likeliness of reaction between N₂ plasma and Al vapor to form aluminum nitride instead of Al-rich IMCs.

The type of shielding gas can have influence on the corrosion resistance of the weld. Inert gases with higher density can protect the molten pool against oxidation which may benefit the corrosion resistance performance of the weld.

References

- Amo, J.M., Duran, J., Chao, J., Fernandez-Saez, J., 1996. Laser welding of Al55–Zn coated steel sheet. *J Mater Sci* 31, 6595–6607.
- ArcelorMittal Tailored Blanks, [Online]. Available: <http://www.arcelormittal.com>.
- Ayres, K.R., Hilton, P.A., 1994. CO₂ laser butt welding of coated steels for the automotive industry. *Weld Met Fabr* 62, 10–12.
- Borrisutthekul, R., Yachi, T., Miyashita, Y., Mutoh, Y., 2007. Suppression of intermetallic reaction layer formation by controlling heat flow in dissimilar joining of steel and aluminum alloy. *Mater Sci Eng A* 467, 108–113.
- Bruckner, J., 2005. Cold Metal Transfer Has a Future Joining Steel to Aluminum. *Welding Journal* 84 (6), 38–40.
- Chen, Y.C., Komazaki, T., Tsumura, T., Nakata, K., 2008. Role of zinc coat in friction stir lap welding Al and zinc coated steel. *Mater Sci Technol* 24, 33–39.
- Chen, W., Ackerson, P., Molian, P., 2009. CO₂ laser welding of galvanized steel sheets using vent holes. *Mater Des* 30, 245–251.
- Chen, H.C., Pinkerton, A.J., Li, L., Mistry, A.T., 2009. Fibre laser welding of Zn-coated steel in Al alloy for next generation lightweight vehicles. *Proceedings of the 28th International Congress on Applications of Lasers and Electro-optics*, Orlando, Florida USA.
- Chen, H.C., Pinkerton, A.J., Li, L., Liu, Z., Mistry, A.T., 2011. Gap-free fibre laser welding of Zn-coated steel on Al alloy for light-weight automotive applications. *Mater Des* 32, 495–504.
- Dasgupta, A.K., Mazumder, J., Li, P., 2007. Physics of zinc vaporization and plasma absorption during CO₂ laser welding. *Journal of Applied Physics* 102, 053108–15.
- Dharmendra, C., Rao, K.P., Wilden, J., Reichb, S., 2011. Study on laser welding–brazing of zinc coated steel to aluminum alloy with a zinc based filler. *Materials Science and Engineering A* 528, 1497–1503.
- Ding, J.J., Huang, H.J., Peyre, P., Fabbro, R., 2006. Temperature criterion of laser welding for joining aluminum alloy with low-carbon steel. *Mater Manuf Processes* 21, 59–61.
- Eva, V.C., Joaquin, V.G., 2012. Laser Beam Welding and Automotive Engineering, in “Structural Connections for Lightweight Metallic Structures”. vol. 8, Springer, Berlin, pp. 59–81.
- Fabbro, R., Coste, F., Goebels, D., Kielwasser, M., 2006. Study of CW Nd-YAG laser welding of Zn-coated steel sheets. *J Phys D Appl Phys* 39, 401–409.
- Furukawa, K., 2005. Welding Process of Iron-Aluminum. *Welding Technology* 53 (8), 94–102.
- Katayama, S., Sung-Min, J., Mizutani, M., Han-Sur, B., 2005. Laser weldability of aluminum alloy and steel. *Mater Sci Forum* 502, 481–486.
- Katayama, S., Nagayama, H., Mizutani, M., Kawahito, Y., 2009. Fibre laser welding of aluminium alloy. *Weld Int* 23, 744–752.
- Kodama, S., Ishida, Y., Asai, K., Mizumoto, M., Namekata, T., Nagasaki, H., 2010. Development of Stainless Steel Welding Wire for Galvanized Steel Sheets. *Welding in the World* 54 (1-2), 42–48.

- Kwok, C.T., Fong, S.L., Cheng, F.T., Man, H.C., 2006. Pitting and galvanic corrosion behavior of laser-welded stainless steels. *J Mater Process Technol* 176, 168–178.
- Laukant, H., Wallmann, C., Korte, M., Glatzel, U., 2005. Flux-less joining technique of aluminium with zinc-coated steel sheets by a dual-spot laser beam, in "Advanced Materials Research". vol. 6–8, Trans Tech Publications Ltd, Uetikon-Zuerich, Switzerland.
- Lee, K.J., Kumai, S., Arai, T., 2005. Interfacial microstructure and strength of steel to aluminum alloy lap joints welded by a defocused laser beam. *Mater Trans* 46, 1847–1856.
- Lee, K.J., Kumai, S., Ishikawa, N., Furuya, K., 2006. Interfacial microstructure of A6111/ steel lap joint fabricated by defocused laser beam welding, 10th International conference on aluminium alloys (ICAA-10), Vancouver, Canada.
- Li, X., Lawson, S., Zhou, Y., Goodwin, F., 2007. Novel technique for laser lap welding of zinc coated sheet steels. *J Laser Appl* 19, 259–264.
- Ma, J., Harooni, M., Carlson, B., Kovacevic, R., 2014. Dissimilar joining of galvanized high-strength steel to aluminum alloy in a zero-gap lap joint configuration by two-pass laser welding. *Materials and Design* 58, 390–401.
- Meco, S., Pardal, G., Ganguly, S., Miranda, R.M., Quintino, L., 2013. Overlap conduction laser welding of aluminium to steel. *Int J Adv Manuf Technol* 67, 647–654.
- Milberg, J., Trautmann, A., 2009. Defect-free joining of zinc-coated steels by bifocal hybrid laser welding. *Prod Eng Res Devel* 3, 9–15.
- Ono, M., Yoshitake, A., Omura, M., 2004. Laser weldability of high-strength steel sheets in fabrication of tailor welded blanks. *Weld Intern* 18 (10), 777–784.
- Ozaki, H., Kutsuna, M., Nakagawa, S., Miyamoto, K., 2010. Laser roll welding of dissimilar metal joint of zinc coated steel to aluminum alloy. *J Laser Appl* 22 (1), 1–6.
- Park, Y.W., Park, H., Rhee, S., Kang, M., 2002. Real time estimation of CO2 laser weld quality for automotive industry. *Optics & Laser Technology* 34, 135–142.
- Rathod, M.J., Kutsuna, M., 2004. Joining of aluminum alloy 5052 and low-carbon steel by laser roll welding. *Weld J* 83, 16–26.
- Reisgen, U., Markus, S., Mokrov, O., Essam, A., 2010. Shielding gas influences on laser weldability of tailored blanks of advanced automotive steels. *Applied Surface Science* 257, 1401–1406.
- Sastri, V.S., Ghali, E., Elboujdaini, M., 2007. Zinc and zinc alloys, in "Corrosion Prevention and Protection: Practical Solutions". John Wiley & Sons, Chichester, UK, p 290.
- Sierra, G., Peyre, P., Deschaux-Beaume, F., Stuart, D., Fras, G., 2007. Steel to aluminium key-hole laser welding. *Mater Sci Eng A* 447, 197–208.
- Spöttl, M., Mohrbacher, H., 2014. Laser-based manufacturing concepts for efficient production of tailor welded sheet metals. *Adv Manuf* 2, 193–202.
- Torkamany, M.J., Tahamtan, S., Sabbaghzadeh, J., 2010. Dissimilar welding of carbon steel to 5754 aluminum alloy by Nd: YAG pulsed laser. *Mater Des* 31, 458–465.
- Tzeng, Y.F., 2000. Process characterization of pulsed Nd:YAG laser seam welding. *Int J Adv Manuf Technol* 16, 10–18.
- Vollertsen, F., Thomy, C., 2005. Welding with fibre lasers from 200 to 17000 W, ICALEO 2005 – 24th international congress on applications of laser and electro-optics, Miami, FL, USA.
- Vollertsen, F., 2005. Developments and trends in laser welding of sheet metal, *Adv Mater Res* 6–8, 59–70.
- Visuttipitukul, P., Aizawa, T., Kuwahara, H., 2003. Feasibility of Plasma Nitriding for Effective Surface Treatment of Pure Aluminum. *Materials Transactions* 42 (7), 1412–1418.
- Yan, X.J., Yang, D.Z., Liu, X.P., 2007. Corrosion behavior of a laser-welded NiTi shape memory alloy. *Mater Charact* 58 (7), 623–628.

Publication IV

Tasalloti, H., Eskelinen, H., Kah, P., and Martikainen, J.

An integrated DFMA–PDM model for the design and analysis of challenging similar and dissimilar welds

Reprinted with permission from

Materials and Design

Vol. 89, pp. 421-431, 2016

© 2015, Elsevier Ltd.



Contents lists available at ScienceDirect

Materials and Design

journal homepage: www.elsevier.com/locate/jmad

An integrated DFMA–PDM model for the design and analysis of challenging similar and dissimilar welds



H. Tasalloti*, H. Eskelinen, P. Kah, J. Martikainen

Lappeenranta University of Technology, P. O. Box 20, 53851 Lappeenranta, Finland

ARTICLE INFO

Article history:

Received 14 July 2015
 Received in revised form 1 October 2015
 Accepted 3 October 2015
 Available online 9 October 2015

Keywords:

Concurrent engineering (CE)
 Design for manufacturing and assembly (DFMA) for welding
 Product data management (PDM)
 Selection strategy for materials, welding processes, and filler metals
 Dissimilar metal welding (DMW)
 Arctic materials

ABSTRACT

To permit effective adoption of concurrent engineering (CE) in the design of welded structures, a new model is proposed that integrates the design for manufacturing and assembly (DFMA) strategy with a product data management (PDM) system. To enable effective integration, a traditional DFMA procedure was adapted to comply with the requirements of welding as an independent design module. The PDM system was integrated to the DFMA as a database of welding processes, materials, consumables, standards and guidelines, as well as for storing and tracking changes in the weldment design. An application-based selection method was also introduced to further facilitate selection of the base material, welding process and filler metals. An application was developed as a proof of principle and tested with Arctic conditions as the nominated service environment. The generic nature of the model makes it applicable to many welding operations if relevant databases and guidelines are prepared. The proposed approach can also be used in conjunction with CAD applications and manufacturers' PDM software to enhance the design of weldments and expedite decision-making as its use by designers requires only minimum welding and metallurgy knowledge.

© 2015 Elsevier Ltd. All rights reserved.

1. Introduction

Successful design of a welded structure relies on selecting suitable base metals, proper joint geometries and thicknesses commensurate with the demanded load carrying capacity, life expectancy and service environment. However, these criteria cannot guarantee the performance of the weldment if the characteristics of the weld, including metallurgical aspects, are not carefully considered. The mechanical and metallurgical properties of the weld are the result of complex interactions of base metals, base and filler metals, and the welding process and its parameters. Traditional design processes and commercial CAD/CAE software usually employ the thermo-mechanical characteristics of the base materials together with joint geometries to assess the design as regards fulfillment of service stipulations, while neglecting the importance of the weld metallurgy and its properties as a significant building block of a weldment. Usually the weld properties (e.g. corrosion resistance, ductility, strength, and hardness) are only considered at the manufacturing stage, when the detailed design is done. This can increase the risk of costly reworks and delays due to possible incompatibilities between the base metals, welding process, and thicknesses and joint geometries. On the other hand, evaluating the properties and

metallurgical features of the weld at the design stage demands in-depth understanding of materials science and welding processes, which places a considerable burden on designers. However, this missing part in the design process and the gap existing between the design and manufacturing stages are serious challenges that can cause catastrophic failure, especially in critical applications and demanding service environments. A solution to address these challenges could be adoption of the concurrent engineering (CE) concept and design for manufacturing and assembly (DFMA) methodology to the purpose of welded structures design.

CE was developed to enable simultaneous involvement of the technical and business aspects of a product throughout its life cycle [1,2]. Design for manufacturing and assembly (DFMA) is one of the main methodologies used to achieve CE [3,4]. DFMA emphasizes the responsibility of the designer to ensure the functionality, reliability and manufacturing feasibility of the design [5].

The success of a DFMA strategy relies on the effectiveness of data distribution within the multidisciplinary product development teams involved. Streamlined data distribution can be achieved by integrating DFMA with the product data management (PDM) systems used to organize, access, and control product data as well as to manage the life cycle of products [6].

Many researchers have studied the possibility of incorporating DFMA into welding operations [7–16]. However, an integrated view of PDM and DFMA for welded structures has yet to be presented. Sokolov et al. [7] used experimental data to provide DFMA based guidelines for

* Corresponding author.
 E-mail addresses: hamed.tasalloti.kashani@lut.fi (H. Tasalloti), harri.eskelinen@lut.fi (H. Eskelinen), paul.kah@lut.fi (P. Kah), jukka.martikainen@lut.fi (J. Martikainen).

laser beam welding of structural steel. The work used the weldability function of software developed for a high power fiber laser (HPFL) to explain weld imperfections as a correlation of the interplay of welding parameters, materials, joint setup and surface conditions. Salminen et al. [8] proposed a design procedure for laser welding that combined DFMA and CE principles. Their approach is based on the DFMA procedure initially presented by Boothroyd et al. [9]. LeBacq et al. [10] developed a computer based DFMA model for selecting an applicable joining process for a specified design. In their model, they adopted a task-based approach [11] that uses a series of questionnaires regarding joint specifications, geometry and material to narrow down the available choices of joining methods to the most suitable one. The predefined questions are simple and manageable by non-expert users. However, over simplification, especially in terms of material properties, may sometimes lead to non-optimal solutions. Maropoulos et al. [12] examined a computerized aggregate process planning system for DFMA analysis of weldment assembly design. The discussed model uses design attributes such as geometry, orientation, joint class and weld features to evaluate fabrication constraints. A drawback to this approach can be the difficulty of assigning multiple attributes to different super- and sub-classes of assembly components. Kwon et al. [13] developed a numerical model integrated with a commercial CAD program to calculate welding process parameters for maximum productivity based on the joint geometry. Their approach calculates the weld bead cross-section according to structural standards constraints for fillet welds to determine the welding process parameters required to build up the weld bead with maximum travel speed. The model is capable of analyzing sheet metal thicknesses up to 6.4 mm to be joined with a single pass fillet weld. This approach can be useful for design assessment and alterations to find effective solutions at the initial stage of the design. However, the applicability of the derived output welding parameters remains questionable due to the geometric deviations that real parts usually have from the CAD source model and also due to the simplifications that usually exist in the model algorithm when compared with an actual welding operation. Moreover, the derived parameters for maximum heat input might not always result in a valid solution because of the adverse effects on the mechanical properties of the heat affected zone (HAZ). Niebles et al. [14] developed a DFMA procedure for welded products using a wide range of factors involved in the design and product development stages. Their approach can be used for different products when combined with related standards and codes and a heuristic knowledge base. However, their model remains mainly theoretical since the connection to the required actions in design and welding practice is not explicitly defined.

The objective of this study is to use the concept of CE to facilitate and improve the design process of welded structures, especially complex structures, where different design teams are involved and great caution in design and manufacturing is required. For this purpose, the traditional DFMA model was modified to enable improved usability for structural welding applications. In this revised model, welding is considered as a separate design module in the integration with PDM data. The model is intended to expedite the decision-making process by using an application-based selection approach that provides the designers with a permitted list of materials and welding procedures specifications (WPS) together with concise data and analysis to guide the designer to find an optimal solution. An application was developed as a proof of concept and tested using the task of selecting appropriate dissimilar base metals and filler metal for a nominated application with demanding service conditions, namely, the Arctic environment.

This study outlines a DFMA model that can be computerized using a unified interface with the companies' PDM system to ease and enhance the design and fabrication of weldments through an application-based selection method and smooth distribution of data among the design teams involved. The application-based selection approach makes the model practicable for designers with limited knowledge of welding and metallurgy. The model can be used for many similar and dissimilar

welded structures on condition that pertinent DFMA rules and guidelines are provided for the application.

2. Concurrent engineering, DFMA methodology, and product data management (PDM)

Concurrent engineering (CE) methodologies aim to reduce development time and costs and improve product quality and competitiveness by integrating different points of view of a product throughout its life cycle [5]. CE requires the cooperation of multidisciplinary design teams providing optimization from the technical and business points of view [1,5]. Design for manufacturing and assembly (DFMA) is considered one of the main approaches to achieving CE [3,4]. Traditional DFMA combines two concepts, namely, design for assembly (DFA) and design for manufacturing (DFM). Fig. 1 illustrates typical steps of the DFMA procedure. As shown in the figure, analysis of a design concept is usually initiated with DFA, which aims to improve the ease of assembly by reducing the parts count and variation as well as minimizing the variety of assembly instructions and complexity. For this purpose, each part is examined to rate its criticality in terms of difficulty and time demand as regards collecting, carrying, orienting, inserting and fastening. Subsequently, the most critical parts are revised to simplify the assembly and reduce the number of time demanding features [9,15,16]. The analysis is followed by DFM using the framework provided by DFA. DFM aims to improve the product design at minimum manufacturing cost for maximum manufacturing quality using the best techniques and practices available [4,15,17].

For successful implementation of CE design and DFMA strategy, the data associated with the cross-functional design teams must be brought together so that all the teams have proper access to the latest data and changes made during the design process [8]. This can be achieved using product data management (PDM) systems. PDM tools are used to capture and keep track of changes during the lifecycle of a product and to support the product development process based on the specific way a company operates [2,6]. A PDM system has a repository for data storage of the CAD/CAM files and revisions, specifications, documentation and standards, manufacturing information and requirements, calculations, illustrations and suppliers. PDM programs are increasingly being used to promote systematic, modular and cost-effective design and manufacture of products [2]. While PDM software can effectively help designers to reuse design modules and specifications, it generally cannot provide solutions for improving the functionality and fabrication friendliness of designs nor for determining the optimum manufacturing

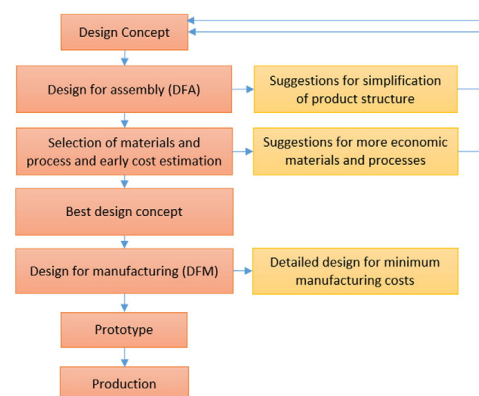


Fig. 1. Boothroyd and Dewhurst DFMA procedure [9].

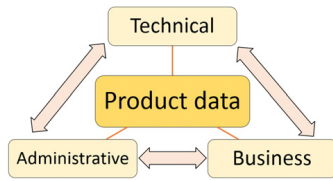


Fig. 2. Categories of product data [2].

technology. These shortcomings can be overcome if the PDM system is properly interfaced with DFMA rules and guidelines. The following sections discuss the new DFMA procedure interfaced with a PDM system that has been developed for structural welding applications.

3. A new DFMA model interfaced with PDM for welded structures

Traditional design processes burden welding engineers with a need to take into consideration metallurgical properties and incompatibilities when trying to meet requested functionality, e.g. corrosion resistance, ductility, strength, and hardness. These material and weld considerations are usually addressed when the detailed design is done, which can lead to costly reworks and delays. DFMA methodology can provide a solution to such late revisions if properly extrapolated to structural welding applications. As was discussed in the previous section, distribution of data among the different design teams can be done efficiently through a PDM system. For this purpose, the DFMA data should be interfaced with the related technical product data stored in the PDM system. It can be difficult to clearly differentiate the part of PDM data specifically related to particular technical aspects of products since technical data is usually to some extent connected with both business and administrative data (see Fig. 2) [2].

To develop an integrated DFMA–PDM model for welded structures, the DFMA aspects of the weldment design and welding stages must

first be carefully defined. Then DFMA aspects should be considered in relation to the technical data in the PDM system. Fig. 3 shows important factors in the DFMA of welded structures.

The factors shown in Fig. 3 are categorized under four main DFMA considerations, namely complexity, compatibility, quality and cost, all of which are interrelated and can affect one another. For example, reducing the complexity of a design by improvement in the geometry and tolerances as well as a reduction in the weight and number of components can reduce the manufacturing cost of the product. In the same manner, quality can be affected by the metallurgical compatibility of the base and filler metals, the compatibility of the welding process with the plate thicknesses and required weld deposition, as well as the compatibility of the welding procedure with the material and joint position and configuration. It is obvious that improved compatibility and quality can also reduce costs by minimizing defects and waste.

Fig. 4 illustrates the integrated DFMA–PDM model developed in the current study to improve and enhance the previously discussed approaches in [2,9,14] for weldment design. Unlike approaches such as those in [7–13], the current model considers weldment as a separate design module to address the requirements of welded products more specifically. This makes the model easily applicable to various welded products, given that a relevant database and DFMA guidelines are provided. In addition, integration with the PDM system can provide additional advantages, including:

- Up-to-date data of all the changes and revisions for all the teams involved in the design.
- Ability to keep track of all revisions and a history of why and by whom a revision has been made.
- Properly controlled access to the database by defining roles and privileges so that authorized roles according to their need can have access to the categorized database of CAD designs and drawings, materials, filler metals, welding processes, cutting and bending processes, documents and standards, costs and prices, suppliers, manufacturers and subcontractors.
- Unified interface for DFMA and PDM tasks.

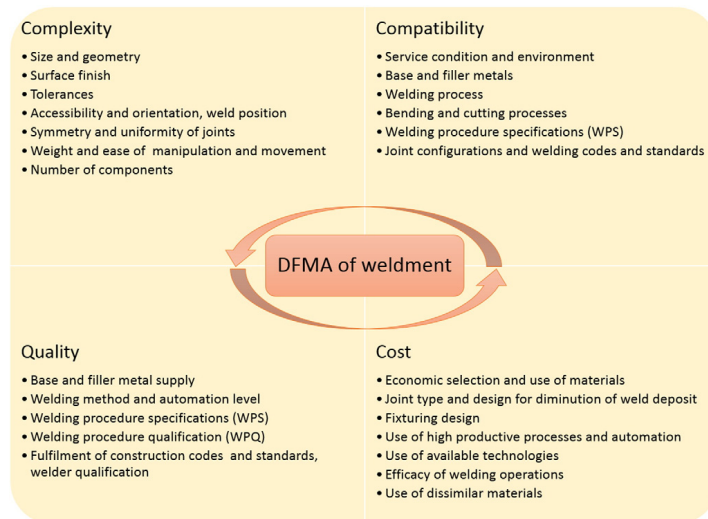


Fig. 3. Influential factors in DFMA of weldments.

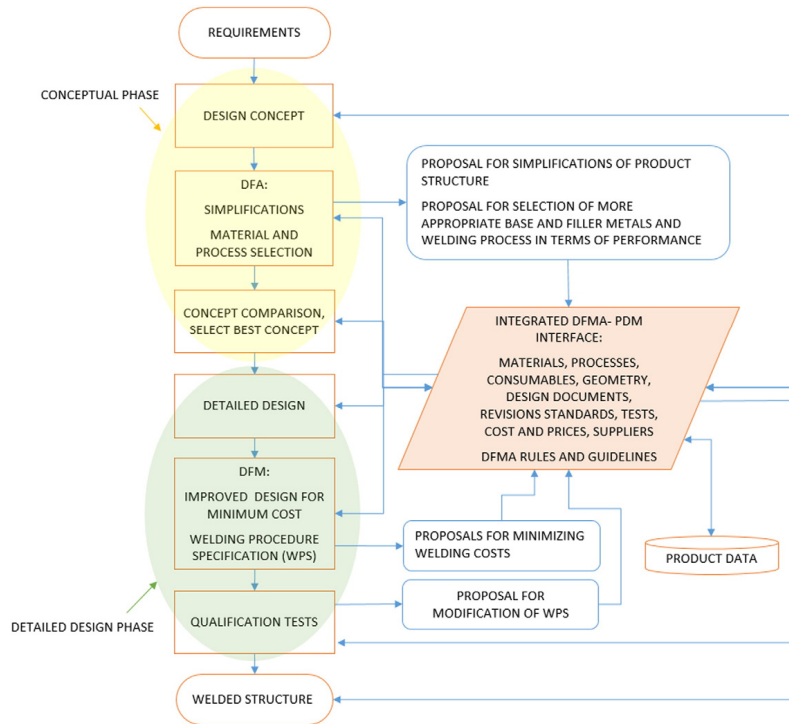


Fig. 4. Integrated DFMA-PDM procedure of for welded structures.

In this model, DFMA rules and guidelines are conjointly used with the PDM database to enable designers to select optimal configurations, materials, filler metal and welding processes. As can be seen from Fig. 4, the database is a supportive knowledge base with benchmarks for decision making in both the conceptual and detailed design phases. All the design documents, changes and modification proposals are captured, stored and distributed through the PDM system.

The current study proposes an application-based selection method, which is a variation of the questionnaire-based approach in [18], combined with an inductive reasoning strategy [18–21]. Different selection strategies for materials and manufacturing processes can be found in the literature [22–25]. However, the approach proposed in this work can considerably shorten the decision-making procedure and can also remove the risk of improper selection due to its built-in expertise. For material selection, for example, the designer first selects the application (e.g. Arctic region) in the PDM system. Subsequently, based on the requirements, suitable materials are loaded from the database prior to being available for selection. As is shown in Fig. 5, the selection can be done either manually with the help of the DFMA guidelines or through automatic ranking by weighting of the required material properties such as strength, toughness, corrosion resistance, weldability, formability, machinability and cost.

In a similar way, the welding process is selected from the PDM database based on the application (i.e. the materials to be welded, thicknesses, homogenous or non-homogenous welding) and then ranked according to availability, applicability, cost and productivity.

Filler metals are categorized and indexed based on the application (i.e. materials to be welded, dissimilar or similar metals and welding process) and selected according to the suitability of the predicted microstructure and the ease of the process, shown in Fig. 6.

In the model, additional DFMA rules and guidelines linked to the relevant PDM data are required for weldment design and structural welding standards, welding procedures specifications (WPS), welding procedure qualification tests (WPQT) and welder qualification tests (WQT). The WPS should be compatible with the selected base materials and processes and should include comprehensive instructions required to produce the weld, such as joint type and preparation, weld type, welding parameters, technique, consumables, interpass temperature and heat treatments. WPS is qualified using WPQT provided by the DFMA guideline. Depending on the requirements of the relevant standards and the functional requirements of the structure, the WPQT may include various destructive tests such as tensile, toughness, hardness and bending, crack tip opening displacement (CTOD) and corrosion tests as well as different nondestructive tests. WPQT results will determine if the WPS is qualified or modifications are needed. Fig. 7 shows a more detailed view of the proposed DFMA procedure illustrating actions commonly needed at each stage.

The following section discusses the feasibility of the application-based approach for the Arctic environment as a nominated application with demanding service conditions. Within the scope of the current study it is not possible to characterize the complete database and all the guidelines related to process parameters, joint and design standards and specification and qualification tests. Hence, this the approach is only

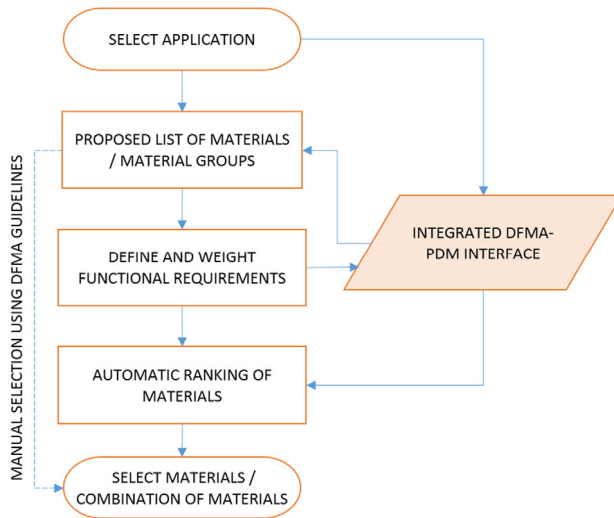


Fig. 5. Application-based selection of materials using the integrated DFMA–PDM interface.

presented, as a proof of principle, for selection of the base and filler metals using an application developed for this purpose.

4. Example of application-based selection method in practice

The application-based selection approach considers selection of materials as the initial and most critical stage of design, since the functional

requirements, fabrication method and cost are all affected by the type of material used. Selection of material cannot rely on mechanical properties alone, as in traditional geometry-driven design methods, the type of application and service environment should also be taken into account. In the Arctic environment, for example, the mechanical properties of many materials can differ significantly from those found at higher temperatures [26]. In such cases, the application-based selection

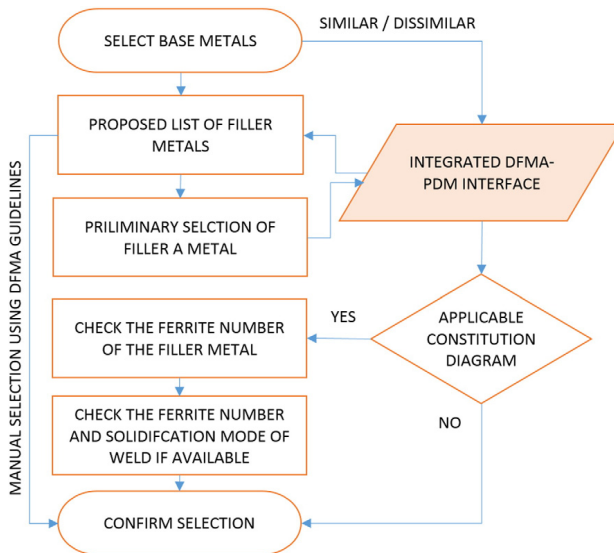


Fig. 6. Procedure for selecting the filler metal in the integrated DFMA–PDM interface.

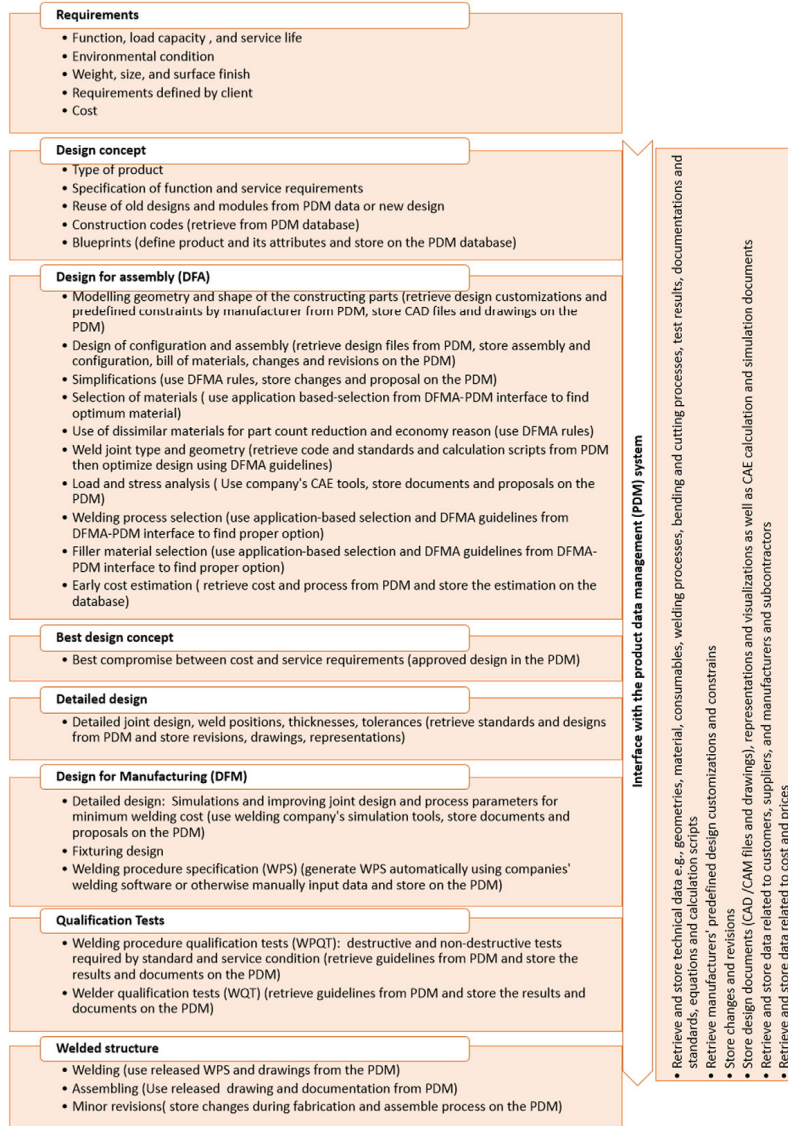


Fig. 7. DFMA procedure of welded structures integrated with the PDM system showing typical actions required in each stage.

approach, by precluding unsuitable combinations, can considerably reduce the risk of improper selection. The approach also incorporates cost and manufacturing features (i.e. machinability, formability and weldability) in selection of material to ensure manufacturability and economical justification of design in addition to functional fulfillment.

Figs. 8–11 and 13–16 present the interface of a simplified application developed for the purpose of this study based on the flowsheets presented in Figs. 5–7. The application can potentially be used in conjunction with the material database of CAD and CAE tools or companies' PDM systems. In this study, however, the method is proposed without making any changes to CAD and PDM programs. In this example, the



Fig. 8. Application selection in DFMA-PDM integrated interface.

Arctic environment was chosen as the nominated application due to the special functionality and fabrication considerations associated with weldment design in this region.

Fig. 8 shows initiation of the material selection by specifying the application. Fig. 9 shows a selection of materials recommended for Arctic applications. In the current study, four materials are considered; namely, A 633 high strength low alloy steel, (HSLAS), S 960 ultra-high strength steel (UHSS), 316 L austenitic stainless steel (ASS) and 1.4529 super-austenitic stainless steel (SASS).

A 633 is a normalized HSLA steel with enhanced notch toughness, which makes it suitable for welded structures operating in ambient temperatures as low as $-45\text{ }^{\circ}\text{C}$ [27]. S 960 is a low-carbon, low-alloyed direct-quenched steel which is characterized by a favorable combination of very high strength, good toughness at temperatures even below $-40\text{ }^{\circ}\text{C}$, as well as satisfactory formability and weldability [28–30]. Alloy 316 L is a low-carbon ASS with excellent resistance to atmospheric corrosion. 316 L possesses excellent strength and toughness at cryogenic temperatures and shows resistance to intergranular corrosion in marine environments [31,32]. Alloy 1.4529 offers excellent toughness at cryogenic temperature together with good formability and weldability [32]. This SASS is remarkably stronger than other 300 ASS series and shows superior resistance to numerous corrosive environments [33,34]. The chemical composition of the four alloys is shown in Table 1.

As is shown in Fig. 9, material selection can be done either manually or automatically from the list containing recommended metals.

For manual selection, the designer needs to decide which material(s) would best meet the design requirements using the technical information tabulated in the form of a guideline next to each material, shown in Fig. 10. The guideline includes mechanical properties, weldability, formability and machinability information as well as carbon equivalent (C_{eq}) when applicable. The C_{eq} is calculated using Eq. (1) [35]:

$$C_{eq} = C + Mn/6 + (Cr + Mo + V)/5 + (Ni + Cu)/15. \quad (1)$$

For automatic selection, the designer needs to define how important a specific property of the material is for the design purpose. As shown in Fig. 11, a range of attributes are presented to be rated by the designer. These attributes are divided into quantitative and qualitative properties

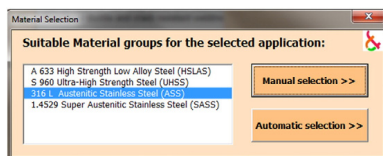


Fig. 9. Material selection. Recommended materials can be loaded from the PDM or CAD material database.

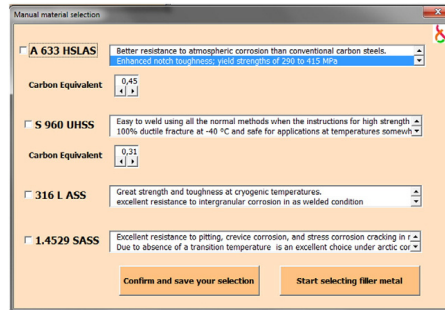


Fig. 10. Manual material selection interface. The guideline next to the each material aids the designer in selection of suitable material.

to provide a baseline for ranking and comparison. Table 2 shows the properties that are quantitatively compared.

The best property within a range (e.g. strength) is valued with a 5 on a scale where 0 equals “unsuitable” and 5 equals “best value”, and the other properties are proportionally calculated in comparison with the best value. An example of the comparison of quantitative attributes is presented in Table 3.

Material properties that are difficult to characterize with a definite quantity due to a lack of valid experimental data or their nature are qualitatively compared. As can be seen from Table 4, weldability, formability, and machinability are qualitatively evaluated from 0 to 5 where 0 means a property is unsuitable while 5 evaluates a property as excellent. The values are given based on data extracted from material handbooks and supplier catalogues [27,31–33,36].

Weldability, for instance, is assessed based on chemical composition, hardening, microstructure, thermal expansion, needed pre-work and post-heat treatment, joint preparation and heat input precaution. These aspects are indicated in the overall weldability shown in Fig. 12.

In the rating menu, shown in Fig. 11, a weight should be defined for each property on the basis of the service requirements. The weights can be assigned from 0 to 5, where each number in sequence stands for “not relevant”, “not important”, “important”, “very important” and “crucial”. The ranking is done simply by comparing the overall score of each material, which is obtained from summation of the defined weights multiplied with the relevant comparative values.

Fig. 13 shows the ranking done by the application according to the weighting shown in Fig. 11. For dissimilar welding, the first and second ranked materials can freely be selected to fulfill the service requirements.



Fig. 11. Rating menu for assigning the weight of different material attributes in a design.

Table 1
Chemical composition of four steel recommended for Arctic application.

Material	Composition wt.% (max)										
	C	Mn	Cr	Ni	Mo	Nb	Cu	N	P + S	Si	Ti
A 633	0.2	1.5	–	–	–	0.05	–	–	0.09	0.5	–
S 960	0.11	1.2	–	–	–	–	–	0.04	0.25	0.07	–
316 L	0.02	–	16.9	10.7	2.6	–	–	0.1	0.075	0.75	–
1.4529	0.01	–	20.5	24.8	6.5	–	1	0.2	0.04	0.5	–

The type of filler material is another critical element that determines many of the properties of a welded joint, including strength, toughness, corrosion resistance and surface properties. Thus, design of a weldment cannot only rely on the joint geometry and base metal properties, rather the combination of these two with a proper filler metal. Figs. 14–16 present the interface of the developed application for selecting filler metal with an assumption of GMAW as the welding process. As shown in Fig. 6, suitable filler metals for the selected base metals and similar or dissimilar welding are loaded from the database. For dissimilar welding and the selected metals in Fig. 13, appropriate filler metals for GMAW include 904 L, 316 L-Si, 307 L and P12, which in this particular case are derived from the Avesta welding manual [37] although other manuals could also be used. The recommended list of filler metals is shown in Fig. 14.

A guideline next to each filler metal containing technical information can aid the designer in the selection process, as seen in Fig. 14. An important factor in dissimilar welding of ASS is the ferrite number. For cryogenic applications, a fully austenitic structure would be favorable for maximum toughness. However, this increases the risk of solidification cracking and requires low heat input and accurate interpass temperature control. A small percentage of ferrite up to 4% would minimize this risk with minimum adverse effects on the toughness and corrosion resistance of the weld [38]. The ferrite number of the filler metal and the predicted ferrite number of the weld metal are also provided as an additional benchmark for decision-making, as shown in Fig. 14.

The ferrite numbers are obtained from the Welding Research Council (WRC) -1992 [39] constitution diagram using Cr and Ni equivalents presented in Eqs. (2) and (3) and with an assumption of equal dilution of 15% from either base metal in the weld.

$$Cr_{eq} = Cr + Mo + 0.7Nb \quad (2)$$

$$Ni_{eq} = Ni + 35C + 20N + 0.25Cu \quad (3)$$

As shown in Figs. 15 and 16, the ferrite numbers and solidification mode can also be checked on the WRC-1992 diagram using the option available on the interface of the developed application, illustrated in Fig. 14.

5. Discussion

The main objective of this study was to utilize CE strategy to achieve a more efficient weldment design procedure. For this purpose, the traditional DFMA model was modified to address the weldment considerations shown in Fig. 3. One CE imperative is effective cooperation of the different design teams involved in development of a product. The integrated DFMA-PDM model shown in Figs. 4 and 7 efficiently connects

Table 2
Comparison of the proposed materials based on properties having quantitative value.

Quantitative properties	A 633	S 960	316 L	1.4529
Ultimate tensile strength (MPa)	≈630	≈960	570	670
Charpy impact values at –40 °C (J)	34	50	180	200
Price per ton (\$)	≈800	≈1200	≈3000	≈5000

Table 3
Comparative values calculated with respect to the best corresponding material property valued with a 5 on a scale where 0 equals "unsuitable" and 5 equals "best value".

Material	Comparative values		
	Ultimate tensile strength	Charpy impact	Price per ton
A 633	3.3	0.9	5
S 960	5	1.3	3.3
316 L	3	4.5	1.3
1.4529	3.5	5	0.8

the different design teams so that they can collaborate in real-time to attain optimum solutions for the design. The PDM side of the model provides additional desirable features such as improved revision tracking and control, an interface with CAD/CAM tools, and control of access of the integrated DFMA-PDM database. The database is extensive and includes CAD designs and drawings, materials, consumables, processes, processes, documentations and standards, costs and prices, suppliers, manufacturers and subcontractors. The integrated view of DFMA-PDM enables weld engineers to cooperate proactively with the other design teams to make the DFA and DFM optimizations.

The distinctive feature of the current model over the approaches in [7–13] is that the weld is considered as a separate design module to enable more specific consideration of the weld requirements. To this end, metallurgical aspects of the weld are included in the model. This feature considerably increases the ability of the model to provide viable solutions for the design because it accounts for the importance of the metallurgy of the weld in determining key characteristics such as strength, hardness, toughness, and corrosion resistance. This feature also makes the model more reliable compared to the approaches in [8–12] and the traditional design method, which considers predominantly the thermomechanical properties of the base materials. The current DFMA model takes into account the interaction of the base and filler metals and the welding process and its parameters in the design stage, which can substantially reduce the risk of incompatibilities and the need for rework during the manufacturing stage. However, the inclusion of metallurgical aspects in the model necessitates design engineers having a high level of knowledge of material science and welding technology. This can be seen as a drawback to this approach since it is not always possible to find such well-qualified designers. The application-based selection approach that was proposed in Section 3 and demonstrated in Section 4 can help address this problem.

The application-based selection approach guides the designer to the best option in the list using a modified questionnaire-based selection strategy [18] combined with an inductive reasoning selection method [18–21] for selection of materials, welding processes and filler metals. The modification to the current DFMA model reduces the number of potentially demanding questions faced by designers, which makes the approach more user-friendly than those in [10,12]. The approach defines a clear path for weldment design, which starts from selection of materials for the intended application. This is done by weighting material features relevant to the design intent. These features can include mechanical, physical and chemical characteristics, as well as cost-related attributes and manufacturability considerations, such as machinability, formability and weldability. The approach ensures that

Table 4
Qualitative properties are evaluated from 0 to 5 where each number in succession stands for "bad", "fair", "good", "very good" and "excellent", respectively. Due to lack of experimental data the properties indicated with "" are compared qualitatively.

Qualitative properties	A 633	S 960	316 L	1.4529
Weldability	3	4	4	3
*Formability	5	3	3	3
*Machinability	4	2	3	1
*Corrosion resistance	3	3	5	5

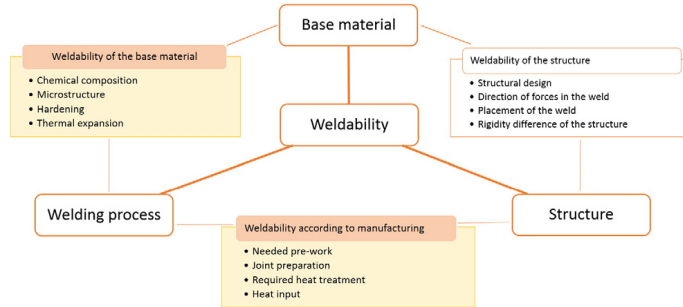


Fig. 12. Weldability evaluation criteria [5]. The colored boxes indicate aspects used in the current study to assess weldability.

the selected materials can fulfill the requirements of the application as well as manufacturing considerations. The most conspicuous advantage compared to conventional feature-based design [40,41] supported by modern CAD/CAM systems is that designers interact in creation and modification of features based on the application, function, manufacturing and cost considerations; while, in conventional method the system only warns the designer about the functionality of the design based on some rigid preset features and rules that are usually only related to manufacturing and do not take the intended use of the welded part into account to the same extent [42–46]. Using the presented approach, when the materials have been selected (which embeds utilization, manufacturing and cost features) geometries and joints are designed commensurably. The approach provides significant advantages over traditional geometry-driven design, where finding proper materials for the defined geometries after the conceptual design phase can lead to much iterative work, and trial and error. There is the possibility that the designer may select materials that are not permitted for the desired application and/or lack easy manufacturability. Such design decisions can cause devastating failures during operation or costly rework during manufacturing. The integration with PDM proposed in this paper has the potential to provide additional control on the fabricability of designs by enabling interaction with weld engineers, who can comment on and request revision of the geometries, joint designs and positions simultaneously with development of the product. This improved communication enables designers to develop a product compatible with the manufacturing capabilities of the companies. The approach can also be advantageous in providing a more realistic cost estimation of the weldment since all the components involved in making the weld are taken into account in the design stage.

The approach constrains selection to an approved list of materials, welding processes and parameters, and filler metals, for a specified application. However, the inductive reasoning feature of this approach

helps not to entirely exclude the intellectual freedom of designers. This feature adds more flexibility to the model and allows the designer to test and analyze different options and make decisions based on personal knowledge or the technical data provided. The built-in expertise benefits most designers without specialized knowledge of welding and metallurgy. The benefits include a reduced risk of improper selection and consequent design failure, as well as facilitated decision-making process and decreased design time. It should be noted that the approach could be a very effective tool for an experienced designers as well. An experienced designer may select materials based on his knowledge and understanding and compare them with materials suggested by the application to evaluate and verify his selection. The database is created, maintained and continuously developed by experts and an experienced designer can update the database with new solutions that have not been realized previously.

One difficulty in building the material database can be differences in designations of materials in different national standards and possible inconsistency in terms of equivalences of materials between different standards such as ASTM, EN, DIN, etc. The issue can be addressed by adding an option to enable the designer to filter out results based on different standards. A more customized solution would be to make the database in compliance with the standard that a company has adopted. A further difficulty in materials database construction is the various proprietary and nonstandard metals that are usually known by a tradename and may not have an identical equivalent in official standards. This group of materials should be differentiated with proper notice to the designer that the properties and technical data are based

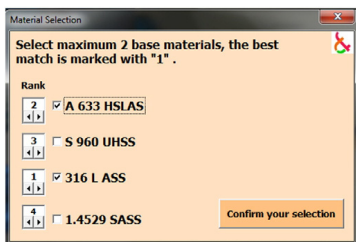


Fig. 13. Proposed materials ranked by their suitability for the design purpose.

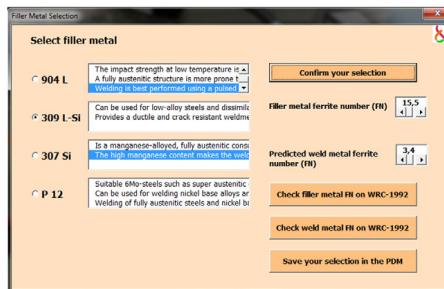


Fig. 14. Filler metals and their specifications recommended for a dissimilar weld between A633 and 316 L steels. The integrated DFMA–PDM interface has an option to check the WRC-1992 diagram for the weld and filler metal.

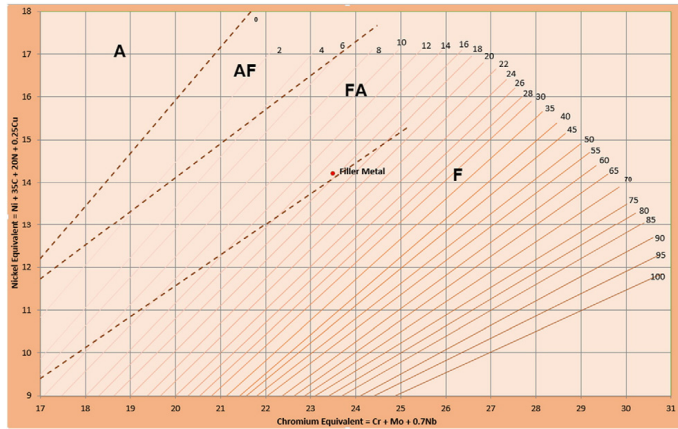


Fig. 15. 309 L-Si filler metal positioned on the WRC-1992 diagram.

on suppliers' catalogues and datasheets. Both the above-mentioned issues are valid for filler metals as well and can be addressed in a similar way as with base materials. A further possible limitation to the model is the extensive data and skill required to characterize all the lists, standards and guidelines for each application. However, this information can be compiled gradually according to the companies' needs and resources.

The tool demonstrated in Section 4 was made as proof of concept for the application-based selection method using a limited number of materials for one nominated application. For any new application, an expert (or experts) should supplement the database with recommended materials and index them for the application. Furthermore, the relevant qualitative and quantitative chemophysical and mechanical features should be extracted from material handbooks and other certified resources to be assigned to materials. The link between welding

processes and materials is made as the material type and grade is defined. Proper filler metals and their chemical compositions should be also stored in the database and indexed with relevant material and welding process. If the new application requires a specific DFMA guideline regarding compatibility, complexity, cost, and quality, this should be also stored in the database.

Although the approach cannot easily be used for innovation, the model offers optimal solutions within the confines of current knowledge and reduces the chance of erroneous design decisions, which is an important consideration in critical applications.

This study outlines a DFMA-PDM integrated model that can be computerized to ease and enhance the design and fabrication of weldments. The kernel of the approach consists of DFMA rules for welded structures, the PDM system and the application-based selection. The model can be customized with a unified interface for companies' PDM, CAD and CAE

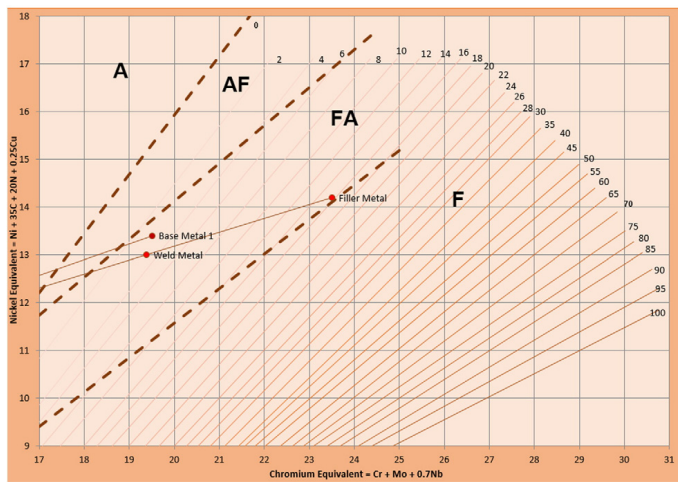


Fig. 16. Prediction of ferrite number and solidification mode for a weld between A 633 and 316 L made using 309 L-Si filler metal with 70% dilution.

tools to take full advantage of the model through correlative development of a weldment (i.e. selection of materials, defining geometries, mechanical calculation and analysis, selection of welding process and filler metals) with simultaneous incorporation of the design teams involved.

6. Conclusions

In this study, a new design for manufacturing and assembly (DFMA) model integrated with a product data management (PDM) system was developed in order to exploit the advantages of concurrent engineering (CE) in the design of welded structures. The model was constructed so that it enables the design of the weld as a separate design module simultaneously with other structural components and thus consistent with CE strategy. To facilitate decision-making, an application-based selection method was introduced for determining suitable base materials, the welding process and filler metals. The usability of this approach was illustrated for selection of the base and filler metals for an Arctic application. For the specific example considered in this work, the proposed model offers easier and faster selection of material and filler metals and enables designers to expeditiously evaluate different material and filler metal options. However, further studies are required to assess the efficacy and validity of the model for other applications in terms of selection of materials, welding processes and filler metals as well as design reliability and manufacturability.

Acknowledgments

The authors would like to thank Mr. Peter Jones for his comments and assistance with the English language.

References

- [1] V. Riboulet, P.R. Marin, S. Gowers, F. Wurtz, A framework supporting collaborative optimisation for multi professional design teams, *Advances in Integrated Design and Manufacturing in Mechanical Engineering*, Springer, Dordrecht, The Netherlands 2005, pp. 123–134.
- [2] H. Eskelinen, Aspects of integration between DFMA approaches and PDM data, *Proceedings of the PDM2013 Conference*, Lappeenranta, 2013.
- [3] K.H. Chen, S.J. Chen, L. Lin, S.W. Changchien, An integrated graphical user interface (GUI) for concurrent engineering design of mechanical parts, *Comput. Integr. Manuf. Syst.* 11 (1998) 91–112.
- [4] P. Selvaraj, P. Radhakrishnan, M. Adithan, An integrated approach to design for manufacturing and assembly based on reduction of product development time and cost, *Int. J. Adv. Manuf. Technol.* 42 (2009) 13–29.
- [5] H. Eskelinen, Review of traditional DFMA principles, in: H. Eskelinen (Ed.), *Advanced Approaches to Analytical and Systematic DFMA Analysis*, Lappeenranta University of Technology, Lappeenranta 2013, pp. 6–30.
- [6] B. Gascoigne, PDM: the essential technology for concurrent engineering, *World Class Design to Manufacture*, 2 (1) 1995, pp. 38–42.
- [7] M. Sokolov, H. Eskelinen, Design guideline for thick section butt joint laser beam welding of structural steels, in: H. Eskelinen (Ed.), *Advanced Approaches to Analytical and Systematic DFMA Analysis*, Lappeenranta University of Technology, Lappeenranta 2013, pp. A-40–A-49.
- [8] A. Salminen, J. Kara, M. Vattulainen, A. Piironen, *Product Design for Welding*, Proceedings of the 36th International MATADOR Conference, Manchester, 2010.
- [9] G. Boothroyd, P. Dewhurst, W.A. Knight, *Product Design for Manufacture and Assembly*, Marcel Dekker, NY, 2000.
- [10] C. LeBacqz, Y. Brechet, H.R. Shercliff, T. Jeggy, L. Salvo, Selection of joining methods in mechanical design, *Mater. Des.* 23 (2005) 405–416.
- [11] A.M. Lovatt, H.R. Shercliff, Manufacturing process selection in engineering design. Part 2: a methodology for creating task-based process selection procedures, *Mater. Des.* 19 (5–6) (1998) 217–230.
- [12] P.G. Maropoulos, Z. Yao, H.D. Bradley, K.Y.G. Par, An integrated design and planning environment for welding: part 1: product modelling, *J. Mater. Process. Technol.* 107 (2000) 3–8.
- [13] Y. Kwon, T. Wu, J.O. Saldivar, SMWA: a CAD-based decision support system for the efficient design of welding, *Concurrent. Eng. Res. A* 12 (4) (2004) 295–304.
- [14] E. Niebles, H. Maury, H. Gómez, C. Riba, Definition and validation of a knowledge base and the architecture of a computer tool to assist the design and manufacturing of welded products, 10th International Research/Expert Conference: Trends in the Development of Machinery and Associated Technology, Barcelona-Lloret de Mar, Spain, 2006.
- [15] W.A. Knight, *Integrated design for manufacture, service and environment*, *Advances in Integrated Design and Manufacturing in Mechanical Engineering*, Springer, Dordrecht, The Netherlands 2005, pp. 17–23.
- [16] X.F. Zha, S.Y.E. Lim, S.C. Fok, Integrated intelligent design and assembly planning: a survey, *Int. J. Adv. Manuf. Technol.* 14 (1998) 664–685.
- [17] T.C. Kuo, S.H. Huang, H.C. Zhang, Design for manufacture and design for 'X': concepts, applications, and perspective, *Comput. Ind. Eng.* 41 (2001) 241–260.
- [18] M.F. Ashby, M.F. Ashby, Y.J.M. Bre'chet, D. Cebon, L. Salvo, Selection strategies for materials and processes, *Mater. Des.* 25 (2004) 51–67.
- [19] J.L. Kolodner, *Case Based Reasoning*, Morgan Kaufmann, San Mateo, CA, 1993.
- [20] J.L. Kolodner, An introduction to case-based reasoning, *Artif. Intell. Rev.* 6 (1992) 3–24.
- [21] M.F. Ashby, K.W. Johnson, *Classification and Choice in Product Design*, Cambridge Engineering Design Centre, Cambridge, 2001.
- [22] G.E. Dieter, *Engineering Design: A Materials and Processing Approach*, fifth ed. McGraw-Hill, NY, 2012.
- [23] J.A. Charles, F.A.A. Crane, J.A.G. Furness, *Selection and Use of Engineering Materials*, third ed. Butterworth-Heinemann, Oxford, 1997.
- [24] M.M. Farag, *Selection of Materials and Manufacturing Processes for Engineering Design*, Englewood Cliffs, NJ, Prentice Hall, 1989.
- [25] M.F. Ashby, *Materials Selection in Mechanical Design*, second ed. Butterworth-Heinemann, Oxford, 1999.
- [26] E. Eranti, G.C. Lee, *Cold Region Structural Engineering*, J. Zseleaky, I.M. Stocknuzl (Eds.), Miami, FL, McGraw Hill Higher Education, 1986.
- [27] High-strength low-alloy steels, in: J.R. Davis (Ed.), *Alloying: Understanding the Basics*, Ohio, ASM International 2001, pp. 193–206.
- [28] F. Kalkhorani, J. Siltanen, A. Salminen, High power fiber laser welding of direct-quenched ultra high strength steels: evaluation of hardness, tensile strength, and toughness properties at subzero temperatures, *J. Manuf. Sci. Eng.* 137 (6) (2015) 061012–1–061012-10.
- [29] M. Hemmälä, A. Hirvi, J. Kömi, M. Laitinen, M. Laitinen, P. Mikkonen, D. Porter, J. Savola, S. Tihinen, Technological Properties of Direct-quenched Structural Steels with Yield Strength 900–960 MPa as cut Length and Hollow Sections, Corporation, Raumarukki, 2010.
- [30] S. Pallasparao, T. Linnell, P. Suikkan, T0–T28] correlation of low-carbon ultra-high-strength quenched steels, *Procedia Mater. Sci.* 3 (2014) 1032–1037.
- [31] J.R. Davis (Ed.), *ASM Specialty Handbook: Stainless Steels*, ASM International, 1995.
- [32] *Materials for cryogenic service – engineering properties of austenitic stainless steel (4368)*, Nickel Institute, 2015 (Retrieved from <http://www.nickelinstiute.org>, 20.02.2015).
- [33] *Handbook of Stainless Steel*, Outokumpu Oyj, Espoo, Finland, 2013 (Retrieved from <http://www.outokumpu.com>, 2013 (25.02.2015)).
- [34] Practical guidelines for the fabrication of high performance austenitic stainless steels, Retrieved from http://www.euro-inox.org/fla_195_EN.html, (20.02. 2015).
- [35] J. Dearden, H. O'Neil, A guide to the selection and welding of low alloy structural steels, *Trans. Int. Weld.* 3 (10) (1940) 203–214.
- [36] ASM International Handbook Committee (Ed.), *ASM Handbook, Properties and Selection: Irons, Steels, and High-Performance Alloys*, vol. 01, ASM International, 1990.
- [37] M. Larén (Ed.), *The Avesta Welding Manual: Practice and Products for Stainless Steel Welding*, Avesta Welding AB, Sweden, 2004.
- [38] H. Tasalloti, P. Kah, J. Martikainen, Effects of welding wire and torch weaving on GMAW of S355MC and AISI 304L dissimilar welds, *Int. J. Adv. Manuf. Technol.* 71 (2014) 197–205.
- [39] D.J. Kotecki, T.A. Siewert, WRC-1992 constitution diagram for stainless steel weld metals: a modification of the WRC-1988 diagram, *Weld. J.* 71 (1992) 171s–178s.
- [40] J.J. Shah, M. Mantyla, *Parametric and feature-based CAD/CAM: concepts, techniques, and applications*, John Wiley, 1995.
- [41] O.W. Salomons, F.J.A.M. van Houten, H.J.J. Kal, Review of research in feature-based design, *J. Manuf. Syst.* 12 (2) (1993) 113–132.
- [42] T. Szecsi, A.S.M. Hoque, Implementing manufacturing features in mechanical design, *Key Eng. Mater.* 502 (2012) 73–78.
- [43] M. Zhou, M.Y. Wang, Engineering feature design for level set based structural optimization, *Comput. Aided Des.* 45 (2013) 1524–1537.
- [44] L. Yang, S.K. Ong, A.Y.C. Nee, A new history-independent modeling approach for feature-based design, *Int. J. Adv. Manuf. Technol.* 59 (2012) 841–858.
- [45] A. Wubneh, Y.S. Ma, Feature-based mechanism design, in: Y.S. Ma (Ed.), *Semantic Modeling and Interoperability in Product and Process Engineering: A Technology for Engineering Informatics*, Springer 2013, pp. 303–351.
- [46] H.C. Fang, S.K. Ong, A.Y.C. Nee, Product remanufacturability assessment and implementation based on design features, *Procedia CIRP* 26 (2015) 571–576.

Publication V

Tasalloti Kashani, Hamed, Kah, Paul
A DFMA-Based Approach for the Design of Challenging Welds

Reprinted with permission from
International Society of Offshore and Polar Engineers (ISOPE)
pp. 189-196, 2016
© 2016, ISOPE

A DFMA-Based Approach for the Design of Challenging Welds

Hamed Tasalloti Kashani, Paul Kah
Department of Mechanical Engineering, Lappeenranta University of Technology,
Lappeenranta, Finland

ABSTRACT

The concept of concurrent engineering (CE) and design for manufacturing and assembly (DFMA) strategy was adopted to facilitate and improve decision-making in the design of welded structures. To this end, an application-based selection method was introduced for selection of the base material, welding process and filler metals. An application was developed as a proof of principle and tested with offshore conditions as the nominated service environment. The generic nature of the model makes it applicable to many welding operations if relevant databases and guidelines are prepared. The proposed approach can enhance the design of weldments and expedite decision-making as its use by designers requires only minimum welding and metallurgy knowledge.

KEY WORDS: Concurrent engineering (CE); Design for manufacturing and assembly (DFMA) for welding; Selection strategy for materials; Welding processes, and filler metals; Dissimilar metal welding (DMW); Offshore materials

INTRODUCTION

Successful design of a welded structure relies on selecting suitable base metals, proper joint geometries and thicknesses commensurate with the demanded load carrying capacity, life expectancy and service environment. However, these criteria cannot guarantee the performance of the weldment if the characteristics of the weld, including metallurgical aspects, are not carefully considered. The mechanical and metallurgical properties of the weld are the result of complex interactions of base metals, base and filler metals, and the welding process and its parameters. Usually the weld properties (e.g. corrosion resistance, ductility, strength, and hardness) are only considered at the manufacturing stage, when the detailed design is done. This can increase the risk of costly reworks and delays due to possible incompatibilities between the base metals, welding process, and thicknesses and joint geometries. On the other hand, evaluating the properties and metallurgical features of the weld at the design stage demands in-depth understanding of materials science and welding processes, which places a considerable burden on designers. However,

this missing part in the design process and the gap existing between the design and manufacturing stages are serious challenges that can cause catastrophic failure, especially in critical applications and demanding service environments. A solution to address these challenges could be adoption of the concurrent engineering (CE) concept and design for manufacturing and assembly (DFMA) methodology to the purpose of welded structures design.

CE was developed to enable simultaneous involvement of the technical and business aspects of a product throughout its life cycle (Riboulet, 2005; Eskelinen, 2013). Design for manufacturing and assembly (DFMA) is one the main methodologies used to achieve CE (Chen, 1998; Selvaraj, 2009). DFMA emphasizes the responsibility of the designer to ensure the functionality, reliability and manufacturing feasibility of the design (Eskelinen, 2013).

Many researchers have studied the possibility of incorporating DFMA into welding operations, from different points of view (LeBacq, 2005; Lovatt, 1998; Maropoulos, 2000; Kwon, 2004; Niebles, 2006). The objective of this study is to use the concept of DFMA to facilitate and expedite the decision-making process by using an application-based selection approach that provides the designers with a permitted list of materials and welding procedures specifications (WPS) together with concise data and analysis to guide the designer to find an optimal solution. An application was developed as a proof of concept and tested using the task of selecting appropriate dissimilar base metals and filler metal for a nominated application with demanding service environment, namely, offshore conditions.

This study outlines a DFMA-based decision making model that can be computerized to ease and enhance the design and fabrication of weldments through an application-based selection method. The application-based selection approach makes the model practicable for designers with limited knowledge of welding and metallurgy. The model can be used for many similar and dissimilar welded structures on condition that pertinent DFMA rules and guidelines are provided for the application.

DFMA FOR WELDMENT AND APPLICATION-BASED SELECTION MODEL

Traditional design processes burden welding engineers with a need to take into consideration metallurgical properties and incompatibilities when trying to meet requested functionality, e.g. corrosion resistance, ductility, strength, and hardness. These material and weld considerations are usually addressed when the detailed design is done, which can lead to costly reworks and delays. DFMA methodology can provide a solution to such late revisions if properly extrapolated to

structural welding applications. Thus, the DFMA aspects of the weldment design must first be carefully defined. Fig. 1 shows important factors in the DFMA of welded structures. The factors shown in Fig. 1 are categorized under four main DFMA considerations, namely complexity, compatibility, quality and cost, all of which are interrelated and can affect one another. For example, reducing the complexity of a design by improvement in the geometry and tolerances as well as a reduction in the weight and number of components can reduce the manufacturing cost of the product. In the same manner, quality can be affected by the metallurgical compatibility of the base and filler metals, the compatibility of the welding process with the plate thicknesses and required weld deposition, as well as the compatibility of the welding procedure with the material and joint position and configuration. It is obvious that improved compatibility and quality can also reduce costs by minimizing defects and waste.

guidelines or through automatic ranking by weighting of the required material properties such as strength, toughness, corrosion resistance, weldability, formability, machinability and cost. In a similar way, the welding process is selected from the database, based on the application (i.e. the materials to be welded, thicknesses, homogenous or non-homogenous welding) and then ranked according to availability, applicability, cost and productivity. Filler metals are categorized and indexed based on the application (i.e. materials to be welded, dissimilar or similar metals and welding process) and selected according to the suitability of the predicted microstructure and the ease of the process, shown in Fig. 3.

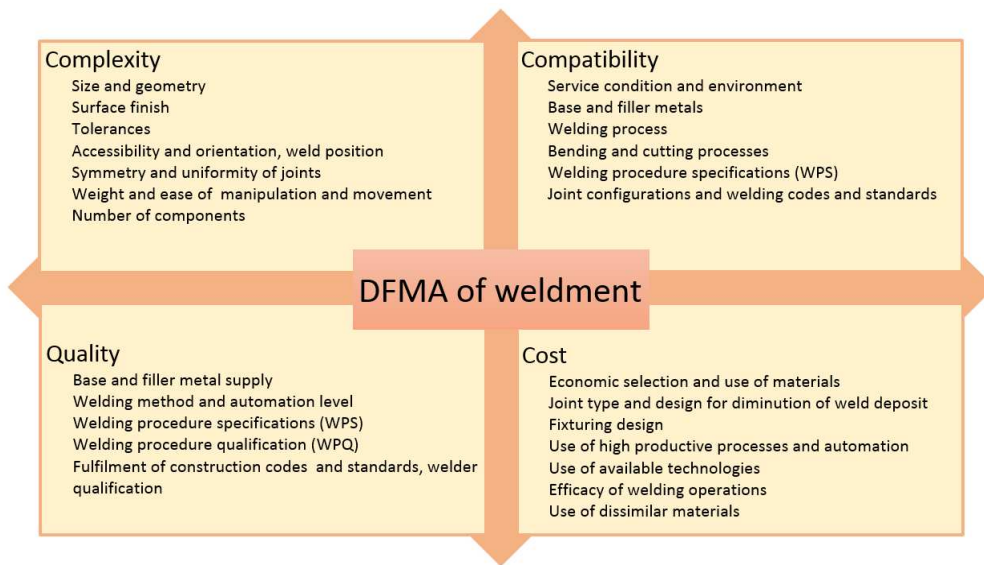


Fig. 1. Influential factors in DFMA of weldments (Tasalloti, 2016).

The current study proposes an application-based selection method, which is a variation of the questionnaire-based approach in (Ashby, 2004), combined with an inductive reasoning strategy (Ashby, 2004; Kolodner, 1993; Kolodner, 1992; Ashby, 2001). Different selection strategies for materials and manufacturing processes can be found in the literature (Dieter, 2012; Charles, 1997; Farag, 1989; Ashby, 1999). However, the approach proposed in this work can considerably shorten the decision-making procedure and can also remove the risk of improper selection due to its built-in expertise. For material selection, for example, the designer first selects the application (e.g. offshore construction) in the DFMA-based system. Subsequently, based on the requirements, suitable materials are loaded from the system database prior to being available for selection. As is shown in Fig. 2, the selection can be done either manually with the help of the DFMA

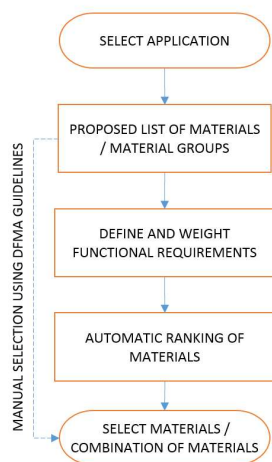


Fig. 2. Procedure for selecting the materials using application-based selection interface.

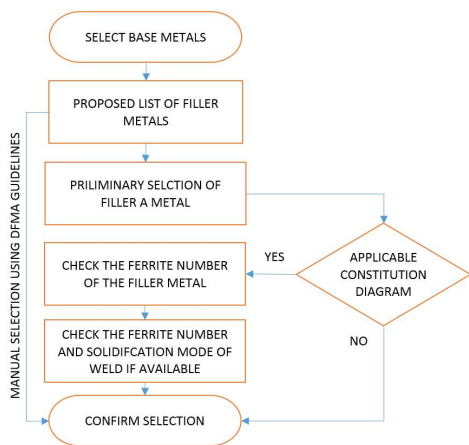


Fig. 3. Procedure for selecting the filler metal using application-based selection interface.

In the model, additional DFMA rules and guidelines are required for weldment design and structural welding standards, welding procedures specifications (WPS), welding procedure qualification tests (WPQT) and welder qualification tests (WQT). The WPS should be compatible with the selected base materials and processes and should include comprehensive instructions required to produce the weld, such as joint type and preparation, weld type, welding parameters, technique, consumables, interpass temperature and heat treatments. WPS is

qualified using WPQT provided by the DFMA guideline. Depending on the requirements of the relevant standards and the functional requirements of the structure, the WPQT may include various destructive tests such as tensile, toughness, hardness and bending, and corrosion tests as well as different nondestructive tests. WPQT results will determine if the WPS is qualified or modifications are needed.

EXAMPLE OF APPLICATION-BASED SELECTION METHOD IN PRACTICE

The application-based selection approach considers selection of materials as the initial and most critical stage of design, since the functional requirements, fabrication method and cost are all affected by the type of material used. Selection of material cannot rely on mechanical properties alone, as in traditional geometry-driven design methods, the type of application and service environment should also be taken into account. The application-based selection approach, by precluding unsuitable combinations, can considerably reduce the risk of improper selection. The approach also incorporates cost and manufacturing features (i.e. machinability, formability and weldability) in selection of material to ensure manufacturability and economical justification of design in addition to functional fulfilment.

Figs. 4-11 present the interface of a simplified application developed for the purpose of this study based on the flowsheets presented in Figs. 2-3. The application can potentially be used in conjunction with the material database of CAD tools. In this study, however, the method is proposed without making any changes to CAD programs. In this example, the offshore environment was chosen as the nominated application due to the significance of the application and fabrication considerations associated with weldment design in this ambience.

Fig. 4 shows initiation of the material selection by specifying the application. Fig. 5 shows a selection of materials recommended for offshore applications. In the current study, five materials are considered; namely, A 633 high strength low alloy steel (HSLAS), S 960 QC direct-quenched ultra-high strength steel (UHSS), 316 L austenitic stainless steel (ASS), 1.4529 super-austenitic stainless steel (SASS) and AISI 2205 duplex stainless steel (DSS).

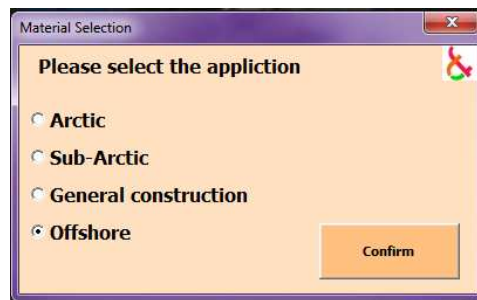


Fig. 4. Selection of application in the application-based interface.

A 633 is a normalized HSLA steel with enhanced notch toughness, which makes it suitable for welded structures operating in ambient temperatures as low as -45 °C (High-Strength Low-Alloy Steels, 2001). S 960 QC is a low-carbon, low-alloyed direct-quenched steel which is characterized by a favorable combination of very high strength, good toughness at temperatures even below -40 °C, as well as satisfactory formability and weldability (Farrokhi, 2015; Hemmilä, 2010; Pallaspuro, 2014). Alloy 316 L is a low-carbon ASS with excellent

resistance to atmospheric corrosion. 316 L possesses excellent strength and toughness at cryogenic temperatures and shows resistance to intergranular corrosion in marine environments (Davis, 1995). Alloy 1.4529 offers excellent toughness at cryogenic temperature together with good formability and weldability. This SASS is remarkably stronger than other 300 ASS series and shows superior resistance to numerous corrosive environments (Handbook of Stainless Steel, 2013). AISI 2205 is a duplex stainless steel with excellent resistance to general corrosion as well as stress corrosion cracking. In addition, AISI 2205 exhibits good toughness down to -45 °C, superior mechanical strength to austenitic grades, and good weldability (Handbook of Stainless Steel, 2013). The chemical composition of the five alloys is shown in Table 1.

Table 1. Chemical composition of four steel recommended for offshore application

Mat.	C	Mn	Cr	Ni	Mo	Nb	Cu	N	P+S	Si	Ti
A 633	.2	1.5	-	-	-	.05	-	-	.09	.5	-
S 960 QC	.09	1.05	.82	.04	.158	.003	.029	-	.002	.21	.07
316 L	.02	-	16.9	10.7	2.6	-	-	.1	.075	.75	-
1.4529	.01	-	20.5	24.8	6.5	-	1	.2	.04	.5	-
AISI 2205	.015	1.34	22.6	5.79	3.24	.009	.25	.179	.02	.39	-

As is shown in Fig. 9, material selection can done either manually or automatically from the list containing recommended metals.



Fig. 5. Material selection. Recommended materials can be loaded from the application database.

For manual selection, the designer needs to decide which material(s) would best meet the design requirements using the technical information tabulated in the form of a guideline next to each material, shown in Fig. 6. The guideline includes mechanical properties, weldability, formability and machinability information as well as carbon equivalent (C_{eq}) when applicable. The C_{eq} is calculated using Equation 1 (Dearden, 1940):

$$C_{eq} = C + Mn / 6 + (Cr + Mo + V) / 5 + (Ni + Cu) / 15 \quad (1)$$

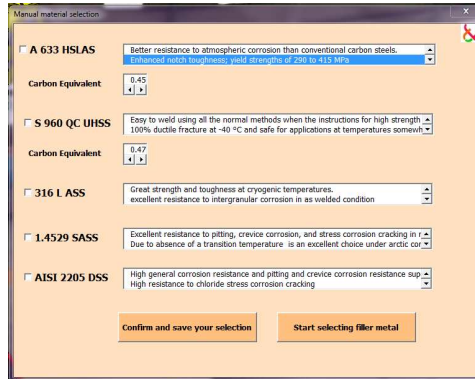


Fig. 6. Manual material selection interface. The guideline next to each material aids the designer in selection of suitable material.

For automatic selection, the designer needs to define how important a specific property of the material is for the design purpose. As shown in Fig. 7, a range of attributes are presented to be rated by the designer. These attributes are divided into quantitative and qualitative properties to provide a baseline for ranking and comparison. Table 2 shows the properties that are quantitatively compared.

Table 2. Comparison of the proposed materials based on properties having quantitative value.

Quantitative properties	A 633	S 960	316 L	1.4529	AISI 2205
Ultimate tensile strength (MPa)	≈ 630	1114	570	670	825
Charpy impact values at -40 °C (J)	34	60	180	200	50
Estimated price / ton (\$)	800	1200	3000	5000	2000

The best property within a range (e.g. strength) is valued with a 5 on a scale where 0 equals “unsuitable” and 5 equals “best value”, and the other properties are proportionally calculated in comparison with the best value. An example of the comparison of quantitative attributes is presented in Table 3.

Table 3. Comparative values calculated with respect to the best corresponding material property valued with a 5 on a scale where 0 equals “unsuitable” and 5 equals “best value”.

Material	Comparative values		
	Ultimate tensile strength	Charpy impact	Price per ton
A 633	2.8	0.9	5
S 960 QC	5	1.5	3.3
316 L	2.5	4.5	1.3
1.4529	3	5	0.8
AISI 2205	3.7	1.2	2

Material properties that are difficult to characterize with a definite quantity due to a lack of valid experimental data or their nature are qualitatively compared. As can be seen from Table 4, weldability, formability, and machinability are qualitatively evaluated from 0 to 5

where 0 means a property is unsuitable while 5 evaluates a property as excellent. The values are given based on data extracted from material handbooks and supplier catalogues (Handbook of Stainless Steel, 2013; Davis, 1995) (High-Strength Low-Alloy Steels, 2001) (ASM International Handbook Committee, 1990).



Fig. 7. Rating menu for assigning the weight of different material attributes in a design.

Table 4. Qualitative properties are evaluated from 0-5 where each number in succession stands for “unsuitable”, “fair”, “good”, “suitable” and “excellent”, respectively. Due to lack of experimental data the properties indicated with “*” are compared qualitatively.

Qualitative properties	A 633	S 960 QC	316 L	1.4529	AISI 2205
Weldability	3	3	4	3	3
*Formability	4	3	4	3	3
*Machinability	4	2	3	1	1
*Corrosion resistance	1	2	4	5	5

Weldability, for instance, is assessed based on chemical composition, hardness, microstructure, thermal expansion, needed pre-work and post-heat treatment, joint preparation and heat input precaution.

In the rating menu, shown in Fig. 7, a weight should be defined for each property on the basis of the service requirements. The weights can be assigned from 0-5, where each number in sequence stands for “not relevant”, “not important”, “important”, “very important” and “crucial”. The ranking is done simply by comparing the overall score of each material, which is obtained from summation of the defined weights multiplied with the relevant comparative values.

Fig. 8 shows the ranking done by the application according to the weighting shown in Fig. 7. For dissimilar welding, the first and second ranked materials can freely be selected to fulfill the service requirements.

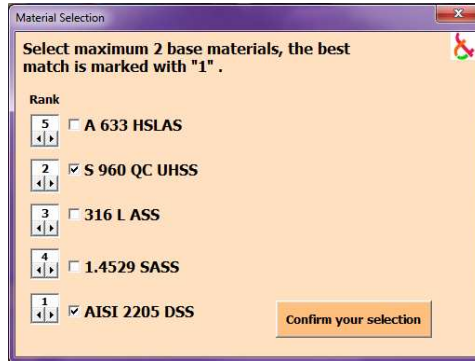


Fig. 8. Proposed materials ranked by their suitability for the design purpose.

The type of filler material is another critical element that determines many of the properties of a welded joint, including strength, toughness, corrosion resistance and surface properties. Thus, design of a weldment cannot only rely on the joint geometry and base metal properties, rather the combination of these two with a proper filler metal. Figs. 9-11 present the interface of the developed application for selecting filler metal with an assumption of GMAW as the welding process. As shown in Fig. 9, relevant filler metals for the selected base metals and similar or dissimilar welding are loaded from the database. For dissimilar welding and the selected metals in Fig. 8, applicable filler metals for GMAW include 904 L, 316 L-Si, 307 L, P 12, 16.55 which in this particular case are derived from the Avesta and Esab welding manual (Welding Consumables Handbook, 2005; Larén, 2004), although other manuals could also be used.

A guideline next to each filler metal containing technical information can aid the designer in the selection process, as seen in Fig. 9. An important factor in dissimilar welding of stainless steels is the ferrite number. A fully austenitic structure would be favorable for an improved mechanical properties and corrosion resistance. However, this increases the risk of solidification cracking and requires low heat input and accurate interpass temperature control. A small percentage of ferrite up to 4% would minimize this risk with minimum adverse effects on the toughness and corrosion resistance of the weld (Tasalloti, 2014). The ferrite number of the filler metal and the predicted ferrite number of the weld metal are also provided as an additional benchmark for decision-making, as shown in Fig. 9.

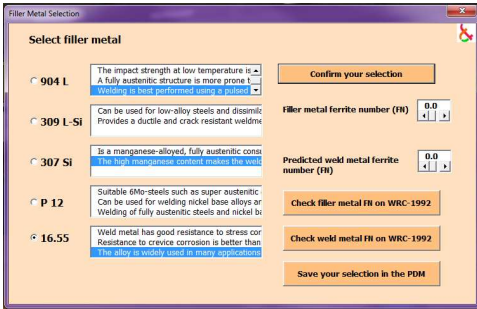


Fig. 9. Filler metals and their specifications recommended for a dissimilar weld between AISI 2205 and S 960 QC. The interface has an option to check the WRC-1992 diagram for the weld and filler metal.

The ferrite numbers are obtained from the Welding Research Council (WRC) -1992 (Kotecki, 1992) constitution diagram using Cr and Ni equivalents presented in Equation 2 and 3 and with an assumption of equal dilution of 15% from either base metal in the weld.

$$Cr_{eq} = Cr + Mo + 0.7 Nb \quad (2)$$

$$Ni_{eq} = Ni + 35 C + 20 N + 0.25 Cu \quad (3)$$

As shown in Fig.10 and Fig.11, the ferrite numbers and solidification mode can also be checked on the WRC-1992 diagram using the option available on the interface, illustrated in Fig. 9. For instance, a fully-austenitic solidification mode can be expected using 16.55 austenitic filler metal and selected base metals shown in Fig. 8.

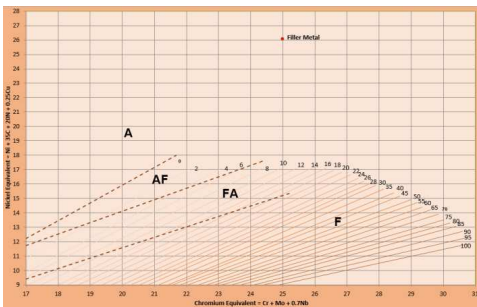


Fig. 10. 16.55 filler metal positioned on the WRC-1992 diagram.

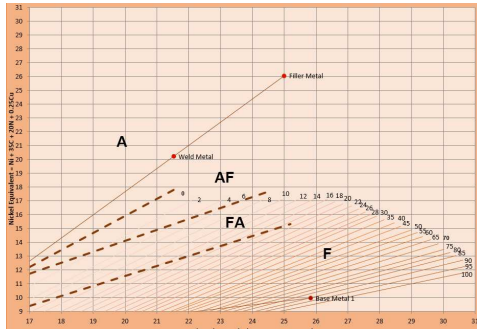


Fig. 11. Prediction of ferrite number and solidification mode for a weld between S 960 QC and AISI 2205 made using 16.55 filler metal with 70% dilution.

DISCUSSION

The main objective of this study was to utilize CE and DFMA strategy to achieve a more efficient weldment design procedure. For this purpose, a DFMA-based decision-making model was proposed to address the weldment considerations in terms of materials, welding process and filler metals. The current application-based selection approach takes into account the interaction of the base and filler metals and the welding process and its parameters in the design stage, which can substantially reduce the risk of incompatibilities and the need for rework during the manufacturing stage. In addition, this feature considerably increases the ability of the model to provide viable solutions for the design because it accounts for the importance of the metallurgy of the weld in determining key characteristics such as strength, hardness, toughness, and corrosion resistance. This feature can make the model more reliable compared to the approaches in (LeBacq, 2005; Lovatt, 1998; Maropoulos, 2000) and the traditional design method, which considers predominantly the thermomechanical properties of the base materials.

The application-based selection approach guides the designer to the best option in the list using a modified questionnaire-based selection strategy (Ashby, 2004) combined with an inductive reasoning selection method (Ashby, 2004; Kolodner, 1993; Kolodner 1992; Ashby, 2001) for selection of materials, welding processes and filler metals. The modification to the current approach reduces the number of potentially demanding questions faced by designers, which makes the approach more user-friendly than those in (LeBacq, 2005; Maropoulos, 2000). The approach defines a clear path for weldment design, which starts from selection of materials for the intended application. This is done by weighting material features relevant to the design intent. These features can include mechanical, physical and chemical characteristics, as well as cost-related attributes and manufacturability considerations, such as machinability, formability and weldability. The approach ensures that the selected materials can fulfil the requirements of the application as well as manufacturing considerations. Using the presented approach, when the materials have been selected (which embeds utilization, manufacturing and cost features) geometries and joints are designed commensurably. The embedded features in material selection can provide significant advantages over traditional geometry-driven design, where finding proper materials for the defined geometries after the conceptual design phase can lead to much iterative work, and trial and error. There is the possibility that the designer may

select materials that are not permitted for the desired application and/or lack easy manufacturability. The proposed approach can prevent such mistakes in design decisions and consequent failures during operation or costly rework during manufacturing. The approach can also be advantageous in providing a more realistic cost estimation of the weldment since all the components involved in making the weld are taken into account in the design stage.

The inductive reasoning feature of this approach helps not to entirely exclude the intellectual freedom of designers. This feature adds more flexibility to the model and allows the designer to test and analyze different options and make decisions based on personal knowledge or the technical data provided. The built-in expertise benefits most designers without specialized knowledge of welding and metallurgy. The benefits include a reduced risk of improper selection and consequent design failure, as well as facilitated decision-making process and decreased design time.

A possible limitation to the model is the extensive data and skill required to characterize all the lists, standards and guidelines for each application. However, this information can be compiled gradually according to the manufacturers' needs and resources. The database is created, developed, and maintained by experts and experienced designers. The database should be continuously updated with new solutions that have not been realized previously. The tool demonstrated in this study was made as proof of concept for the application-based selection method using a limited number of materials for one nominated application. For any new application, an expert (or experts) should supplement the database with recommended materials and index them for the application. Furthermore, the relevant qualitative and quantitative chemophysical and mechanical features should be extracted from material handbooks and other certified resources to be assigned to materials. The link between welding processes and materials is made as the material type and grade is defined. Proper filler metals and their chemical compositions should be also stored in the database and indexed with relevant material and welding process. If the new application requires a specific DFMA guideline regarding compatibility, complexity, cost, and quality, this should be also stored in the database.

Although the approach cannot easily be used for innovation, the model offers optimal solutions within the confines of current knowledge and reduces the chance of erroneous design decisions, which is an important consideration in critical applications.

CONCLUSIONS

In this study, the advantages of design for manufacturing and assembly (DFMA) strategy and concurrent engineering (CE) were exploited, in order to facilitate decision-making procedure in weldment design. An application-based selection method was introduced for determining suitable base materials, the welding process and filler metals. The usability of this approach was illustrated for selection of the base and filler metals for an offshore application. For the specific example considered in this work, the proposed model offers the following advantages:

- Easier and faster selection of material and filler metals.
- Enables designers to expeditiously evaluate different material and filler metal options, with no extra expertise required of designers.
- Minimized risk of failure during service since the built-in expertise constrains selection to an approved list of base and filler metals, for a specified application.

However, further studies are required to assess the efficacy and validity of the model for other applications in terms of selection of materials, welding processes and filler metals as well as design reliability and manufacturability.

REFERENCES

- Ashby MF (1999). *Materials Selection in Mechanical Design*, Oxford, Butterworth Heinemann.
- Ashby MF, and Johnson, KW (2001). *Classification and choice in product design*, Cambridge, Cambridge Engineering Design Centre.
- Ashby, MF, Brechet, YJM, Cebon, D, and Salvo, L (2004) "Selection strategies for materials and processes," *Materials and Design* 25, 51–67.
- ASM International Handbook Committee, ed., (1990). *ASM Handbook Vol. 01: Properties and Selection: Irons, Steels, and High-Performance Alloys*, ASM International.
- Charles, JA, Crane, FAA, and Furness, JAG (1997). *Selection and Use of Engineering Materials*, Oxford, Butterworth Heinemann.
- Chen, K-H, Chen, S-J, Lin, L, and Changchien, SW (1998). "An integrated graphical user interface (GUI) for concurrent engineering design of mechanical parts," *Comput Integr Manuf Syst*, 11, 91–112.
- Davis, JR, ed., (1995). *ASM Specialty Handbook: Stainless Steels*, ASM International.
- Davis, JR, ed., (2001). "High-Strength Low-Alloy Steels" In: *Alloying: Understanding the Basics*, Ohio, ASM International, 193–206.
- Dearden, J, and O'Neil, H (1940). "A guide to the selection and welding of low alloy structural steels," *Trans Int Weld*, 3(10), 203–214.
- Dieter, GE (2012). *Engineering Design, a Materials and Processing Approach*, New York, McGraw-Hill.
- Eskelinen, H (2013). "Aspects of integration between DFMA approaches and PDM data," Huhtala, M, and Eskelinen, H, ed., *Proceedings of the PDM 2013 Conference*, Lappeenranta, 13–21.
- Eskelinen, H (2013). "Review of traditional DFMA principles," In: *Advanced Approaches to Analytical and Systematic DFMA Analysis*, Eskelinen, H, ed., Lappeenranta University of Technology, 6–30.
- Farag, MM (1989). *Selection of Materials and Manufacturing Processes for Engineering Design*. Englewood Cliffs, NJ, Prentice Hall.
- Farrokhi, F, Siltanen, J, and Salminen, A (2015). "Fiber Laser Welding of Direct Quenched Ultra High Strength Steels-Evaluation of Hardness, Tensile Strength, and Toughness Properties at Subzero Temperatures," *J Manuf Sci Eng*, 137(6), 061012-061012-10.
- Handbook of Stainless Steel (2013), Outokumpu Oyj, Espoo, Finland, www.outokumpu.com.
- Hemmilä, M, Hirvi, A, Kömi, J, Laitinen, M, and et al. (2010). *Technological properties of direct-quenched structural steels with yield strength 900-960 MPa as cut length and hollow sections*. Rautaruukki Corporation.
- Kolodner, J (1993). *Case Based Reasoning*, San Mateo, CA: Morgan Kaufmann.
- Kolodner, JL (1992). "An introduction to case-based reasoning," *Artificial Intelligence Review*, 6, 3–34.
- Kotecki, DJ, and Siewert, TA (1992). "WRC-1992 Constitution Diagram for Stain-less Steel Weld Metals: A Modification of the WRC-1988 Diagram," *Weld J*, 71, 171s–178s.
- Kwon, Y, Wu, T, and Saldivar, JO (2004). "SMWA: A CAD-based decision support system for the efficient design of welding," *Concurrent Engineering* 12(4), 295–304.
- Larén, M, ed., (2004). *The Avesta Welding Manual*, Practice and products for stainless steel welding, Sweden, Avesta Welding AB.
- LeBacqz, C, Brechet, Y, Shercliff, HR, Jeggy, T, and Salvo, L (2005). "Selection of joining methods in mechanical design," *Mater Des*, 23, 405–416.
- Lovatt, AM, and Shercliff, HR (1998). "Manufacturing process selection in engineering design. Part 2: a methodology for creating task-based process selection procedures," *Mater Des*, 19(5–6), 217–

- Maropoulos, PG, Yao, Z, Bradley, HD, and Par, KYG (2000). "An integrated design and planning environment for welding, Part 1: Product modelling." *Journal of Materials Processing Technology*, 107, 3–8.
- Niebles, E, Maury, H, Gómez, H, and Riba, C (2006) "Definition and validation of a knowledge base and the architecture of a computer tool to assist the design and manufacturing of welded products." 10th International Research/Expert Conference, Trends in the Development of Machinery and Associated Technology, Barcelona-Lloret de Mar, Spain.
- Pallaspuro, S, Limnell, T, and Suikkan, P (2014). "T₀ – T₂₈₁ correlation of low-carbon ultra-high-strength quenched steels," *Procedia Mater Sci*, 3, 1032–1037.
- Riboulet, V, Marin, PR, Gowers, S, and Wurtz, F, (2005). "A framework supporting collaborative optimisation for multi professional design teams," In: *Advances in Integrated Design and Manufacturing in Mechanical Engineering*, Dordrecht, The Netherlands, Springer, 123–134
- Selvaraj, P, Radhakrishnan, P, and Adithan, M (2009). "An integrated approach to design for manufacturing and assembly based on reduction of product development time and cost," *Int J Adv Manuf Technol*, 42, 13–29.
- Shah, JJ, and Mantyla, M (1995). *Parametric and Feature-Based CAD/CAM: Concepts, Techniques, and Applications*. John Wiley.
- Tasalotti, H, Eskelinen, H, Kah, P, and Martikainen, J (2016). "An integrated DFMA–PDM model for the design and analysis of challenging similar and dissimilar welds," *Mater Des*, 89, 421–431.
- Tasalotti, H, Kah, P, and Martikainen, J (2014). "Effects of welding wire and torch weaving on GMAW of S355 MC and AISI 304 L dissimilar welds," *Int J Adv Manuf Technol*, 71, 197–205.
- Welding Consumables Handbook (2005), ESAB. www.esab.com.

Publication VI

Tasalloti, H., Kah, P., and Martikainen, J.

**Effect of heat input on dissimilar welds of ultra high strength steel and duplex stainless steel:
Microstructural and compositional analysis**

Reprinted with permission from
Materials Characterization
Vol. 123, pp. 29-41, 2017
© 2016, Elsevier Inc.



Contents lists available at ScienceDirect

Materials Characterization

journal homepage: www.elsevier.com/locate/matchar

Effect of heat input on dissimilar welds of ultra high strength steel and duplex stainless steel: Microstructural and compositional analysis

H. Tasalloti^{*}, P. Kah, J. Martikainen

Lappeenranta University of Technology (LUT), School of Energy Systems, Welding Laboratory, P.O. Box 20, 53851 Lappeenranta, Finland

ARTICLE INFO

Article history:

Received 14 May 2016
 Received in revised form 7 November 2016
 Accepted 12 November 2016
 Available online 14 November 2016

Keywords:

Direct-quenched ultra high strength steel
 Duplex stainless steel
 Dissimilar welding
 Microstructural analysis
 Chemical composition analysis
 Macrosegregation

ABSTRACT

The effect of heat input on the microstructure and compositional heterogeneity of welds of direct-quenched ultra high strength steel (Optim 960 QC) and duplex stainless steel (UNS S32205) was studied. The dissimilar welds were made using GMAW with a fully austenitic filler wire. In addition to grain coarsening in the heat affected zone (HAZ) of the ferritic side, it was found that an increase in heat input correlatively increased the proportional volume of bainitic to martensitic phases. Coarse ferritic grains were observed in the duplex HAZ. Higher heat input, however, had a beneficial effect on the nucleation of austenite in the HAZ. Heat input had a regulatory effect on grain growth within the austenitic weld and more favorable equiaxed austenite was obtained with higher heat input. On the ferritic side of the welds, macrosegregation in the form of a martensitic intermediate zone was observed for all the cooling rates studied. However, on the duplex side, macrosegregation in the fusion boundary was only noticed with higher cooling rates. Microstructural observations and compositional analysis suggest that higher heat input could be beneficial for the structural integrity of the weld despite higher heat input increasing the extent of adverse coarse grains in the HAZ, especially on the ferritic side.

© 2016 Elsevier Inc. All rights reserved.

1. Introduction

Direct-quenched (DQ) ultra high strength steel (UHSS) is a rather recent development that combines lower production cost with enhanced strength, toughness and weldability compared to traditional quenched and tempered (QT) grades [1,2]. These advantages are achieved using a thermomechanical controlled process that can potentially improve steel strength to a level that is only achievable in QT grades by an increase in alloying contents [3]. The features of ultra high strength DQ steels can be beneficial in a wide range of weldment designs where resistance to intense load and suitability for demanding service conditions are required.

In many welding applications, dissimilar combination of metals is desirable, and dissimilar welding of ferritic steels and stainless steels has been a prominent application in numerous fields of industry, mainly for economic reasons. Of the stainless steels available, duplex grades offer outstanding mechanical properties together with superb resistance to different forms of corrosion at a modest price compared to high Ni grades [4]. The ability to achieve high quality welds of ultra high strength steel (DQ) and duplex stainless steel would extend the application range of dissimilar welding to many areas of construction, oil and gas exploration, transportation and other applications requiring

a combination of good mechanical properties and high corrosion resistance where cost and weight are major considerations.

Similar welding of QT and dual-phase (DP) grades of ultra high strength steel has been the subject of much study in the literature [5–9]. There is also abundant scientific work on welding of duplex stainless steels (DSS) [10–13]. In contrast, study of welding of DQ grades of UHSS, particularly as regards microstructure and mechanical properties, is in its infancy. Moreover, dissimilar welding of direct-quenched UHSS and DSS has not been widely studied. Further work is thus required to develop a comprehensive understanding of the weld metallurgy and characteristics of such welds as functions of the welding process parameters and welding specifications. In such dissimilar welding, selection of the welding parameters is complicated by considerations arising from the characteristics of each parent metal. The practical difficulties can increase further when filler metal of a dissimilar composition to the parent metals is used.

With UHSS, regardless of the specific welding process and alloy used, major documented problems include: heat affected zone (HAZ) cracking, HAZ softening, and insufficient toughness and ductility [5–7]. The aforementioned defects generally stem from inappropriate heat input and cooling rate, the chemical composition of the material, the formation of coarse grains, and variation in the proportion of ductile to brittle morphologies in the microstructure of the HAZ and weld [6,8,9].

With DSS, degradation of mechanical properties and corrosion resistance are the main issues presented in the literature. These problems are generally identified as being a consequence of inappropriate heat input and excessive thermal cycles that can cause disparity between

^{*} Corresponding author at: Laboratory of Welding, Lappeenranta University of Technology, Skinnarilankatu 34, 53850 Lappeenranta, Finland.

E-mail addresses: hamed.tasalloti.kashani@student.lut.fi (H. Tasalloti), paul.kah@lut.fi (P. Kah), jukka.martikainen@lut.fi (J. Martikainen).

the volume percentage of ferrite and austenite, and deleterious precipitations such as sigma (σ), chi (χ), and chromium nitride (Cr_2N) in the fusion zone and HAZ of DSSs [10–13].

Although dissimilar welding of direct-quenched UHSS and DSS has received little attention, dissimilar welding of DSS and high-strength low alloy (HSLA) steel as well as carbon steel is well presented in the literature. Similarities in the microstructure and mechanical behavior of these steels make this previous work of relevance to the current study. Eghlimi et al. [14] reported that repeated thermal cycles increased the growth of secondary austenite (γ_2) with a dominant Widmanstätten morphology in DSS. Wang et al. [15] argued that favorable mechanical properties can be obtained with a higher amount of austenite. They indicated that a higher heat input extended the decarburized layer at the fusion boundary of HSLA steel. Sadeghian et al. [16] reported that increased austenitic nucleation with higher heat input, on the duplex side, resulted in increased impact strength of the weld. Srinivasan et al. [17] identified a soft C-depleted boundary at the fusion line of low alloy steel as a result of intense heat and the carbon affinity of Cr-rich DSS weld metal. Mendoza et al. [18] stated that lower cooling during multipass welding could favor the growth of austenite and result in improved mechanical properties of the weld, while accelerated cooling rates can cause precipitation of intermetallic phases and degradation of mechanical properties. Wang et al. [19] recommended a lower cooling rate for prevention of hydrogen induced cracking at the ferritic side of the weld. Odegard et al. [20] noted that higher dilution from carbon steel promoted ferritic growth in the weld and resulted in degeneration of corrosion resistance and mechanical properties. They proposed that higher heat input can make the weld susceptible to solidification cracking. Barnhouse et al. [21] suggested that filler metal plays a greater role than heat input in controlling the balance between the ferritic and austenitic phases. They recommended a combination of duplex grade filler wire, high heat input, and limited dilution from the carbon steel in the root pass for improved corrosion resistance and toughness of the weld. However, for cryogenic temperatures, they recommended Ni-based fillers for superior ductility. In addition, some studies have indicated the formation of a martensitic band contiguous with the fusion boundary at the ferritic side [14,16].

In the current study, dissimilar welding of a commercial grade of a direct-quenched ultra high strength steel (UHSS), Optim 960 QC, and a duplex stainless steel (DSS), UNS S32205, was done using an automatic GMAW process and a fully austenitic filler wire. The objective of the study is to provide detailed understanding of the microstructural and solidification behavior of dissimilar welds of UHSS DQ and DSS under the influence of different heat inputs. To this end, detailed analysis of the microstructure and chemical composition in the weld, fusion boundaries and HAZs is presented. The outcome of this research can be beneficial for assessment of the suitability of such dissimilar metal combinations for engineering applications.

2. Experimental Procedure

Single pass dissimilar welds were made on 5 mm thick plates of a commercial direct-quenched ultra high strength steel (UHSS), Optim 960 QC, and a duplex stainless steel (DSS), UNS S32205, using fully automated GMAW. The as-received plates were machined to dimensions of $350 \times 150 \times 5$ mm in accordance with EN ISO 15614-1. The plates were machined to prepare single V-groove butt joint configurations with an angle of 60° . Removable fiberglass tape was used for backing and the root-face and airgap were both zero. A schematic of the weld joint is shown in Fig. 1.

Butt joints were made at three different welding speeds, namely, 7.1 m/s, 8 m/s and 9 m/s. Table 1 presents the parameters used to make the weld samples. Esab OK Autrod 16.55 (AWS A5.9: ER 385), a fully austenitic filler wire (1 mm diameter), was used as the filler wire, and a mixture of 98% Ar + 2% CO_2 was supplied as a shielding gas at a constant flowrate of 15 l/min. The tip-to-work (stick out)

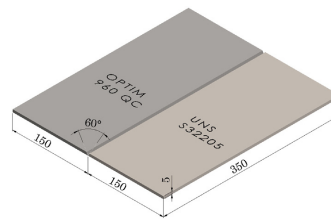


Fig. 1. Schematic of the joint setup used in the experiments.

distance was maintained at 13 mm throughout the entire welding process. The chemical composition of the base and filler metals are presented in Table 2.

Two sets of thermocouples at a distance of 2 and 3 mm from the fusion line on each side of the weld were used to measure the cooling rate of the HAZ. Metallography samples were polished (final polish with $1 \mu\text{m}$ diamond paste) and etched in compliance with EN ISO 17639 standard for microscopic examination of welds and ISO/TR 16060 for etchants. The DSS side was etched using a standard Cuprochloric solution 2 (5 g $\text{CuCl}_2 + 100 \text{ ml HCl} + 100 \text{ ml C}_2\text{H}_5\text{OH} + 100 \text{ ml H}_2\text{O}$) and Nital (95 ml $\text{C}_2\text{H}_5\text{OH} + 5 \text{ ml HNO}_3$) was used for etching the UHSS side. The etching time was 15 s and 30 s for Nital and Cuprochloric solution 2, respectively.

The samples were inspected using light microscopy as well as scanning electron microscopy (SEM). In addition, energy dispersive spectroscopy (EDS) analysis was performed to identify compositional variations in the weld specimens. Prior to the EDS analysis, the specimens were cleaned in an ultrasonic bath of hot $\text{C}_3\text{H}_8\text{O}$ and $\text{C}_2\text{H}_6\text{O}$ to ensure removal of any external dirt. For convenience, the base and filler metals are henceforth referred to as S 960, S 32205 and 16.55, and the weld samples are named WS 7.1, WS 8, and WS 9, based on the welding speed used.

3. Results and Discussion

3.1. Macrostructure

A macrograph of the weld specimens prepared for this study is shown in Fig. 2. In the figure, the effect of grain coarsening can be discerned on the HAZ of both the S 960 and S 32205 base metals, on the left and right side of the welded joints, respectively. However, the appearance of coarse grains extends over a wider span on the S 960 side than the S 32205 side, which is indicative of higher sensitivity of the S 960 base metal to the heat input than the S 32205 metal. On the ferritic steel side, intense grain coarsening was noticeable to a maximum distance of about 3.5, 2.5, and 1.5 mm from the fusion line for the WS 7.1, WS 8 and WS 9, respectively, measured around the weld throat. In comparison, severe grain coarsening on the HAZ of the S 32205 was only appreciable to a distance range about 2, 1.5, and 1 mm for the WS 7.1, WS 8 and WS 9, respectively, measured from the fusion line on the weld throat.

Table 1
Welding parameters used for the weld samples: arc current (I), arc voltage (U), welding speed (v), wire feed speed (WFS), arc energy (E), and heat input (Q).

I (A)	U (V)	v (mm/s)	WFS (m/min)	E (kJ/mm)	Q (kJ/mm)
257	29.8	7.1	10.6	1.08	0.86
224	28.7	8	10	0.80	0.64
204	26.4	9	9	0.60	0.48

Table 2
Chemical composition (wt.%) of the base and filler metals.

Metal	C	Si	Mn	P + S	Al	Nb	Cu	Cr	Ni	Mo	Other
S 960	0.09	0.21	1.05	0.014	0.030	0.003	0.025	0.82	0.04	0.158	0.002 (B) 0.008 (V) 0.032 (Ti)
S 32205	0.015	0.39	1.34	0.026	–	0.009	0.25	22.59	5.79	3.24	0.130 (Co) 0.179 (N)
16.55	0.02	0.4	1.7	–	–	–	1.4	20.5	25	4.5	–

3.2. Microstructure

SEM images of the as-received parent metals are shown in Fig. 3. The microstructure of S 960 contains fine martensitic-bainitic grains that are formed in the rolling direction, as can be seen in Fig. 3(a). The martensitic phase appears in the form of pancaked or elongated prior austenite (γ) grains in the rolling direction [3]. Fig. 3(b) shows a typical DSS microstructure with nearly equal elongated lamella of ferritic-austenitic regions.

The microstructure of the HAZ of the weld samples on the UHSS side at a distance of about 1 mm from the fusion boundary is shown in Fig. 4(a)–(c). The micrographs show significant grain coarsening. Moreover, it appears that the amount and morphology of the formed phases have been to some extent influenced by the heat input. For instance, bainitic phase is dominant in WS 7.1, while martensite dominates in the HAZ of WS 9, as can be seen in Fig. 4(a) and (c) respectively. In contrast, bainite and martensite are almost evenly distributed in the HAZ of WS 8, as seen from Fig. 4(c).

Fig. 5 presents a time-temperature graph of the HAZ (at 2 and 3 mm distance from the fusion line) on the UHSS side, plotted on a continuous cooling transformation (C.C.T.) diagram of a quenched and tempered steel with very close chemical composition to S 960 [22]. From the figure, it is apparent that with initiation of welding, the HAZ temperature almost instantaneously rose to ranges beyond the upper intercritical temperature (AC_2), where the microstructure, theoretically, mostly transferred to γ . This is followed by cooling below the lower intercritical temperature (AC_1), at which decomposition of γ started. Subsequently, further cooling, down to a temperature of about 550 °C, inaugurated bainitic transformation, which preceded martensitic formation at lower temperatures. It is clear from the diagram that the bainite start temperature decreases as the cooling rate increases. Thus, more bainitic phase can be expected with lower cooling rates, in agreement with the observation in Fig. 4. Note that the diagram reached a plateau above AC_2 due to the temperature exceeding the upper-limit of the thermocouples used.

The SEM image shown in Fig. 6 reveals details of the HAZ microstructure. In the figure, only the HAZ of WS 9 is shown, as the microstructural features were similar for all the samples. A network of prior- γ boundaries is clearly visible in the figure.

Martensitic structure is detectable with a characteristic of barely etched almost uniform plates within prior- γ boundaries.

The bainitic phase consists of dominantly lower bainite (B_L) and upper bainite (B_U) morphology in a lower proportion. The bainitic regions featuring laths of lower and upper bainite are indicated on Fig. 6. As can be seen from the figure, the coarse laths of B_L generally partition the prior- γ grains intersecting each other, which differentiates them from B_U with almost parallel laths filling the prior- γ grains [23]. Fig. 7 presents a high magnification BSE image of the bainitic constituent within the outlined region shown in Fig. 6. The distinct appearance of lower bainite laths is associated with fast cooling rates and rapid propagation of bainitic plates [23,24]. However, the mechanism of bainite formation is not well established and still remains somewhat unclear. The explicative hypotheses generally involve either a diffusional [25] or a displacive mechanism [26], the detailed consideration of which is beyond the scope of the current study. Nonetheless, it should be noted that the observations suggest that nucleation of bainite involves paraequilibrium partitioning of carbon. In the case of upper bainite, cementite precipitates from C-enriched austenite entirely between the laths of bainitic ferrite. In the case of lower bainite, reduction in transformation temperature reduces the diffusion rate, which results in some precipitation of fine carbide in the supersaturated bainitic ferrite plates [26]. As can be seen from Fig. 7, cementite (CM) with a grayish appearance in this figure is placed between and within the sheaf-like B_L . The protruding features that appear as elongated and parallelly-aligned islands were identified as γ or M/ γ constituent [27].

A number of studies have shown the beneficial effects of bainitic morphology on strength and toughness due to the high dislocation density in their lath-like structure [28–30]. However, superior mechanical properties are associated with lower bainite than upper bainite. The more uniform and finer distribution of carbide in lower bainite has been suggested in the literature as the reason for the outstanding mechanical properties [29]. Additionally, Abbaszadeh et al. [28] proposed that partitioning of prior- γ grains by the lower bainite can result in refinement of the martensite substructures and thus increase the strength.

Fig. 8 shows a martensitic grain formed from a prior- γ grain; the prior- γ boundary is clearly visible. Within the grain, blocks of martensite are formed from laths parallelly aligned to each other and parallel blocks having a common habit plan with the prior- γ grain configure packets of martensite [31]. The boundary of one packet divided into blocks of martensite laths is delineated with a dotted line in Fig. 8 for better identification. As can be seen from the figure, within each packet,

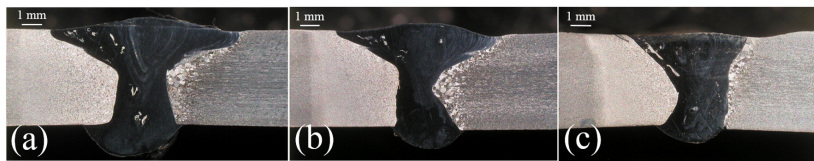


Fig. 2. Macrograph of weld samples: (a) WS 7.1; (b) WS 8; (c) WS 9. In the figure, the effect of grain coarsening can be noticed on the HAZ of the S 960 base metal (left side of the welded joint) and S 32205 (right side of the welded joint).

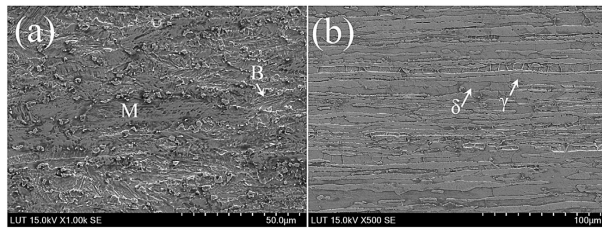


Fig. 3. SEM images of as-received parent metals: (a) S 960 containing bainite (B) and martensite (M); (b) S 32205 containing nearly parallel lamella of austenite (γ) and ferrite (δ).

the crystallographic orientations of retained γ are almost identical, which is in agreement with observations in [32]. The retained γ is C-enriched during bainitic transformation, which improves its stability at room temperature [27,33].

Some research has suggested positive effects of highly deformed retained γ on transformation-induced plasticity (TRIP) properties [27, 32]. The TRIP phenomenon is associated with transformation of metastable retained γ to martensite during straining of the steel, which can contribute significantly to both tensile strength and ductility of the steel [27,33,34]. It is believed that a higher volume fraction of retained γ leads to an increased strain-hardening coefficient and thus an increase in elongation [35]. It is suggested that the presence of thin film-like plastically deformed retained γ in the vicinity of the fracture path can blunt the propagating cracks and contribute to improvement in the toughness of the steel [30,33,34].

From the C.C.T. diagram in Fig. 5, it can be seen that martensitic growth is limited to increased cooling rates, which can also cause increase in dislocation density and hardness [24]. The interaction of higher dislocation density and TRIP effects can enhance the tensile strength and ductility of the steel [32].

The microstructure of the HAZ on the DSS side is illustrated in Fig. 9(a)–(c). The final microstructure of the HAZ is determined by solid state phase transformations from γ to δ and vice versa that take place during welding [36]. As seen in the figure, the HAZ has undergone a distinct change in microstructure. The main morphology of γ is grain boundary austenite (GBA), which is detectable by allotriomorphic formations at the prior- δ grain boundaries [10,14], and which is evident at the boundaries of coarse ferrite grains in Fig. 9. The morphology of GBA is better visible in the BSE image shown in Fig. 10. For S 32205, transformation from γ to δ starts at a temperature around 855 °C and observations in [37] suggest nearly complete decomposition of γ to δ as the temperature exceeds 1350 °C.

As can be seen from the cooling rate diagram in Fig. 11, the temperature in the HAZ (at 2 mm distance from the fusion line) exceeded 1100 °C for a period of less than 10 s, which can be considered too short for full ferritization. Thus, upon cooling, GBA started to nucleate from larger untransformed γ , which created the jagged appearance that is clearly visible in Fig. 10.

Widmanstätten austenite (WA), another common morphology, nucleates at lower temperatures than GBA [38]. WA grows as needle-like elongated plates, usually initiating from GBA and extending toward the δ grains [14], as can be seen in Figs. 9 and 10. In addition, some growth of intragranular austenite (IGA), scattered within the δ grains, can be discerned in Fig. 9. The lattice diffusion of IGA is known to be slower than the allotriomorphic growth of GBA and WA. As a result, IGA will mainly grow when enough undercooling is available [14]. Consequently, IGA morphology only appeared in a small amount in comparison with GBA and WA, as can be seen in Fig. 9.

Chromium nitride (Cr_2N) precipitation is a commonly reported feature in the HAZ of DSS. Severe degradation of corrosion resistance and toughness is associated with Cr_2N precipitation [10,12]. In some studies, Cr_2N formation is characterized as clusters of dark etched particles (depending on the etchant used), mainly within the ferrite grains [39], and to a lower extent at δ/δ and δ/γ grain boundaries [10]. A similar characteristic in the form of coarse and dark etched colonies was observed primarily in the middle of δ grains, visible in Fig. 9(a)–(c).

Fig. 11 presents temperature over time for the HAZ (measured at 2 and 3 mm distance from the fusion boundary) plotted on a time temperature precipitation (T.T.P.) diagram of S 32205 [22]. From the figure, it seems that cooling of the HAZ has taken place in a much shorter period of time than is required for formation of Cr_2N and other types of precipitation. However, it should be noted that T.T.P. diagrams are generally derived from isothermal heat treatments and do not take the effect of different cooling rates into consideration [22]. While, Cr_2N can form under both isothermal and cooling conditions [40], it is well established in the literature that rapid cooling rates could favor precipitation of Cr_2N [10,37,40–43]. As can be seen from Fig. 11, the initiation of welding almost instantaneously heated the HAZ of S 32205 to temperatures above 1100 °C, i.e. temperatures at which the austenite starts to dissolve into ferrite. The DSSs are alloyed with nitrogen, which is almost entirely retained in solid solution within the austenite, which has a high nitrogen solubility relative to the ferrite. As the partially or totally ferritized microstructure of the HAZ cools rapidly to temperatures below 1100 °C, the ferrite becomes supersaturated in nitrogen [10]. Consequently, the transformation behavior will not conform to that of a duplex structure but will be as a nitrogen supersaturated ferrite

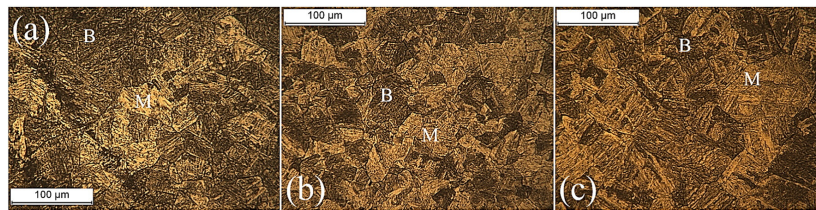


Fig. 4. Formation of coarse grains in the HAZ at the S 960 side. Bainite (B) with darker appearance can be differentiated from martensite (M). (a) WS 7.1, predominantly bainitic morphologies; (b) WS 8, roughly even balance of bainitic and martensitic morphologies; and (c) WS 9, predominantly martensitic morphologies.

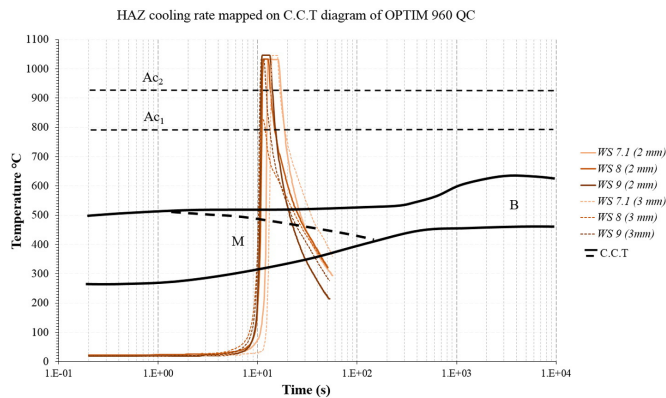


Fig. 5. HAZ time-temperature diagram plotted on a C.C.T. diagram of a quenched and tempered steel of a comparable composition to S 960. Variation of temperature with time as a result of welding was measured at distances of 2 and 3 mm from the fusion boundary in the HAZ of the S 960 metal.

structure with very low solubility of nitrogen, which can result in competition between Cr_2N and austenite precipitation [10]. Hence, a very rapid cooling rate in the HAZ cannot restrain the precipitation of Cr_2N [10,40,41,43].

The EDS analyses presented in Fig. 12 and Table 3 provide a comparison between the compositions of a coarse etched ferritic domain with that of a ferritic grain and an austenitic grain. As can be seen, no meaningful variation between the compositions of the fine etched and coarse etched ferritic domains can be ascertained. Thus, the observed contrast between the ferritic regions can be attributed to the effect of etchant on the topography of the surface. It should be noted that wt.% of C is excluded from the results due to inaccuracy related to the technical difficulties of analysis of light elements by EDS.

A high magnification SEM image of the coarse etched ferritic region also suggests that no detrimental precipitations have taken place in this region, Fig. 13.

The microstructure of the fusion boundary on the UHSS side of the dissimilar weld can be seen in Fig. 14(a)–(c). The figure shows fully austenitic structures without noticeable formation of ferrite in the interdendritic regions. This can indicate a fully austenite (A) solidification mode [44].

It is claimed that type-A solidification can occur where $\text{Cr}_{\text{eq}}/\text{Ni}_{\text{eq}}$ of the interdendritic liquid is sufficiently low that it precludes reaching the eutectoid composition and, consequently, impedes the nucleation of eutectoid ferrite [45]. The relation between $\text{Cr}_{\text{eq}}/\text{Ni}_{\text{eq}}$ and the solidification mode can be observed from a schematic of the pseudo-binary diagram [44] shown in Fig. 15. However, the EDS analysis, discussed in the next section, revealed ferrite stabilizing elements (i.e. Cr and Mo) partitioned into the interdendritic regions at some parts of the weld metals (Figs. 21 and 22). Therefore, formation of a small percentage of δ in the interdendritic regions during the last stage of solidification can be deduced, which further suggests a primary austenite (AF) solidification mode [46].

Equiaxed grain growth of γ in WS 7.1, in contrast with columnar and dendritic growth in WS 8 and WS 9, is also noticeable in Fig. 13. In steels and stainless steels, fine equiaxed grains are generally considered to be advantageous for increasing resistance to solidification cracking as well as improving the ductility and fracture toughness of the weld [47]. It is theorized that equiaxed growth takes place when a sufficiently long constitutional undercooling is available, while columnar growth is a concomitant of high cooling rates [38,47]. This is in agreement with the more columnar dendrites observed in WS 8 and WS 9 with higher cooling rates.

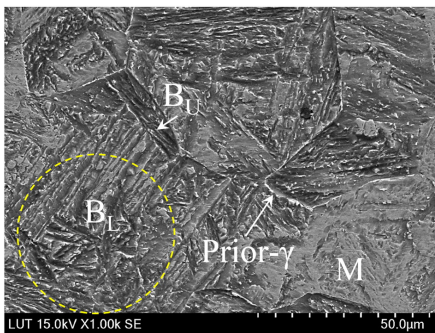


Fig. 6. Microstructure of the HAZ on the S 960 side of WS 9. The SEM image shows the coexistence of martensite (M), lower bainite (B_L) laths (within the region circled with a dotted line), and upper bainite (B_U) laths within a prior-austenite (γ) grain. Prior- γ boundaries are clearly visible.

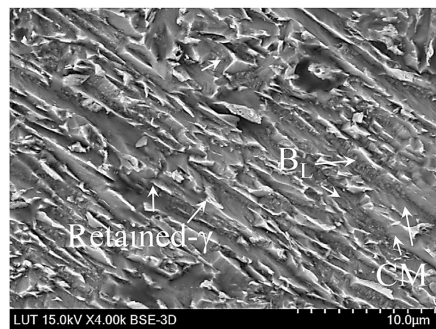


Fig. 7. SE and BSE SEM images of lower-bainite (B_L) in the HAZ of WS 9. Cementite (CM) positioned between the bainite laths; decomposition products of prior-austenite (γ) (retained- γ /martensite) are evident as elongated and roughly parallel islands.

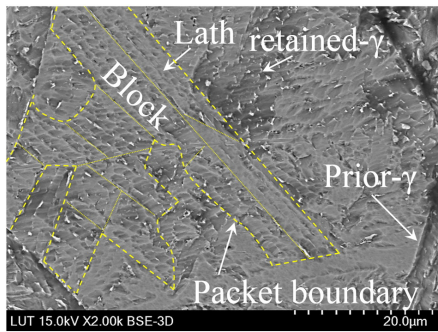


Fig. 8. BSE image of a martensitic grain within a prior-austenite (γ) grain boundary. Laths, packets, and blocks of martensite (M) are discernible from the orientation of the retained austenitic phases. The boundaries of a packet of M and its constituent blocks are outlined in the figure with a dotted line.

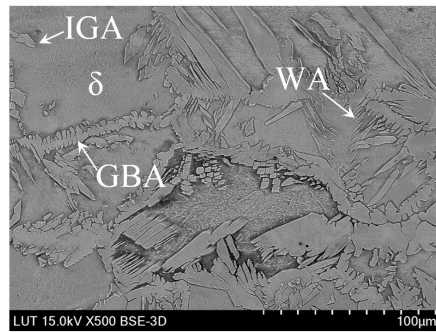


Fig. 10. BSE image of the HAZ on the S 32205 side. Different morphologies of austenite are seen, namely: grain boundary austenite (GBA), Widmanstätten austenite (WA), and intragranular austenite (IGA). Fine etched and coarse etched domains of ferrite (δ) are also detectable.

A notable feature of the weld metal in Fig. 14(a) and (c) is a narrow unetched intermediate zone with a planar solidification. Such a characteristic is commonly found at the weld interface of austenitic and ferritic steels and is generally identified as martensite in the literature [48]. Doody [49] reported a martensitic zone when welding carbon steel to stainless steel using Ni-based filler metals. He used the term “beaches” to describe this intermediate mixed zone with a composition between the compositions of the base and bulk weld metal.

Fig. 14(b) shows a distinct intermediate zone with a composite appearance of base and weld metals that characterizes a partially mixed zone (PMZ) [47]. Omar [50] reported such regions as beaches of martensite and peninsulas possessing base metal constitution. Both aforementioned intermediate zones are classified as macrosegregation in the literature [47,51] because the compositions have a gradient over a bulky span (100–200 μm), whereas in microsegregation the compositions differ over the span of a dendrite arm or cell spacing [51].

Another form of macrosegregation with resemblance to islands that illustrates the base metal structure [50] was found along the fusion boundary of WS 9, as clearly seen in Fig. 16. Kou et al. [51] explained the formation of segregated islands as occurring as a result of the difference in liquidus temperature of the base ($\sim 1530^\circ\text{C}$) and weld metal ($\sim 1400^\circ\text{C}$). According to their theory, given that the liquidus temperature of the BM ($T_{L,B}$) is higher than that of the weld metal ($T_{L,W}$), which is the case in this experiment, the liquid weld metal in the expanse square ahead of the mushy zone can be below $T_{L,B}$. As a result, the liquid base metal swept from the mushy zone into this cooler region by convection can solidify quickly without substantial mixing with the liquid weld metal [51].

Fig. 17(a) and (b) present a SE/BSE scan of the PMZ and the associated martensitic band. The martensitic layer formed in all the weld

samples, although this feature was more prominent in WS 7.1, clearly visible with a width of $\sim 20\ \mu\text{m}$ in Fig. 16(a). By comparison, the PMZ contiguous with the weld metal in WS 8 features a composite structure comprising a predominant martensitic region and some parts with bainitic characteristic, typically surrounded with ghost prior- γ boundaries, seen in Fig. 17(b).

Earlier studies have shown that the martensitic layer has a composition between the ferritic steel and the austenitic weld metal [47–49,51–54] due to the existence of a layer of stagnant or laminar flow of liquid base metal across the weld pool boundaries [51] and rapid cooling from the weld thermal cycle on the fusion boundary [55]. According to Ormath et al. [55], when the cooling time is not long enough to permit liquid diffusion across the intermediate layer, the composition of the layer can shift toward the martensitic range of the constitutional diagram. Consequently, martensite can form upon non-equilibrium cooling [48]. The amount of dilution, which is conditioned by the amount of heat input, can be decisive in creation of a martensitic layer [14]. Fig. 18 illustrates the composition of the base and filler metals superimposed on the WRC-1992 [56] constitution diagram. The composition of the transition region would span the composition range represented by the tie-line between the base and weld metals. As can be deduced from the figure, a higher dilution by the ferritic side, transfers the composition (i.e., Ni_{eq} and Cr_{eq}) of the transition region toward the martensitic boundary, meaning an increased potential of martensite formation within this region [48,52]. Accordingly, the formation of martensite in the PMZ observed in Fig. 17(a) and (b) can be justified by compositional gradient in this region. It should be noted that the segregation of alloying elements (i.e., Ni, Cr, Mo) across the PMZ is further confirmed by EDS results presented in the next section and shown in Figs. 21 and 22.

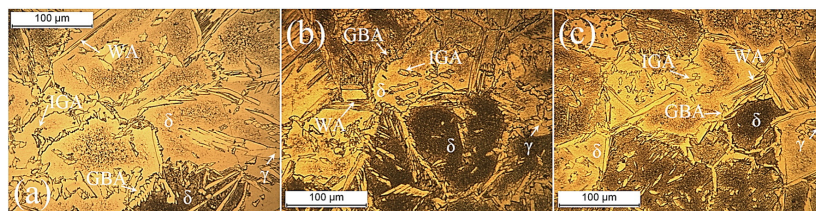


Fig. 9. Microstructure of the HAZ of S 32205: (a) WS 7.1, (b) WS 8, (c) WS 9. Different morphologies of austenite (γ) namely, grain boundary austenite (GBA), Widmanstätten austenite (WA) and intragranular austenite (IGA) are discernible in the figure.

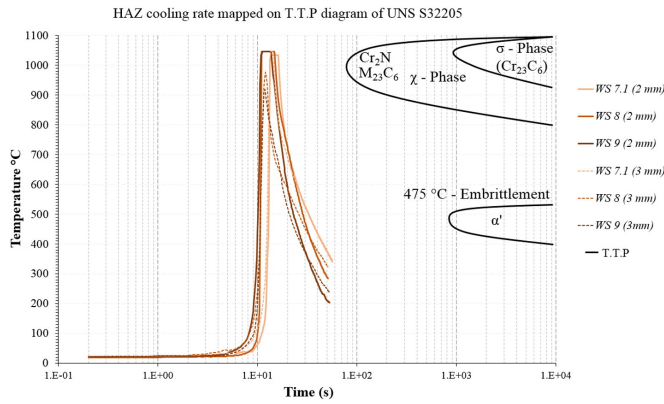


Fig. 11. Time temperature precipitation (T.T.P.) diagram for S 32205 [22] and temperature variation against time in the HAZ of S 32205.

Diffusion of C from the ferritic base metal to the Ni-based weld metal is another crucial factor in formation of a martensitic layer [52]. However, no carbon migration of significance is usually found in as-welded condition, and it is only of importance during postweld heat treatment (PWHT) [57].

Concerning the appearance of bainitic morphology structure in the PMZ, observed in Fig. 17(b), it can be assumed that the PMZ in these regions primarily maintains the composition of the S 960 base steel without substantial mixing with the weld metal.

An interesting feature of the HAZ in this work was formation of grains almost parallel to the fusion boundary, at the root and face of the weld, close to the surface. The parallel grains were formed abreast of the fusion boundary, observable in Fig. 17(a). This type of grains were mostly noticed in WS 7.1. The anomalous grain orientation may

be a by-product of a sharp temperature gradient from the fusion boundary to the free face of the parent metal. It has been demonstrated that a temperature gradient can induce grain boundary movement toward the direction of the gradient due to entropy of the boundaries [58]. It can be presumed that with higher applied heat input, there was more time available for growth and reorientation [58], hence, parallel grains were predominantly formed in WS 7.1. Thus, HAZ microstructure may not only be influenced by distance from the fusion boundary but can also be affected by the thickness direction of the joint parallel to the fusion line [59]. The parallel growth displays a similar appearance to a Type II boundary in weld metal, which has been reported in dissimilar weld metal between austenitic and ferritic steels and which is known for high susceptibility for providing a crack propagation path to the base metal [52].

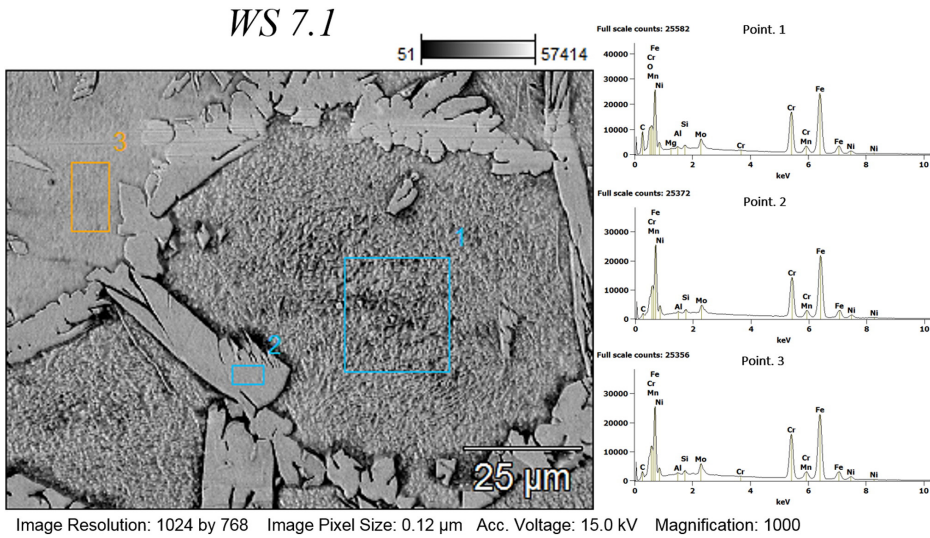


Fig. 12. EDS analysis of compositional elements within (1) a coarse etched ferritic domain, (2) an austenitic grain, and (3) a fine etched ferritic grain.

Table 3

Chemical composition (wt.%) analysis of (1) a coarse etched ferritic domain, (2) an austenitic grain, and (3) a ferritic grain. Note that the wt.% of C is excluded from the results, due to probable inaccuracy in EDS analysis of light elements.

Points of analysis	Si	Cr	Mn	Fe	Ni	Mo
Point 1 (coarse etched δ)	0.5	21.1	1.6	55.4	4.3	2.9
Point 2 (δ)	0.5	23.4	1.7	64.1	5.3	2.8
Point 3 (γ)	0.5	23.4	1.5	62.1	4.6	3.4

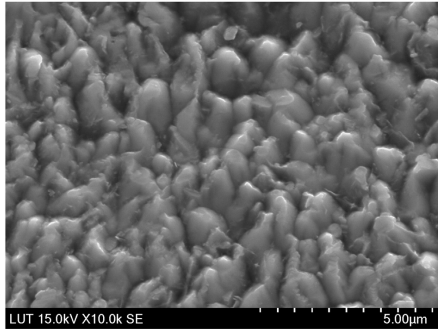


Fig. 13. SEM image of the microstructure of coarse etched ferritic sites. No detrimental secondary precipitation is detectable in the micrograph.

It is known that PMZ is susceptible to liquation and hydrogen cracking and can suffer from loss of strength and ductility [47]. Liquation cracking is intergranular and can occur when weakened grain boundaries of PMZ are pulled by solidification shrinkage of solidifying weld metal [47]. Savage et al. [60] pointed out that formation of a liquated film on the PMZ grain boundaries can provide a favored path for hydrogen diffusion across the fusion boundary and, hence, increase the hydrogen cracking risk. There are some reports indicating that the liquated material can solidify with severe segregation, resulting in a weak PMZ microstructure [47].

Fig. 19(a)–(c) reveals a fully austenitic microstructure of the weld metal on the duplex side of the weld. As can be seen, the grain growth is mainly perpendicular to the fusion line for all samples, because of a high thermal gradient perpendicular to the fusion boundary, as well as the easy growth direction of the austenitic structure [14,47]. Nearly equiaxed cellular growth was prominent in WS 7.1, while columnar growth of dendrites or a combination of cellular and columnar growth were observed for WS 8 and WS 9. It should be noted that in Fig. 19 the austenite grains look darker than the intergranular region due to

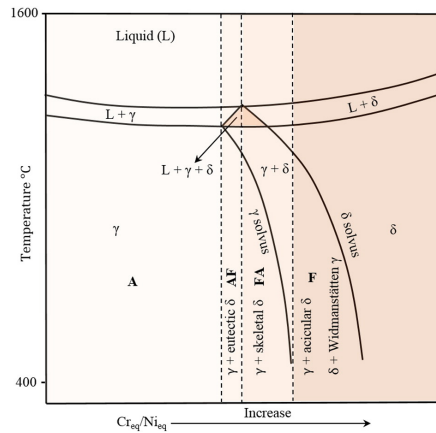


Fig. 15. Schematic of a pseudo-binary diagram [44] for an alloy containing about 70 wt.% Fe. In the diagram, values are not assigned to Cr_{eq}/Ni_{eq} ratios and temperatures since the composition of the alloy used may not correspond with that in the original diagram.

the effect of the secondary etchant used for the duplex side. Similar to the ferritic side, accumulation of Cr and Mo was noticed in some interdendritic areas (Fig. 23), which can be a corroborative indication of ferrite formation and AF solidification mode.

Fig. 19(b) and (c) clearly reveal the existence of an intermediate zone with a different structure from the base and bulk weld metal. In like manner as on the S 960 side, macrosegregation is considered to be the reason for the variation in chemical composition that led to a different solidification mode in the intermediate region. In Fig. 19(b), macrosegregation characterizes the PMZ, while in Fig. 19(c) it presents as a composite structure made of a PMZ and unmixed zone (UMZ).

The PMZ indicates a primary ferritic solidification (FA) mode during which primary- δ transformed to γ through a peritectic-eutectic reaction in the liquid state [38]. The structure comprises a vermicular or skeletal morphology of the delta ferrite in a matrix of γ , delineated in Fig. 19(b) and (c). FA solidification can occur when Cr_{eq}/Ni_{eq} is slightly higher than the eutectic composition [44]. Most of the primary formed ferrite is unstable and transforms to γ via diffusion-controlled transformation [61] upon cooling. However, during the final transient stage of solidification, Cr partitions to the dendrite interstices and the Cr-enriched, Ni-depleted ferrite remains stable at room temperature [44]. It is well established that the retention of δ in the FA mode can considerably ameliorate hot cracking susceptibility of austenitic weld metals [47,62].

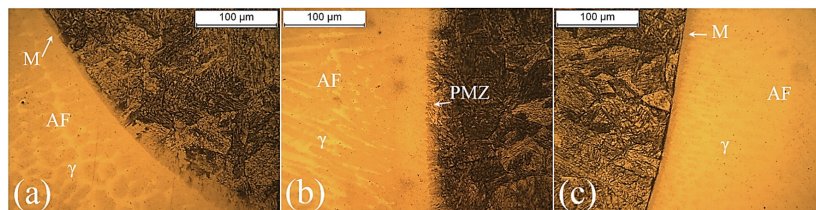


Fig. 14. Microstructure of weld metal proximate to the fusion boundary on the S 960 side of the weld. (a) WS 7.1, (b) WS 8, and (c) WS 9. The weld metal characterizes primary austenite (AF) solidification mode. Equiaxed grain growth of γ is distinguishable in WS 7.1, which contrasts with columnar and dendritic growth in WS 8 and WS 9. Martensitic layers (M) and partially mixed zone are marked on the micrographs.

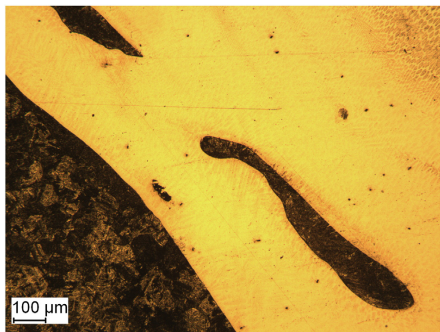


Fig. 16. Macrosegregation formed inside the weld metal, parallel to the fusion boundary. The islands appear to have a similar structure as the base metal.

The UMZ, which appeared in the form of a peninsula in Fig. 19(c), signifies a ferritic structure similar to the coarse grains formed in the HAZ. It is hypothesized, with reference to fluid mechanics [63], that

the UMZ can form due to a stagnant or laminar flow layer at the solid-liquid interface between the weld pool and base metal [51].

In Fig. 19(c), a dark line analogous to a micro-crack is detectable which is a scratch made on the surface prior to etching. It is worth mentioning that DSSs are generally reported as being very resistant to solidification cracking, HAZ liquation cracking and hydrogen induced cracking [64–67].

The nucleation of γ dendrites within the PMZ and UMZ were generally epitaxial, having a similar crystallographic orientation relationship to the substrate γ grains formed in the HAZ.

In line with expectations, as the cooling rate slowed down with increase of distance from the fusion boundary toward the weld axis, equiaxed growth became more dominant in all weld samples, as can be seen in Fig. 20. In addition, a heterogeneous nucleation of γ with random disorientation can be noticed in the figure. One explanation for this feature may be variation in composition due to inconsistent mixing of the liquid filler and base metal and/or possible inclusions that could act as independent nucleation sites within the weld metal [47].

3.3. Chemical Composition

In arc welding of dissimilar metals, multiple factors prevent a complete and consistent mixing between the base metals and filler metal

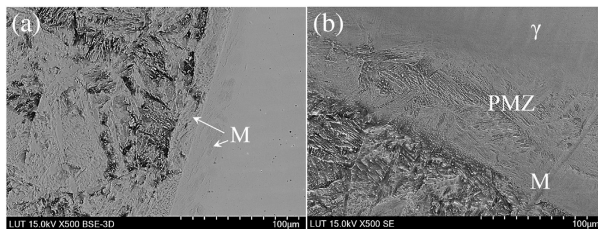


Fig. 17. SE and BSE SEM images of the WS 7.1 and WS 8 fusion boundary on the S 960 side. (a) BSE image of the WS 7.1 fusion boundary shows planar solidification of the martensitic band and formation of martensitic grains parallel to the fusion line. (b) SEM image of the partially mixed zone (PMZ) along the fusion boundary of the WS 8. The PMZ is characterized by a composite structure, dominantly martensite (M), and some regions resembling a bainitic structure, generally boarded by the remains of a prior-austenite (γ) boundary.

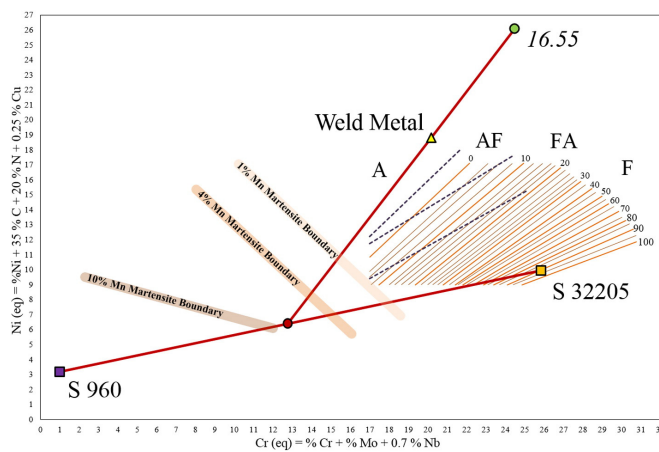


Fig. 18. WRC-1992 constitution diagram [56] with the composition of the S 960 and S 32205 base metals and 16.55 filler metal overlaid on the diagram. The dilution (%) is assessed from the weld cross-sectional area of the WS 7.1 specimen and is estimated as 17.5% and 19.4% for the S 960 and S 32205, respectively.

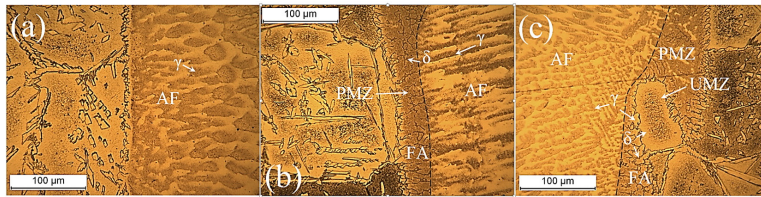


Fig. 19. Microstructure of the fusion boundary and weld metal at the S 32205 side of (a) WS 7.1, (b) WS 8, and (c) WS 9. Micrographs (b) and (c) delineate an intermediate zone in the form of a partially mixed zone (PMZ) and unmixed zone (UMZ). Primary ferrite (FA) solidification in the PMZ is noticeable in contrast to primary austenite (AF) in the weld zone. Austenite (γ) grains and retained skeletal ferrite (δ) are also seen in this figure.

(if used). These factors include thermochemical differences, the welding technique and welding parameters, joint design, nature of fluid flow, and rejection of solute from the molten alloy as it solidifies under non-equilibrium solidification [68]. The latter can be further explained by the expectation that under true equilibrium, for the duration of solidification and after solidification, no composition gradient is theoretically possible.

Segregation of alloying elements toward the core of cells or dendrite arms upon non-equilibrium solidification results in microsegregation, which can have a consequential effect on solidification cracking [47, 68]. In contrast, macrosegregation occurs as a consequence of incomplete mixing of constituents from the two parent metals and filler metal, and is referred to as a marbling effect in the literature [68]. Despite a desire for uniform dilution and thereby a homogenous microstructure and chemical-mechanical properties of the weld, heterogeneity is virtually inevitable in dissimilar welding practices [68]. Convection is the most prominent phenomenon causing stirring of the weld pool. However, convection alone cannot usually induce flawless mixing [68].

Fig. 21 presents EDS mapping of the major alloying elements (i.e. Fe, Cr, Ni, Mo) across the weld metals. It should be mentioned that C is excluded due to uncertainty in the analysis as a result of its light element character. A chemical composition gradient in the weld samples is clearly visible in Fig. 21(a)–(c). It should be noted that for WS 9, the figure is mirrored relative to (a) and (b), i.e. for WS 9 the UHSS is on the right and DSS on the left side of the figure.

Generally, three forms of macrosegregation are promulgated in the literature [47,51,68,69]. These macrosegregation types are filler-depleted zones along the fusion boundary (i.e. PMZ and UMZ) or across the width of the weld as its centerline approaches (i.e. islands with composition between the base metal and bulk weld metal) and a filler-enriched zone at the weld bottom. All of the above-mentioned forms are observable in Fig. 21(a)–(c).

As noted earlier, numerous factors can affect mixing efficiency in the weld pool and understanding their interrelated effects in mixing

becomes more demanding when three different metals are involved (i.e. two base metals and the filler metal) with different melting temperatures and remarkably different compositions. The mechanism behind macrosegregation phenomena in dissimilar arc welding is still not entirely understood [21,51] and is beyond the scope of the current study. However, in this work efforts to explain the compositional heterogeneity are made using available theories in the literature.

As was noted earlier, a PMZ and a narrow martensitic band were observed on the ferritic side of the welds (Figs. 14 and 17). Ormath et al. [55] confirmed that this narrow band is richer in Fe and Cr than Ni. Such a composition is detectable at the intermediate boundary of all the samples, shown in Fig. 21(a)–(c). As previously explained, macrosegregation in the intermediate zone can move the composition toward the martensitic range. It has been presented that as the Ni content increases, the segregation band declines, and the band no longer exists where Ni content is high enough to permit primary- γ solidification [48,50,55]. An increase in the concentration gradient of Ni can be reasonably implied from EDS analysis of WS 7.1, shown in Fig. 22. As can be seen, the PMZ has appreciable Fe and Cr contents, while Ni appears as a minor alloying element. However, Ni concentration rises substantially in a direction toward the weld center. Accordingly, austenite is stabilized and the formation of the martensitic band is restrained.

Filler-depleted islands are another distinct feature highlighted in Fig. 21(a) and (c). The composition suggests that the islands in Fig. 21(a) originated from the S 960 side and solidified prior to being mixed and dispersed in the weld pool. The composition of the islands in Fig. 21(c) indicates that they solidified with minimal mixing with the weld metal and primarily the composition of the parent metal. A mechanism associated with formation of these islands, suggested by Kou et al. [51], was expounded in the previous section. Suffice to say here that the liquid weld metal that is swept to the weld pool by convection can be surrounded by cooler liquid weld metal, immediately after the mushy zone, and solidify without significant mixing. In the case of WS 7.1, however, the segregated islands are located either at the centerline or very close to it. Messler [68] suggested that this macrosegregation pattern

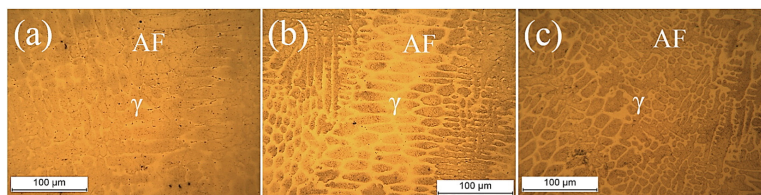


Fig. 20. Microstructure of the weld metal around the weld axis: (a) WS 7.1, (b) WS 8, and (c) WS 9. In all samples, more granular and equiaxed austenitic growth was noticed at the lower cooling rates farther from the fusion line.

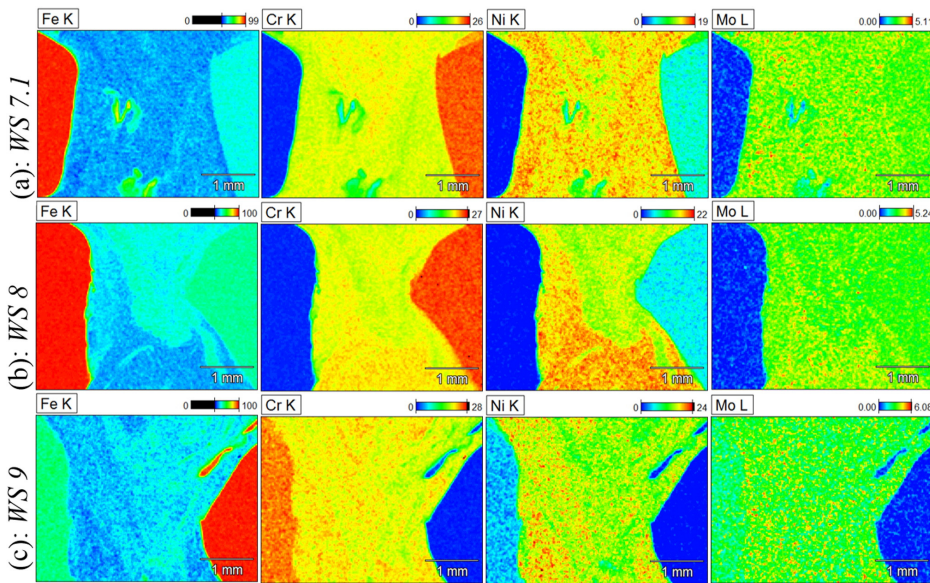


Fig. 21. Concentration gradient of some major alloying elements (Fe, Cr, Ni, and Mo) through the weld as shown by EDS analysis of (a) WS 7.1, (b) WS 8, and (c) WS 9. Note that the ferritic and duplex side is mirrored in (c), i.e. UHSS is on the right side and DSS on the left side of the figure.

can mainly form from solute ahead of the solidification front that is swept to the last liquid zone at the centerline and caught by the advancing solidification front from either side of the weld before being truly mixed. He further argued that this type of macrosegregation can be intensified by shrinkage of the liquid metal upon solidification [68].

Another form of macrosegregation is apparent in Fig. 21(b) as accumulation of alloying elements within the weld-bottom, which is referred to in the literature as a filler-rich zone [69]. The macrosegregation at the weld-bottom could be explained by a mechanism that was put forward by Yang et al. [69] for when the liquidus temperature of the filler metal (T_{LF}) < T_{LB} . The liquidus temperature condition is valid for the current experiment having an austenitic filler with $T_{LF} \approx 1400$ °C and S 960 base metal with $T_{LB} \approx 1530$ °C. Depending on the amount of dilution, the composition of the weld metal can vary between that of the filler and base metals; hence, it can be assumed that $T_{LW} < T_{LB}$. The composition of partially mixed filler metal close to the weld pool bottom at the solidification front may be closer to that of filler metal. Thus, it can be assumed that the liquidus temperature of the filler

metal (T_{LFPM}) < $T_{LW} < T_{LB}$, in this region. A layer of stagnant or laminar-flow can be expected to prevail along the pool boundary, because of an apparent “no-slip” boundary condition at a solid wall, according to fluid mechanics [63]. Therefore, the filler-rich liquid in this region can solidify prior to complete mixing. However, convection can convey some liquid base metal into the cooler filler-rich zone, and it can solidify quickly in the form of filler-depleted “streaks or swirls” within the filler-rich zone [69], detectable in Fig. 21(b).

In the experiment and specific weld pad examined in this work, the segregation probably happened due to asymmetrical geometry of the melted joint, which is clearly visible in Fig. 21(b). It is known that during arc welding, the electromagnetic force enhances mixing in the weld pool by transferring the filler droplets to the bottom of the pool and then driving the melt upward along the fusion boundary and finally pushing the melt toward the center of the pool [70]. However, in the examined weld specimen, projected base metal in the weld pool obstructed the mixing pass, and thus, the transferred filler droplets for the weld bottom mostly found their way upward along the ferritic

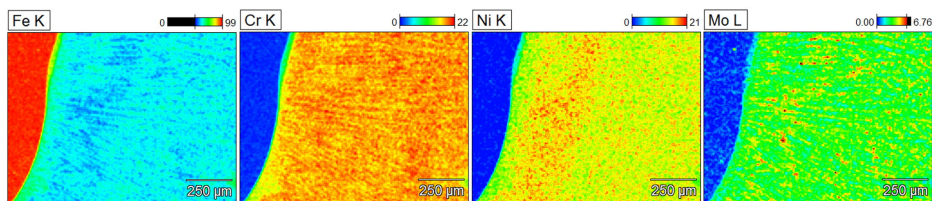


Fig. 22. EDS compositional analysis of WS 7.1 on the ferritic side of the weld.

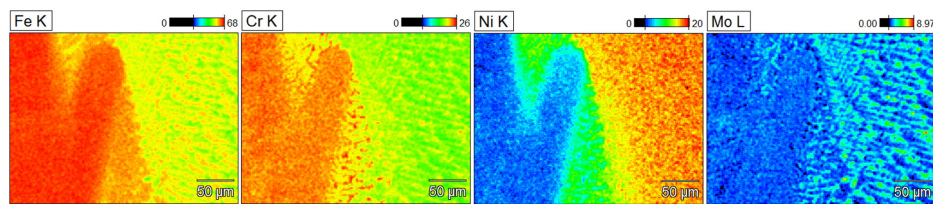


Fig. 23. EDS compositional analysis of WS 9 on the duplex side of the weld.

side of the fusion boundary, while the rest solidified as a filler-rich area at the bottom of the weld prior to being able to melt down the projected obstacle.

Although investigating the reason behind the emergence of the asymmetrical profile is not within the scope of this study, it is nonetheless worth briefly noting that the difference in the thermo-physical properties of the parent materials could have a considerable effect on the geometry. The assumption is that the duplex side melts faster at the initiation of welding because of the lower thermal conductivity in comparison with the ferritic side. However, over time, the thermal conductivity of S 32205 sharply increases with increase in the temperature. The S 960 side, however, shows the opposite trend, so that at temperatures around 1550 °C the thermal conductivity dropped below that of the duplex side [71] and it thus melted faster. Nevertheless, this mechanism alone cannot explain fully the unsymmetrical melting, as it did not follow the same pattern in all samples.

The segregation of Cr and Mo (ferrite stabilizers) into interdendritic regions is revealed in Fig. 21 and more clearly in Fig. 22. Segregation of Cr and Mo can be a strong indication for nucleation of eutectic ferrite in the interdendritic regions. According to Lippold et al. [44], during the final transition stage of primary- γ solidification, Cr intensely partitions to the dendritic interstices, while segregation of Ni remains insignificant, which is in agreement with the EDS analysis shown in Fig. 22.

Fig. 23 illustrates the EDS analysis of the PMZ and UMZ detected in the intermediate zone at the duplex side of WS 9 (Fig. 19). In the figure, the PMZ shows Ni content between the base and the bulk weld metals, which provides further evidence for diffusion of Ni from filler metal into this region. The segregation mechanism for PMZ suggested by Kou et al. [51] cannot be associated with this region, since DSS and ASS have almost identical melting temperature. Therefore, as suggested earlier, the limited mixing of the intermediate zone may be a result of a laminar or stagnant liquid flow along the solid/liquid interface walls as well as an increased cooling rate [63].

As was shown in Fig. 19, the PMZ is characterized as primary- δ solidification. This conclusion can also be drawn from Fig. 23. The formation of a PMZ occurred at the Cr-rich side of the eutectic liquidus (Fig. 15), which enabled FA solidification. As can be seen in the figure, Ni is defused to the secondary austenitic phase, while Cr and Mo are rejected from γ and partitioned toward the residual primary- δ , which is retained as skeletal δ within the γ grains [44]. Fig. 23 also reveals the composition of the detected peninsula, which resembles a thumb in this figure. As expected, this region has virtually the same composition as the parent metal, which validates its recognition as UMZ.

4. Conclusions

In the current study, dissimilar GMAW welds of Optim 960 QC (S 960) direct-quenched ultra high strength steel and UNS S32205 (S 32205) duplex stainless steel were made using a fully austenitic filler wire and applying three different welding speeds. Transmutation of the microstructure and characterization of the chemical composition under the influence of different heat inputs were described in detail. The following observations are particularly noteworthy:

When studying the HAZs, higher heat input enhanced bainitic transformation on the ferritic side, and more martensite were observed with the higher cooling rates (WS 8 and WS 9). A beneficial effect of higher heat input was noticed in that it enhanced the austenitic growth on the duplex side (WS 7.1). No detrimental precipitation was observed with the range of heat inputs applied.

When studying the fusion boundaries, macrosegregation was the most prominent feature. Formation of macrosegregation was affected by mismatches in the chemical composition and thermal properties of the base and filler metals as well as the amount of heat input.

It was found that on the ferritic side, macrosegregation resulted in the formation of a martensitic band in all samples and filler-depleted islands in WS 9. On the duplex side, macrosegregation, in the form of partially mixed and/or unmixed zones (PMZ/UMZ) with a different solidification mode than the bulk weld metal, only appeared with higher cooling rates.

In the case of the bulk weld metal, more granular and equiaxed austenite formed with the higher heat input (WS 7), while dendritic and columnar austenitic growth was noticed with the higher cooling rates (WS 8 and WS 9).

The composition of the weld metal was more homogeneous when the higher heat input was applied (WS 7.1). With the lower heat inputs (WS 8 and WS 9) the disparity in the composition (i.e. Cr, Ni and Mo) was considerable.

Acknowledgements

The authors would like to thank Mr. Esa Hiltunen for arranging and supervising the experiments. Special thanks to Toni Väkiparta for planning and assistance in performing the SEM analysis. The authors express their gratitude to Mr. Amir E. Toghiani for his valuable comments. The authors would also like to thank Mr. Peter Jones for his comments and assistance with the English language.

References

- [1] G. Xiao, H. Di, F. Zhu, B. Chen, B. Qiu, Influence of direct quenching on microstructure and mechanical properties of steel plate for large oil storage tanks, *J Mater Eng Perform* 19 (6) (2010) 868–872.
- [2] G.C. Hwang, S. Lee, J.Y. Yoo, W.Y. Choo, Effect of direct quenching on microstructure and mechanical properties of copper-bearing high-strength alloy steels, *Mater Sci Eng A* 252 (1998) 256–268.
- [3] N.C. Muckelroy, K.O. Findley, R.L. Bodnar, Microstructure and mechanical properties of direct quenched versus conventional re-austenitized and quenched plate, *J Mater Eng Perform* 22 (2) (2013) 512–522.
- [4] J.D. Tucker, M.K. Miller, G.A. Young, Assessment of thermal embrittlement in duplex stainless steels 2003 and 2205 for nuclear power applications, *Acta Mater* 87 (2015) 15–24.
- [5] V.H.B. Hernandez, S.S. Nayak, Y. Zhou, Tempering of martensite in dual phase steels and its effects on softening behavior, *Metall Mater Trans A* 42 (10) (2011) 3115–3129.
- [6] J. Wang, L. Yang, M. Sun, T. Liu, H. Li, Effect of energy input on the microstructure and properties of butt joints in DP1000 steel laser welding, *Mater Des* 90 (2016) 642–649.
- [7] F. Farrokhi, J. Siltanen, A. Salminen, Fiber laser welding of direct-quenched ultrahigh strength steels: evaluation of hardness, tensile strength, and toughness properties at subzero temperatures, *J Manuf Sci Eng* 137 (2015) 061012-1–061012-10.

- [8] A. Roshanghias, M. Barzegari, A.H. Kokabi, H.R.M. Hosseini, Welding characteristics of ultrahigh strength steel in annealed and quench-tempered conditions, *J Mater Eng Perform* 19 (2010) 963–969.
- [9] W. Guo, D. Crowther, J.A. Francis, A. Thompson, Z. Liu, L. Li, Microstructure and mechanical properties of laser welded S960 high strength steel, *Mater Des* 85 (2015) 534–548.
- [10] A.J. Ramirez, J.C. Lippold, S.D. Brand, The relationship between chromium nitride and secondary austenite precipitation in duplex stainless steels, *Metall Mater Trans A* 34 (8) (2003) 1575–1597.
- [11] J.M. Pardo, S.S.M. Tavares, M.P.C. Fonseca, J.A. Souza, et al., Deleterious phases precipitation on superduplex stainless steel UNS S32750: characterization by light optical and scanning electron microscopy, *Mater Res* 13 (3) (2010) 401–407.
- [12] C.M. Garzón, A.J. Ramirez, Growth kinetics of secondary austenite in the welding microstructure of a UNS S32304 duplex stainless steel, *Acta Mater* 54 (2006) 3321–3331.
- [13] G. Martin, S.K. Yerra, Y. Bréchet, M. Véron, J.D. Mithieux, B. Chéhab, L. Delannay, T. Pardo, A macro- and micromechanics investigation of hot cracking in duplex steels, *Acta Mater* 60 (2012) 4646–4660.
- [14] A. Eghlimi, M. Shamsianian, M. Eskandarian, A. Zabolian, M. Nezakat, J.A. Szpunar, Evaluation of microstructure and texture across the welded interface of super duplex stainless steel and high strength low alloy steel, *Surf Coat Technol* 264 (2015) 150–162.
- [15] S. Wang, Q. Ma, Y. Li, Characterization of microstructure, mechanical properties and corrosion resistance of dissimilar welded joint between 2205 duplex stainless steel and 16MnR, *Mater Des* 32 (2011) 831–837.
- [16] M. Sadeghian, M. Shamsianian, A. Shafeyi, Effect of heat input on microstructure and mechanical properties of dissimilar joints between super duplex stainless steel and high strength low alloy steel, *Mater Des* 60 (2014) 678–684.
- [17] P.B. Srinivasan, V. Muthupandhi, W. Dietzel, V. Sivan, Microstructure and corrosion behavior of Shielded Metal Arc-welded dissimilar joints comprising duplex stainless steel and low alloy steel, *J Mater Eng Perform* 15 (6) (2006) 758–764.
- [18] B.I. Mendoza, Z.C. Maldonado, H.A. Albitre, P.E. Robles, Dissimilar welding of superduplex stainless steel/HSLA steel for offshore applications joined by GTAW, *Engineering* 2 (2010) 520–528.
- [19] J. Wang, M. Lu, L. Zhang, W. Chang, L. Xu, L. Hu, Effect of welding process on the microstructure and properties of dissimilar weld joints between low alloy steel and duplex stainless steel, *Int J Miner Metall Mater* 19 (6) (2012) 518–524.
- [20] L. Odgaard, C.O. Pettersson, S.A. Fager, The selection of welding consumables and properties of dissimilar welded joints in the superduplex stainless steel Sandvik 2507 to carbon steel and highly alloyed austenitic and duplex stainless steels, *Proc. 4th Int. Conf. Duplex Stainless Steels*, Glasgow, Scotland, 1994.
- [21] E.J. Barnhouse, J.C. Lippold, Microstructure/property relationships in dissimilar welds between duplex stainless steels and carbon steels, *Weld J* (1998) 477s–487s.
- [22] G.V. Voort (Ed.), *Atlas of Time Temperature Diagrams for Irons and Steels*, ASM International, PA, USA, 1991.
- [23] A. Guo, R.D.K. Misra, J. Xub, B. Guob, S.G. Janstoc, Ultrahigh strength and low yield ratio of niobium-microalloyed 900 MPa pipeline steel with nano/ultrafine bainitic lath, *Mater Sci Eng A* 527 (2010) 3886–3892.
- [24] Y.Q. Zhang, W.M. Liu, H. Houb, Effects of Nb on microstructure and continuous cooling transformation of coarse grain heat-affected zone in 610 MPa class high-strength low-alloy structural steels, *Mater Sci Eng A* 499 (2009) 182–186.
- [25] H.A. Aaronson, W.T. Reynolds, G.J. Shiflet, G. Spanos, Bainite viewed three different ways, *Metall Trans A* 21 (6) (1990) 1343–1380.
- [26] H.K.D.H. Bhadeshia, *Bainite in Steels*, second ed. The Institute of Materials, Cambridge, 1992.
- [27] G. Gao, H. Zhang, X. Gui, P. Luo, Z. Tan, B. Bai, Enhanced ductility and toughness in an ultrahigh-strength Mn–Si–Cr–C steel: the great potential of ultrafine filmy retained austenite, *Acta Mater* 76 (2014) 425–433.
- [28] K. Abbaszadeh, H. Saghaian, S. Kheirandish, Effect of bainite morphology on mechanical properties of the mixed bainite-martensite microstructure in D6AC steel, *Mater Sci Technol* 28 (4) (2012) 336–342.
- [29] R. Bakhtiari, A. Ekrami, The effect of bainite morphology on the mechanical properties of a high bainite dual phase (HBDP) steel, *Mater Sci Eng A* 525 (2009) 159–165.
- [30] H.K.D.H. Bhadeshia, Martensite and bainite in steels: transformation mechanism & mechanical properties, *J Phys IV France* 7 (1997) (C5-367–C5-376).
- [31] J. Hidalgo, M.J. Santofimia, Effect of prior austenite grain size refinement by thermal cycling on the microstructural features of as-quenched lath martensite, *Metall Mater Trans A* 1–14 (2016).
- [32] X. Tan, Y. Xu, X. Ang, Z. Liu, D. Wu, Effect of partitioning procedure on microstructure and mechanical properties of a hot-rolled directly quenched and partitioned steel, *Mater Sci Eng A* 594 (2014).
- [33] M.J. Santofimia, L. Zhao, R. Petrov, J. Sietsma, Characterization of the microstructure obtained by the quenching and partitioning process in a low-carbon steel, *Mater Charact* 59 (2008) 1758–1764.
- [34] Q. Zhou, L. Qian, J. Tan, J. Meng, F. Zhang, Inconsistent effects of mechanical stability of retained austenite on ductility and toughness of transformation-induced plasticity steels, *Mater Sci Eng A* 578 (2013) 370–376.
- [35] K. Yana, K.-D. Liss, I.B. Timokhina, E.V. Pereloma, In situ synchrotron X-ray diffraction studies of the effect of microstructure on tensile behavior and retained austenite stability of thermo-mechanically processed transformation induced plasticity steel, *Mater Sci Eng A* 662 (2016) 185–197.
- [36] W. Zhang, T. DeRoy, T.A. Palmer, J.W. Elmer, Modeling of ferrite formation in a duplex stainless steel weld considering non-uniform starting microstructure, *Acta Mater* 53 (16) (2015) 4441–4453.
- [37] T.A. Palmer, J.W. Elmer, S.S. Babu, Observations of ferrite/austenite transformations in the heat affected zone of 2205 duplex stainless steel spot welds using time resolved X-ray diffraction, *Mater Sci Eng A* 374 (2004) 307–321.
- [38] M. Rahmani, A. Eghlimi, M. Shamsianian, Evaluation of microstructure and mechanical properties in dissimilar austenitic/super duplex stainless steel joint, *J Mater Eng Perform* 23 (2014) 3745–3753.
- [39] K. Bettahar, M. Bouabdallah, R. Badji, M. Gaceb, C. Kahloun, B. Bacroix, Microstructure and mechanical behavior in dissimilar 13Cr/2205 stainless steel welded pipes, *Mater Des* 85 (2015) 221–229.
- [40] N. Pettersson, R.F.A. Pettersson, S. Wessman, Precipitation of chromium nitrides in the super duplex stainless steel 2507, *Metall Mater Trans A* 46 (3) (2015) 1062–1072.
- [41] R.I. Hsieh, H.Y. Liou, Y.T. Pan, Effects of cooling time and alloying elements on the microstructure of the Gleeble-simulated heat affected zone of 22% Cr duplex stainless steels, *J Mater Eng Perform* 10 (5) (2001) 526–536.
- [42] D.H. Kang, H.W. Lee, Effect of different chromium additions on the microstructure and mechanical properties of multipass weld joint of duplex stainless steel, *Metall Mater Trans A* 43 (12) (2012) 4678–4687.
- [43] S. Hertzman, P.J. Ferreira, B. Brolund, An experimental and theoretical study of heat-affected zone austenite reformation in three duplex stainless steels, *Metall Mater Trans A* 28 (2) (1997) 277–285.
- [44] J.C. Lippold, W.F. Savage, Solidification of austenitic stainless steel weldments: part I—a proposed mechanism, *Weld J* (1979) 362s–374s.
- [45] R. Singh (Ed.), *Weld Cracking in Ferrous Alloys*, Woodhead Publishing, Cambridge, 2009.
- [46] V.P. Kujanpaa, S.A. David, C.L. White, Formation of hot cracks in austenitic stainless steel welds – solidification cracking, *Weld J* (1986) 203s–212s.
- [47] S. Kou, *Welding Metallurgy*, John Wiley & Sons, 2003.
- [48] J.N. Dupont, C.S. Kusko, Technical note: martensite formation in austenitic/ferritic dissimilar alloy welds, *Weld J* 86 (2) (2007) 51s–54s.
- [49] T. Doody, Intermediate mixed zones in dissimilar metal welds for sour service, *Weld J* 71 (3) (1992) 55–60.
- [50] A.A. Omar, Effects of welding parameters on hard zone formation at dissimilar metal welds, *Weld J* 77 (2) (1998) 86s–93s.
- [51] S. Kou, Y.K. Yang, Fusion-boundary macrosegregation in dissimilar-filler welds, *Weld J* 86 (2007) 303s–312s.
- [52] J.C. Lippold, S.D. Kiser, J.N. DuPont, *Welding Metallurgy and Weldability of Nickel-base Alloys*, John Wiley & Sons, New Jersey, 2009.
- [53] M. Mukherjee, T.K. Pal, Influence of heat input on martensite formation and impact property of ferritic-austenitic dissimilar weld metals, *J Mater Sci Technol* 28 (4) (2012) 343–352.
- [54] Z.R. Chen, Y.H. Lu, TEM observation of martensite layer at the weld interface of an A508III to Inconel 82 dissimilar metal weld joint, *Metall Mater Trans A* 46 (12) (2015) 5494–5498.
- [55] F. Ormth, J. Soudry, B. Weiss, I. Minkoff, Weld pool segregation during the welding of low alloy steels with austenitic electrodes, *Weld J* 60 (1991) 227s–230s.
- [56] D.J. Kotecki, T.A. Siewert, WRC-1992 constitution diagram for stainless steel weld metals: a modification of the WRC-1988 Diagram, *Weld J* 71 (1992) 171s–178s.
- [57] C.D. Lundin, Dissimilar metal welds—spanion joints literature review, *Weld J* (1982) 58s–63s.
- [58] T.W. Lau, J.T. Bowker, R.B. Lazor, First report of HAZ study, *Proc. Int. Conf. Welding for Challenging Environments*, Toronto, 1985.
- [59] P. McHenry (Ed.), *Fatigue and Fracture Testing of Weldments*, ASTM, Philadelphia, 1990.
- [60] W.F. Savage, E.F. Nippes, E.S. Szekeress, Hydrogen induced cold cracking in a low alloy steel, *Weld J* 55 (1976) 276s–284s.
- [61] A. Saha, G. Ghosh, G.B. Olson, Microstructural transformations of dissimilar austenite-ferrite stainless steels welded joints, *Acta Mater* 53 (1) (2005) 141–149.
- [62] H. Tasalloti, P. Kah, J. Martikainen, Effects of welding wire and torch weaving on GMAW of S355MC and AISI 304L dissimilar welds, *Int J Adv Manuf Technol* 71 (2014) 197–205.
- [63] S. Kou, *Transport Phenomena and Materials Processing*, Wiley & Sons, NY, 1996.
- [64] R.N. Gunn (Ed.), *Duplex Stainless Steels, Microstructure, Properties and Applications*, Abington Publishing, Cambridge, 1997.
- [65] J.R. Davis (Ed.), *Corrosion of Weldments*, ASM International, OH, 2006.
- [66] J.R. Davis (Ed.), *ASM Specialty Handbook: Stainless Steels*, ASM International, 1995.
- [67] M.J. Cieslak, A.M. Ritter, W.F. Savage, Solidification cracking and analytical electron microscopy of austenitic stainless steel weld metals, *Weld J* (1982) 1s–8s.
- [68] R.W. Messler Jr., *Principles of Welding: Processes, Physics, Chemistry, and Metallurgy*, Wiley-VCH, NY, 2004.
- [69] Y.K. Yang, S. Kou, Weld-bottom macrosegregation caused by dissimilar filler metals, *Weld J* 86 (2007) 379s–387s.
- [70] S. Kou, Y.H. Wang, Weld pool convection and its effect, *Weld J* (1986) 63s–70s.
- [71] E. Ranjbarodeh, S. Serajzadeh, A. Kokabi, A. Fischer, Prediction of temperature distribution in dissimilar arc welding of stainless steel to carbon steel, *Proc. Inst. Mech. Eng. B*, 2012.

Publication VII

Tasalloti, H., Dabiri, M., Kah, P., and Martikainen, J.

Effect of GMAW heat input on the microstructure and mechanical and fatigue behavior of dissimilar welds of ultrahigh strength steel and duplex stainless steel

Reprinted with permission from

ASME: 36th International Conference on Ocean, Offshore & Arctic Engineering (Accepted)

Vol., pp. -, 2017

© 2017, ASME

OMAE2017-62646

EFFECT OF GMAW HEAT INPUT ON THE MICROSTRUCTURE AND MECHANICAL AND FATIGUE BEHAVIOR OF DISSIMILAR WELDS OF ULTRAHIGH STRENGTH STEEL AND DUPLEX STAINLESS STEEL PUT PAPER TITLE HERE

Hamed Tasalloti Kashani
Lappeenranta University of Technology (LUT)
Lappeenranta, Finland

Mohammad Dabiri
Lappeenranta University of Technology (LUT)
Lappeenranta, Finland

Paul Kah
Lappeenranta University of Technology (LUT)
Lappeenranta, Finland

Jukka Martikainen
Lappeenranta University of Technology (LUT)
Lappeenranta, Finland

ABSTRACT

The effect of heat input on the microstructure and mechanical properties of dissimilar welds of direct-quenched ultrahigh strength steel (Optim 960 QC) and duplex stainless steel (UNS S32205) was studied. The effect of heat input on grain coarsening and the proportion of bainite-martensite on the ferritic side and ferrite-austenite on the duplex side was clearly evident. The hardness profile showed a trend of increasing hardness with lower heat input. Enhancement in tensile strength corresponded to lower heat input and increase in hardness. The elongation values and bend behavior were roughly the same for all the specimens; there was no clear link to the heat input. Moderate heat input gave optimum impact toughness in the weld and the ferritic HAZ. The fatigue performance of the specimens demonstrated the profound influence of geometrical effects. However, the effect of microstructural characteristics on fracture location was also observed.

INTRODUCTION

Selection of materials is always a major step in modern engineering design and can directly affect the life expectancy, performance and cost of the final product [1]. In recent years, many newly developed materials with different material properties have been added to the already lengthy list of available options. In the case of structural and weldment design, new grades of steel are being developed to meet new challenges in terms of chemicophysical and mechanical properties. In addition to new engineering requirements, demands for more cost-effective materials give additional impetus to the continued

development of new grades. Direct-quenched (DQ) ultrahigh strength steel (UHSS) is a relatively new development that offers a combination of lower production cost and superb engineering properties. Knowledge of the weldability of UHSS DQ in similar and dissimilar configurations is a necessity to enable full exploitation of the promising features of this new steel grade. The mechanical and fracture properties of welded UHSS DQ have recently become the focus of research.

Farrokhi et al. [2] in study of welding of UHSS DQ with a high-power fiber laser process reported a high-quality weld with slight HAZ softening and satisfactory tensile strength. Guo et al. [3], also using a laser welding process, demonstrated a defect-free weld with a matching strength to that of the base metal. However, they reported a drop and rise in the hardness of the HAZ and fusion zone, respectively. In addition, they noticed a reduction in impact toughness of the weld compared with the base metal. Wallin et al. [4] reported lower fracture toughness of the weld in comparison with the base metal. They stated that the HAZ adjacent to the fusion boundary was the most brittle region. Siltanen et al. [5] studied welds of UHSS DQ made using either a laser or hybrid laser and GMAW welding process. They noticed HAZ softening occurred regardless of the process. However, in the case of autogenous laser welding, the softening was limited to a narrow region. They recommended an under-matching filler wire for improved impact toughness when using hybrid processing. Nykänen et al. [6] estimated a 12-21% reduction in fatigue strength for an as-welded joint made using GMAW, based on experimental and analytical data.

Although similar welding of UHSS DQ has been the subject of several studies in the literature [2-7], dissimilar welding of this grade has received little attention [8]. The current study evaluates dissimilar welding of UHSS DQ and duplex stainless steel (DSS). The excellent mechanical properties and acceptable cost of the two grades, together with the excellent corrosion resistance of DSS, imply that such welds have significant potential for many contemporary industrial applications, such as offshore construction, lightweight structures and transportation, as well as for novel applications requiring a combination of high mechanical performance and good corrosion resistance where cost and weight are major considerations. However, the weldability of such a combination in terms of microstructure and mechanical characteristics is not sufficiently understood.

The objective of this study is to provide new insights and a comprehensive understanding of the microstructural properties and mechanical and fatigue behavior of such dissimilar welds under the influence of different heat inputs. To this end, dissimilar welds were made between Optim 960 QC, a commercial UHSS DQ grade, and UNS S32205 duplex stainless steel using GMAW with an austenitic filler wire and applying three different heat inputs. The study analyzes the mechanical properties and fatigue behavior of the weld samples with reference to the amount of heat input and the resultant microstructural characteristics.

EXPERIMENTAL PROCEDURE

As-received plates of Optim 960 QC ultrahigh strength steel (UHSS) and UNS S32205 duplex stainless steel (DSS) were machined to dimensions of 350×150×5 mm (ISO 15614-1) and V-grooves prepared with an angle of 60° in butt joint configuration. The root-face and airgap were both zero and removable fiberglass tapes were used for backing. Single pass welds were made on the joints using a fully automated GMAW machine with three different welding speeds, namely, 7.1 mm/s, 8 mm/s and 9 mm/s. An austenitic filler wire, Esab OK Autrod 16.55 (1 mm diameter), was utilized for the welds under a constant shielding gas (98 % Ar + 2 % CO₂) at a flowrate of 15 l/min, and with a fixed tip-to-work distance of 13 mm. A schematic of the weld joint is shown in Fig. 1. The chemical composition of the base and filler metals are presented in Table 1. The three sets of parameters used for the welding samples are presented in Table 2.

It should be noted that a fully austenitic filler wire was used with the aim of obtaining a welded joint with desirable strength, ductility and toughness. The composition of the filler metal was selected based on estimations obtained from the WRC-1992 [9] constitution diagram for minimum potential martensite formation at the weld interface on the ferritic steel side. The shielding gas mixture used was selected for a broad penetration and enhanced weld bead quality for the combination of the base and filler metals used. In the current study, for convenience, the base and filler metals are denominated as S 960, S 32205 and

16.55, and the weld samples are named WS 7.1, WS 8, WS 9, according to the welding speed used when producing the weld.

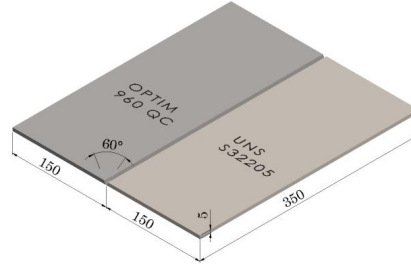


FIGURE 1. SCHEMATIC OF THE JOINT SETUP USED IN THE EXPERIMENTS.

TABLE 1. CHEMICAL COMPOSITION (WT. %) OF THE BASE AND FILLER METALS.

Metal.	C	Si	Mn	P+S	Al	Nb	Cu	Cr	Ni	Mo
S 960	0.09	0.21	1.05	0.014	0.030	0.003	0.025	0.82	0.04	0.158
S 32205	0.015	0.39	1.34	0.026	-	0.009	0.25	22.59	5.79	3.24
16.55	0.02	0.4	1.7	-	-	-	1.4	20.5	25	4.5

TABLE 2. THREE SETS OF WELDING PARAMETERS USED FOR PREPARING THE SAMPLES: ARC CURRENT (I), ARC VOLTAGE (U), WELDING SPEED (v), WIRE FEED SPEED (WFS), ARC ENERGY (E) AND HEAT INPUT (Q).

I (A)	U (V)	v (mm/s)	WFS (m/min)	E (kJ/mm)	Q (kJ/mm)
257	29.8	7.1	10.6	1.08	0.86
224	28.7	8	10	0.80	0.64
204	26.4	9	9	0.60	0.48

The weld specimens were cut from the as-welded plates in accordance with EN ISO 15614-1 for destructive tests. The ferrite number (FN) of the welds were measured using a ferritescope device according to EN ISO 8249 standard. Metallography samples were polished (final polish with 1 μm diamond paste) and etched in compliance with EN ISO 17639 standard for microscopic examination of welds and ISO/TR

16060 for etchants. The DSS side was etched using a standard Cuprochloric solution 2 (5g CuCl₂ + 100 ml HCl + 100 ml C₂H₅OH + 100 ml H₂O) and Nital (95 ml C₂H₅OH + 5 ml HNO₃) was used for etching the UHSS side. The etching time was 15 s and 30 s for Nital and Cuprochloric solution 2, respectively. Light microscopy and scanning electron microscopy (SEM) were used to delineate the microstructural features in the HAZs and fusion zones.

Vickers hardness tests (HV_s) were carried out on the etched samples at room temperature using 49.03 N force, in compliance with EN ISO 9015-1 and ISO 6507-1.

Weld specimens were machined to the geometries recommended by EN ISO 4136, EN ISO 5173 and EN ISO 9016 standards for tensile, bending and Charpy impact tests, respectively. Tensile tests were performed at room temperature on two sets of samples made from each type of weld. Transverse face bending (TFB) and transverse root bending (TRB) tests were separately performed on two specimens made for each type of weld. The Charpy V-notch impact test was performed at -40 °C using a pendulum impact testing machine with an impact energy of 150 J. The test was replicated on 6 specimens with a notch either on the weld center or 1 mm offset from the weld center toward the UHSS base metal. In addition, three specimens of each type of weld were machined for fatigue testing and the results were analyzed according to IIW recommendations [10].

MACROSTRUCTURE

A macrograph of the weld specimens prepared for this study is shown in Fig. 2. In the figure, the effect of grain coarsening can be discerned on the HAZ of both the S 960 and S 32205 base metals, on the left and right side of the welded joints, respectively. However, the appearance of coarse grains extends over a wider span on the S 960 side than the S 32205 side, which is indicative of higher sensitivity of the S 960 base metal to the heat input than the S 32205 metal.



FIGURE 2. MACROGRAPH OF WELD SAMPLES: (a) WS 7.1; (b) WS 8; (c) WS 9. IN THE FIGURE, THE EFFECT OF GRAIN COARSENING CAN BE NOTICED ON THE HAZ OF THE S 960 BASE METAL (LEFT SIDE OF THE WELDED JOINT) AND S 32205 (RIGHT SIDE OF THE WELDED JOINT).

MICROSTRUCTURE

The microstructure of the HAZ of the weld samples on the S 960 side at a distance of about 1 mm from the fusion boundary is shown in Fig. 3 (a)-(c).

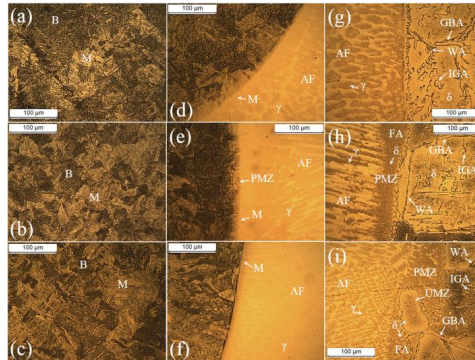


FIGURE 3. MICROSTRUCTURE OF COARSE GRAINED HAZ AND FUSION ZONE ON THE S 960 AND S 32205 SIDE OF THE WELDS. IN THE HAZ OF THE S 960, LATHS OF BAINITE (B) WITH DARKER APPEARANCE CAN BE DIFFERENTIATED FROM MARTENSITE (M): (a) WS 7.1, PREDOMINANTLY BAINITIC; (b) WS 8, ROUGHLY EVEN BALANCE OF BAINITIC AND MARTENSITIC MORPHOLOGIES; AND (c) WS 9, MOSTLY MARTENSITIC. MICROSTRUCTURE OF THE WELD METAL PROXIMATE TO THE FUSION BOUNDARY ON THE S 960 SIDE OF THE WELD: (d) WS 7.1, (e) WS 8 AND (f) WS 9. MICROSTRUCTURE OF THE FUSION BOUNDARY AND WELD METAL ON THE S 32205 SIDE OF THE WELD: (g) WS 7.1, (h) WS 8, AND (i) WS 9.

The micrographs show significant grain coarsening as a result of austenitization of the HAZ. With initiation of welding, the temperature of the coarse HAZ almost instantaneously rises to ranges beyond the upper intercritical temperature (AC₂) at which the microstructure mostly transfers to austenite. Following cooling below the lower intercritical temperature (AC₁), decomposition of austenite starts. Subsequently, further cooling inaugurates bainitic transformation, which proceeds by martensitic formation at lower temperatures [8]. It appears that the amount and morphology of the formed phases are to some extent influenced by the heat input. For instance, bainitic phase is dominant in WS 7.1, while martensite dominates in the HAZ of WS 9, as can be seen in Fig 3 (a) and (c) respectively. By comparison, bainite and martensite are almost evenly distributed in the HAZ of WS 8, as seen from Fig. 3 (b).

The SEM image shown in Fig. 4 illustrates details of the HAZ microstructure. In this figure, only the HAZ of WS 9 is shown, as the microstructural features were similar for all the samples. It can be seen from the micrographs that the bainitic constituent in the HAZ is predominantly made of lower bainite laths. The laths of lower bainite generally partition the prior-austenite grains and intersect each other, as can be seen within the region circled with a dotted line in Fig. 4. In contrast, laths of upper bainite are almost parallelly-aligned and fill the prior-austenite grains [11].

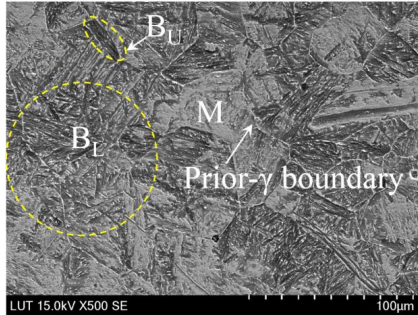


FIGURE 4. MICROSTRUCTURE OF THE HAZ ON THE S 960 SIDE OF WS 9. THE SEM IMAGE SHOWS THE COEXISTENCE OF MARTENSITE (M), LOWER BAINITE (B_L) LATHS (WITHIN THE REGION CIRCLED WITH A DOTTED LINE), AND UPPER BAINITE (B_U) LATHS (WITHIN THE REGION DELINEATED WITH AN OVAL).

The microstructure of the fusion boundary on the S 960 side of the dissimilar weld can be seen in Fig. 3 (d)-(f). The figure shows primary-austenite (AF) solidification mode for all samples [12]. Equiaxed grain growth of austenite is visible in WS 7.1, in contrast with columnar and dendritic growth in WS 8 and WS 9. It has been found that equiaxed growth takes place over a long constitutional undercooling, while columnar growth is a concomitant of high cooling rates [13,14]. This is in agreement with the more columnar dendrites observed in WS 8 and WS 9 with higher cooling rates. It should be mentioned that the cooling rate is conditioned by the heat provided during welding. As the welding speed increases, the amount of heat input decreases which results in a faster cooling rate.

A notable feature of the weld metal in Fig. 3 (d)-(f) is a narrow unetched intermediate zone with a planar solidification. Such a characteristic is commonly found on the weld interface of austenitic and ferritic steels and is generally identified as martensite in the literature [15,16]. Fig. 5 (a) presents a BSE image of the martensitic band contiguous with the fusion boundary of the WS 7.1. The martensitic layer formed in all the weld samples, although this feature was more prominent in WS 7.1, and is clearly recognizable with a width of $\sim 20 \mu\text{m}$ in Fig. 5 (a).

Fig. 3 (e) shows a distinct intermediate zone with a composite appearance of base and weld metals that characterizes a partially mixed zone (PMZ) [14]. Omar [17] reported such regions as beaches of martensite and peninsulas possessing base metal constitution. Fig. 5 (b), presents a high magnification SEM image of the PMZ adjacent to the weld metal in the WS 8. As can be seen from the figure, the PMZ features a composite structure comprising a predominantly martensitic region and some parts with bainitic characteristic, typically surrounded with ghost prior-austenite boundaries.

Both aforementioned intermediate zones (Fig. 5 (a) and (b)) are classified as macrosegregation in the literature [14,18] because the compositions have a gradient over a broad span ($100\text{-}200 \mu\text{m}$), whereas in microsegregation the compositions differ over the span of a dendrite arm or cell spacing [18]. The amount of dilution, which is conditioned by the amount of heat input, can be determining in creation of a martensitic layer [19]. Earlier studies have shown that the martensitic layer has a composition between the ferritic steel and the austenitic weld metal [15,18] due to the presence of a layer of stagnant or laminar flow of liquid base metal across the weld pool boundaries [18] and rapid cooling on the fusion boundary [20]. When the cooling time is not long enough to enable liquid diffusion across the intermediate layer, the composition of the layer can shift toward the martensitic range of the constitutional diagram. As a result, martensite can form upon non-equilibrium cooling [8,15,20].

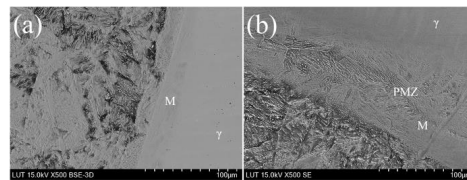


FIGURE 5. SE AND BSE SEM IMAGE OF THE FUSION BOUNDARY ON THE S 960 SIDE. (a) BSE IMAGE OF THE WS 7.1 FUSION BOUNDARY SHOWS FORMATION OF A MARTENSITIC BAND. (b) SEM IMAGE OF THE PARTIALLY MIXED ZONE (PMZ) ALONG THE FUSION BOUNDARY OF THE WS 8.

The microstructure of the HAZ and fusion boundary on the DSS side is illustrated in Fig. 3 (g)-(i). The final microstructure of the HAZ is determined by solid-state phase transformations from austenite to ferrite and vice versa that take place during welding [21]. As seen in the figure, the HAZ has undergone a distinct change in microstructure, and grain coarsening is evident.

The main morphology of austenite is grain boundary austenite (GBA), which is detectable by allotriomorphic formations on the prior-ferrite grain boundaries [19,22], and GBA is evident on the boundaries of coarse ferrite grains in Fig. 3 (g)-(i). Widmanstätten austenite (WA), another common morphology, nucleates at lower temperatures than GBA [13]. WA grows as needle-like elongated plates, usually initiating from GBA and extending toward the ferrite grains [19], as can be seen in Fig. 3 (g)-(i). The different morphologies of austenite are better visible in the SEM image in Fig 6.

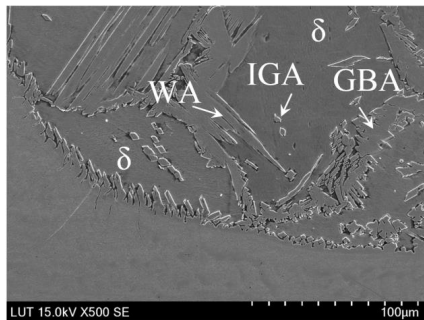


FIGURE 6. SEM IMAGE OF THE HAZ OF WS 7.1 ADJACENT TO THE FUSION BOUNDARY ON THE S 32205 SIDE. DIFFERENT MORPHOLOGIES OF AUSTENITE (γ) ARE SEEN, NAMELY: GRAIN BOUNDARY AUSTENITE (GBA), WIDMANSTÄTTEN AUSTENITE (WA), AND INTRAGRANULAR AUSTENITE (IGA). FINE ETCHED DOMAINS OF FERRITE (δ) ARE ALSO DETECTABLE.

In Fig. 6, some growth of intragranular austenite (IGA), scattered within the ferrite grains can be seen (also discernable in Fig. 3 (g)-(i)). The lattice diffusion of IGA is known to be slower than allotriomorphic growth of GBA. As a result, IGA will mainly grow when enough undercooling is available [19]. Thus, in this study, IGA morphology only appeared in small amounts compared with GBA and WA [23]. It is worth mentioning that precipitation of chromium nitride (Cr_2N), is a commonly reported feature in the HAZ of DSS [8,22]. However, such precipitation was not noticed in the current experiment.

Similar to the ferritic side, primary-austenite solidification of the weld metal on the duplex side of the fusion zone can be detected from the micrographs. It should be noted that in Fig. 3 (g)-(i) austenite grains appear darker than the intergranular region due to the effect of the secondary etchant used for the duplex side.

Fig. 3 (h) and (i) clearly reveal the existence of an intermediated zone with a different structure from the base and bulk weld metal. In like manner as on the S 960 side, macrosegregation is considered to be the reason for the variation in chemical composition leading to a different solidification mode in the intermediate region. In Fig. 3 (h), macrosegregation characterizes a PMZ, while in Fig. 3 (i) it presents as a composite structure made of a PMZ and unmixed zone (UMZ). The PMZ indicates a primary ferritic solidification (FA) mode during which primary-ferrite transformed to austenite through a peritectic-eutectic reaction in the liquid state [13]. FA solidification can occur when Cr_{eq}/Ni_{eq} is slightly higher than of the eutectic composition [24]. The structure comprises a vermicular or skeletal morphology of the delta ferrite in a matrix of austenite, delineated in Fig. 3 (h) and (i).

The microstructure of the fusion zone around the weld axis is shown in Fig 7 (a)-(c). As can be observed from the figure, as the cooling rate slowed down with increase of distance from the fusion boundary toward the weld axis, equiaxed growth became more dominant in all weld samples.

The average ferrite number (FN) of the austenitic weld metal, obtained from six ferrite readings, was 1.8, 1.2 and 1.1 for the WS 7.1, WS 8, and WS 9, respectively. It can be deduced that the higher heat input resulted in a higher dilution by the base metals, and thus increase of the FN.

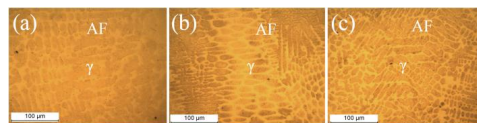


FIGURE 7. MICROSTRUCTURE OF THE WELD METAL AROUND THE WELD AXIS: (a) WS 7.1, (b) WS 8, AND (c) WS 9.

HARDNESS

Hardness values were obtained across a parallel distance of about 1 mm from the free faces of the weld samples along the indentation line shown in Fig. 8.

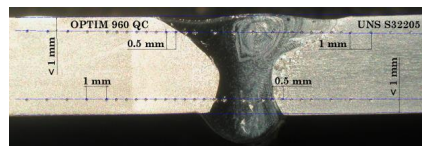


FIGURE 8. INDENTATION ALONG FACE AND ROOT SIDE OF THE WELD SPECIMEN.

The hardness profile of the face and root side of the specimens is shown in Fig. 9 and Fig. 10, respectively. In the diagrams, the labeled hardness values are associated with the indents that were placed approximately on the unaffected parent metals, initiation of the coarse grain heat affected zones, proximate to the fusion boundaries, and on the weld centerlines.

As can be seen from Fig. 9 and 10, the hardness of the unaffected S 960 was between 310-340 HV_5 . It can be clearly seen that the hardness declines in the direction toward the fusion boundary. In addition, HAZ softening is more severe in WS 7.1, with about 25 % decline in hardness at the lowest level, close to the fusion boundary. However, the reduction in hardness ameliorated when lower heat inputs were applied, so that for WS 9 the maximum reduction was only about 16 %.

Intermittent increases in hardness to a level close to that of the base metal (300-320 HV_5) can be seen in correlation with the martensitic phase in the microstructure. Hardness values of about 290 HV_5 can be associated with the bainitic phase. Moving forward from the coarse grain HAZ toward the fusion boundary, substantial attenuation of hardness at some points can

be noticed. The hardness of the softened points varies between 231-258 HV₅ in WS 7.1, 250-262 HV₅ in WS 8, and 268-269 HV₅ in WS 9. The low dislocation density of the new coarse grains formed from the intercritical austenite at this region can be significant contributor to this softening [3,25].

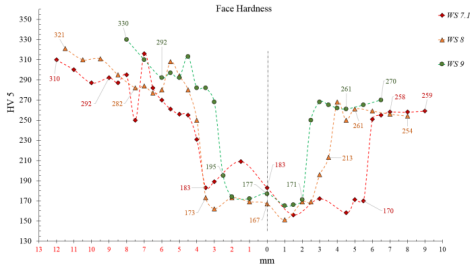


FIGURE 9. HARDNESS PROFILE AT A DISTANCE LESS THAN 1 MM FROM THE FACE SIDE OF THE WELDMENTS, IN THE TRANSVERSE DIRECTION FROM UNAFFECTED S 960 BASE METAL (LEFT) TOWARD UNAFFECTED BASE METAL S 32205 (RIGHT). THE VERTICAL DOTTED LINE APPROXIMATELY INDICATES THE CENTER LINE OF THE WELD SAMPLES. THE POINTS THAT ARE LABELED WITH VALUES ARE APPROXIMATELY ON THE UNAFFECTED BASE METALS, THE BEGINNING OF COARSE GRAIN HEAT AFFECTED ZONES, WELD METAL ADJACENT TO THE FUSION BOUNDARIES AND THE CENTERLINE OF THE WELDS.

The variation of hardness in the HAZ of the duplex side is less considerable. However, a moderate increasing trend in hardness profile can be discerned as measurements approach the fusion boundary, except for WS 7.1 on the face side. This increase may be related to the increased ferrite to austenite proportion ratio in the HAZ as a result of the thermal cycle experienced [26].

The austenitic fusion zone characterizes the softest region with hardness magnitudes in the range of 150-190 HV₅. The hardness values were generally higher for WS 8 and WS 9 than WS 7.1. The harder weld metal can be a result of the change in the austenitic weld texture from more equiaxed grains in WS 7.1 to more dendritic and columnar forms in WS 8 and WS 9. In addition, possible variations in the chemical composition as a result of macrosegregation in the weld may affect the hardness [8].

Formation of a hard martensitic layer was not seen in the hardness profile, possibly because the distance between the indentations was spaced too far apart to effectively ascertain a hardness layer that has a maximum width of 20 μm.

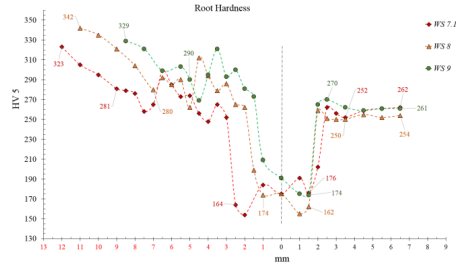


FIGURE 10. HARDNESS PROFILE AT A DISTANCE LESS THAN 1 MM FROM THE ROOT SIDE OF THE WELDMENTS, IN THE TRANSVERSE DIRECTION FROM UNAFFECTED S 960 BASE METAL (LEFT) TOWARD UNAFFECTED BASE METAL S 32205 (RIGHT). THE VERTICAL DOTTED LINE APPROXIMATELY INDICATES THE CENTER LINE OF THE WELD SAMPLES. THE POINTS THAT ARE LABELED WITH VALUES ARE APPROXIMATELY ON THE UNAFFECTED BASE METALS, THE BEGINNING OF COARSE GRAIN HEAT AFFECTED ZONES, WELD METAL ADJACENT TO THE FUSION BOUNDARIES AND THE CENTERLINE OF THE WELDS.

BEND PROPERTIES

Transverse root and face bending tests were carried out on the specimens using a mandrel with a diameter of 65 mm. The results are summarized in Table 3.

TABLE 3. TRANSVERSE FACE BENDING (TFB) AND TRANSVERSE ROOT BENDING (TRB). THE RESULTS ARE IN DEGREE ANGLE.

Specimen	TFB	TRB
WS 7.1	180°	67°
WS 8	180°	64°
WS 9	180°	37°

As can be seen from the results, all weld samples presented excellent ductile properties and passed the face bending test. However, all the specimens failed at the root side. It should be noted that the accumulation of strain mainly took place at the narrow soft fusion zone and proceeded by plastic deformation beyond the endurance of the weld metal and consequent fracture. A lower strain capacity can be expected on the root side as it has a narrower weld cross-section compared with the face side. The narrower fusion zone resulting from the lower heat input can also explain the decrease in ductility and failure angle of WS 9.

TENSILE BEHAVIOR

The yield and ultimate tensile strength of the samples are presented and compared with those of the parent metals in Table 4. The diagram shown in Fig. 11 gives a comparison of the average strength values. All specimens failed at the weld. This may be a consequence of stress concentration at this soft region

leading to a strain outside the range of the weld endurance and subsequent fracture. As can be seen in Fig. 11, increase in strength shows a direct correlation with decrease in heat input. It can be seen from Fig. 9 and 10 that lower heat input generally increased the hardness throughout the fusion zone and HAZ, by altering either the microstructural phases or the texture of the HAZ and weld metal. A slight increase in the hardness could more effectively constrain plastic deformation, thus increasing the strength.

TABLE 4. YIELD STRENGTH AND ULTIMATE TENSILE STRENGTH. TEST RESULTS OBTAINED FROM TWO REPLICATES (TEST 1 AND TEST 2) FOR EACH WELD SAMPLE. THE AVERAGE (AVE.) QUANTITIES ARE CALCULATED FROM TEST 1 AND TEST 2. (*) INDICATES VALUES FOR THE BASE METALS TAKEN FROM THE SUPPLIER'S CERTIFICATE.

Specimen	Yield strength (N/mm ²)			Ultimate tensile strength (N/mm ²)			Elongation Ave. (%)
	Test 1	Test 2	Ave.	Test 1	Test 2	Ave.	
WS 7.1	636.83	643.27	640.05	681.91	684.90	683.40	5.76
WS 8	651.43	666.34	658.88	687.02	701.99	694.51	5.10
WS 9	680	663.88	671.94	720.98	713.06	717.02	6.20
S 960	-	-	1004.5 *	-	-	1114.50 *	11.5
S 32205	-	-	631 *	-	-	825 *	28.5

The results show that the yield strength of the specimens declined compared with that of the S 960 base metal, with a drop of 36 % in WS 7.1 and 33 % in WS 9. However, the yield values still remained 1.5 % - 6.5 % higher than that of the S 32205 parent metal. In comparison, the ultimate strength of the specimens was 35% - 36% lower than that of S 960 and 13 % - 17% lower than S 32205.

It can be seen from Fig. 11 that the variation in elongation of the specimens was insignificant and did not have a coherent relation to the heat input. As mentioned above, the strain and the plastic deformation was mainly concentrated at the weld, which constitutes the softest region. Therefore, the elongation results may mainly represent the fracture strain of the weld metal.

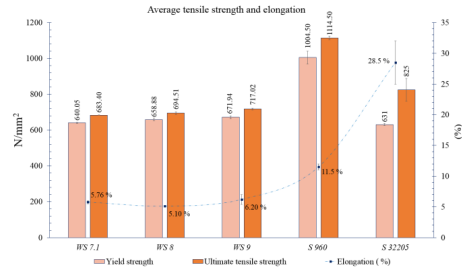


FIGURE 11. COMPARISON BETWEEN THE WELD SPECIMENS AND THE PARENT METALS IN TERMS OF AVERAGE YIELD AND ULTIMATE STRENGTH AS WELL AS ELONGATION (%).

IMPACT TOUGHNESS

Table 5 presents a summary of absorbed energy values from the Charpy V-notch impact test. The impact energies of the weld metal and HAZ were obtained from three sets of tests that were performed separately on the specimens with a notch either on the weld center or at 1 mm distance from the center toward the S 960 side, respectively. Average impact toughness values are also listed in the table.

TABLE 5. IMPACT TEST RESULTS OBTAINED WHEN APPLYING 150 J IMPACT ENERGY AT -40 °C. THREE SETS OF EXPERIMENTS WERE PERFORMED SEPARATELY ON THE WELD SPECIMENS WITH A V-NOTCH EITHER ON THE WELD CENTER OR WITH 1 MM OFFSET TOWARD HAZ OF THE S 960 SIDE. (*) INDICATES VALUES TAKEN FROM THE SUPPLIER'S CERTIFICATE.

Specimen	Weld metal (J.cm ⁻²)				HAZ of S 960 (J.cm ⁻²)			
	Test 1	Test 2	Test 3	Ave.	Test 1	Test 2	Test 3	Ave.
WS 7.1	71	31	50	50.67	43	23	48	38
WS 8	56	45	54	51.67	35	70	61	55.33
WS 9	44	41	46	43.67	43	59	44	48.67
S 960	60*	60*	57*	59*	-	-	-	-
S 32205	40*	60*	-	50*	-	-	-	-

Fig. 12 presents a comparison between the median absorbed impact energy of the specimens and the impact toughness of the parent metals. As can be seen from the figure, all the weld samples passed the minimum requirement of 27 J for the weld. However, the magnitudes were 14 % to 26 % lower than the absorbed energy of the S 960 base metal.

The results show outstanding impact toughness for WS 8, whereas WS 9 showed the highest brittleness. The impact toughness of the welds roughly matches the duplex base metal, except for WS 9, where the toughness was about 12 % lower than that of S 32205.

The HAZ of WS 7.1 showed highest embrittlement with an absorbed energy about 35.5 % less than that of the S 960 base

metal. However, the toughness was still well above the minimum requirement. In contrast, the impact toughness of WS 8 was 55.33 J, only about 6 % lower than that of S 960 but about 10 % higher than that of S 32205. For the HAZ of WS 9, the absorbed energy was roughly between that of WS 7.1 and WS 8 and about 17 % lower than that of S 960. The higher amount of hard martensite could be the principal cause of the brittleness in WS 9.

The superior impact toughness of WS 8 implies that the moderate heat input had a beneficial effect on the microstructure. The improved toughness of the HAZ may be a result of more balanced martensitic-bainitic phases in the HAZ as well as less intense grain coarsening compared with WS 7.1.

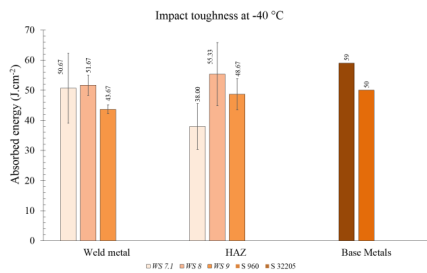


FIGURE 12. AVERAGE IMPACT STRENGTH AT THE WELD AND IN THE HAZ OF S 960. THE RESULTS WERE OBTAINED BY APPLYING 150 J IMPACT ENERGY AT -40 °C AND COMPARED WITH THE IMPACT STRENGTH OF THE BASE METALS AT THE SAME TEMPERATURE. THE V-NOTCH WAS ON THE WELD CENTER AND AT A DISTANCE OF 1 MM FROM THE WELD METAL TOWARD THE S 960 SIDE FOR WELD METAL AND HAZ, RESPECTIVELY.

FATIGUE BEHAVIOR

A servo hydraulic testing machine capable of 100 kN was used to perform the fatigue tests. The geometry of welded specimens used for fatigue testing can vary considerably, depending on the capability of the testing machine. However, for a satisfactory result, a transverse section of butt weld with a width of 70-75 mm is recommended [27]. The reason for having a wide weld section is that it represents a larger volume of the weld sample and, correspondingly, provides a higher probability of sampling regions containing a flaw (unintentional weld defect) [27]. In addition, butt welds in real structures are usually fairly wide. In this study, the fatigue strength of butt welds of dissimilar joints was assessed by conducting the cyclic tests on nine specimens with a geometry shown in Fig. 13.

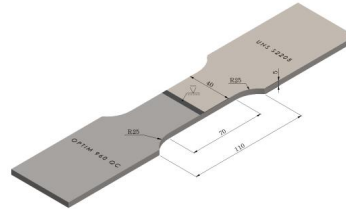


FIGURE 13. SCHEMATIC OF THE SPECIMENS PREPARED FOR THE FATIGUE TESTS.

Determined attempts were made to eliminate any possible misalignment in the samples during the welding and testing. For the class of weld used, full penetration is required (unless otherwise stated) and the misalignment should be less than 10 percent of the plate thickness, according to the standard [28]. These requirements were met for this study. Neither pre-treatments, such as preheating and edge-preparation, nor post-treatments, such as, stress relieving and reinforcement machining, were done, and all the tests were performed on specimens in as-weld condition.

Tests were conducted in three different stress ranges for each power class. The stress ratio for two repetitions (Test 1 and Test 2) was kept at R= 0.1 in order to compare the results with a standard design curve. All tests were performed at room temperature and frequency of 8 Hz. The results are illustrated in Fig 13.

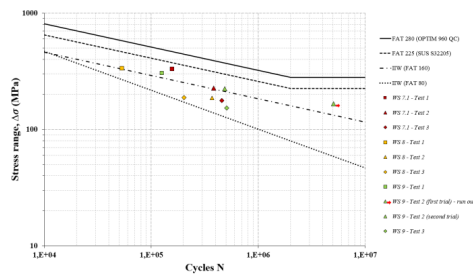


FIGURE 14. COMPARISON OF FATIGUE TEST RESULTS FOR DIFFERENT POWER CLASSES. FATIGUE RESISTANCE S-N CURVES (PF = 2.3 %) BASED ON IIW RECOMMENDATION [28] AND VALUES FROM STUDY OF THE BASE MATERIALS [29] ARE INCLUDED.

It should be noted that Fig. 14 presents a log-log plot of the data. The standard design curve is based on the equation (1) for the FAT class 80 corresponding to the type of welded joint tested [30]:

$$N = \frac{C}{\Delta\sigma^m} \quad (1)$$

In this equation, N and $\Delta\sigma$ stand for the number of cycles and stress range, respectively. The values of the slope, m , and the design value of the fatigue capacity, C , are considered as 3 and 1.024×10^{12} , respectively [28]. At each power class, specimen 3 was tested at $R=0.5$ in order to simulate the high residual stresses occurring in real structures. It is noteworthy that the endurable or permissible nominal stress amplitudes could be substantially reduced by high tensile residual stresses caused by welding in large structural members in contrast with small test specimens [30]. These permissible stresses are independent of mean stress (R ratio) in standard recommended curves. Therefore, fatigue testing to determine permissible stress amplitudes in welded joints should generally be performed with high R -values ($R=0.5$) to reflect appropriately the detrimental effect of high residual stresses in large structures when using laboratory test specimens. Another recommendation is to conduct the test at low stress ratio ($R=0$) and lower the fatigue limit at 2 million cycles by 20 % [28]. This modification makes the slope of the curve steeper.

It can be seen from the results (Fig. 14) that specimens tested at higher stress ratios to simulate conditions in real structures are the closest ones to the recommended curve for this weld class (FAT 80). It can be concluded that FAT class 80 works well for all power classes of dissimilar joints in this study, although it is slightly conservative for specimens tested at low stress ratios. It is recommended [28] that the upper band should be limited by the S-N curve of the parent material, if properly verified test data is available. Otherwise, FAT class 160 for steels is recommended [28]. This line has been added to Fig. 14 to check the scatter of the results. All specimens tested at high stress ratios are located between the limits, with the upper limit being slightly conservative for tests at low stress ratios.

To add the upper limits as the S-N curve of the base materials, the results of study on the same materials by Laitinen et al. [29], cut with different thermal and mechanical methods, are used. Laitinen et al. suggested FAT 280 for 960 QC and FAT 225 for material with yield strength between 600-700 MPa. Although it can be clearly seen from Fig. 14 that all the test results are covered by the curve for the weaker parent material (S 32205), using the upper bands based on the S-N curves of the parent materials cannot be considered as a safe criterion and the IIW recommendation of using FAT class 160 for the upper boundary is more conservative in real structures.

From the results, no clear correlation between the fatigue strength and heat input variations can be derived. This finding can be explained by the fact that the specimens were tested in as-welded condition without reinforcement removal, and as a consequence, geometrical effects could have a dominant influence on the fatigue results. It can be conjectured that the effect of heat input in dissimilar welds of such combinations should not be used as a prime determinant factor in the fatigue

life where the joints are expected to be used in as-welded condition and with no subsequent heat treatment. Conversely, geometrical effects can be taken as the major cause of failure in the specimens.

DISCUSSION

The objective of the current work was to study the influence of heat input on dissimilar welds between S 960 ultrahigh strength steel and S 32205 duplex stainless steel. To this end, butt welds were made between the base metals using an austenitic filler wire and applying three different heat inputs. The mechanical properties (i.e. hardness, strength, bend and impact toughness) as well as fatigue performance of the weldments were characterized in relation to the microstructural transitions in the HAZs, fusion boundary and fusion zone.

It was found that the hardness almost constantly increased as the heat input decreased for all the specimens, as seen from Fig. 9 and Fig. 10. However, the heat input had very different effects on the structure of the base and the weld metals. In the HAZ of S 960, nearly complete austenitization occurred as the temperature passed the upper-critical temperature (AC_2) close to the fusion boundary. Subsequent phase transition was to some extent affected by the cooling rate. At the most rapid cooling rate, martensite laths were prevalent in the microstructure. In contrast, transition to ductile bainite with predominantly lower bainite morphology was enhanced by increase in the heat input.

Some exceptionally high values in the hardness profile, in the range of 320 HV₅ to 340 HV₅, may be associated with thin laths of martensite with high dislocation density. Hardness values in the range of 260-300 HV₅ can reflect the hardness of twisted laths of lower bainite with a high dislocation density [31]. However, both bainite and martensite can have lower hardness magnitudes with intensified grain coarsening, leading to lower dislocation density. The detrimental effect of coarse grain on hardness is clearly reflected in the hardness profile, which shows a steep drop to a range from 180 HV₅ to 220 HV₅ as it approaches the fusion line. The intense grain coarsening can explain the severe degradation of hardness on the HAZ of WS 7.J welded with the highest heat input.

It is known that austenitic weld metal is not hardenable. However, the ascertained hardness values were slightly higher for welds made with higher cooling rates (i.e. WS 8 and WS 9). Different sources in the literature have identified hardness increase in the austenitic fusion zone [13,32]. Possible causes of this hardness increase include precipitation hardening effects, residual stresses, the texture of the weld, and microstructure refinement due to rapid solidification of the weld pool [32]. The influence of weld heat input on the weld texture is clearly seen in Fig. 2 (d)-(f). It appears that the columnar and dendritic grain growth in the austenitic weld metal to some extent increased the hardness indexes of WS 8 and WS 9.

Inconsistency in the chemical composition of the weld could be another significant source of variation in hardness. It should be noted that formation of macrosegregation as filler-

depleted and filler-enriched zones is quite probable due to the pronounced mismatch in the chemico-physical characteristics of the filler and base metals [8,14,18,33]. Segregation of Ni, Cr, and Mo are especially important in the mechanical properties of austenitic weld metals. It is well established that a higher concentration of Ni can improve ductility and strength, whereas a higher Cr and Mo content will promote hardness [26,34,35].

Despite the grain coarsening on the duplex side, the hardness indexes of the coarse HAZ were comparatively higher closer to the fusion boundary. The microstructure of this region was composed of large ferrite domains embedding a small portion of newly formed or retained austenite, as seen from the micrographs in Fig. 3 (g)-(i) and Fig. 6. The increase in hardness can indicate a higher proportion of ferrite to austenite phases in the coarse HAZ [13]. Higher cooling rates further restrict the austenitic growth. Thus, a higher ferrite portion and a harder structure can be expected for the coarse HAZ of WS 8 and WS 9 in comparison with WS 7.1, which is in agreement with the hardness profile.

The higher hardness of ferrite compared with austenite can be attributed to a higher amount of Cr and Mo, i.e. ferrite stabilizing elements, partitioned into the ferritic domains concomitant with the formation of ferrite [24,26]. Nonetheless, the short thermal cycle experienced at the HAZ can constrain elemental partitioning [36]. As a result, a slight difference between the composition of ferrite and newly formed austenite phases would only cause a marginal, yet noticeable, effect on hardness values.

The restrictive effect of a harder structure on the strain can be clearly seen from the tensile tests. The results indicate that increase in strength corresponds with increase in hardness as a result of higher cooling rates. Regarding the S 960 HAZ, a complex of a higher proportioned fraction of martensite in the matrix, reduced extent of grain coarsening and size of the intercritical austenite grains, as well as a higher amount of retained strain and dislocation density consequent on the higher cooling rates could have favored the strength of the WS 8 and WS 9 [35,37].

The strength of the S 32205 HAZ can be regulated by the ferritic phase as well as the amount, form and distribution of the austenite [36]. This emphasizes the role of heat input in ferritization and consequent growth of austenite in the HAZ [19,23]. It is hypothesized that strain initially partitions equally between the ferrite and austenite phases, but, it soon transfers to the ferritic phase as the austenite loses its coherence. Consequently, the deformation to the yield point is chiefly accommodated by ferrite [38,39]. Therefore, it can be assumed that the presence of a higher amount of harder ferrite could have contributed to the increase in strength of WS 8 and WS 9.

It was noted that all samples fractured at the highly ductile austenitic weld, which is the softest region of the joint. The considerably under-matching hardness of the weld metal could affect the overall evaluation of tensile and yield strength. It can be postulated that the plastic deformation at the weld initiated at the lower stress ranges required for adjacent HAZs to reach to

their yield point. Therefore, the results may not properly describe the tensile and yield behaviors occurring as a result of the microstructural alterations in the HAZ on the ferritic and duplex sides.

The concentration of strain on the austenitic weld metal can also explain the elongation results showing no apparent relation to the amount of heat input and no distinct variations between the samples. It can be suggested that the elongation values are not truly a measure of the whole structure; they principally demonstrate the plastic capacity of the austenitic fusion zone.

The bend test provided contradictory outcomes for the root and face side of the samples. All specimens show similarly perfect ductile behavior on the face side and passed the TFB test. However, they all failed the TRB test. As was discussed above, for proper interpretation of the results, it is critical that strain accumulation at the soft fusion zone be taken into consideration. Previously, Shi et al. [40] have demonstrated that the size of the plastic zone is directly connected to the yield strength in three-point bend testing. Thus, it can be assumed that the narrower weld at the root side failed due to lower strain capacity compared with the wider cross-section at the face side.

It could also be correct to suggest that the fracture angle at the root side decreased as the weld became narrower correlatively with the lower heat input. However, the effect of geometry on tension distribution, macrosegregation and local micro-hardness variations as well as the contribution of the neighboring HAZs in the ductile behavior of the joint cannot be entirely disregarded. It should be noted that a longitudinal bending test is recommended for dissimilar welds with considerable mismatches in mechanical properties. However, in this study this test was not performed due to insufficient material to prepare the specimens. Therefore, additional tests are required to enable more accurate conclusions to be made regarding the bend behavior of the welded joint.

The impact test results show inconsistent toughness properties for the fusion zone and the HAZ on the S 960 side. As expected, the austenitic weld metal exhibited favorable ductile properties and the absorbed energies at -40 °C matched the duplex side and were quite close to those of the S 960 side, with the exception of WS 9.

It has been shown that variations in the toughness of austenitic weld metal can be related to the solidification mode and grain growth pattern [14]. As was noted in the microstructural observations, the solidification mode was primary-austenite in all weld samples. Hence, the toughness variation could be partly a result of weld texture and/or compositional inhomogeneity. In addition, a reduction in impact toughness can be expected when the strain is concentrated on the narrow soft weld metal [5]. Therefore, the lower absorbed energy of WS 9 could to some extent be explained on the grounds of the narrower weld profile of WS 9 in comparison with the other samples. Moreover, the impact toughness degradation could be induced by the macrosegregation in the weld that appeared in connection with lower heat inputs.

The HAZ of *WS 7.1* showed the lowest impact toughness, which was consistent in the three sets of tests performed. The low impact toughness could be considered as unexpected for the predominantly bainitic structure of the *WS 7.1* HAZ. However, the result provides a credible indication of the grain coarsening effect. As was mentioned earlier, higher heat inputs extend and enlarge the coarse grains, which can severely degrade the toughness, since the prior-austenite grain boundaries have an inhibitive effect on crack propagation. The detrimental effect of large intercritical austenite grains on crack propagation resistance and the consequent impact toughness has been reported in several studies [3,37,41]. Guo et al. [3] have stated that the pernicious effects of coarse grains are so significant that they outweigh any advantages that could be obtained from the reduction in hardness and the soft structure.

The benefit of having a finer grain structure can be observed also from the impact toughness of the *WS 9* HAZ in comparison with that of the *WS 7.1* HAZ. It is known that the impact toughness value of hard martensite is significantly less than that of the bainitic phase [37,42]. In addition, the growth of strong martensite can induce plastic deformation in the surrounding grains and increase the dislocation density, which tends to degrade toughness [37]. However, Tomita et al. [43] have shown that the strength and toughness of martensite and bainite can vary significantly depending on the prior-austenite grain size. That being the case, a more moderate grain coarsening in *WS 9* could have favored its superior toughness compared with the *WS 7.1*, despite having a higher amount of hard martensite. Moreover, the martensitic phase may be partially autotempered due to the special composition of the *S 960*, which would improve the toughness in spite of the increased hardness [37].

The absorbed impact energy of *WS 8* was comparable to that of the *S 960* parent metal. This result suggests that a microstructure comprising a mixture of bainite and martensite would appreciably improve ductility and toughness of the HAZ, in agreement with the work presented in [44] and [45]. Based on the current experiment, a regulated cooling time to prevent the occurrence of coarse grain as well as to create a balance between the martensite and bainite morphologies can be recommended for optimum impact toughness properties without significant deterioration in strength and hardness.

The fatigue test demonstrated that the fatigue strength of the samples is covered by the S-N curve of the weaker base metal, which in this case is *S 32205*. In addition, the results of all specimens tested at high stress ratios are located above the recommended lower limit (FAT 80). However, at lower stress ratios, the recommended upper limit (FAT 160) seems to be relatively conservative and all the specimens were marginally placed above the curve.

A notable characteristic of the current test is that the dissimilar weld interface is characterized by considerable mechanical heterogeneity, which may substantially affect the fracture resistance and crack growth paths in different locations of the interface. It has been determined that local stress and

strain distributions ahead of cracks and crack growth paths are significantly governed by local mismatches in strength and hardness as well as by fracture intrinsic toughness around crack tips [46]. It has also been shown that strength mismatches in the weld interface generally divert the crack propagation toward the lower strength intrinsic toughness region [46,47]. However, mechanical mismatches are primarily significant in low-cycle fatigue strength, and they can thus be discounted in the high-cycle fatigue region in the current study [48].

As is shown in Fig. 14, the fatigue performance did not show a clear trend in correlation with the heat input variation. However, the fracture location may to some extent be affected by the microstructure resultant from the heat input. It was noticed that in the case of *WS 7.1* and *WS 8*, all weld samples failed at the weld toe on the *S 960* side, while for *WS 9*, only one sample failed on the *S 960* side and the other samples fractured at the toe on the *DSS* side. This failure pattern could be the result of geometrical effects combined with the microstructural features of the fusion boundary. The fatigue life of a welded joint is determined by the crack initiation followed by crack propagation. The presence of weld reinforcement can act as a stress raiser and concentrate the stress at the weld toe, which triggers the crack initiation at the point of stress concentration [6].

It is known that in the welded joints, crack initiation time is short, due to inherent flaws such as micro-voids. The propagation of cracks, which is the result of coalescence of micro-voids and the growth of micro- and meso- cracks, is affected by the ductile properties around the crack tips. It appears that the fracture resistance of the coarse austenitic-ferritic structure of the *DSS* side of the interface was superior to that of the predominantly coarse martensitic-bainitic structure at the ferritic side in the majority of the samples. The presence of a hard martensitic band as well as dendritic and columnar growth of austenite at the ferritic side of the weld interface could to some extent have enhanced the crack propagation in this region. Earlier, Shang et al. [49] have demonstrated that the fatigue crack path and propagation rate in a weld between austenitic stainless steel and ferritic steel is highly influenced by the microstructural properties, including columnar grain growth of austenite in the weld region, a martensitic layer at the interface, and coarse martensite in the HAZ [49]. They emphasized the significance of columnar grain growth in the crack propagation transgranularly parallel to the dendrite structure.

The microstructural observations in this study showed that with the lowest heat input, the integrity of the *WS 9* weld on the duplex side was clearly affected by macrosegregation in the form of a partially mixed and unmixed zone at the *DSS* side. The impaired integrity could have affected the fracture strength and intrinsic ductile properties of the weld interface with the *DSS* base metal. Nevertheless, the occurrence of macrosegregation might not be consistent throughout the weld, which could account for the inconsistent failure pattern in *WS 9*.

As the tests were performed on as-welded samples without removal of the reinforcement, it can be suggested that the geometrical effects were greater than the effect of heat input and the consequent microstructure. Based on the findings in this study, it could be assumed that in practical applications of such dissimilar welds, the heat input would only have a marginal impact on the fatigue performance compared to the geometrical effects. Nevertheless, supplementary tests on specimens with removed reinforcements are necessary to remove uncertainty regarding the effect of heat input and microstructural characteristics on fatigue performance.

CONCLUSIONS

In the current study, dissimilar GMAW welds of Optim 960 QC (S 960) direct-quenched ultrahigh strength steel and UNS S32205 (S 32205) duplex stainless steel were made using a fully austenitic filler wire and applying three different welding speeds. The effect of different heat inputs on the microstructural and mechanical characteristics and fatigue behavior of the welds was studied. The following observations and conclusions were drawn:

When studying the HAZs, severe grain coarsening was noticed on both the ferritic and duplex sides. Higher heat input enhanced bainitic transformation on the ferritic side, and more martensite was observed with higher cooling rates (WS 8 and WS 9). On the duplex side, macrosegregation appeared with higher cooling rates on the fusion boundary in the form of partially mixed and/or unmixed zones (PMZ/UMZ) with a different solidification mode than the bulk weld metal.

In the bulk weld metal, more granular and equiaxed austenite formed with the higher heat input (WS 7.1), while dendritic and columnar austenitic growth was noticed with the higher cooling rates (WS 8 and WS 9).

Coarse grain formation and reduced dislocation density in the HAZ of S 960 caused a substantial reduction in the hardness close to the fusion boundary.

With lower heat input, more martensitic transformation and limited austenitic transition increased the hardness in the HAZ of S 960 and S 32205, respectively.

Improvement in tensile and yield strength showed a direct correlation with the harder structure of the weldments. Accordingly, the highest tensile and yield strength were recorded for WS 9.

The bend test results were affected by the thickness of the soft austenitic weld metal. Accumulation of the strain in the narrow soft weld in root bending caused fracture in all specimens, despite showing excellent ductile behavior on the face side.

The impact toughness of the specimens was well above the minimum 27 J requirement, both in the weld and in the S 960 HAZ.

In the ferritic HAZ, superior impact toughness, comparable to that of the S 960 parent metal, was achieved with a moderate heat input (WS 8). This finding may indicate the beneficial

effect of a balanced bainitic-martensitic structure on the toughness properties.

The fatigue test results indicate that the fatigue life of the specimens was principally influenced by geometrical effects rather than variations in the microstructure consequent on the amount of heat input. The location of the fracture could be affected by the microstructure of the fusion boundary and macrosegregation in this region.

ACKNOWLEDGMENTS

The authors would like to thank Mr. Peter Jones for his comments and assistance with the English language.

REFERENCES

- [1] Tasalloti, H., Eskelinen, H., Kah, P., and Martikainen, J., 2016, "An integrated DFMA-PDM model for the design and analysis of challenging similar and dissimilar welds," *Mater. Des.*, 89, pp. 421–431.
- [2] Farrokhi, F., Siltanen, J., and Salminen, A., 2015, "Fiber laser welding of direct-quenched ultrahigh strength steels: evaluation of hardness, tensile strength, and toughness properties at subzero temperatures," *J. Manuf. Sci. Eng.*, 137, pp. 061012-1–10.
- [3] Guo, W., Crowther, D., Francis, J.A., Thompson, A., Liu, Z., and Li, L., 2015, "Microstructure and mechanical properties of laser welded S960 high strength steel," *Mater. Des.*, 85, pp. 534–548.
- [4] Wallin, K., Pallaspuuro, S., Valkonen, I., Roikonen, P.K., and Suikkanen, P., 2015, "Fracture properties of high performance steels and their welds," *Eng. Fract. Mech.*, 135 pp. 219–231.
- [5] Siltanen, J., Tihinen, S., and Kömi, J., 2015, "Laser and laser gas-metal-arc hybrid welding of 960 MPa direct-quenched structural steel in a butt joint configuration," *J. Laser Appl.*, 27 (52), pp. S29007-1–8.
- [6] Nykänen, T., Björk, T., and Laitinen, R., 2012, "Fatigue strength prediction of ultra high strength steel butt-welded joints," *Fatigue Fract. Eng. Mater. Struct.*, 36, pp. 469–482.
- [7] Dabiri, M., Isakov, M., Skriko, T., and Björk, T., 2016 "Experimental fatigue characterization and elasto-plastic finite element analysis of notched specimens made of direct-quenched ultra-high-strength steel," *Proc IMechE Part C: J Mechanical Engineering Science*, pp.1–18.
- [8] Tasalloti, H., Kah, P., and Martikainen, J., 2017, "Effect of heat input on dissimilar welds of ultra high strength steel and duplex stainless steel: Microstructural and compositional analysis," *Mater. Charact.*, 123, pp. 29–41.
- [9] Kotecki, D.J., and Siewert, T.A., 1992, "WRC-1992 constitution diagram for stainless steel weld metals: a modification of the WRC-1988 Diagram," *Weld. J.*, 71, p.p. 171s–178.
- [10] Hobbacher, A.F., 2016, *Recommendations for Fatigue Design of Welded Joints and Components*, Springer.

- [11] Guo, A., Misra, R.D.K., Xu, J., Guo, B., and Janstoc, S.G., 2010, "Ultrahigh strength and low yield ratio of niobium-microalloyed 900 MPa pipeline steel with nano-ultrafine bainitic lath", *Mater. Sci. Eng. A*, 527, pp. 3886–3892.
- [12] Kujanpaa, V.P., David, S.A., and White, C.L., 1986, "Formation of hot cracks in austenitic stainless steel welds—solidification cracking," *Weld. J.*, pp. 203-s–212-s.
- [13] Rahmani, M., Eghlimi, A., and Shamanian, M., "Evaluation of microstructure and mechanical properties in dissimilar austenitic/super duplex stainless steel joint," *J. Mater. Eng. Perform.*, 23, pp. 3745–3753.
- [14] Kou, S., 2003, *Welding Metallurgy*, John Wiley & Sons.
- [15] Dupont, J.N., and Kusko, C.S., 2007, "Technical note: martensite formation in austenitic/ferritic dissimilar alloy welds," *Weld. J.*, 86 (2), pp. 51-s–54-s.
- [16] Doody, T., 1992, "Intermediate mixed zones in dissimilar metal welds for sour service," *Weld. J.*, 71 (3), pp. 55–60.
- [17] Omar, A.A., 1998, "Effects of welding parameters on hard zone formation at dissimilar metal welds," *Weld. J.*, 77 (2), pp. 86-s–93-s.
- [18] Kou, S., and Yang, Y.K., 2007, "Fusion-boundary macrosegregation in dissimilar-filler welds," *Weld. J.*, 86, pp. 303-s–312-s.
- [19] Eghlimi, A., Shamanian, M., Eskandarian, M., Zabolian, A., Nezakat, M., and Szpunar, J.A., 2015, "Evaluation of microstructure and texture across the welded interface of super duplex stainless steel and high strength low alloy steel," *Surf. Coat. Technol.*, 264, pp. 150–162.
- [20] Ornath, F., Soudry, J., Weiss, B., and Minkoff, I., 1991 "Weld pool segregation during the welding of low alloy steels with austenitic electrodes," *Weld. J.*, 60, pp. 227-s – 230-s.
- [21] Zhang, W., DebRoy, T., Palmer, T.A., and Elmer, J.W., 2005, "Modeling of ferrite formation in a duplex stainless steel weld considering non-uniform starting microstructure," *Acta Mater.*, 53 (16), pp. 444–4453.
- [22] Ramirez, A.J., Lippold, J.C., and Brand, S.D., 2003, "The relationship between chromium nitride and secondary austenite precipitation in duplex stainless steels," *Metall. Mater. Trans. A*, 34, pp.1575–1597.
- [23] Atamert, S., and King, J.E., 1991, "Elemental partitioning and microstructural development in duplex stainless steel weld metal," *Acta Metall. Mater.*, 39 (3), pp. 273-285.
- [24] Lippold, J.C., and Savage, W.F., 1979, "Solidification of austenitic stainless steel weldments: part I—a proposed mechanism," *Weld. J.*, pp. 362-s– 374-s.
- [25] Qiu, J., Ju, X., Xin, Y., Liu, S., Wang, Y.L., Wu, H.B., and Tang, D., 2010, "Effect of direct and reheated quenching on microstructure and mechanical properties of CLAM steels," *J. Nucl. Mater.*, 407, pp. 189–194.
- [26] Sadeghian, M., Shamanian, M., Shafyei, A., 2014, "Effect of heat input on microstructure and mechanical properties of dissimilar joints between super duplex stainless steel and high strength low alloy steel," *Mater. Des.*, 60, pp. 678–684.
- [27] Gurney, T., 1979, *Fatigue of Welded Structures*, Cambridge University Press, Cambridge, UK.
- [28] Hobbacher, A., 2013, *Recommendations for Fatigue Design of Welded Joints and Components*, International Institute of Welding, Doc. No. XIII-2460-13/XV-1440-13, Paris.
- [29] Laitinen, R., Valkonen, I., and Kömi, J., 2013, "Influence of the base material strength and edge preparation on the fatigue strength of the structures made by high and ultra-high strength steels," 5th Fatigue Design Conference.
- [30] Radaj, D., Sonsino, C., and Fricke, W., 2006, *Fatigue Assessment of Welded Joints by Local Approaches*, Woodhead Publishing Limited, Cambridge.
- [31] Zhang, Y.Q., Liu, W.M., H. Hou, 2009, "Effects of Nb on microstructure and continuous cooling transformation of coarse grain heat-affected zone in 610 MPa class high-strength low-alloy structural steels," *Mater. Sci. Eng. A*, 499, pp. 182–186.
- [32] Sathiya, P., Mishra, M.K., and Shanmugarajan, B., "Effect of shielding gases on microstructure and mechanical properties of super austenitic stainless steel by hybrid welding," *Mater. Des.*, 33 pp. 203–212.
- [33] Robert, W., and Messler, Jr., 2004, *Principles of Welding: Processes, Physics, Chemistry, and Metallurgy*, WILEY-VCH, NY, USA.
- [34] Midawi, A.R.H., Santos, E.B.F., Huda, N., Sinha, A.K., Lazor, R., and Gerlich, A.P., 2015, "Microstructures and mechanical properties in two X80 weld metals produced using similar heat input," *J. Mater. Process. Technol.*, 226, pp. 272–279.
- [35] Karlsson, L., and Bhadeshia, H.K.D.H., 2011, "Some European developments in welding consumables," *Journal of the Japan Welding Society*, 80, pp. 110-119.
- [36] Wang, J., Lu, M., Zhang, L., Chang, W., Xu, and L., Hu, L., 2012, "Effect of welding process on the microstructure and properties of dissimilar weld joints between low alloy steel and duplex stainless steel," *Int. J. Miner. Metall. Mater.*, 19 (6), pp. 518–524
- [37] Kömi, J., 2016, "Direct-Quenched Structural Steels," *Encyclopedia of Iron, Steel, and Their Alloys*, CRC Press, pp. 1–17.
- [38] Balancin, O., Hoffmann, W.A.M., and Jonas, J.J., 2000, "Influence of microstructure on the flow behavior of duplex stainless steels at high temperatures," *Metall. Mater. Trans. A*, 31, pp.1353–1364.
- [39] Krupp, U., Giertler, A., Söker, M., Fub, H., Dönges, B., Christ, H.-J., Hüsecken, A., Pietsch, U., Fritzen, C.-P., and Ludwig, W., 2015, "The behavior of short fatigue cracks during Very High Cycle (VHCF) Fatigue of duplex stainless steel," *Eng. Fract. Mech.*, 145, pp.197–209.
- [40] Shi, Y., Han, Z., and Fu, J., 1998, "Effects of weld strength undermatch on fracture toughness of HAZ notched weldments in a HSLA steel," *Int. J. Fract.*, 91, pp.349–358.

- [41] Babu, N.K., Suresh, M.R., Sinha, P.P., and Sarma, D.S., 2006, "Effect of austenitizing temperature and cooling rate on the structure and properties of a ultrahigh strength low alloy steel," *J. Mater. Sci.*, 41, pp. 2971–2980.
- [42] Esfahani, M.N., Coupland, J., and Marimuthu, S., 2014, "Microstructure and mechanical properties of a laser welded low carbon–stainless steel joint," *J. Mater. Process. Technol.*, 214, pp. 2941–2948.
- [43] Tomita, Y., and Okabayashi, K., 1986 "Effect of microstructure on strength and toughness of heat-treated low alloy structural steels," *Metall. Trans. A*, 17, pp. 1203–1209.
- [44] Narasimha Rao, T.V.L., Dikshit, S.N., Malakondaiah, G., Rama Rao, P., 1990, "On mixed upper bainite-martensite in an AISI 4330 steel exhibiting an uncommonly improved strength-toughness combination," *Scripta Metall. Mater.*, 24 (7), pp.1323-1328.
- [45] Abbaszadeh, K., Saghafian, H., and Kheirandish, S., 2012, "Effect of bainite morphology on mechanical properties of the mixed bainite-martensite microstructure in D6AC steel," *Mater. Sci. Technol.*, 28 (4), pp. 336–342.
- [46] Fan, K., Wang, G.Z., Xuan, F.Z., and Tu, S.T., 2016, "Local failure behavior of a dissimilar metal interface region with mechanical heterogeneity," *Eng. Fail. Anal.*, 59, pp. 419–433.
- [47] Gubeljak, N., 1999, "Fracture behaviour of specimens with surface notch tip in the heat affected zone (HAZ) of strength mis-matched welded joints," *Int. J. Fract.*, 100, pp. 155–167.
- [48] Saiprasertkit, K., Hanji, T., and Miki, C., 2012, "Fatigue strength assessment of load-carrying cruciform joints with material mismatching in low- and high-cycle fatigue regions based on the effective notch concept," *Int. J. Fatigue*, 40, pp. 120–128.
- [49] Shang, Yi-Bo, Shi, Hui-Ji, Wang, Zhao-Xi, and Zhang, Guo-Dong, 2015, "In-situ SEM study of short fatigue crack propagation behavior in a dissimilar metal welded joint of nuclear power plant," *Mater. Des.*, 88, pp. 598–60.

ACTA UNIVERSITATIS LAPPEENRANTAENSIS

711. KUORIKOSKI, TERO. Kohti resonoivaa urheilujohtamista – Tavoitteen muodostuminen urheilun kentässä. 2016. Diss.
712. LAHTELA, VILLE. Improving the properties of solid Scots pine (*Pinus sylvestris*) wood by using modification technology and agents. 2016. Diss.
713. NEVARANTA, NIKO. Online time and frequency domain identification of a resonating mechanical system in electric drives. 2016. Diss.
714. FANG, CHAO. Study on system design and key technologies of case closure welding for ITER correction coil. 2016. Diss.
715. GARCÍA PÉREZ, MANUEL. Modeling the effects of unsteady flow patterns on the fireside ash fouling in tube arrays of kraft and coal-fired boilers.
716. KATTAINEN, JARI. Heterarkkisen verkostoyhteistyön johtamistarpeet verkoston muotoutumisvaiheessa. 2016. Diss.
717. HASAN, MEHDI. Purification of aqueous electrolyte solutions by air-cooled natural freezing. 2016. Diss.
718. KNUTAS, ANTTI. Increasing beneficial interactions in a computer-supported collaborative environment. 2016. Diss.
719. OVASKA, SAMI-SEPPO. Oil and grease barrier properties of converted dispersion-coated paperboards. 2016. Diss.
720. MAROCHKIN, VLADISLAV. Novel solutions for improving solid-state photon detector performance and manufacturing. 2016. Diss.
721. SERMYAGINA, EKATERINA. Modelling of torrefaction and hydrothermal carbonization and heat integration of torrefaction with a CHP plant. 2016. Diss.
722. KOTISALO, KAISA. Assessment of process safety performance in Seveso establishments. 2016. Diss.
723. LAINE, IGOR. Institution-based view of entrepreneurial internationalization. 2016. Diss.
724. MONTECINOS, WERNER EDUARDO JARA. Axial flux permanent magnet machines – development of optimal design strategies. 2016. Diss.
725. MULTAHARJU, SIRPA. Managing sustainability-related risks in supply chains. 2016. Diss.
726. HANNONEN, JANNE. Application of an embedded control system for aging detection of power converter components. 2016. Diss.
727. PARKKILA, JANNE. Connecting video games as a solution for the growing video game markets. 2016. Diss.
728. RINKINEN, SATU. Clusters, innovation systems and ecosystems: Studies on innovation policy's concept evolution and approaches for regional renewal. 2016. Diss.
729. VANADZINA, EVGENIA. Capacity market in Russia: addressing the energy trilemma. 2016. Diss.

730. KUOKKANEN, ANNA. Understanding complex system change for a sustainable food system. 2016. Diss.
731. SAVOLAINEN, JYRKI. Analyzing the profitability of metal mining investments with system dynamic modeling and real option analysis. 2016. Diss.
732. LAMPINEN, MATTI. Development of hydrometallurgical reactor leaching for recovery of zinc and gold. 2016. Diss.
733. SUHOLA, TIMO. Asiakaslähtöisyys ja monialainen yhteistyö oppilashuollossa: oppilashuolto prosessi systeemisenä palvelukokonaisuutena. 2017. Diss.
734. SPODNIAK, PETR. Long-term transmission rights in the Nordic electricity markets: An empirical appraisal of transmission risk management and hedging. 2017. Diss.
735. MONTONEN, JUHO. Integrated hub gear motor for heavy-duty off-road working machines – Interdisciplinary design. 2017. Diss.
736. ALMANASRAH, MOHAMMAD. Hot water extraction and membrane filtration processes in fractionation and recovery of value-added compounds from wood and plant residues. 2017. Diss.
737. TOIVANEN, JENNI. Systematic complaint data analysis in a supply chain network context to recognise the quality targets of welding production. 2017. Diss.
738. PATEL, GITESHKUMAR. Computational fluid dynamics analysis of steam condensation in nuclear power plant applications. 2017. Diss.
739. MATTHEWS, SAMI. Novel process development in post-forming of an extruded wood plastic composite sheet. 2017. Diss.
740. KÄHKÖNEN, TOMMI. Understanding and managing enterprise systems integration. 2017. Diss.
741. YLI-HUUMO, JESSE. The role of technical dept in software development. 2017. Diss.
742. LAYUS, PAVEL. Usability of the submerged arc welding (SAW) process for thick high strength steel plates for Arctic shipbuilding applications. 2017. Diss.
743. KHAN, RAKHSHANDA. The contribution of socially driven businesses and innovations to social sustainability. 2017. Diss.
744. BIBOV, ALEKSANDER. Low-memory filtering for large-scale data assimilation. 2017. Diss.
745. ROTICH, NICOLUS KIBET. Development and application of coupled discrete and continuum models in solid particles classification. 2017. Diss.
746. GAST, JOHANNA. The cooperation-innovation nexus: Investigating the role of cooperation for innovation in SMEs. 2017. Diss.
747. KAPOOR, RAHUL. Competition and disputes in the patent life cycle. 2017. Diss.
748. ALI-MARTTILA, MAAREN. Towards successful maintenance service networks – capturing different value creation strategies. 2017. Diss.

